Biogeochemistry of dissolved aluminium and manganese in the Indian Ocean

A thesis submitted in partial fulfilment of the requirements for the degree of

Doctor of Philosophy

by

Naman Deep Singh

(Roll No.: 15330003)

under the supervision of

Prof. Sunil Kumar Singh
Professor (on Lien), Geosciences Division,
PHYSICAL RESEARCH LABORATORY;
Director,
CSIR-NATIONAL INSTITUTE OF OCEANOGRAPHY, GOA

and co-supervision of

Prof. Ravi Bhushan
Professor, Geosciences Division,
PHYSICAL RESEARCH LABORATORY

DISCIPLINE OF EARTH SCIENCES

INDIAN INSTITUTE OF TECHNOLOGY GANDHINAGAR

March, 2021

DECLARATION

I, **Naman Deep Singh**, hereby declare that the research work incorporated in the present thesis titled **"*Biogeochemistry of dissolved aluminium and manganese in the Indian Ocean*"** is my own work and is original. This work (in part or in full) has not been submitted elsewhere for the award of a Degree or a Diploma. I have properly acknowledged the material collected from secondary sources wherever required.

I solely own the responsibility for the originality of the entire content.

Date: (Naman Deep Singh)

CERTIFICATE

It is certified that the work contained in this thesis titled "***Biogeochemistry of dissolved aluminium and manganese in the Indian Ocean***", by Naman Deep Singh (Roll No.: 15330003), has been carried out under my supervision.

I am satisfied with the analysis of data, interpretation of results and conclusions drawn.

I recommend the submission of the thesis.

Date:

Prof. Sunil Kumar Singh (supervisor)
Professor (on Lien), Geosciences Division,
Physical Research Laboratory,
Ahmedabad, India;

Director,
CSIR-National Institute of Oceanography,
Goa, India

Prof. Ravi Bhushan (co-supervisor)
Professor, Geosciences Division,
Physical Research Laboratory,
Ahmedabad, India

Dedicated to

my Mom and loving memories of my Papa

Contents Page

ACKNOWLEDGEMENTS

The research work done in this thesis could not have been completed without the support and care of a number of individuals. I would like to thank them all for their help and guidance.

First of all, I would like to extend my deepest gratitude to my thesis supervisor, Prof. Sunil Kumar Singh, who has always been there to share with me his knowledge and skills on the subject of trace metal biogeochemistry. Even smallest of the discussions with him has been an important lesson on the subject and provided crucial inputs to the research. Most importantly, he has always encouraged me to go about a research problem or idea in my own way, which I personally feel has nurtured me to be an independent researcher. I shall always be indebted to him for giving enough time for my guidance out of his busiest of the schedules.

I am sincerely grateful to my doctoral committee members, Prof. Ravi Bhushan (co-supervisor) and Dr. Neeraj Rastogi, for their consistent guidance and encouragements throughout the Ph.D. tenure. Their support, in both academic and non-academic matters, has allowed me to sail smoothly through the toughest of the situations. Scientific discussions with Prof. M. M. Sarin have always been fruitful and improved the understanding at early stages of the research work.

I am obliged to all the other geosciences division faculty members, Prof. J. S. Ray, Prof. R. D. Deshpande, Prof. M. G. Yadava, Dr. Sanjeev Kumar, Dr. Arvind Singh, Dr. Vineet Goswami, Dr. A. K. Sudheer, Dr. A. D. Shukla and Dr. A. H. Laskar, for their discussions and critical evaluation of my research work during the area seminars.

I am sincerely grateful to Dr. Anil Bhardwaj, Director, Prof. D. Pallamraju, Dean, and Prof. P. Janardhan, former Dean, for providing necessary analytical facilities to carry out my research. Thanks are due to the Academic Committee, PRL, for reviewing and providing useful comments on my research progress throughout the PhD tenure.

I am thankful to the captains, crew and all the participants of GI-01, GI-05 and GI-06 (Leg A and B) cruises for their invaluable support during the clean seawater sampling and onboard analysis of chemical parameters. I express my gratitude to Mr. Manan Shah for the automation of the aluminium and manganese flow injection analysis system and Mr. Lakan Singh for his help in solving the technical issues with the system, encountered during analytical operations.

I would like to thank my lab-mates, Upasana, Damodar, Subha, Venkatesh, Muruga, Chandana, Satish, Anil, Ravikant, Chinmay, Harsh Raj, Mahesh, Romi, Arvind, Nirmalya, Bisweshwar, Chhaya, Rakhil, Jaldhi, Sanjukta, Abhishek, Priyanka, Nisha, Deepika, Partha, Rahul, Ramsha, Deep, Bankim bhai, Pravin bhai and Rashmik bhai for their help and support in the laboratory and during the field works.

My stay at PRL has been full of beautiful memories shared with my lovely friends, which have made my stay pleasant at PRL. Mishra ji and Richu are friends cum guardians, who have always been there to take care of my well-being. Together, we are the three musketeers and I shall always cherish the memories that we have made together during several birthday and festive celebrations, trips and home parties. I could share all my feelings without any hesitations with Anil bhai at good and odd times and he has taken care of me like a big brother; I shall always be grateful to him for all his support. Dance practice sessions and performances with my all seasons dance partner Sarika were highlights of my journey at PRL. The fun get-togethers with the Goswami family (Vineet bhaiya, Dimpy bhabhi and Cheeku) were always cheering.

Last but not the least, I would like to thank my family that has been a source of constant support and love during my PhD tenure. My parents’ sacrifices and efforts are countless for making me achieve whatever I have till date.

ABSTRACT

This thesis presents extensive studies on the biogeochemical cycling of dissolved aluminium (dAl) and manganese (dMn) over the vertical water column in the tropical and subtropical Indian Ocean. Towards this, trace metal clean seawater sampling and analytical protocols were established for precise and accurate measurements of dAl and dMn concentrations in seawater. In the Bay of Bengal (BoB), fluvial discharge of lithogenic sediments and subsequent release of labile Al from the sediments play a dominant role in controlling the surface dAl distribution. Considering the steady-state balance between dAl input from lithogenic sediments and removal via passive scavenging, the fractional solubility of Al from the lithogenic sediments supplied to the BoB surface waters is constrained to lie in the range of 1.1-4.7%. During the late winter monsoon period (January-February), advective mixing between the low-salinity, dAl-rich BoB surface waters and the high-salinity, dAl-poor surface waters of the open southern Arabian Sea governs the surface dAl distribution in the eastern and central Equatorial Indian Ocean. Deep-water (>2000-3500m) dAl concentrations in the equatorial Indian Ocean region are generally low and uniform (~2.0-2.5 nM). A steady-state and vertical advection-diffusion-scavenging model is used to estimate the deep-water scavenging residence time of dAl in the equatorial Indian Ocean and found to vary in the range of 92-141 yr. The deposition of Australian dust and advection of Indonesian Throughflow Water translates to the dAl enrichment in the upper water column (<500m) at the northern end of the Indian Subtropical Gyre.

Surface dAl distribution in the Arabian Sea demonstrates an east-west gradient, i.e., elevated dAl (12.7-20.9 nM) close to the Indian coastal region and low dAl (1.5-3.3 nM) along the western boundary of the Arabian Sea. Rapid surface dAl removal, due to relatively high biological productivity and a decrease in atmospheric dust deposition flux during the fall-intermonsoon, results in the low surface dAl levels observed in the western Arabian Sea region. Given that the Arabian Sea is marked by significant spatio-temporal changes in surface dAl levels, a simple one-dimensional, non-steady-state model was constructed to simulate, for the first time, the seasonal variability in surface dAl concentrations in the west-central Arabian Sea region (14-20°N, 57-65°E) and to understand the

control of seasonal changes in dust deposition input and scavenging removal fluxes on the surface dAl distribution. Such a model could be utilized as a first-order tool to estimate the seasonal variations in dust deposition flux using the surface dAl variations, and vice-versa, in highly meteorologically dynamic basins such as the Arabian Sea. In the western equatorial Indian Ocean, a relative increase observed in the surface dAl concentrations, compared to the western Arabian Sea and the central equatorial region, suggests a local dAl input, presumably, due to the dust influx from the Somali coast.

The intrusions of the high salinity water masses (the Arabian Sea High Salinity Water and the Persian Gulf Water) in the thermocline depths (~75-300 m) are observed to carry the dAl-rich signal of their formation regions to the open Arabian Sea; however, mostly restricted to the northern and north-western Arabian Sea during the period of this study (fall intermonsoon). In the deeper waters (>1000m), elevated dAl levels were observed at the stations sampled near some of the major ridges, i.e., the Murray Ridge (~13.0 nM), the Laxmi Ridge (~10.0 nM) and the Carlsberg Ridge (~4.5 nM), in the Arabian Sea and the equatorial Indian Ocean. dAl input from the Al dissolution/desorption from the margin sediments and/or influx of dAl-rich sediment pore waters to the ambient ocean water column could explain the observed rise in dAl levels close to the ridges.

Dissolved Mn (dMn) distribution is determined in the southern and central Arabian Sea water column to understand the biogeochemistry of dMn in these regions. dMn distribution show surface maxima at all the sampled regions of the Arabian Sea. The estimated mean annual dMn input flux to the Arabian Sea surface waters from the atmospheric mineral dust deposition (dry) ranges between 28.6-239.4 nmol m^{-2} d^{-1}, across the Arabian Sea. Compared to the atmospheric dMn input, dMn removal from the surface waters via bio-assimilation is insignificant (4.4-24.3 nmol m^{-2} d^{-1}). Surface dMn removal through Mn-oxidation and passive scavenging (51.9-276.0 nmol m^{-2} d^{-1}) is estimated to set a dominant control. The residence time of dMn in the Arabian Sea surface waters is calculated (1.0-9.3 yr) considering the steady-state condition and using the atmospheric dMn input and surface mixed layer dMn inventory.

Significant positive dMn anomalies were observed in the oxygen-deficit, lower thermocline waters (~200-600m) near the western continental margin of India (dMn anomaly ~0.2-0.5 nmol kg^{-1}) and in the perennial denitrification zone of the Arabian Sea (dMn anomaly ~2-4 nmol kg^{-1}). dMn diffusion from pore waters of the reducing sediments of the western Indian continental margin to the ambient seawater and subsequent lateral advection may lead to dMn-enrichment in the thermocline depths close to the margin. Mn release due to organic matter remineralization and/or *in situ* reductive dissolution of Mn-oxyhydroxides over the thermocline water column results in highly elevated dMn levels in the denitrification zone of the Arabian Sea.

LIST OF TABLES

LIST OF FIGURES

Chapter 1

Introduction

The ocean productivity and the carbon cycle are controlled by the availability of nutrients and micronutrients (trace elements) in the ocean (Coale, 1991; Falkowski et al., 2000; Field et al., 1998; Martin and Fitzwater, 1988). The distributions of the trace elements and their isotopes (TEIs) in seawater are governed by their input from continental and hydrothermal sources and several biogeochemical processes operating in the seawater column and at various interfaces (i.e., land-ocean, sediment-water and ocean-atmosphere boundaries; Bruland et al., 2014). The distributions of some of the trace elements are also influenced by anthropogenic activities. The sources and processes for the external input of trace elements to the ocean include various pathways such as (1) deposition of atmospheric dust, derived from arid/semi-arid regions of continents, (2) riverine discharge of the dissolved and particulate (suspended or deposited over the shelves and slopes) matter at the continental margins, (3) fluid and particulate inputs to the ambient waters from the hydrothermal vents, concentrated over the mid-oceanic ridges and (4) resuspension of particulate matter and release/diffusion of pore waters from the ocean margins (Bruland et al., 2014). Removal processes of trace elements from the water column broadly involve passive chemical precipitation and/or adsorption on the biogenic or non-biogenic particulate matter and active uptake by biology (Balistrieri et al., 1981; Bruland et al., 2014), followed by the settling of the carrier particulate phases out of the water column. In addition to these, various other internal oceanic processes, such as organic matter remineralization, varying redox conditions throughout the water column, ocean water circulation, etc., play an essential role in the redistribution of the trace elements from one phase to another and their inter or intra-basin transportation. The distributions of selected trace elements regulate specific marine processes. For instance, the availability of the bio-essential Fe, Zn, Mn, Ni, etc., in the surface waters is observed to impact the primary biological productivity and diversity (Martin et al., 1990; Coale, 1991). Also, increased levels of some trace metals (e.g., Cu, Hg, Pb) are observed to show a toxic effect on the growth of certain species of the primary producers (Sunda, 1989). Given that the trace elements and their isotopes are an integral part of different marine biogeochemical processes and undergo redistribution/fractionation during these processes, the observed fractionations in distributions of TEIs in the global ocean basins have been used as proxies of the prevailing marine biogeochemical processes. The basis for such studies is the contrasting response of a given trace element to different oceanic processes depending on its physiochemical properties in a given marine environment and its biological role (Bruland et al., 2014; Sunda, 2012).

The initial surge in the availability of the TEIs dataset and the understanding of their cycling in the ocean came after the inception of the GEOSECS (Geochemical Ocean Section Studies) program in the 1970s, which was the first international collaborative effort to understand the physical and chemical processes governing the TEIs distribution in the global ocean (Moore, 1984). However, the bulk of the dataset produced during the GEOSECS was from the North Atlantic and North Pacific (Bruland et al., 2014). The paucity of the studies on the cycling of TEIs in the other major basins (South Atlantic, South Pacific, the Indian Ocean and the Polar Oceans) hindered the efforts to better understand the inter-basin cycling of and the impact of diverse environmental conditions on the TEIs distribution. Also, since the end of the GEOSECS, the development of new TEIs proxies to probe different biogeochemical processes and the advancement in the sampling and analytical techniques well-staged the need for another international study on the marine biogeochemical cycling of trace elements and their isotopes in the global ocean. This lead to the launch of the GEOTRACES (2007-present) program, a new internationally collaborated research program with the guiding mission (GEOTRACES Planning Group, 2006) as follows:

"To identify processes and quantify fluxes that control the distributions of key trace elements and isotopes in the ocean, and to establish the sensitivity of these distributions to changing environmental conditions."

In this context, the GEOTRACES Planning Group (2006) suggested a list of key parameters (TEIs) to be studied for probing different biogeochemical processes in the ocean (Fig. 1.1). This thesis is part of the GEOTRACES-India program, which aims to understand the biogeochemical cycling of the key parameters in different Indian Ocean basins. In this thesis, the distribution and cycling of dissolved aluminium and manganese in the Indian Ocean waters are studied. In the following text, I shall briefly discuss the present understanding of the biogeochemical cycling of dissolved aluminium and manganese in seawater. Further, I shall discuss the diverse biogeochemical processes prevailing in the Indian Ocean basins and list the specific objectives of the thesis laid down to qualitatively or quantitatively understand the relationship between the dissolved Al and Mn distribution and the biogeochemical processes.

Key Parameter	Example of Use
Trace Elements	
Fe	Essential micronutrient
Al	Tracer of Fe inputs (from mineral dust and elsewhere)
Zn	Micronutrient; potentially toxic at high concentration
Mn	Tracer of Fe inputs and redox cycling
Cd	Essential micronutrient; palaeoproxy for nutrient content of waters
Cu	Micronutrient; potentially toxic at high concentration
Stable isotopes	
δ^{15}N (nitrate)	Modern and palaeoproxy for nitrate cycling
δ^{13}C	Modern and palaeoproxy for nutrient content and ocean circulation
Radioactive isotopes	
^{230}Th	Constant flux monitor in sediments; tracer of modern ocean circulation and particle scavenging
^{231}Pa	Palaeoproxy for circulation and productivity; tracer of modern particle processes
Radiogenic isotopes	
Pb isotopes	Tracer of natural and contaminant sources to the ocean
Nd isotopes	Tracer of natural sources of TEIs to the ocean

Fig. 1.1: Key parameters (trace elements and isotopes) suggested by the GEOTRACES Planning Group for the measurements during the GEOTRACES Ocean section cruises. This figure is reproduced in a modified form after GEOTRACES Planning Group (2006)

1.1 Motivation and Background

Continental crust material, supplied through atmospheric dry or wet mineral dust deposition and fluvial (both freshwater and particulate matter) discharge at the continental margins, is a prominent source of trace elements to the global ocean. For the open ocean regions, the atmospheric dust deposition is the most important source of bio-essential trace nutrients (e.g., Fe, Zn, Mn), required to sustain the primary production (Jickells et al., 2005). In this regard, the estimation of atmospheric dust deposition fluxes over the surface ocean waters is critical to better understand and simulate the global primary biological production and, therefore, the associated atmospheric carbon (in the form of dissolved CO_2) sequestration rate by the biological pump (inorganic carbon fixation via primary production and subsequent removal by settling to the seafloor). Understanding the efficiency of the biological pump has implications for global carbon cycling and, therefore, climate. There have been constant efforts for direct atmospheric dust measurements in the marine boundary layer over major oceanic basins, either through short-term shipboard or long-term land-based aerosol sampling (Duce et al., 1991; Heimburger et al. 2012; Tindale and Pease, 1999). However, there is still a paucity of such observations in large parts of the global ocean, most evidently in the remote regions. Further, the temporal variability in the atmospheric dust levels is difficult to be realized using the short-term (hours or days long) direct shipboard measurements in a given region. Extrapolations of long-term, land-based atmospheric dust estimates to off-shore areas are associated with large errors and mismatches with corresponding field-based data. Moreover, estimations of dry dust deposition fluxes based on the direct measurements of aerosol composition in the marine boundary layer rely on highly variable dry deposition velocity. Given the above limitations, several studies (Grand et al., 2015; Measures et al., 2008; Measures and Vink, 2000) have adopted an indirect tracer approach where the dissolved concentration of crustal-derived trace elements are exploited to estimate the time-integrated (time scale depended on the trace element residence time) mineral dust deposition flux over the surface ocean.

Previous studies (Dammshäuser et al., 2011; Measures et al., 2000; Orians and Bruland, 1988) have shown that the surface ocean distributions of some trace elements such as Al, Ti, Ga, Mn, Fe, etc., are significantly controlled by the deposition of atmospheric mineral dust deposition, given that the crustal material is an important source of these elements to the ocean. However, not all of these are equally useful in tracking the extent and pattern of atmospheric dust deposition due to their varying residence timescales and biogeochemical controls in seawater. Fe and Mn are bio-essential trace metals and, therefore, the effect of biological cycling is superimposed over that of the atmospheric dust deposition in their distribution. The surface distribution of Ti and Ga are found to be correlated with the dust deposition (Dammshäuser et al., 2011; Orians and Bruland, 1988); however, their residence timescales in the surface waters are of the order of decades and, therefore, reflect the long-term average of the depositional pattern, while unable to capture any important short-term variations (Tindale and Pease, 1999; Dammshäuser et al., 2011). Surface water dissolved Al (dAl) distribution is suggested and successfully (and extensively) used as a proxy to the atmospheric mineral dust deposition over the ocean (Measures and Vink, 2000). Al is the most abundant metal (8.04 wt%; McLennan, 2001) in the upper continental crust. The surface water residence time of dAl is relatively short (generally between a few months to 4 years; Orians and Bruland, 1986; Han et al., 2008) and, therefore, its surface distribution is shown to reflect the effect of smaller timescale variations in the atmospheric dust deposition over a given region (Measures and Vink, 1999). Al is not known to have any active biological function and its chemical speciation is insensitive to the redox changes over the water column; these properties render the dAl variations to be decoupled with the active biological and redox processes. Moreover, the composition of Al in the upper continental crust is largely invariant, which results in better constrains (with lesser uncertainty) on the mineral dust deposition fluxes over the surface ocean.

In the open ocean regions, the balance between the input from the deposition, and subsequent partial dissolution, of atmospheric dust and removal via passive particle scavenging of Al predominantly controls the surface dAl distribution (Hydes, 1979; Measures et al., 2015). Passive adsorption on the biogenic particles, particularly biogenic silica (opal), is considered to be one of the major removal mechanisms for the surface dAl (Dixit and Van Cappellen, 2002; Dymond et al., 1997). Field and laboratory studies (Koning et al., 2007; Moran and Moore, 1988) have shown dAl removal by the authigenic formation of aluminosilicate over the biogenic siliceous particulates. Middag et al. (2015) have suggested that the relationship between the scavenged Al and biogenic opal may not be causal, instead involve removal by adsorption on miscellaneous biogenic particles where biogenic silica provides the ballast effect for the export of biogenic particulates. However, in the coastal regions, other processes such as the riverine influx of lithogenic suspended particulate matter, resuspension of the continental shelf sediments may also exert additional control on the vertical dAl distribution (Mackin and Aller, 1984, 1986; Middag et al., 2009). The advection of water masses may also influence the dAl distribution, where the water circulation timescales are comparable to or smaller than the residence time of dAl (Baker et al., 2016). Therefore, a comprehensive understanding of dAl cycling is important before exploiting the dAl distribution as a tracer of continental material input (via atmospheric deposition, fluvial discharge and/or resuspension of margin sediments) to the ocean water.

Mn is an essential micronutrient required by the phytoplankton (Sunda, 2012). Mn finds its crucial place in the water oxidizing (splitting water into protons and molecular oxygen gas) component of the protein complex, photosystem II, active during the photosynthesis (Raven, 1990). An essential role of Mn in phytoplankton is also realized as an activator for the enzyme superoxide dismutase, which is responsible for the removal of reactive oxygen species produced as by-products during photosynthesis (Peers and Price, 2004). In the modern oceans, the predominant oxidation states of Mn are Mn(II), Mn(III) and Mn(IV). Mn(III) and Mn(IV) are the stable redox states in oxygen-rich seawater and exist as insoluble Mn-oxyhydroxides. Mn(II) is thermodynamically unstable in the oxygenated ocean waters and should convert to the insoluble oxidized forms (Mn(III) and Mn(IV)) by reacting with molecular oxygen (O_2). However, the kinetics of the homogeneous oxidation Mn(II) by molecular O_2 in the seawater is extremely slow (half-life of the order of 500 yr; Morgan, 1967). This allows Mn(II) to predominantly exist as soluble Mn^{2+} and $MnCl^{+}$ inorganic species in the seawater (Morgan, 2005). The rate of Mn(II)-oxidation may significantly increase when it proceeds either as a heterogeneous reaction on the surfaces of particulate metal oxides (half-life of the order of few months; Morgan, 2005) or biotically-mediated oxidation, where Mn (II) is oxidized at the outer-cell polysaccharide layers of some bacteria and fungi (half-life of the order of few hours; Morgan, 2005). The *in situ* formation of particulate Mn oxides play an important role in removing other trace metals (and itself) from the ocean water column (Yamagata and Iwashima, 1963) and, therefore, regulate their cycling. In the surface ocean, however, the heterogeneous (on metal surfaces or biotically-mediated) Mn-oxidation is significantly slowed down due to (1) reduction of Mn-oxides in the presence of sunlight (photo-reduction; Sunda and Huntsman, 1994) and (2) photo-inhibition of biotically-mediated Mn-oxidation (Moffett, 1997; Sunda and Huntsman, 1988). Dominant sources of Mn in the surface waters include (1) deposition and partial dissolution of atmospheric mineral dust (Baker et al., 2016), (2) river water discharge (Aguilar-Islas and Bruland, 2006) and (3) reducing shelf sediments, where the reductive dissolution of Mn-oxides and other reactive Mn phases may enrich the pore waters in Mn which may diffuse into the ambient water column and laterally advect (Homoky et al., 2016). Relatively, lower Mn-oxidation rates in, and atmospheric Mn input to, the surface ocean are observed to result in surface dissolved Mn maxima over a large part of the global ocean (van Hulten et al., 2017 and references therein).

With the decrease in the incident solar radiation in the sub-surface waters, the biotically-mediated Mn-oxidation increases significantly and dominates the removal flux for dissolved Mn (Sunda and Huntsman, 1988). This results in a sharp decline in the dissolved Mn (dMn) concentrations below the surface mixed layer and more uniform dMn levels (~0.1-0.2 nmol kg^{-1}) in the deeper waters (below ~500m), in most of the global ocean regions (van Hulten et al., 2017 and references therein). However, this general trend may be altered significantly under the changing redox conditions over the water column, by lateral transport of water masses or hydrothermal plume intrusion in the sub-surface or deep waters (Johnson et al., 1996; Lewis and Luther, 2000). In the oceans, two processes primarily control the redox conditions (by changing the dissolved O_2 levels) in the water: (1) advection of water masses with different dissolved O_2 content and/or (2) bacterial mediated, aerobic degradation of organic matter, which consumes dissolved O_2 in the seawater. Ocean basins with high surface primary productivity and export (and therefore, with high organic matter degradation rate) and/or reduced water ventilation rate in the sub-surface depths may significantly be depleted in dissolved O_2, leading to suboxic or anoxic conditions in the thermocline waters. These conditions may further result in the reductive dissolution of particulate Mn-oxide over the water column and release of the soluble Mn(II) form. Further, low levels of dissolved O_2 lead to the decrease of Mn-oxidation rate in the water column (Morgan, 2005) and, therefore, play a role in stabilizing the elevated dMn levels in the water column resulting from Mn released from organic matter degradation (i.e., the release of the biologically assimilated Mn) and/or dissolution of Mn-oxyhydroxides. These biogeochemical characteristics of dissolved Mn in seawater may be exploited as the tracer of changing redox conditions over the water column. In the regions of active hydrothermal venting, highly elevated dMn concentrations are observed in the hydrothermal fluids near the vents, which may advect laterally with their dMn-rich signal over regional distances as hydrothermal plumes in the deep waters (Gamo et al., 2015; Middag et al., 2011; Gamo et al., 1996; Resing et al., 2015).

1.2 Indian Ocean-a unique natural laboratory

Indian Ocean basins, having distinct biogeochemical dynamics, offer a unique opportunity to understand the controls of different ocean processes on the cycling of trace elements. In the north-eastern Indian Ocean (i.e., the Bay of Bengal and the Andaman Sea), the huge fluvial input, in the form of freshwater and suspended sediments (Robinson et al., 2007; Sengupta et al., 2006), may influence the biogeochemistry of the lithogenic trace metals throughout the water column (Chinni et al., 2019; Singh et al., 2012), a process which is not accounted for by the modeling studies on dAl cycling (Gehlen et al., 2003; Han et al., 2008; van Hulten et al. 2013). The Arabian Sea (north-western Indian Ocean) is subjected to large spatio-temporal variations in dust input and productivity, which may impact the distribution and cycling of dAl and dMn in the surface and thermocline waters (Measures and Vink, 1999; Thi Dieu Vu and Sohrin, 2013). Overall, high evaporation (E) and low precipitation (P) rates (E-P ~0.7-1.2 m yr^{-1} (annual mean); Pokhrel et al., 2012) in the Arabian marginal seas (the Persian Gulf and the Red Sea) and the northern Arabian Sea results in the formation of the high salinity water-masses, namely, the Persian Gulf Water (PGW), the Red Sea Water (RSW) and the Arabian Sea High Salinity Water

(ASHSW), respectively (Shenoi et al., 1993; Shetye et al., 1994). The intrusion of these water masses to the thermocline depths of the open Arabian Sea may impact the distribution of trace elements through the transport of their pre-formed trace metal signature. The Arabian Sea is also characterized as a region with high primary productivity. High continental dust input, strong coastal upwelling (and subsequent advection of waters to the open Arabian Sea region) during the summer monsoon and convective mixing in the upper water column during the winters ensure a large supply of (macro and micro) nutrients to the surface waters of the Arabian Sea to sustain the primary production. High productivity in the surface water supports the large and continuous export of organic matter out of the surface waters into the sub-surface depths. Bacterial-mediated degradation (oxidation) of the exported organic matter via the consumption of dissolved oxygen results in the formation of extreme oxygen-depleted conditions in the Arabian Sea sub-surface waters. Changes in redox conditions over the water column may have a significant impact on the distribution of dMn.

Under the influence of summer and winter monsoon currents, enormous exchange of surface and thermocline waters takes place between the Arabian Sea and the BoB (Kumar et al., 2004; Schott et al., 2009), where the equatorial Indian Ocean region acts as a connecting pathway between the two basins. In the equatorial Indian Ocean region, south of Sri Lanka (~5°N), mean transport in the upper water column (~60-100m) of about 8 Sverdrup eastward (towards the Bay of Bengal) and 12 Sverdrup westward (towards the Arabian Sea) is estimated during the southwest and the northeast monsoon period, respectively (Schott et al., 2009 and references therein). For this reason, the dAl and dMn distribution in the surface and thermocline waters of the equatorial Indian Ocean region will be indirectly influenced by the Al and Mn cycling in the northern Indian Ocean basins.

Several active hydrothermal venting sites have been discovered in the Indian Ocean basins (Gamo et al., 2015; Srinivasan et al., 2004). Due to limited studies on full vertical water column profiles of trace metals, the hydrothermal trace metal fluxes to the deep waters of the Indian Ocean basins are poorly constrained.

1.3 Objectives of the thesis

Broadly, this thesis aims to understand the controls of different biogeochemical processes on the distribution of dissolved Al and Mn in different Indian Ocean basins. Under this broader theme, we focus on achieving the following specific objectives:

1) To quantify and compare the relative impact of dAl input from atmospheric mineral dust deposition and fluvial discharge in the Bay of Bengal and the Andaman Sea.

2) To study and model the influence of seasonally reversing monsoonal climatology on the surface dAl and dMn distribution in the Arabian Sea via associated changes in dust flux, primary production and upper water circulation.

3) To assess the impact of the advection of distinct water masses on the dAl and dMn distribution in the Indian Ocean basins.

4) To examine the sensitivity of dMn distribution to the redox changes over the vertical water column of the Arabian Sea.

5) To investigate the relative influence of the active hydrothermal activities on the deep-water distribution of dissolved Al and Mn in the Indian Ocean.

1.4 Structure of the thesis

Chapter 1: Introduction

This chapter discusses the background information on the dissolved Al and Mn cycling in seawater and underlines the existing research gaps in the understanding of the biogeochemistry of these trace metals (Al and Mn) in the Indian Ocean basins. The major objectives pursued in the thesis are also provided in this chapter.

Chapter 2: Materials and Methods

This chapter details the materials and different sampling and analytical methods used/established during different studies of this thesis. The efforts to establish the accuracy and precision of the dissolved Al and Mn data generated using the analytical methodologies are also discussed in this chapter.

Chapter 3: Dissolved aluminium cycling in the northern, equatorial and subtropical gyre region of the Indian Ocean

In this chapter, the biogeochemical controls on the vertical distribution of dissolved Al in the Bay of Bengal (BoB), Andaman Sea, central and eastern regions of the Equatorial Indian Ocean, and northern reaches of the Indian Ocean subtropical gyre are discussed. Major objectives of the study are to (1) decipher the relative influence of the huge fluvial (freshwater and sediment) discharge vis-à-vis atmospheric mineral dust deposition in the Bay of Bengal, (2) study the impact of surface monsoonal current on the redistribution of dAl in the BoB, the Andaman Sea and the Equatorial Indian Ocean and (3) understand the role of seawater interaction with margin sediments and hydrothermal fluid injection on the dAl distribution. Estimation of the deep-water dAl residence time in the Equatorial Indian Ocean using the 1D advection-diffusion-scavenging model (Craig, 1974) is discussed.

Chapter 4: Distribution and cycling of dissolved aluminium in the Arabian Sea and the western equatorial Indian Ocean

This chapter discusses the impact of seasonal reversing climatology and associated changes in mineral dust flux, biological productivity, and surface circulation on the Arabian Sea surface dAl distribution. The observed seasonal variations in surface dAl concentration in the Arabian Sea are simulated using a simple non-steady-state model and described in this study. Further, the relative influence of the intrusion of high salinity water masses from the Arabian marginal seas and the northern Arabian Sea on the thermocline dAl distribution in the open Arabian Sea region is examined. This study is also the first attempt to understand the dissolved Al cycling in the western equatorial Indian Ocean.

Chapter 5: The biogeochemical cycling of dissolved manganese in the Arabian Sea

This chapter focuses on understanding the biogeochemistry of dissolved Mn in the southern and central Arabian Sea. Major emphasis is given on quantifying Mn input to the surface seawater via atmospheric mineral dust deposition and removal via different pathways, including bio-assimilation and Mn-oxidation. The impact of changing redox conditions over the vertical water column on dissolved Mn distribution is also investigated.

Chapter 6: Summary and future research plans

The major findings of all the studies carried out are summarised in this chapter. Further, some of the future perspectives on the research work done in this thesis are discussed.

Chapter 2

Material and Methods

As noted in the previous chapter, the broad aim of this thesis is to study the impact of diverse marine biogeochemical processes, active in different basins of the Indian Ocean, on the distribution of dissolved Al (dAl) and Mn (dMn) over the full vertical water column. Comprehensive understanding of the dAl cycling in the Indian Ocean basins has implications for the supply of continental material (atmospheric mineral dust, lithogenic suspended matter from the riverine discharge, resuspended lithogenic margin sediments) to the Indian Ocean waters. The input of continental material to the ocean waters acts as an important source vector for various trace nutrients (or micro-nutrients such as Fe, Zn, Mn). Mn as a bio-essential and redox-sensitive trace metal in seawater may regulate primary production and diversity and track redox changes in the water column. Understanding of the biogeochemistry of dMn is crucial to (1) constrain the impact of significant spatio-temporal changes in Mn sources (atmospheric mineral dust, riverine flux, shelf sediments), observed in the tropical Indian Ocean, on phytoplankton production and their community structure and (2) establish the sensitivity of dMn distribution to changing redox state in the northern Indian Ocean water column.

To achieve these objectives, the distributions of dAl and dMn were determined in different Indian Ocean basins by collecting seawater samples along four different GEOTRACES-Indian cruise transects (Fig. 2.1). The general hydrographic features of the Indian Ocean (mostly restricted to the studied regions) are described in the following section. Specific details on sampling strategy, different materials and analytical methods used to measure the dAl and dMn concentrations in the seawater samples are also discussed.

2.1 General hydrography of the Indian Ocean

Several ocean current systems and water masses are reported over the vertical water column of the tropical Indian Ocean (Kumar and Li, 1996; Mantyla and Reid, 1995; Schott et al., 2009; Tomczak and Godfrey, 2003a,b; You and Tomczak, 1993; You, 1997, 2000; Shetye et al., 1994; Singh et al., 2012; Wyrtki, 1973). The dispersal of the water masses in the Indian Ocean, under the influence of major current systems, plays a significant role in the redistribution of trace elements at an inter or intra-basin scale (Saager et al., 1989; Schüβler et al., 2005; Goswami et al., 2014). Using the observed basic hydrographic data (salinity, temperature and dissolved oxygen), the general circulation pattern and water mass structure of the studied regions are deduced and are briefly discussed here.

A huge freshwater discharge (on the order of ~10^3 km^3 yr^{-1}; Sengupta et al., 2006) from the Himalayan (the Ganga and the Brahmaputra), the Indian peninsular rivers and the Indo-Mynamar rivers to the north-eastern Indian Ocean (BoB) is manifested as low-salinity (<34) surface waters, particularly in the northern and central BoB, and the Andaman Sea. This low-salinity signal is further transported to the surface waters of the Equatorial Indian Ocean and south-eastern Arabian Sea region by eastward-flowing Northeast Monsoon Current (NMC) and the northward-flowing East Indian Coastal Current (EICC), which develop during the winter period (November-February; Schott et al., 2009; Wyrtki, 1973). Annually, the excess of evaporation (E) over the rainfall (P) (E-P ~2 m yr^{-1}; Pokhrel et al., 2012) in the northern Arabian Sea, the Persian Gulf and the Red Sea results in the formation of high-salinity water masses, namely, the Arabian Sea High Salinity Water (ASHSW), Persian Gulf Water (PGW) and Red Sea Water (RSW), respectively (Shenoi et al., 1993; Shetye et a, 1994). These water masses intrude into the thermocline water depths (~50-1000m; Schott et al., 2009; Shetye et al., 1994) of the open Arabian Sea and may impact the trace elements distributions. Further, the outflow of these high-salinity water masses into the open Arabian Sea is highly seasonal (Maillard and Soliman, 1986; Prasad et al., 2001; You, 1997). The intrusion of the warm and low-salinity Indonesian Throughflow Water (ITW), under the influence of South Equatorial Current, is observed in the north-western reaches of the subtropical gyre region of the Indian Ocean (~8-15°N). Before entering the Indian Ocean, the ITW interacts with the sediments of the continental margins surrounding the Indonesian seas (Nozaki and Yamamoto, 2001). Boundary exchange of trace elements over the margins of the Indonesian seas may impact the trace element budget of the ITW, which, in turn, can affect the trace element distribution in the subtropical Indian Ocean with the advection of the ITW (Obata et al., 2004; Grand et al., 2015b).

The deeper water column (>2000m) in the Indian Ocean basins is occupied by the Modified North Atlantic Deep Water (MNADW) and the Antarctic Bottom Water (AABW). MNADW is formed by the mixing of the North Atlantic Deep Water (NADW) with the Circumpolar Deep Water (CDW) in the Indian Ocean sector of the Southern Ocean (You, 1999). AABW entering the western Indian Ocean basins is primarily sourced from the Weddle Sea (Mantyla and Reid, 1995). The source of AABW reaching the eastern and central Indian Ocean basins is the dense waters of the Ross Sea and the Adelie coast (Mantyla and Reid, 1995). These deeper water masses undergo significant change in their chemical and physical properties as they advected towards the northern Indian Ocean. These changes are forced by advective mixing, interaction with seafloor and continental margin sediments and *in situ* recycling of biogenic and non-biogenic particulate matter settling over the deep-water column (You, 1997; Chinni et al., 2019). Another unique feature of the deep-water dynamics in the northern Indian Ocean is the presence of significant dianeutral mixing (You, 1999, 2000).

The relative impact of ocean circulation and water mass structure on the dissolved Al and Mn distribution in the studied regions is discussed in chapters 3, 4 and 5.

2.2 Seawater sampling and storage

Seawater samples for the measurement of dissolved Al were collected along three separate GEOTRACES-India cruise transect (Fig. 2.1a), namely, GI-01, GI-05 and GI-06 (Leg A; hereafter, GI-06(A)) onboard research vessel Sagar Kanya. The GI-01 cruise (Fig. 2.1a) was carried out during the spring-intermonsoon period (26 March to 19 April) of 2014. During this cruise, samples were collected offshore Vishakhapatnam (GI-01/1) followed by a meridional transect near 87°E (GI-01/2 to GI-01/9; Fig. 2.1a) through the BoB and the equatorial Indian Ocean. The cruise continued southwest through the equatorial and Indian Subtropical Gyre region for further sampling (Fig. 2.1a). The GI-05 cruise took place during the fall inter-monsoon period (22 September to 17 October) of 2015. Starting from the western Indian continental shelf region near Goa (GI-05/1, Fig. 2.1a), seawater samples were initially collected across the eastern and central AS (GI-05/2 to GI-05/4, Fig. 2.1a). Following this, sampling was conducted along a meridional sub-transect in the central Arabian Sea towards the northern region of the Sea (GI-05/5 to GI-05/7, Fig. 2.1a). Finally, seawaters samples were collected along the western boundary of the Arabian Sea and in the western Equatorial Indian Ocean (GI-05/8 to GI-05/17, Fig. 2.1a). The last sampled station of the cruise (GI-05/18, Fig.2.1a) lies in the northern edge of the subtropical gyre region of the Indian Ocean. The GI-06(A) cruise (Fig. 2.1a) took place during the late winter monsoon period (29 January to 1 March) of 2017. Sampling during this cruise was carried out across the central and southern BoB, and the equatorial Indian Ocean (Fig. 2.1a). Additional stations were sampled in the southern Andaman Sea and the south-eastern Arabian Sea (Fig. 2.1a).

Dissolved Mn concentrations were measured in seawater samples from 17 stations occupied along the GI-06 (Leg B; hereafter, GI-06(B)) cruise transect (Fig. 2.1b) in the central and southern Arabian Sea regions, onboard research vessel Sindhu Sadhana. The sampling was carried out during the late winter monsoon period (January-February) in the year 2020. The sampling stations were located over the continental shelf in the south-east Arabian Sea (GI-06(B)/1, GI-06(B)/2 and GI-06(B)/3, Fig 2.1b), along a zonal transect at 9°N (from 75.5 to 60°E) in the southern Arabian Sea (GI-06(B)/4 to GI-06(B)/14, Fig 2.1b), and the central Arabian Sea (GI-06(B)/15 to GI-06(B)/18, Fig 2.1b). The stations GI-06(B)/16, 17 and 18 lie in the intense oxygen depletion and denitrification zone of the Arabian Sea (Naqvi, 1991), where dissolved oxygen levels drop below 5µM in the thick thermocline water column (~150-900m).

Trace elements, including Al and Mn, exist in extremely low, i.e., picomolar to nanomolar, concentrations in seawater. Therefore, contamination-free seawater sampling, processing, and storage are essential prerequisites for analytical measurements of trace elements in seawater. To ensure the same, samples were collected using a trace metal clean seawater sampler consisting of 24, 12L Niskin-X bottles (Teflon coated, level-action type, General Oceanics) mounted on a rosette-type, epoxy-coated Al frame (Fig. 2.2). At each sampling station, the seawater sampler was deployed using an 8km long, non-metallic Kevlar hydrowire (Fig. 2.2) to collect the samples from the surface (5-25 m) to the bottom of the ocean (~50-150 m above the sediment-water interface). Once recovered from the ocean to the deck, the Niskin-X bottles were immediately transferred to a clean room container (class-1000, Fig. 2.2) for filtration and further sub-sampling. From the 12L Niskin bottles, ~1L aliquots of seawater were collected in acid-cleaned LDPE bottles (Tarsons Products Pvt. Ltd.) after filtration through 0.2µm filter capsules (AcroPak^{TM} 500 with Supor$^{®}$

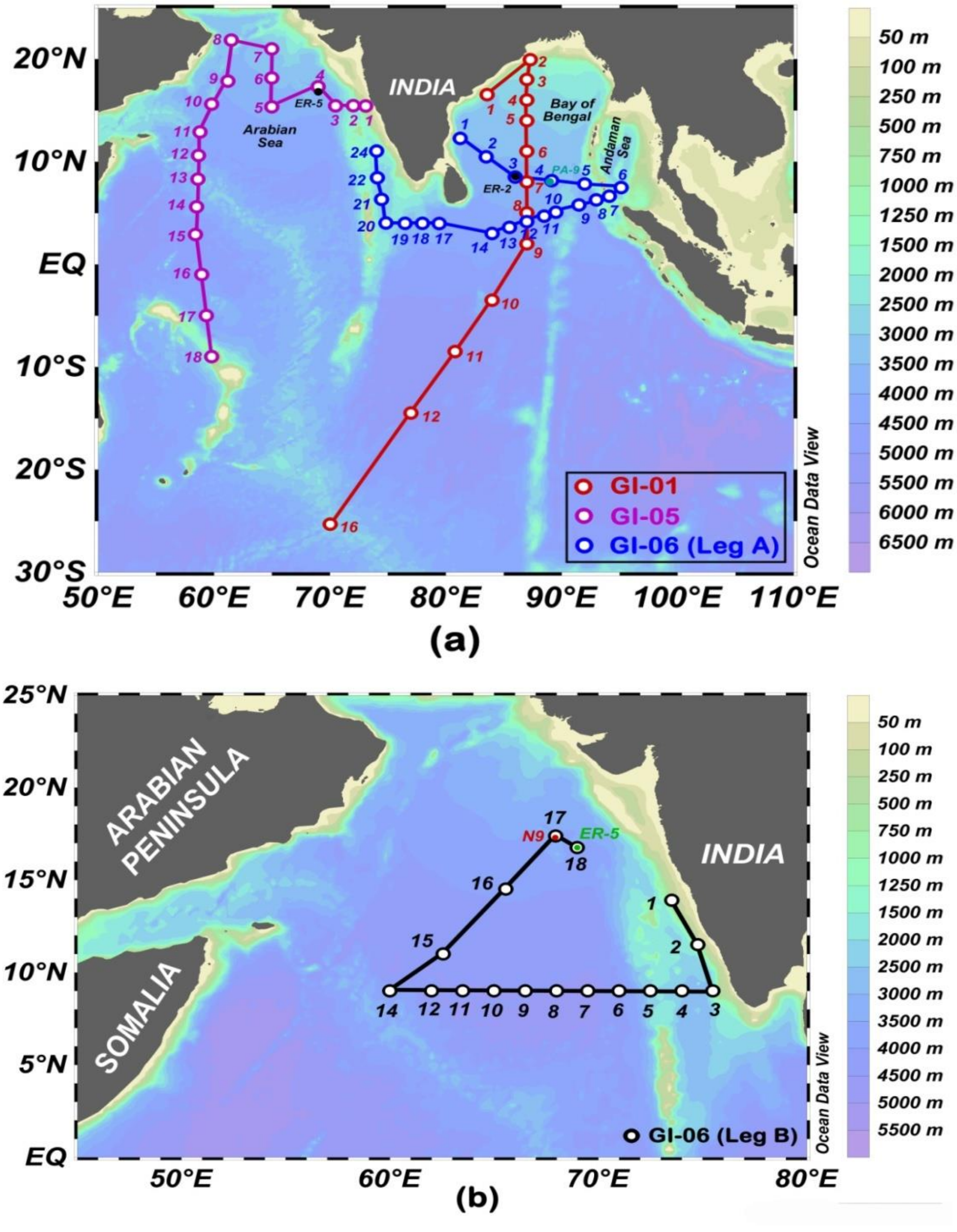

Fig. 2.1: Seawater sampling locations for (a) dissolved Al and (b) dissolved Mn measurements. Crossover or nearby stations from previous studies (Lewis and Luther, 2000; Obata et al., 2004; Thi Dieu Vu and Sohrin, 2013) are also plotted.

Membrane, PALL Life Sciences; rinse volume: 30ml) under filtered and pressurized air. The filtered sub-samples were acidified to pH <2 (0.024N HCl) using ultrapure HCl (32-35%; Optima$^{\text{TM}}$, Fisher Scientific) under a class-100 laminar flow bench facility inside the clean-room container. Finally, the acidified sub-samples were stored in a double layer of LDPE zip-bags (Tarson Products Pvt. Ltd.) and later used for shore-based trace metal analysis. From these stored seawater samples, ~30 ml aliquots were transferred to 60mL wide-mouth LDPE bottles (Tarsons Products Pvt. Ltd.) for measurements of dissolved Al and Mn concentrations using different analytical methods discussed later (section 2.2 and 2.3). Before use, the LDPE bottles (1L and 60mL) were thoroughly and sequentially cleaned with 2% alkaline solution

Fig. 2.2: Top: Rosette-based, trace metal clean sampler with 24, 12L Niskin bottles (top left) and clean winch equipped with non-metallic, Kevlar wire (top right). Bottom: Image showing the processes of seawater sample filtration inside the clean air (class 1000) container.

(Extran® MA 01, Merck), 4M HCl prepared using concentrated quartz distilled (from 37% HCl, EMPARTA®, Merck) HCl and 1M ultrapure HNO_3 (Optima™, Fisher Scientific). During acid cleaning, the bottles were soaked for at least one day at 60°C in a hot air oven. Between each cleaning step, the bottles were thoroughly rinsed 2-3 times with ultra-high pure water (resistivity: 18.2MΩ cm; hereafter, MQ water), which was prepared using Millipore Milli–Q® Element System. Moreover, in the process of sample collection or transfer, the bottles were conditioned by rinsing them 2-3 times with the respective seawater sample.

2.3 Analysis of dissolved Al

Dissolved Al concentrations in the sampled seawaters were measured using an in-house developed flow injection analysis system (Al-FIAS). The Al-FIAS can be divided into three major components (1) sample introduction component, (2) chemical analysis component, and (3) detection and data acquisition and processing component (Fig. 2.3 and 2.4). The sample introduction component consists of a robotic arm programmed to be used as an auto-sampler during the analysis. The component has a sample tray where, at a time, 42 seawater samples can be placed for analysis. The user can pre-define the analysis sequence for the samples placed on the tray from a graphical user interface, which ìs a part of the data processing and acquisition component

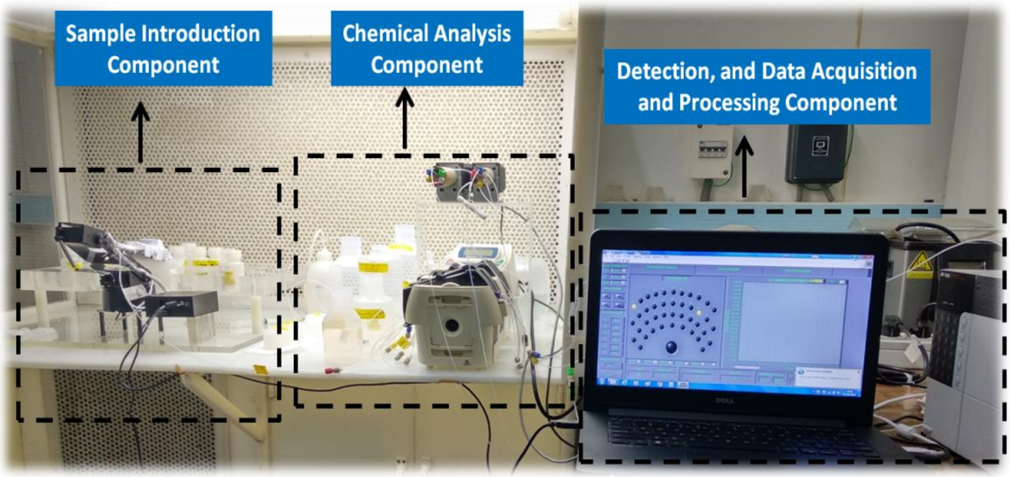

Fig. 2.3: General structure of flow injection analysis systems used for measurements of dissolved Al and Mn in seawater.

(described later). The details on the hardware of the auto-sampler are given in Chinni (2018).

The chemical analysis component consists of two 6-port, 2-positions valves (VICI, Valco Instruments) and a pre-concentration column, both embedded in a PTFE material tubing (internal diameter: 0.8mm, Cole-Parmer) manifold. An 8-channel peristaltic pump (GILSON MINIPULS Evolution®) is used, as part of the component, to pump sample and different chemical reagents at calibrated flow-rates (Fig. 2.4). Tubings used with the peristaltic pump are the 2-stop, color-coded (for different diameter) PVC tubings (Fisher Scientific). The valves are used to control the flow directions of the sample, injected by the sample introduction component, and other chemical reagents to execute different analytical steps (Table 2.1) during a sequence of sample analyses, which are described here briefly. dAl concentration in the seawater samples was analyzed following the automated in-line flow injection analytical technique of Brown and Bruland (2008). The seawater samples were buffered off-line to pH 5.5±0.2 using ammonium acetate buffer (2M NH_4Ac, hereafter, sample buffer) before the in-line analysis of dAl using the Al-FIAS. The sample buffer was prepared using commercially available high-purity ammonia solution (25%, Suprapur®, Merck) and glacial acetic acid (Optima™, Fisher Scientific); pH of the buffer was adjusted to 9.0±0.1 using the high-purity ammonia solution. Each sample analysis cycle starts with the conditioning of the pre-concentration column, using a column conditioning solution (0.1M NH_4Ac buffer; pH ~5.5) for 30s. The pre-concentration column was prepared

Table 2.1: Different analytical steps followed during the dAl and dMn analyses using Al-FIAS and Mn-FIAS, respectively.

Analytical Step	Valve 1 Position	Valve 2 Position	Time Interval (for Al-FIAS) (sec)	Time Interval (for Mn-FIAS) (sec)
Column Acid Wash	A	B	0-100	0-70
Column Conditioning	A	A	101-130	71-100
Sample Loading	B	A	131-430[a]	101-400
Matrix Wash	A	A	431-460	401-430
Column Elution	A	B	461-1040	431-900

a: variable sample loading time was used for dAl measurements of the open and coastal ocean sample (see text) by packing the iminodiacetic acid resin (TOYOPEARL® AF-Chelate-650 M, Tosoh Bioscience) in a 2cm mini-column (internal volume: 27µL; Global FIA, USA). The column conditioning solution was prepared by diluting the sample buffer with MQ water and adjusting its pH with high-purity glacial acetic acid. Next, the buffered sample was loaded onto the pre-concentration column for 120-300s. Generally, samples with (expected) dAl concentration below 15nM (open ocean samples) and >15nM (coastal surface waters) were pre-concentrated on the column for 300s and 120-180s, respectively. Thereafter, the column was rinsed again with the column conditioning solution for 30s to remove the excess and interfering seawater salts. The Al was then eluted from the column with 0.1M HCl, prepared using concentrated high-purity HCl solution (32-35%, Optima™, Fisher Scientific). The eluent was then mixed

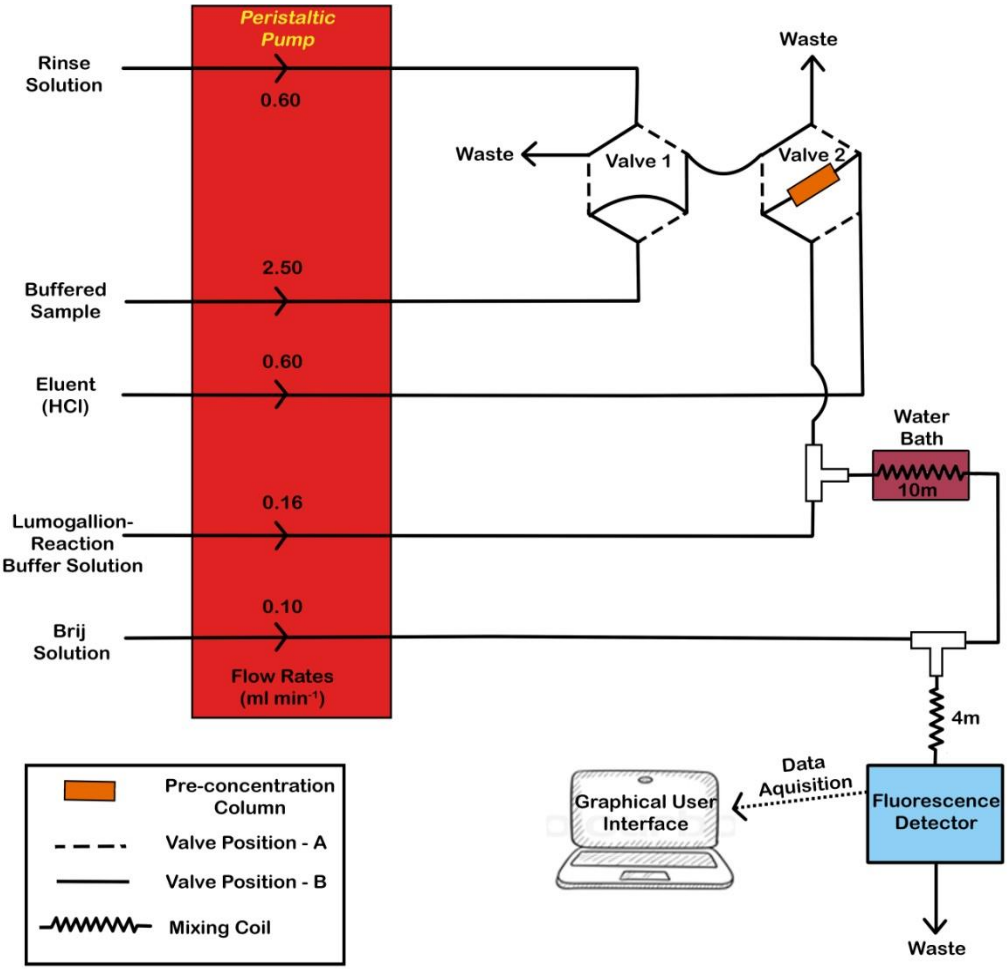

Fig. 2.4: Schematic representation of the Al-FIAS. The sequence of different analytical steps and their time intervals are given in Table 2.1.

with a lumogallion reaction solution to form a fluorescent Al-lumogallion complex. The lumogallion reaction solution is made by adding 2.5ml of lumogallion stock solution (4.8mM; 50mg lumogallion (>98.0%, TCI, Japan) in 30ml MQ water) to 250ml of 4M NH_4Ac buffer solution (pH=6.3±0.1), which was prepared with the high-purity ammonia solution and glacial acetic acid. Complete mixing of the Al-lumogallion complex in the reaction stream was achieved by passing it through a 10m knitted coil (Selavka et al., 1987), kept completely submerged in a 2L water bath (StableTemp, Cole-Parmer) at 50°C (±0.2°C). Brij-35 solution (5% Brij® L23 solution; Sigma-Aldrich) was then added to the reaction stream and their mixture was passed through a 4m knitted reaction coil into the final component of the Al-FIAS for detection. The Brij-35 solution increases the total intensity of fluorescence from the solution of the Al-lumogallion complex formed (Resing and Measures, 1994). Before every batch of analysis (50-60 combined runs of samples, standards and blanks), the pre-concentration column was thoroughly cleaned by passing ~0.5M high-purity HCl solution through it for several hours.

The final reaction solution of the Al-lumogallion complex was introduced into the last component of the Al-FIAS, where the fluorescence from the complex was detected using a fluorescence detector (RF-20A, Shimadzu). The detector was set to the excitation and emission wavelength of 489nm and 559nm, respectively (Brown and Bruland, 2008). A micro-controller board (Arduino Uno) was used to read the analog output from the detector and communicate the same with computer software. The acquisition and processing of the fluorescence data from the detector were achieved by using a software interface written in the Laboratory Virtual Instrument Engineering Workbench (LabVIEW) version 2011. The software provides the user with multiple major controls, which include (1) defining the sequence of sample introduction (analysis) for the samples placed on the sample tray, (2) defining the valves switching time-intervals, (3) displaying the analog signal from the detector in the form of a chromatogram, and (4) processing of data. The data processing consists of (1) defining the time interval for the peak signal of Al-lumogallion fluorescence in the chromatogram to calculate peak area (by integration) or peak height, (2) calibration of the Al-FIAS system by fitting a calibration curve (a linear fit) to peak areas (or heights) observed for different external calibration standards of known dAl concentrations and (2) calculation of the dAl concentration of an unknown seawater sample using the calibration curve.

2.4 Analysis of dissolved Mn

2.4.1 Dissolved Mn analysis using seaFAST-integrated HR-ICP-MS

Dissolved Mn (along with some other trace metals) concentrations were measured in the acidified seawater samples using a seaFAST (seaFAST-SP3, ESI, USA) integrated, (high resolution) magnetic sector inductively coupled mass spectrometer (Attom ES: HR-ICP-MS, Nu Instruments, UK). The seaFAST system is an automated, commercially available module for ICP-MS designed for in-line pre-concentration and/or preparation (dilution, matrix matching and spiking) of liquid samples of varying salinity. For in-line pre-concentration of dissolved Mn (along with other trace metals), we used the pre-installed, S-precon method sequence of the seaFAST software, which is suitable for the analyses of pre-prepared (spiked, diluted) samples having similar matrix composition. The analytic sequence for each sample (acidified to pH~1.7) starts with the sample loading, by an auto-sampler probe, into a 10 ml sample loop using a vacuum pump. Next, the sample is buffered (to pH=6.0±0.2) in-line by mixing it with a sample buffer solution (4M ammonium acetate buffer) in a mixing coil. Before mixing with the acidified sample, the sample buffer solution was cleaned (for trace elements of interest) in-line by passing it through a clean-up column filled with Nobias–PA1 (Hitachi High-Technologies Corporation, Japan) chelating resin. The buffered sample was subsequently loaded onto a separate (but identical to clean-up column) column for in-line pre-concentration of Mn (and other trace elements of interest). Following this, the pre-concentration column was rinsed with the in-line diluted (with MQ water) sample buffer solution for removing excess and interfering salt. Thereafter, the trace metals pre-concentrated onto the column were eluted with ultrapure 1.6N HNO_3 (Optima^{TM}, Fisher Scientific) solution and the eluate was guided towards the HR-ICP-MS for the on-line measurement of dMn (and other dissolved trace metals of interest). After the elution step, both the pre-concentration and sample buffer clean-up columns were cleaned using the ultrapure 1.6N HNO_3 solution. Finally, the pre-concentration column was conditioned by rinsing it with the in-line diluted (with MQ water) sample buffer solution to get it ready for the next sample analysis sequence. Measurement parameters and other operational conditions set for the HR-ICP-MS during trace metal analyses are provided in Table 2.2.

Table 2.2: Measurement parameters and operational conditions during the dMn analysis using the Nu-HR-ICP-MS

RF forward Power:	1300 W
Sampler Cone:	Nickel
Skimmer Cone:	Nickel
Nebuliser:	PFA
Spray Chamber:	Quartz Cyclonic
Sample Flow rate:	200µL/min
Coolant Gas flow:	13 L/min
Auxiliary Gas Flow:	1 L/min
Nebuliser Gas flow:	~20 psi (Daily Optimization)
Instrument Resolution:	4000
Analysis Mode:	Deflector Scan
Scan Window:	600%
Dwell Time per Peak:	7.2ms
Switch Delay per Peak:	100µs
Number of Sweeps:	10
Number of Cycles:	50

2.4.2 Dissolved Mn analysis using flow injection system

An in-house flow injection analysis system (Mn-FIAS) is also developed for the measurement of sub-nanomolar to nanomolar levels of dissolved Mn in seawater. Similar to the Al-FIAS, the Mn-FIAS can be sub-divided into three components: (1) sample introduction component, (2) chemical analysis component and (3) detection and data acquisition and processing component. The sample introduction component of the Mn-FIAS is identical to that of the Al-FIAS. The physical structure of the chemical analysis component of the Mn-FIAS is similar to the Al-FIAS, consisting of two 6-port valves, a pre-concentration column, PTFE tubing manifold, and an 8-channel peristaltic pump with PVC tubings. dMn concentrations in seawater samples were determined by following the chemical analysis technique of Aguilar-Islas et al. (2006). The technique is based on the spectrophotometric detection of an organic dye, malachite green, which is formed by an Mn-catalysed reaction between leucomalachite green (LMG) and sodium periodate ($NaIO_4$). The chemical reagents used during the analysis include (1) sample buffer solution (0.5M $(NH_4)_3BO_3$, pH =9.4±0.05), (2) rinse solution (0.05M $(NH_4)_3BO_3$), (3) reaction buffer solution (3M NH_4Ac + 10.5mM Nitrilotriacetic acid (NTA); pH=5.3±0.1) (4) 0.4mM LMG solution, (5) 0.01M $NaIO_4$ and (6) 0.9M HCl. Details on the reagents preparations are given in Aguilar-Islas et al. (2006). All the reagents were prepared using commercially available high purity, low trace element blank chemicals: HCl (32-35%, Optima^{TM}, Fisher Scientific), NH_3 solution (20-22%, Optima^{TM}, Fisher Scientific), glacial CH_3COOH (Optima^{TM},

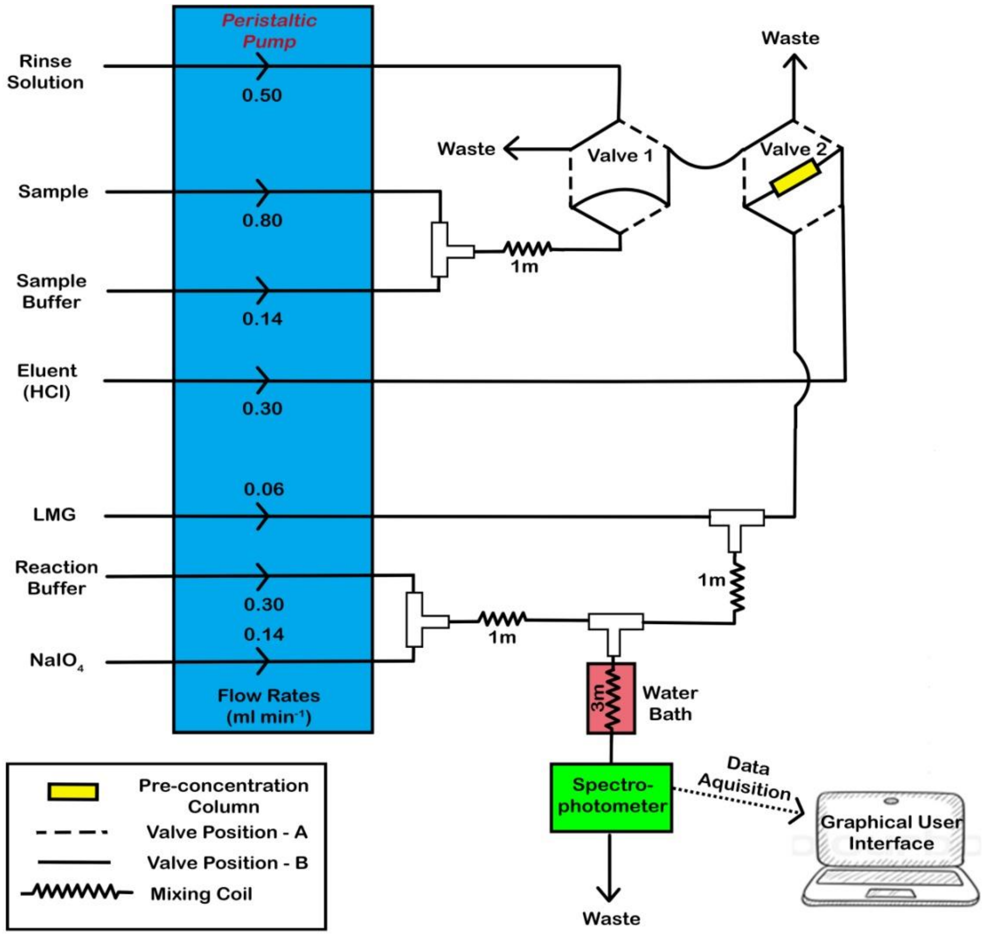

Fig. 2.5: Schematic representation of the Mn-FIAS. The sequence of different analytical steps and their time intervals are given in Table 2.1.

Fisher Scientific), Leucomalachite Green (solid, ACROS Organics™), NTA (≥99%, Sigma-Aldrich), Boric acid (H_3BO_3(s), Suprapur®, Merck) and $NaIO_4$ (ACS reagent, >99.8%, Sigma-Aldrich).

At the start of each analytical sequence, the pre-concentration column (2cm GLOBAL FIA mini-column packed with TOYOPEARL® AF-Chelate-650 M resin) was conditioned by passing the rinse solution through it for 30s. Concurrent to the column rinsing step, the acidified (pH ~1.7) seawater sample was buffered (to pH=8.3±0.2) in-line by mixing it with the sample buffer solution in a 1m mixing coil. Subsequent to the column conditioning, the buffered sample was loaded onto the column for 300s (5min) at the rate of 0.8 ml min^{-1}. After the sample loading, the pre-concentration column was again flushed with the rinse solution for 30s to remove loosely bound matrix elements from the column. Next, the pre-concentrated Mn in the column was eluted by passing 0.9M HCl solution through the column. The eluate was then mixed with the background flow of the LMG solution in a 1m mixing coil. In the background reagents flow, the $NaIO_4$ solution was mixed with the reaction buffer solution in a 1m mixing coil. Finally, the mixtures of LMG-column eluate and $NaIO_4$-reaction buffer react in a 3m reaction coil, submerged in a water bath (StableTemp, Cole-Parmer) kept at 40°C (±0.2°C), to form the organic dye, malachite green. The schematic representation of the Mn-FIAS is shown in Fig. 2.5 and the steps (with time-intervals) followed during every analytical sequence are given in Table 2.1.

The absorbance of the final malachite green solution formed was detected using a UV-VIS spectrophotometer (SPD-20A, Shimadzu) at 620nm (Aguilar Islas et al., 2006). The observed absorbance is proportional to the yield of malachite green, which is controlled by the amount of dissolved Mn (catalyst) in the analyzed sample. The hardware and the software used for data acquisition (from the detector) and processing are similar to those used for the Al-FIAS.

The Mn-FIAS was tested by measuring the dMn distribution in the seawater samples collected at the station GI-06(B)/18. GI-06(B)/18 is a crossover station to the Japanese GEOTRACES station, ER-5. dMn distributions determined for

GI-06(B)/18 using the HR-ICPMS and the Mn-FIAS were compared with that published for the crossover station, ER-5, and discussed later (section 2.5.2).

2.5 Calibration of dissolved Al and Mn analytical systems

All the analytical systems used, i.e., Al-FIAS, Mn-FIAS and seaFAST-integrated HR-ICPMS, were calibrated by running external calibration standards. For the preparation of the calibration standards, primary stock standards of Al and Mn (Al ~240 nM and Mn ~445 nmol kg^{-1}) were made by serial dilutions of single element ICP standards of Al and Mn (1000mg/l, CertiPUR®, Merck) using acidified MQ (pH ~1.7) water. Acidified MQ water was prepared by adding ~1mL high-purity, concentrated HCl (32-35%, Optima™, Fisher Scientific) to 1L of MQ water. Finally, the working external calibration standards for the analytical systems were made by diluting different proportions of the primary stock standards of Al and Mn using (pre-prepared) column-cleaned seawater (CCSW). CCSW was freshly prepared off-line before each batch of analysis (~50-60 combined analysis of samples and standards) by passing a buffered (to pH ~5.5 for Al standards and ~6.0 for Mn standards) deep seawater sample (collected in bulk during the cruise) through a pre-concentration column, filled with the commercial available chelating resin, Nobias-PA1 (Hitachi High-Technologies Corporation, Japan). Since the samples analyzed for dMn using Mn-FIAS and HR-ICPMS were buffered in-line before pre-concentration, the CCSW was re-acidified to pH ~1.7 by adding ~3ml of 6N high-purity HCl (Optima™, Fisher Scientific) to per liter of CCSW collection before using it for the preparation of working external calibration standards.

2.6 Data precision, accuracy and blank level for dissolved Al and Mn measurements

2.6.1 Dissolved Al

SAFe and GEOTRACES reference seawater samples were analyzed for their dAl concentrations. The measured dAl concentrations for the North Atlantic GEOTRACES reference standards (GS and GD) showed very good agreement with their reported consensus values (Table 2.3). However, the dAl values for the SAFe reference standards (SAFe D1 and D2) are ~1.5–2 times higher than the reported consensus values (Table 2.3). The values determined here are similar to the values recently reported (Table 2.3) by Resing et al. (2015). We also carried out multiple analyses of two in-house reference samples (InStd-D: 2.2nM ± 5% (1SD), n=42 and InStd-T: 3.8nM ± 6% (1SD), n=77; Fig. 2.6), which were calibrated for dAl concentration by running them multiple times

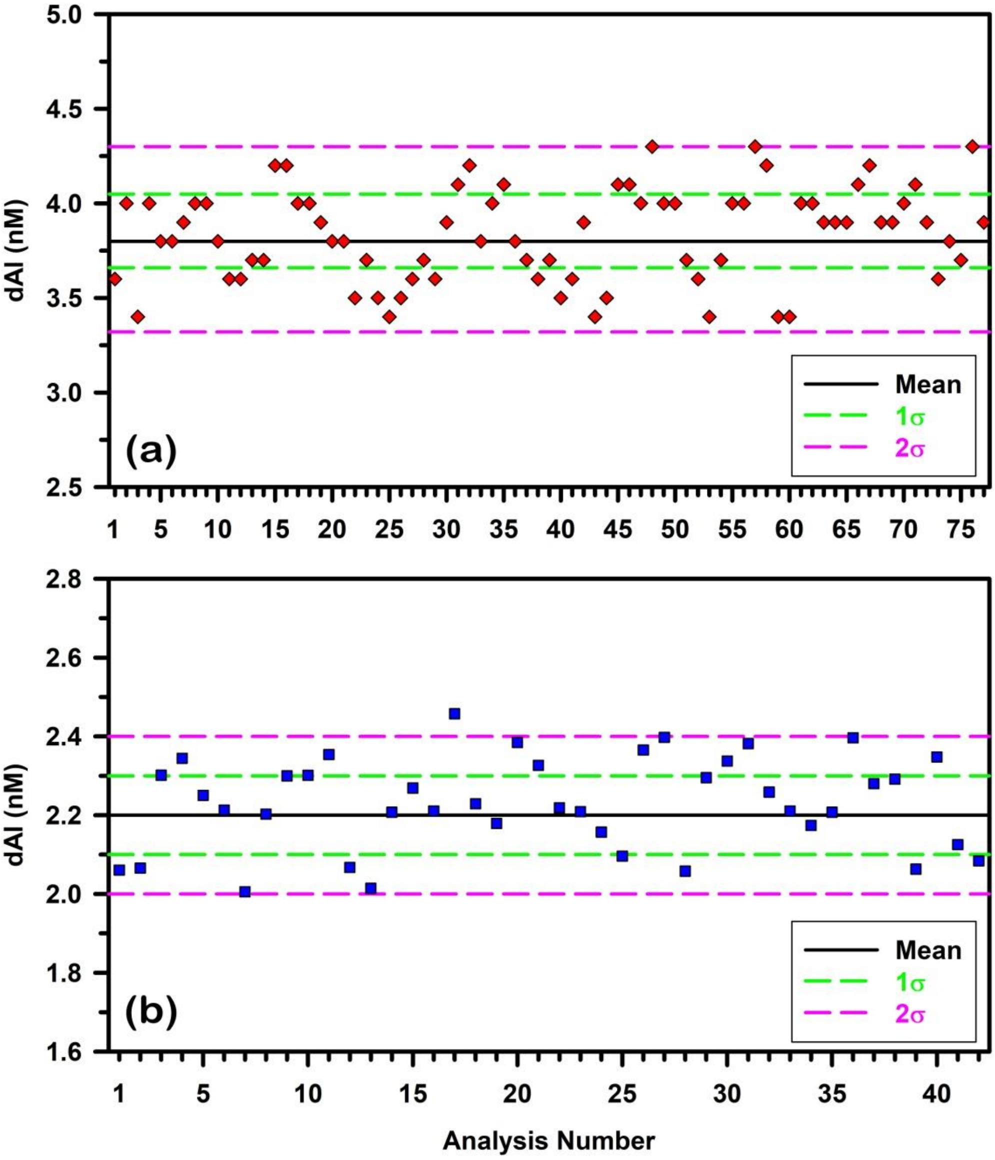

Fig. 2.6: Measured dAl concentrations of all the analytical runs for in-house reference samples (a) InStd-T and (b) InStd-D. The mean dAl values for InStd-T and InStd-D are 3.8nM (±0.24, 1SD) and 2.2nM (±0.1, 1SD), respectively.

along with the North Atlantic GEOTRACES seawater reference standards, GD and GS. InStd-D and InStd-T were sub-samples of acidified, bulk seawater samples (~20L) collected from 4000 m and 200 m water depths, respectively, during a GEOTRACES-India cruise (GI-02) in the western equatorial Indian Ocean region. Based on the InStd-D and InStd-T runs, the precision of dAl measurements are given as 5% at 2.2nM (n=42) and 6% at 3.8nM (n=77). Procedural blank for dAl measurements was estimated by running the column-cleaned seawater (CCSW), generally, 2-3 times during each batch of analysis. The mean of the blank concentrations observed during different days of analysis is 0.29 nM (n=76). For each batch of analysis, the detection limit was estimated by defining it as three times the standard deviation in the blank concentrations. The mean of the detection limits determined during different days of analysis is 0.06nM.

Table 2.3: Comparison of measured dAl concentrations (this study) and their consensus values in SAFe and GEOTRACES reference samples. Results from Resing et al. (2015) for SAFe reference samples are also presented.

Reference Sample	Batch No.	Al Concentration*		
		This Study	Resing et al. [2015]**	Consensus Value**
SAFe D1	D1 #242	1.28 ± 0.12 (1SD, n=4)	1.26 ± 0.11 (1SD, n=32)	0.62 ± 0.03 (1SD)
SAFe D2	D2 #361	1.63 ± 0.08 (1SD, n=3)	1.63 ± 0.13 (1SD, n=26)	1.03 ± 0.09 (1SD)
GEOTRACES GD	GD #163	17.7 ± 0.8 (1SD, n=4)	-	17.7 ± 0.2 (1SD)
	GD #31	17.4 ± 0.2 (1SD, n=3)		
GEOTRACES GS	GS #101	28.6 ± 0.4 (1SD, n=4)	-	27.5 ± 0.2 (1SD)

* The consensus values for the SAFe and GEOTRACES reference samples are in nmol kg^{-1} while their reported values in this study and Resing et al. [2015] are in nM.

** Given values represent the mean and one standard deviation of all the SAFe reference samples analyzed by Resing et al. [2015] and consensus values (as of May 2013) with one standard deviation after inter-laboratory calibration of SAFe and GEOTRACES references samples.

Stations GI-05/4 and GI-06(A)/3 are crossovers to Japanese GEOTRACES stations ER-5 and ER-2, respectively. The vertical dAl profiles observed at the crossover stations were compared to assess the quality of dAl concentration measurements in this thesis (Fig. 2.7a and 2.7b). The dAl trends observed in the deeper waters of the crossover stations GI-05/4 and ER-5 (below 1000 m, i.e., $\gamma^n > 27.6$ kg m^{-3}, Fig. 2.7a) are similar but slight differences in absolute dAl concentrations near 2000m (γ^n ~27.95 kg m^{-3}) and 2500 m (γ^n ~28.02 kg

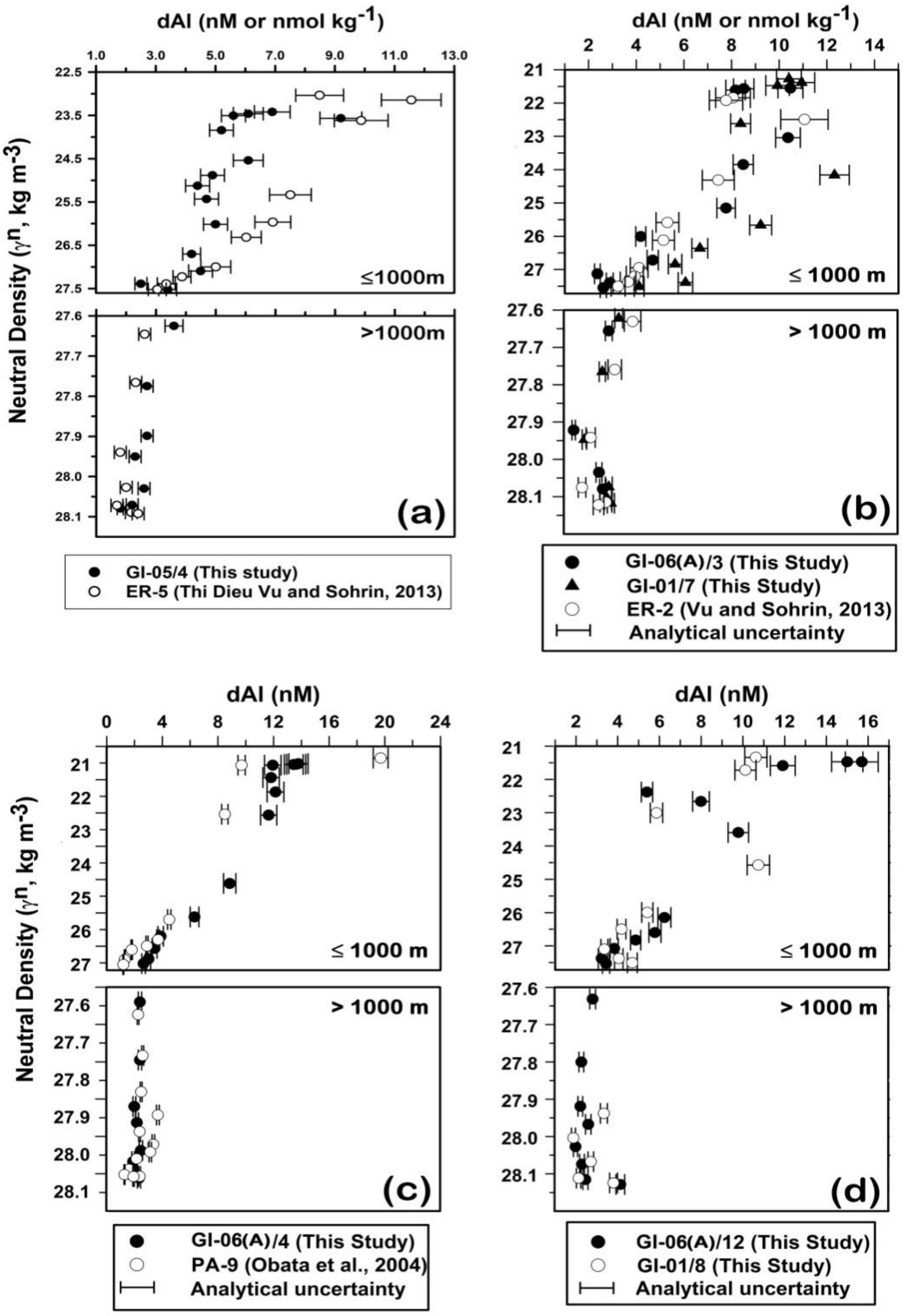

Fig. 2.7: Comparison of dAl distributions at the crossover stations. Analytical uncertainty estimates: (i) ER-2 and ER-5: precision achieved (~9%, 1SD; Thi Dieu Vu and Sohrin, 2013) after repeat analysis of SAFe deep water reference seawater, (ii) PA-9: precision achieved (2.7%, 1SD; Obata et al., 2004) at 2.0 nM and (iii) This study: precision achieved (6%, 1SD) after repeat analysis of in-house reference seawater, InStd-T. Also, the dAl concentrations reported by Thi Dieu Vu and Sohrin (2013) and this study are in nmol kg^{-1} and nM, respectively.

m^{-3}) depths were observed (Fig. 2.7a). These differences are, however, within 15% of the observed dAl values at the two stations. The dAl observed above 300 m (γ^n < 26.5 kg m^{-3}, Fig. 2.7a) at station GI-05/4 (this study) show significantly lower values compared to that measured at ER-5 (Thi Dieu Vu and Sohrin, 2013). In the surface mixed layer, the observed mismatch is not surprising. ER-5 was sampled during the NE monsoon period (December 2009) when atmospheric mineral dust input to the AS is much larger compared to that estimated during the sampling season (autumn or fall inter-monsoon period) of this study (Kumar et al. 2012; Pease et al., 1998; Tindale and Pease, 1999). Below the surface mixed layer, in the upper thermocline waters (25-300 m), the influence of the water mass advection on dAl distribution in the AS is observed and discussed in detail later (refer to section 4.4.2 of Chapter 4). The dense waters formed at the northern AS and the Arabian marginal seas (the Persian Gulf and the Red Sea) intrude into the thermocline water depths in the open AS regions (Shetye et al., 1994). The observed differences in the upper thermocline dAl distribution at the two stations may, therefore, indicate seasonal variations in the advective dAl input (refer to section 4.4.2 of Chapter 4 for more discussion), presumably, due to (1) changes in atmospheric Al input and removal rate (in response to the seasonal changes in biological productivity) at the formation regions of the thermocline water masses (Chen et al., 2008; Hamza et al., 2011; Torfstein et al., 2017) and/or (2) seasonal changes in output flux of the marginal sea waters to the AS (Bower et al., 2000; Maillard and Soliman, 1986; Prasad et al., 2001; You, 1997).

Though the broad dAl distribution patterns are similar for crossover stations GI-06(A)/3 and ER-2, the absolute values show slight differences in the thermocline and deep waters (>100m, i.e., γ^n > 25 kg m^{-3}, Fig. 2.7b) but mostly overlap within 20% of the dAl observed at similar neutral densities of the two stations. Such differences were also evident when the dissolved Fe data at ER-2 and nearby station GI-01/7 (Fig. 2.1a) were compared, particularly below 500 m (refer Fig. 2C of Chinni et al., 2019). Given the long time span (7 years) between occupations of the two stations, these differences may result from interannual variations in lithogenic sediment fluxes to the BoB (Unger et al., 2003), which predominantly controls the dissolved Fe (Chinni et al., 2019) and dAl (refer to section 3.4.1.1 and 3.4.2.1 of Chapter 3 for more discussion) in the region. dAl concentrations in the deeper waters (>1000m) at stations GI-01/7 and GI-06(A)/3, sampled within 130km, compare better (Fig. 2.7b). Station GI-06(A)/4 (8.148°N, 89.148°E) is within 25km of station PA-9 (8.0°N, 89.0°E, Obata et al., 2004; Fig. 2.1a) with dAl below 1000m being comparable or low relative to that at PA-9 (Fig. 2.7c). The dAl distributions at nearby stations GI-01/8 and GI-06(A)/12 also showed comparable results (Fig. 2.7d). In general, the dAl concentrations at crossover or nearby stations show, relatively, large differences in the upper water column (<1000 m, Fig. 2.7) presumably due to a smaller residence time of dAl compared to that in the deeper waters (Orians and Bruland, 1986), and therefore, showing more sensitivity towards seasonal and interannual variations in the dAl input from sources in the BoB.

2.6.2 Dissolved Mn

The Japanese GEOTRACES cruise (GI-04) station, ER-5, was re-occupied during the GI-06(B) cruise (as GI-06(B)/18, Fig. 2.1b) and the dMn vertical profiles observed at the two crossover stations are compared (Fig. 2.8a) to assess the accuracy of the dMn measurements in this study. The dMn distributions at the two stations show good agreement throughout the water column except at the surface layer (<50m), where the dMn concentrations observed during the Japanese cruise are significantly higher (by ~1-3 nM; Fig. 2.8a). The crossover stations, ER-5 and GI-06(B)/18, were sampled during different seasons, i.e., in early (November) and late (February) winter periods, respectively, and therefore, the observed difference in the surface layer dMn concentrations may represent the inter-seasonal variations. This seems plausible given the Arabian Sea is subject to significant seasonal changes in mineral dust flux depositions (Tindale and Pease, 1999), a prominent source of dMn to the surface ocean (van Hulten et al., 2017 and references therein). However, significant differences in the surface mixed layer salinity (ER-5: 36.081 and GI-06(B)/18: 36.531) and potential density anomaly (Fig. 2.8a) were also observed between the crossover stations. The surface mixed layer depths estimated (using the threshold change, i.e. 0.03 kg m^{-3}, in potential density with respect to that at 10m; Holte et al., 2017) during the sampling of

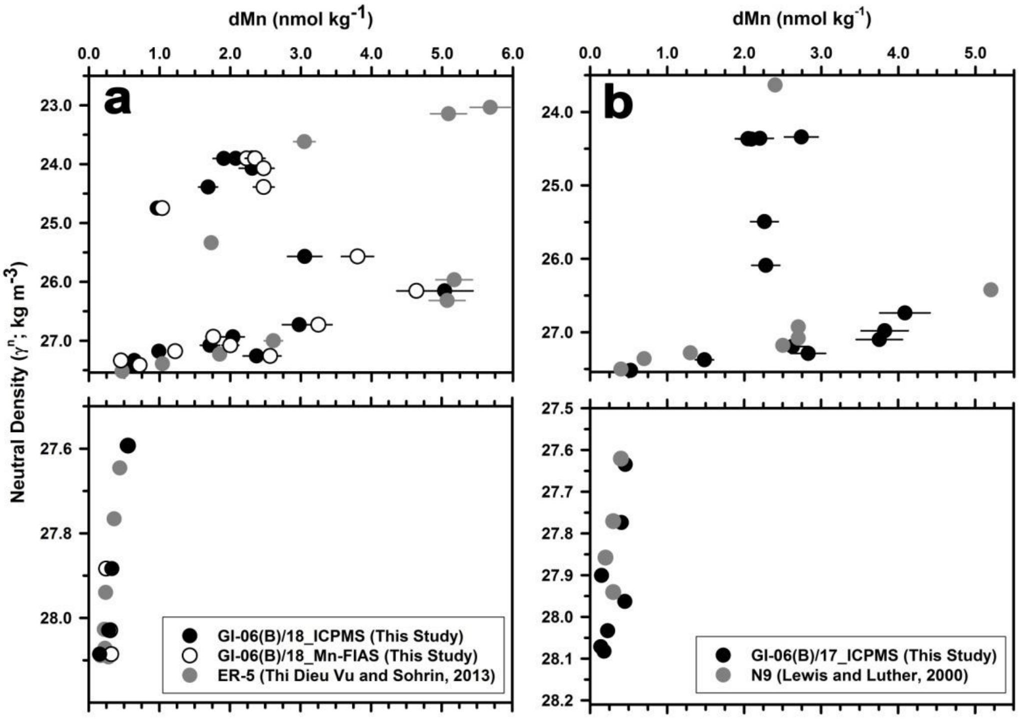

Fig. 2.8: Comparison of dMn distribution at the crossover stations. Analytical uncertainty estimates: (1) ER-5: precision achieved (~5%, 1SD; Thi Dieu Vu and Sohrin, 2013) after repeat analysis of SAFe surface water (SAFe S) reference seawater, (2) This Study: precision achieved (~8%, 1SD, n=68) at 1.09 nmol kg^{-1} using ICPMS and after repeat analysis of GEOTRACES reference sample, GS, (~6%, 1SD, n=4) using Mn-FIAS.

the crossover stations are also significantly different (ER-5: 25m and GI-06(B)/18: 46m). This suggests surface water mixing over deeper depths during the sampling of GI-06(B)/18 compared to that during the ER-5 sampling period. Change in the surface mixed layer depth may result in the redistribution of dMn (mixing of dMn-rich surface waters with, relatively, dMn-poor waters of the deeper depths). The observation that the integrated surface mixed layer dMn inventory (i.e., mixed layer dMn concentration times mixed layer depth) is similar for the crossover stations (ER-5 and GI-06(B)/18) also supports this redistribution (due to change in mixed layer depth) hypothesis. Our sampling station GI-06(B)/17 overlaps in space with station N9, sampled during the US-JGOFS cruise (Fig. 2.1b) for dMn measurements in the vertical water column. dMn concentrations observed at these stations also compare well (Fig. 2.8b).

The analytical precision obtained for the dMn analysis using HR-ICPMS at 1.09 nmol kg^{-1} was 8% (1SD, n=68). The mean procedural blank was estimated from the measurements of CCSW for dMn (using HR-ICPMS) at different analytical sessions and found to be 0.03 nmol kg^{-1} (n=13). The detection limit of dMn measurements (using HR-ICPMS) was defined as three times the standard deviation in the observed blank dMn levels and estimated to be 0.02 nmol kg^{-1}.

The dMn concentrations measured using the Mn-FIAS at station GI-06(B)/18 are consistent with the results obtained using the ICPMS (Fig. 2.8a). Additionally, dMn concentration measured (1.54 ± 0.10 nmol kg^{-1}(1SD), n=4) for the GEOTRACES reference sample, GS, using the Mn-FIAS show excellent agreement with the consensus value (1.50 ± 0.11 (1SD) nmol kg^{-1}).

2.7 Ancillary parameters

The seawater sampling rosette system was equipped with a CTD sensor (SBE-911plus, Sea-Bird Scientific, USA) for continuous measurements of conductivity (salinity), temperature and pressure. Dissolved oxygen levels were measured throughout the water column during sampling using an SBE 43 sensor (Sea-Bird Scientific, USA) mounted on the sampling rosette. An ECO-NTU sensor (WET Labs, Sea-Bird Scientific, USA) was added to the package for continuous measurement of seawater turbidity during the GI-06(A) cruise. All the sensors were calibrated (by Sea-Bird Scientific, USA) before the cruises.

Seawater samples (unfiltered) collected during the GI-01, GI-05 and GI-06(A) were analyzed onboard for the major inorganic nutrients, i.e., silicic acid (H_2SiO_4), phosphate (PO_4^{3-}), nitrate plus nitrite ($NO_3^- + NO_2^-$), based on the colorimetric detection method (Hansen and Koroleff, 1999). The precision of H_2SiO_4, $PO_4^{3-}$and $NO_3^- + NO_2^-$ measurements during the GI-01 and GI-05 cruises were ±0.02 µM, ±0.01 µM and ±0.02 µM, respectively (Chinni et al., 2019; Sarma and Dalabehera, 2019). During the GI-06 cruise, H_2SiO_4, PO_4^{3-} and $NO_3^- + NO_2^-$ were measured with percentage relative standard deviation (% RSD) better than 6%, 2% and 5%, respectively, for repeat analysis.

2.8 Conclusion

Hundreds of filtered seawater samples, collected using a trace metal clean sampling system, were analyzed for dissolved aluminium (Al) and manganese (Mn) concentrations in different Indian Ocean basins. Precise and accurate measurements of sub-nanomolar to nanomolar levels of dissolved Al and Mn were made using in-house developed flow injection analysis systems (Al-FIAS and Mn-FIAS). Such portable systems can be utilized for onboard analysis of dissolved Al and Mn and are useful to realize any possible sampling and sample processing artifacts during the cruise. The majority of the dMn data is produced by analysis using the seaFAST-integrated HR-ICPMS system. The system allows having multi-trace element analysis on sample aliquot of seawater sample with in-line pre-concentration of trace elements.

Good agreement between the measured and consensus levels of dAl and dMn in GEOTRACES and SAFe seawater reference samples ensures the accuracy of the data presented. Moreover, comparable dMn and dAl distribution observed for the crossover stations provides additional confidence in sampling protocol and data accuracy.

Chapter 3

Dissolved aluminium cycling in the northern, equatorial and subtropical gyre region of the Indian Ocean

3.1 Introduction

Dissolved aluminium concentrations in the global ocean have shown large inter-oceanic fractionation due to the varying nature and strength of its external sources and internal cycling in different oceanic basins (Chou and Wollast, 1997; Grand et al., 2015b; Measures and Vink, 1999; Middag et al., 2012; Orians and Bruland, 1986). Deposition and partial dissolution of continental crust derived atmospheric mineral dust is considered as the major source of dAl to the surface ocean waters, particularly in remote ocean regions (Grand et al., 2015b; Hydes, 1979; Measures and Edmond, 1990). Al released from the resuspended sediments over continental margin and seafloor may also act as an important source of dAl to the ambient seawaters (Mackin and Aller, 1984, 1986; Middag et al., 2009, 2015; Moran and Moore, 1991). However, the relative contribution of Al released from suspended particulate matter (due to particle dissolution and/or Al desorption) and diffusive Al flux from dAl enriched sediment pore waters to the water column near sediment-water interface is uncertain due to limited knowledge on particulate Al levels of the resuspended sediments, dAl concentrations of pore waters and diffusivity across the sediment-water interface (Orians and Bruland, 1986). The extent of Al release from sediments near ocean margins depends on the intensity of water turbulence leading to sediment remobilization and availability of reactive Al in the margin sediments (Measures et al., 2015; Middag et al., 2015; Moran and Moore, 1991). Concentration of dissolved silicic acid in ambient ocean waters at sediment-water interface and biogenic silica accumulation rates in margin sediments are observed to control the Al dissolution/desorption from the resuspended sediments in the water column and dAl diffusive flux from the sediment pore waters, respectively (Koning et al., 2007; Mackin and Aller, 1984; Middag et al., 2015; Van Beueskom et al., 1997). Stoichiometric interaction of Al, released from resuspended sediments, with ambient dissolved Si may result in the precipitation of authigenic aluminosilicates and inhibits the build-up of dAl in the dissolved Si-rich ambient seawater (Mackin and Aller, 1984, 1986).

Al is also one of the most concentrated dissolved trace metals in river waters (Gaillardet et al., 2014) but estuarine processes filter out the majority of the dAl before river water discharges to the ocean (Mackin and Aller, 1984). Al released from the atmospheric mineral dust and/or resuspended sediments in the formation regions and/or along the advective pathways of water masses and their subsequent movement to other oceanic regions may also provide a significant share to the total dAl inventory in the water column, at least at basin scale (Measures and Edmond, 1988; Measures et al., 2015; Middag et al., 2009, 2015). Elevated dAl signals in the deep-water hydrothermal plumes, emanating from hydrothermal vents along the mid-oceanic ridges, have been reported in the Atlantic (Lunel et al., 1990; Measures et al., 2015) and the Pacific (Resing et al., 2015) Ocean. From these studies, it could be summarized that the magnitude of the dAl input from the hydrothermal processes to the deep waters is largely controlled by the composition of hydrothermal fluids, dAl content of the deep waters entrained by the hydrothermal plumes near the vents and topographical constraints around the vents (Lunel et al., 1990; Measures et al., 2015; Resing et al., 2015). The topography around the vents is also observed to play a crucial role in controlling the dispersal of the dAl-rich hydrothermal plume (Measures et al., 2015; Resing et al., 2015). However, in view of the limited observations of dAl near active hydrothermal vents and seafloor spreading sites, the relative contribution of hydrothermal dAl input to the global deep waters dAl budget is still debatable and is specifically neglected in simulations by the modeling studies done to date (Gehlen et al., 2003; van Hulten et al., 2013, 2014).

Dominant controls on output flux of dAl from the water column are set by particle scavenging processes (Hydes, 1979; Orians and Bruland, 1985). Biogenic silica particles are one of the main carrier phases of scavenged Al, given the Al chemical affinity (to get adsorbed) towards high negative surface charge density of siliceous particles (Dixit and Van Cappellen, 2002; Dymond et al., 1997; Moran and Moore, 1988). Along with passive scavenging, active uptake of Al by the living diatoms during biosynthesis of frustules is also possible, which has been shown experimentally (Gehlen et al., 2002). This has implications for the export and remineralization of biogenic silica (bSi) and its regeneration since Al integration in the silicate framework has been shown to reduce the solubility of bSi in the seawater (Koning et al., 2007).

Previous studies (Grand et al., 2015a; Measures et al., 2015; Measures et al., 2005; Measures and Vink, 2000) have exploited the surface ocean dAl concentrations to estimate the atmospheric mineral dust fluxes over different ocean basins, considering the steady-state balance between Al input from the partial dissolution of mineral aerosols and output via scavenging by particles and their subsequent removal out of the surface. In general, the order of error associated with this steady-state, 1-D approach is about a factor of 3 due to the uncertainties in Al solubility from mineral dust and dAl scavenging rates (Grand et al., 2015a; Measures and Vink, 1999). Compared to this, the estimates of dust deposition fluxes from atmospheric models have uncertainty on the order of a factor of 10 (Mahowald et al., 2005). Also, in the regions where advective processes and other sedimentary (e.g., continental margin sediments) sources/sinks of Al play a major role in controlling the dAl concentrations, surface dAl-based atmospheric dust fluxes may be over or underestimated using the 1-D, steady-state model (Grand et al., 2015a).

In the Indian Ocean, relatively few measurements of dAl have been reported and, thus, our understanding of Al cycling in this ocean basin is quite limited. Grand et al. (2015b,c) have recently reported high (spatial) resolution dissolved Al concentrations data in the eastern Indian Ocean and across the southern end of the Indian Subtropical Gyre, but their measurements were restricted to the upper water column (<1000 m). Studies reporting full vertical water column profiles for dAl in the Indian Ocean are sparse (Obata et al., 2004; Vu and Sohrin, 2013). In this study, we have measured 34 full vertical profiles of dAl in the northern (the BoB, the Andaman Sea and the Arabian Sea), equatorial and subtropical gyre region of the Indian Ocean to constrain the probable sources, sinks and processes that may control the dAl distribution in these regions. This study greatly increases the spatial density of Al measurements, especially in the deep waters of the Indian Ocean.

3.2 General circulation and water mass structure

Several studies (Kumar and Li, 1996; Mantyla and Reid, 1995; Schott et al., 2009; Tomczak and Godfrey, 2003a,b; You and Tomczak, 1993; You, 1997, 2000; Shetye et al., 1994; Singh et al., 2012; Wyrtki, 1973) have discussed the circulation and structure of the water masses present in the Indian Ocean basins. Here, the circulation patterns and water-mass structure observed during the study period, mostly restricting to the studied regions, are discribed. To facilitate data interpretation and discussion, the study area has been sub-divided into different sub-basins in the Indian Ocean: (1) Bay of Bengal (BoB; north of 5°N, 80-92°E), (2) Andaman Sea (north of 5°N and 94-100°E), (3) Arabian Sea (AS; north of 5°N, 51-73°E), (4) Equatorial Indian Ocean (Eq.IO; 5°N-5°S) and (5) Indonesian Throughflow and Indian Subtropical Gyre (ITF-ISG; south of 5°S) region. Stations GI-06(A)/11 and GI-06(A)/12 (Fig. 3.1) were considered to be in the transitional region from the southern BoB to the Eq.IO. Fig. 3.1

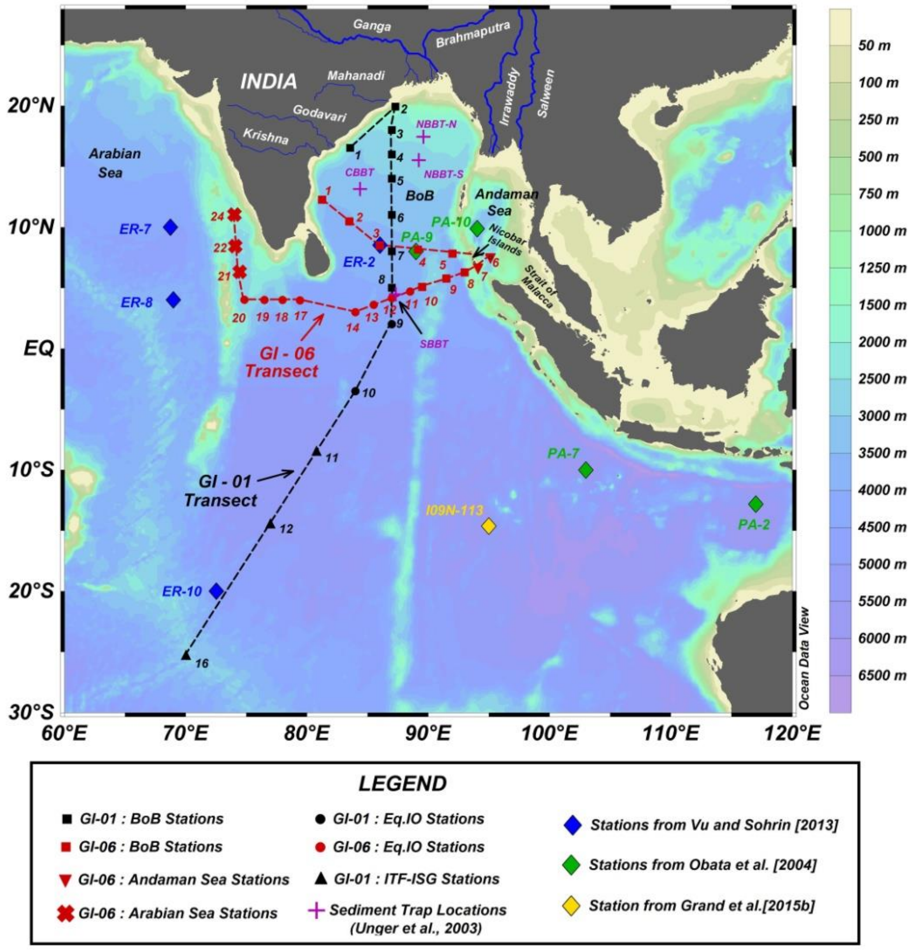

Fig. 3.1: Map showing the stations occupied for clean seawater sampling during the GI-01 (black symbols) and GI-06(A) (red symbols) cruises. Tracks of various major rivers flowing through India and Indo–Myanmar regions to the BoB and the Andaman Sea are shown. Sampling locations for dAl and other ancillary data from earlier studies used during the text discussions are also plotted. This map was prepared using ODV 4.7.9 software (Schlitzer, 2016).

shows the stations occupied in different sub-basins (defined above) during the GI-01 and GI-06(A) cruises in the Indian Ocean.

3.2.1 Surface and thermocline waters

The large annual river water influx from the Himalayan rivers (the Ganga and the Brahmaputra), Indian peninsular rivers (the Mahanadi, the Godavari and the Krishna) and Indo-Myanmar rivers (the Irrawaddy and the Salween) to the north-eastern Indian Ocean (i.e., the BoB and the Andaman Sea) is manifested as low salinity, Bay of Bengal Water (BBW) in the surface water layer of the region. The thickness of the low salinity (<34) surface layer gets shallower in the southern BoB (<50 m) and the Andaman Sea compared to the northern and central BoB (50–100 m; Fig. 3.2a and 3.3a). Dominating the contributions from all the rivers, the Ganga-Brahmaputra (G-B) river system annually discharges freshwater and suspended sediments on the order of 10^3 km^3 and 10^3 Mt (1 Mt = 10^9 kg), respectively, to the BoB (Galy and France-Lanord, 2001; Sengupta et al., 2006, Singh et al., 2008). A comparable freshwater flux and about half of the suspended sediment flux from the G-B river system is discharged by the Irrawaddy and Salween (I-S) river system to the Andaman Sea (Damodararao et al., 2016; Robinson et al., 2007). During the late fall intermonsoon to the late winter monsoon period (November to February), the low salinity BBW is transported to the surface layers of the Arabian Sea by the Northeast Monsoon Current (NMC, Fig. 3.4a), centered along 5°N, and the East Indian Coastal Current (EICC), flowing southward along the east coast of India (Kumar et al., 2004; Schott et al., 2009; Wyrtki, 1973; Goswami et al., 2014). The low surface salinity (33.53-34.18) observed during the late winter period in the south-eastern Arabian Sea (GI-06(A)/21, 22 and 24; Fig. 3.2c) suggests the advection of the BBW to this region.

In general, the surface waters in the BoB showed an anti-cyclonic motion during both the cruises (Fig. 3.4a). Over this general circulation pattern, transits of strong anti-cyclonic (warm-core) eddies at stations GI-01/3 and GI- 01/5 and cyclonic (cold-core) eddies at stations GI-06(A)/2, GI-06(A)/10 and GI-01/7 were observed, which are marked by deepening or shoaling of the neutral density (γ^n; kg m^{-3}) isolines and salinity variations at these stations (Figs. 3.2a, 3.3a and 3.3b).

In the southern Andaman Sea, advection of low salinity, Indonesian Water from the Strait of Malacca (SoM) to the Andaman Sea may also contribute to the surface waters (Rizal et al., 2012). Further, the low salinity surface waters of the southern Andaman Sea may advect to the southern BoB as evident from the surface circulation patterns (refer Fig. 3.4a for a schematic representation) and low surface salinity levels (<34) at stations GI-06(A)/8, 9, 11 and 12, and GI-01/08 in the southern BoB. However, eddy pumping of sub-surface waters to the surface layer erodes this low salinity signal at station GI-06(A)/10 (Fig. 3.3b).

Mixed layer salinity (S_{ML}) in the equatorial stations was higher (33.80-35.33) compared to that in the BoB due to decreasing contribution from the BBW and increased westward (~34.63 at GI-06(A)/13 to ~35.33 at GI-06(A)/19, Fig. 3.3b), presumably, due to the admixing of the equatorial surface waters with high salinity surface waters of the southern Arabian Sea under the influence of the NMC (Fig. 3.4a). Sub-surface (75-100 m) salinity maxima observed in the coastal Arabian Sea and equatorial stations west of 88°E (GI-06(A)/12 to GI-06(A)/20, GI-01/09 and GI-01/10; Figs. 3.2a, 3.3b and 3.3c) indicate the presence of Arabian Sea High Salinity Water.

Further south in the ITF-ISG region (south of 5°S), the surface and thermocline waters (0-1000 m) at stations GI-01/11 and GI-01/12 are impacted by the low salinity, Indonesian Throughflow Water (ITW) carried by the west-flowing South Equatorial Current (SEC) across the latitude range: 8-15°S (Tomczak and Large, 1989; Fig. 4a). This is evident from the low salinity surface waters (Fig. 3.2a) and variations in T-S (potential temperature-salinity) curve at these stations (refer to Fig. 3.5d] resulting from mixing and interleaving between the ITW and the Indian Central Water (ICW) (Tomczak and Godfrey, 2003a; Tomczak and Large, 1989). The ICW is formed in the subtropical convergence zone (40-45°S) by subduction of subtropical surface waters (You and Tomczak, 1993) and represented by thermocline waters at station GI- 01/16, showing its typical T-S curve (θ ~9-15°C, Fig. 3.5d). The upper water column

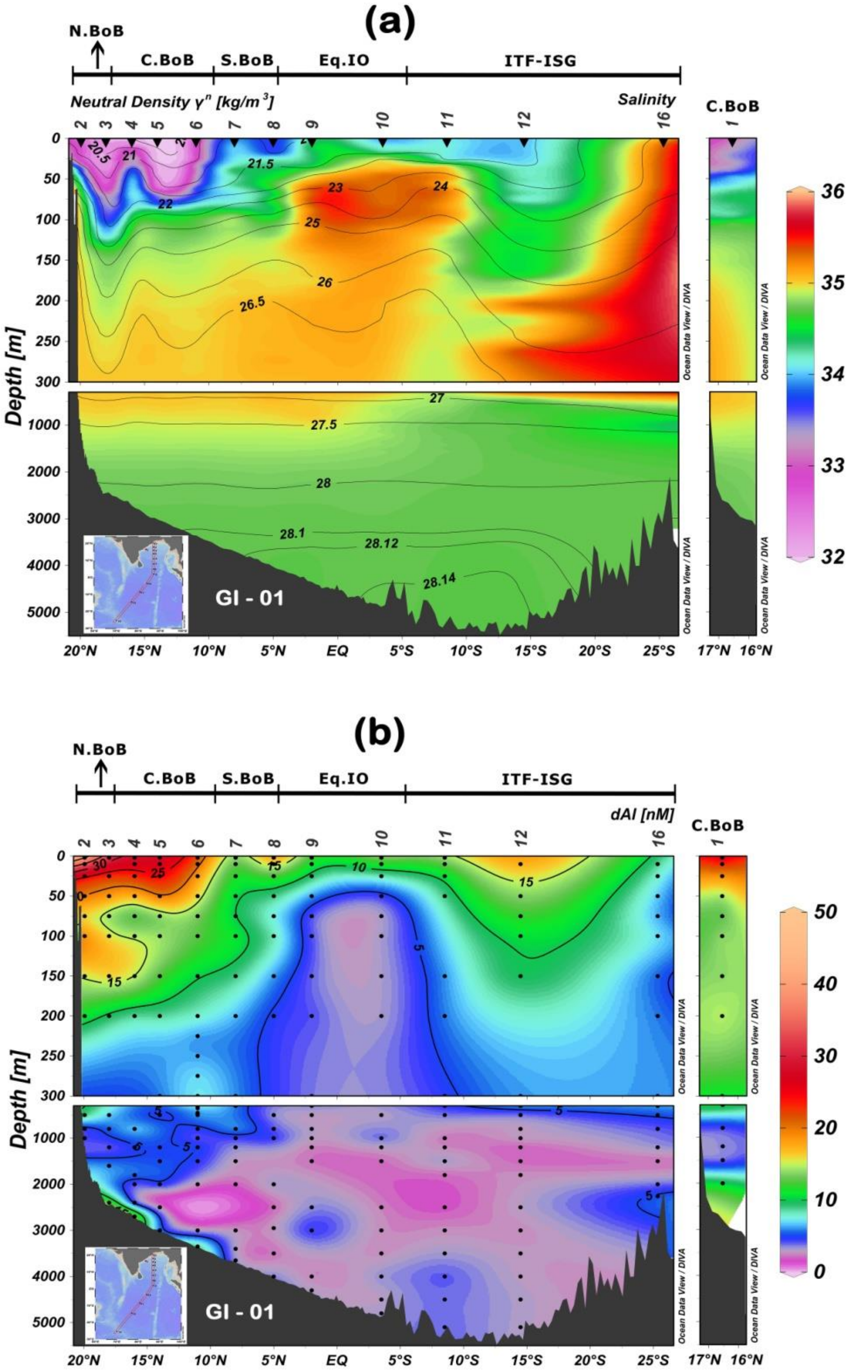

Fig. 3.2: (a) Salinity of and (b) dAl concentrations in the water column sampled along the GI–01 cruise transect (shown in the inset map) during the spring–intermonsoon period (March–April) of 2014. Overlain contours in the top and bottom figures represent the neutral density (γ^n, kg m^{-3}) and dAl concentration (in nM) isolines, respectively. For better visualization of the data in the more dynamic surface and upper thermocline waters (≤300 m), salinity and dAl distributions are shown separately for the upper 300 m water depth and the remaining water column below (≥300 m).

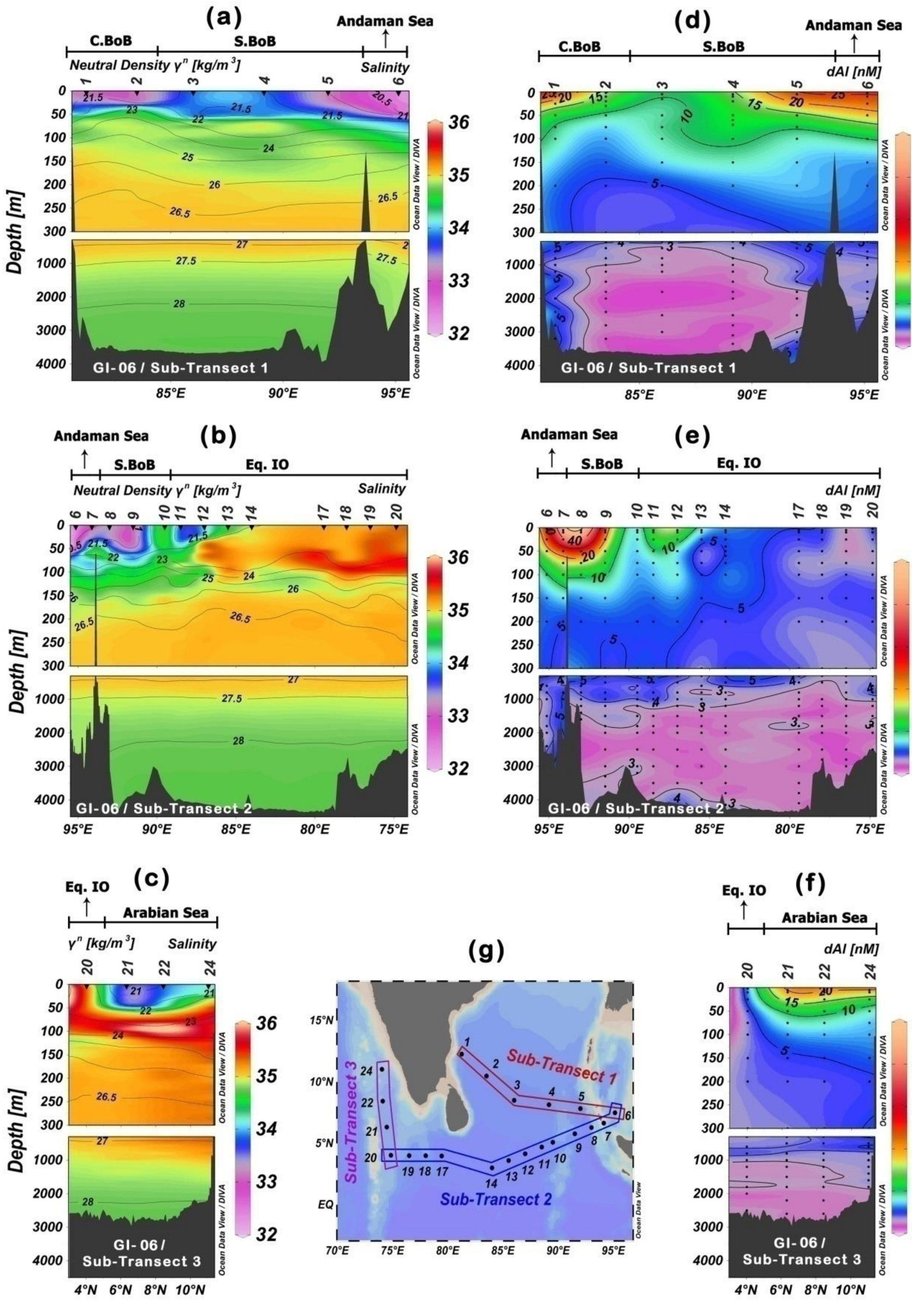

Fig. 3.3: Same as Fig. 2, but the salinity (a–c) and dAl observations (d–f) plotted are for the GI–06 cruise. For better visualization and interpretation, the full GI–06 cruise track was sub-divided into three separate sub-transects. Sub–transect 1 and 2 are the two zonal transects in the southern BoB and the Andaman Sea, and the equatorial Indian Ocean, respectively. Sub-transect 3 is a meridional transect in the south-eastern Arabian Sea. Fig. (g) shows the division of the full GI–06 cruise transect into the above-mentioned sub-transects.

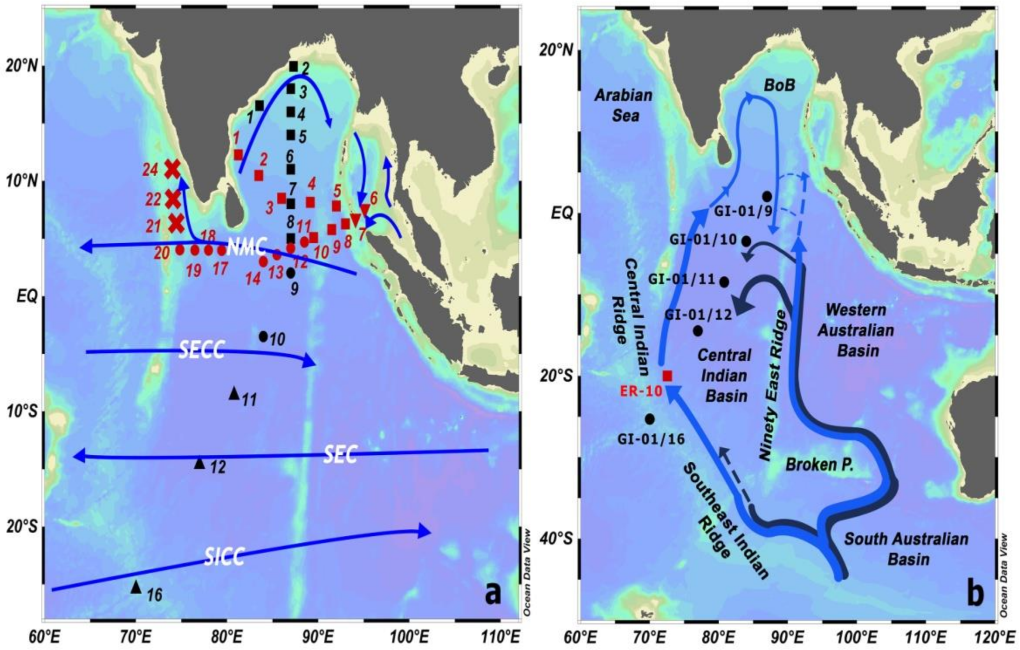

Fig. 3.4: (a) Schematic diagram showing the general surface water circulation during the sampling in the study regions. The diagram is deduced using the Ocean Surface Current Analysis Real-time (OSCAR) third degree (1/3 x 1/3 degree) resolution ocean surface currents data (ESR, 2009). (b) Qualitative representation of deep (light blue) and bottom water (dark blue) circulation pattern for the Central Indian Ocean Basin and the BoB. The circulation scheme is plotted after composite results from Toole and Warren (1993), Mantyla and Reid (1995), Kumar and Li (1996) and You (2000).

(<200 m) of station GI-01/16 in the subtropics (Fig. 3.1) comes under the influence of north-east flowing South Indian Counter Current (SICC, Fig. 3.4a), which is fed by retroflection of Southeast Madagascar Current (SEMC) waters (Schott et al., 2009 and references therein).

3.2.2 Deep and bottom waters (>2500 m)

Principle water-masses filling up the deep and bottom water column depth (>2000 m) in the Indian Ocean are the Modified North Atlantic Deep Water (MNADW) and the Antarctic Bottom Water (AABW) (Kumar and Li, 1996; Singh et al., 2012; Goswami et al., 2014; You, 2000). The MNADW is formed by mixing and entrainment of the North Atlantic Deep Water into the Circumpolar Deep Water (CDW) of the Indian Ocean Sector of the Southern Ocean (Kumar and Li, 1996; You, 1999) and occupies the depth range of 2000–3500 m (You, 1999). The AABW fills the deepest depths (>3500 m) in the Indian Ocean Basins (Tomczak and Godfrey, 2003a; You, 1999). Fig. 3.4b depicts the general circulation scheme of the deep (2000–3500 m) and bottom (>3500 m) waters in the Central Indian Basin and BoB (Kumar and Li, 1996;

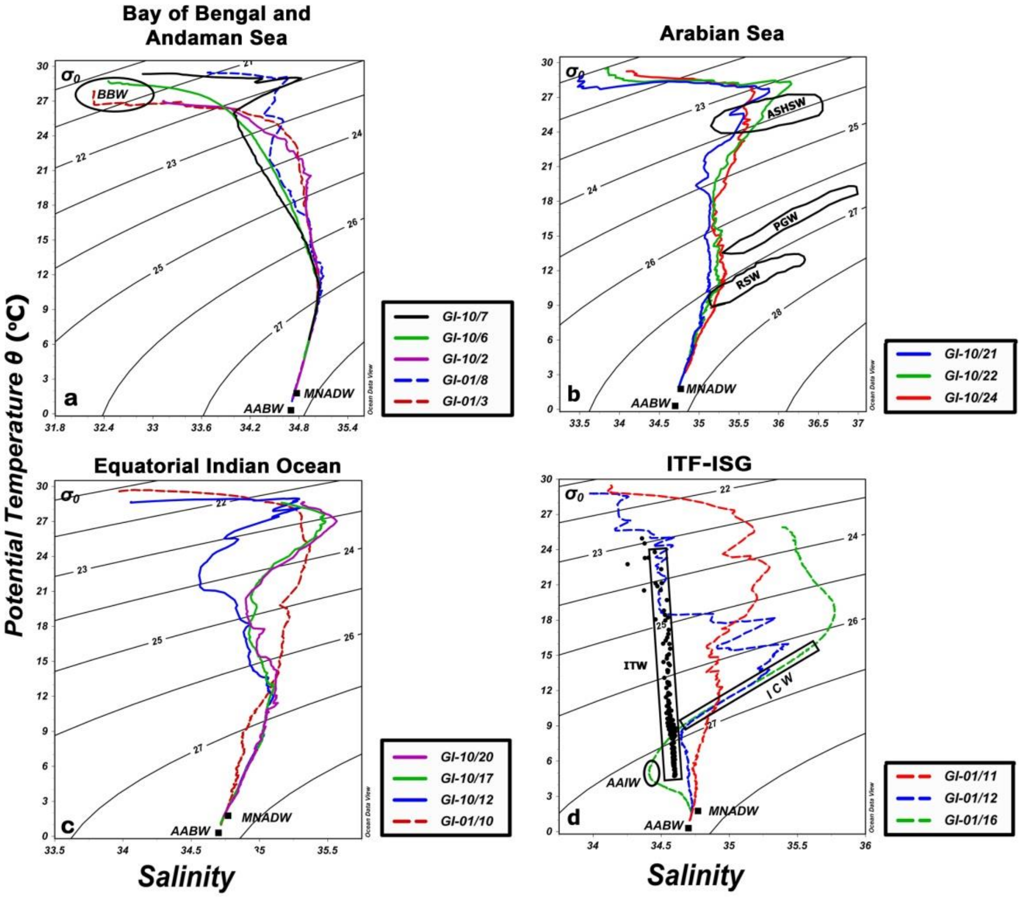

Fig. 3.5: T–S variations in the vertical water column at the representative stations sampled in different Indian Ocean sub-basins during the GI-01 (dashed lines) and the GI-06(A) (solid lines) cruises. Characteristic ranges of T–S values for different water masses present in the water column and potential density anomaly isolines are also traced. AABW: Antarctic Bottom Water, AAIW: Antarctic Intermediate Water, ASHSW: Arabian Sea High Salinity Water, BBW: Bay of Bengal Water, ITW: Indonesian Throughflow Water, MNADW: Modified North Atlantic Deep Water, NIIW: North Indian Intermediate Water, PGW: Persian Gulf Water, RSW: Red Sea Water. Data sources for characteristic ranges of T–S values: AABW and AAIW- Tomczak and Godfrey, 2013a; ASHSW- Shenoi et al., 1993; BBW- T-S data observed in the surface mixed layer of stations GI–01/2 and 3 in the N.BoB of this study; ITW- T-S data variations in the thermocline waters (100-1000 m) observed at the latitudinal and longitudinal ranges of 8-12 °S and 120-123 °E, respectively. The T-S data was derived using the annual statistical mean salinity and temperature data from World Ocean Atlas 2013, version 2 (Locarnin et al., 2013; Zweng et al., 2013); MNADW- Kumar and Li, 1996; NIIW- Singh et al., 2012; PGW and RSW- Shenoi et al., 1993.

Mantyla and Reid, 1995; Toole and Warren, 1993; You, 2000). Deep waters (2000–3500 m) are mainly derived from the South Australian Basin into the Central Indian Basin and BoB through the deep passage between the Broken Plateau and the Southeast Indian Ridge and flow northwards (Fig. 3.4b; You, 2000). On the other hand, bottom waters in the Central Indian Basin are primarily derived from the Western Australian Basin through the deep saddles at ~5°S and 10°S on the Ninety–East Ridge (NER, Fig. 3.4b; Mantyla and Reid, 1995; Tomczak and Godfrey, 2003a; Toole and Warren, 1993). In contrast to the northward movement of deep waters above, the bottom waters, after entering into the Central Indian Ocean Basin, turn and flow southwards (Mantyla and Reid, 1995; Toole and Warren, 1993; refer Fig. 3.4b for a schematic representation).

3.3 Results

3.3.1 dAl distribution in the surface mixed layer and upper thermocline waters (0-300 m)

For better understanding and data interpretation, the BoB region was further sub-divided into the northern (N. BoB; >17°N), the central (C.BoB; 10-17°N) and the southern BoB (S.BoB; 5-10°N). The mean dAl concentrations in the surface mixed layer (dAl_{ML}) observed in the BoB were in the range of 9.2-48.3 nM, combining both the cruises (refer Table A1 in the Appendix A). The meridional section sampled in the BoB during the spring–intermonsoon period (GI-01 cruise) showed a similar latitudinal trend (Fig. 6) in the dAl_{ML} variations as reported earlier by Grand et al. (2015a), showing decreasing dAl_{ML} concentrations from the N.BoB to the S.BoB. Note the general mismatch between the dAlML observed for the C.BoB stations in this study and topmost depth sampled in the C.BoB by Grand et al. (2015a) (Fig. 3.6). The topmost sampling depths of Grand et al. (2015a) in the C.BoB lie below the surface mixed layer observed during their sampling period (refer Figs. 2 and 3 of Grand et al. (2015a)) and therefore probably represent the dAl levels in the strong chemocline (decreasing dAl concentrations) below the surface mixed layer. Independently, this observed mismatch in the C.BoB may also result due to the interannual variations in dAl supply from the sources and/or influence of eddies (given the seven years of time gap between sampling periods of this study and that of Grand et al., 2015b) on the surface dAl. During the spring-intermonsoon period (GI-01 cruise), highly enriched dAl_{ML} value (~47 nM) was observed in the northernmost station, GI-01/2, situated closest to the mouths of the Ganga and Mahanadi rivers (~200 km and ~70 km from the Hooghly (the Ganga) river and the Mahanadi river mouth, respectively) and probably, most influenced by the fluvial inputs (freshwater and sediments) of the G-B river system. South of the station GI-01/2 at GI-01/1 and from stations GI-01/3 to GI-01/5 in the C.BoB, dAl_{ML} showed near-uniform values (mean dAlML = 27.3 ± 0.9 nM, Fig. 3.7) with significant variation in S_{ML} (31.802-33.386). Thereafter, from station GI-01/5, towards the S.BoB, dAl_{ML} decreased

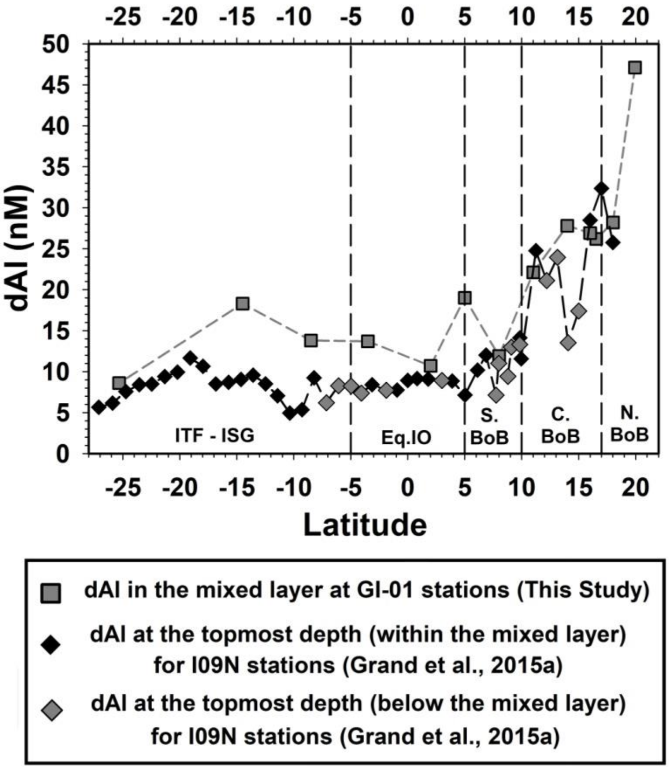

Fig. 3.6: Latitudinal variations of dAl_{ML} (grey squares) observed along the GI-01 cruise track and dAl concentrations measured at the topmost water depth (black and grey diamonds) sampled along the U.S. CLIVAR CO2 Repeat Hydrography I09N cruise in the Indian Ocean. The grey diamonds distinguish the stations where the topmost depth analyzed for dAl concentrations was below the observed mixed layer depth during the U.S. CLIVAR CO2 Repeat Hydrography I09N cruise (Grand et al., 2015a).

linearly ($R^2 = 0.90$, Fig. 3.7) with increasing S_{ML}. During the late winter period (GI-06(A) cruise), dAl enrichment together with decreasing salinity in the surface waters (≤50 m) was observed towards the south-east coast of India (GI-06(A)/1) and the region around the Nicobar Islands (GI-06(A)/5, 6, 7, 8 and 9; Fig. 3.3a, b, d and e). dAl_{ML} concentrations at GI-06(A)/7 and 8 (~43-48 nM; Fig. 3.3e) near the Nicobar Islands were the highest observed during this study. It is interesting to note that at stations GI-01/7 and GI-06(A)/10 in the S.BoB (Fig. 3.1), where the transit of cold-core eddies was observed, a sudden decrease in dAl_{ML} concentrations (Figs. 3.2b and 3.3e) accompanied with a steep increase in S_{ML}, relative to the adjacent stations (Figs. 3.2a and 3.3b), was observed.

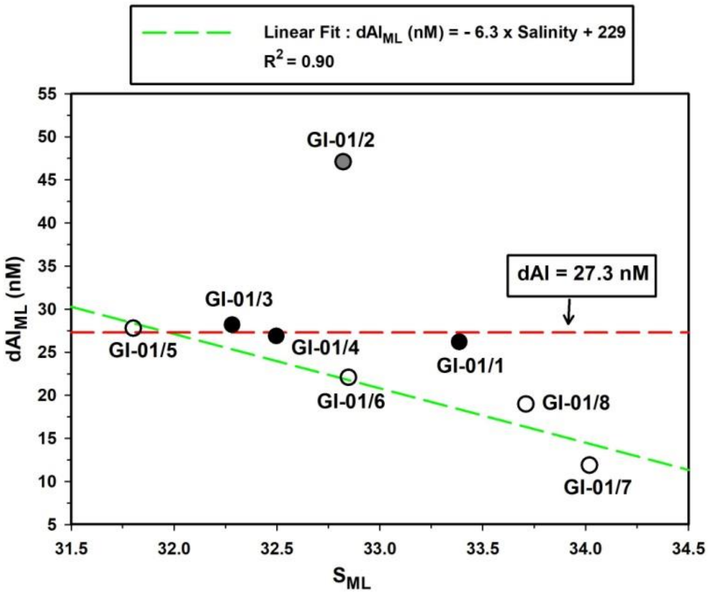

Fig. 3.7: dAl_{ML} plotted against S_{ML} for the stations sampled in the BoB during the GI-01 cruise. The station sampled at the northernmost point in the BoB (GI-01/2; grey circle) showed a highly enriched dAl_{ML} level. The red dashed line represents the mean dAlML for stations GI–01/1, 3, 4 and 5 (see text). The green dashed line represents the apparent mixing line between the C.BoB and the S.BoB waters estimated by a least-square linear fit to the dAlML data at stations GI-01/5, 6, 7 and 8 (refer to Fig. 1 for station locations).

During the spring-intermonsoon period (GI-01 cruise), sub-surface maxima were observed in the dAl profiles of the BoB around 100-150 m (Fig. 3.8). The strength of these sub-surface maxima in the dAl profiles decreased from the northern (~22.8 nM at station GI-01/2) to the southern BoB (~10.7 nM at station GI-01/8). Among the Eq.IO stations, the highest dAl_{ML} levels (13.4-

15.4 nM) were observed at the stations transitional to the S.BoB and the Eq.IO (GI-06(A)/11 and 12), which gradually decreased towards the western equatorial region during the late winter period of sampling (Fig. 3.3e). A tight correlation (R^2 = 0.94, Fig. 3.9) is also observed between the S_{ML} and dAl_{ML} in the equatorial waters.

Highly enriched dAl_{ML} concentration (~18 nM) at GI-01/12 (~14.5°S) and relatively elevated dAl (>4 nM) throughout the upper thermocline waters (<500 m) are the most noteworthy observations in the ITF–ISG region (Fig. 3.2b). High-resolution sampling for dAl measurement by Grand et al. (2015b) in the subtropical Indian Ocean, further east along the 95°E, also showed a similar pattern of elevated dAl concentrations (8.5-11.7 nM) in the surface waters (<25 m) at the central and northern reaches of the subtropical gyre (12.5–23.5°S; Fig. 2c of Grand et al., 2015b). However, it should also be noted that the observed enrichment of dAl in the surface waters at ~8.5°S and ~14.5°S (GI-01/11 and 12) in this study (Fig. 3.6) is about 1.5-2 times higher than those observed by Grand et al. (2015b) over a similar latitudinal range (12.5-23.5°S) eastward at 95°E, which is possibly impacted by dust deposition

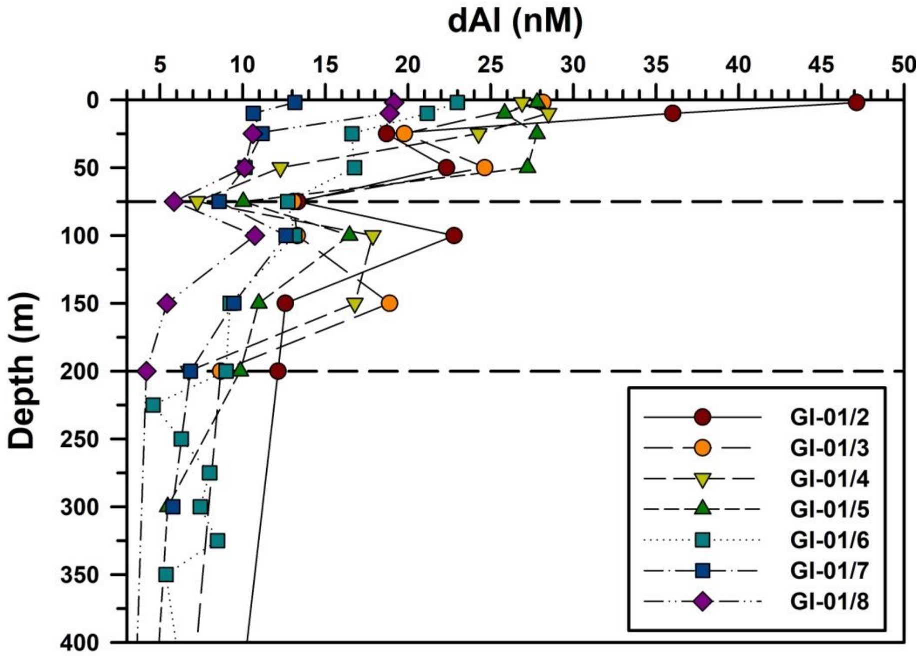

Fig. 3.8: dAl profiles in the surface mixed layer and the upper thermocline waters (0-300 m) along the meridional transect in the BoB (GI-01/2 to GI-01/8) sampled during the GI-01 cruise. The horizontal reference dashed lines (at 75 m and 200 m) are traced to highlight the sub-surface dAl maxima observed around 100-150 m.

(Grand et al., 2015a,b). Further south at the central ISG region (GI–01/16: ~25.3°S, 70°E), dAl_{ML} concentration (8.6 nM) decrease relative to that observed (~14-18 nM) in the northern reaches of the gyre.

3.3.2 dAl distribution in the lower thermocline and deeper waters (>300 m)

During the spring intermonsoon period (GI-01 cruise), the highest dAl levels in the deeper waters (>500 m) were observed in the BoB region, reaching up to ~14-15 nM in the bottom waters of the N.BoB and the C.BoB (Fig. 3.2b). Increasing dAl concentrations were observed towards the seafloor (>2000 m) for all the BoB stations during the GI-01 cruise, more profoundly in the N.BoB and the C.BoB stations (Fig. 3.2b). A similar dAl distribution pattern was also evident near the eastern coast of India (GI-06(A)/1, Fig. 3.3d) during the late winter period (GI-06(A) cruise), showing elevated dAl concentrations in the intermediate and deep waters (>500 m) compared to that at the open ocean stations (GI-06(A)/2, 3 and 4).

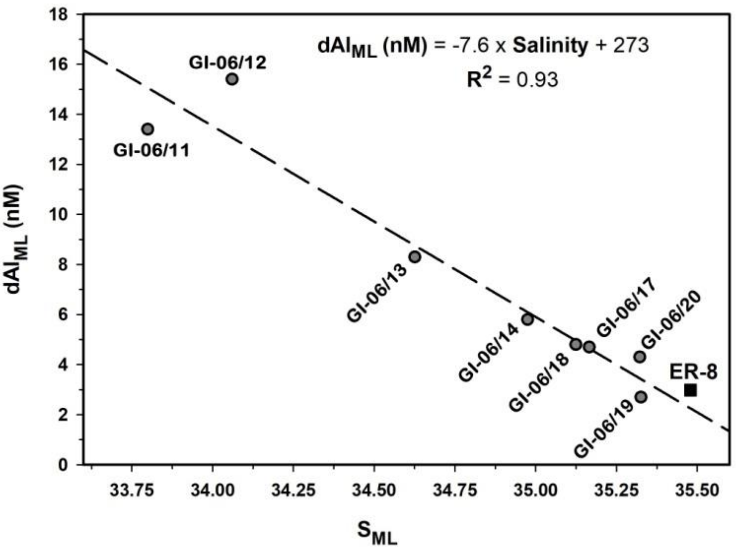

Fig. 3.9: dAl_{ML} variation with S_{ML} for the equatorial stations (GI-06(A)/11 to GI-06(A)/20) sampled during the GI-06(A) cruise. The plot shows a tight linear correlation between the two parameters suggesting admixing of dAl–rich, low salinity surface waters of the S.BoB and the southern Andaman Sea with relatively dAl–poor, high salinity surface waters of the southern Arabian Sea (see text). Data point for station ER–8 occupied in the southern Arabian Sea during the Japanese GEOTRACES cruise (Vu and Sohrin, 2013) is also plotted for comparison

.

At the center of the southern Andaman Sea (GI-06(A)/6), dAl concentrations in the intermediate waters (500-1500 m) showed a similar distribution compared to that observed in the nearby stations in the S.BoB (GI-06(A)/5 and 8; Fig. 3.3d and 3.3e). While dAl levels decreased (to ~2.5-2.7 nM) in the deeper waters below 1500 m (1800-2500 m) at the nearby S.BoB stations (GI-06(A)/5 and 8), dAl concentrations at GI-06(A)/6 showed remarkably uniform distribution (~3.7 nM) in the similar depth range (Figs. 3.3d and 3.10). Similar uniformities in the deep-water profiles for various other physical and chemical tracers (e.g., ^{14}C, REE, 230Th and major nutrients) are also reported in the Andaman Sea (Dutta et al., 2007; Nozaki and Alibo, 2003; Okubo et al., 2004). On the other hand, at GI-06(A)/7 station, sampled very close to the Nicobar Islands, dAl concentrations showed increment below 500 m towards the margin of Andaman-Nicobar Ridge (Fig. 3.10).

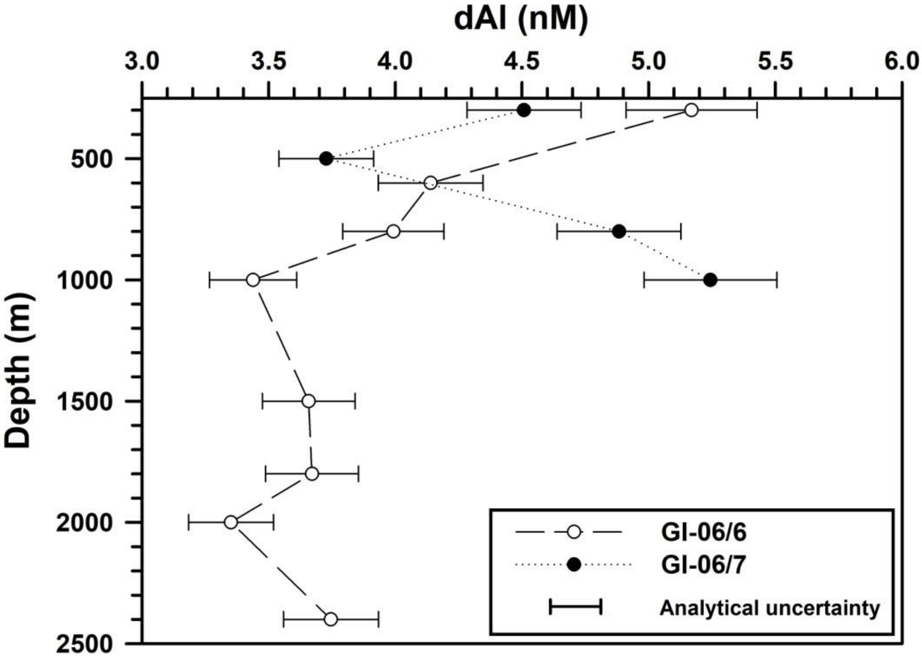

Fig. 3.10: The distribution of dAl in the lower thermocline and deep waters (≥ 300 m) at the stations GI-06(A)/6 and 7 sampled in the southern Andaman Sea. Refer to Fig. 3.1 in the text for the sampling locations. The indicated analytical uncertainty was observed (5 %, 1SD) after repeat analysis of in-house reference seawater, InStd-D, in this study.

In the Arabian Sea region, the dAl concentrations in the lower thermocline and deeper waters (>1000 m) of stations GI-06(A)/21 and 22 (2.4–3.0 nM; Figs. 3.3f and 3.11) were similar to recently reported dAl levels (2.2–2.5 nM; Fig.

3.11) by Vu and Sohrin (2013) at nearby station ER-7 (Fig. 3.1). However, close to the south-east margin of the Arabian Sea (GI-10/24), relatively elevated dAl concentrations (3.3-3.6 nM; Figs. 3.3f and 3.11) were observed at similar deeper depths. Also, a discrete dAl maximum was observed in the thermocline waters at 600 m close to the margin of the Sea (GI-06(A)/24; Fig. 3.11).

During the GI-06(A) cruise, dAl concentrations observed in the deeper waters (≥500 m) of the Eq.IO were low (<5 nM) relative to the N.BoB and the C.BoB but comparable to the S.BoB (Figs. 3.2b, 3.3d and 3.3e). In the same cruise, a continuous increase in dAl values in the bottom waters (>3500 m) towards the seafloor was observed in the eastern equatorial region (GI-06(A)/11, 12, 13 and 14; Fig. 3.3e). Further south in the Eq.IO region at station GI-01/9 (~2°S), dAl maximum (~5 nM) around 3000 m was observed (Fig. 3.2b).

In the Indonesian Throughflow and Indian Subtropical Gyre (ITF-ISG) region, important variations in the dAl concentrations were observed in the deep and bottom waters (>2000 m; Fig. 3.2b). Combining the previously reported data in

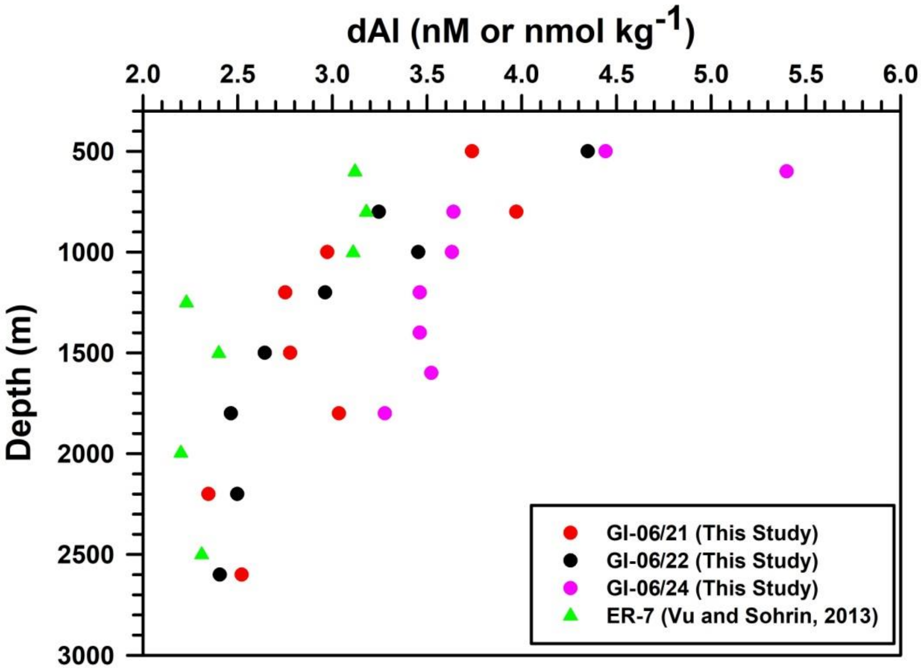

Fig. 3.11: dAl variations in the water column below 300 m at the stations (GI-10/21, 22 and 24) sampled close to the south-eastern margin of the Arabian Sea. dAl data (in nmol kg $^{-1}$) from a nearby station, ER-7 (Vu and Sohrin), sampled during the Japanese GEOTRACES cruise, is also plotted.

the region by Vu and Sohrin (2013) (ER-10: 20.00°S, 72.55°E; Fig. 3.1), we examined the patterns in the distribution of dAl for the deep (2000-3500 m) and bottom waters (>3500 m) in the ITF-ISG region. Average dAl concentration in the bottom waters is relatively elevated (3.9 nM) at the northernmost station of the region, GI-01/11, (~8.5°S, 80.8°E), where dAl maximum at 4000 m was also observed (Fig. 3.12b). At this station, a large proportion of the bottom waters presumably comes from the colder bottom waters of the Western Australian Basin, advected across the deep saddles in the Ninety–East Ridge (NER; Fig. 3.4b) to the Central Indian Ocean, which was also evident from the lower potential temperatures observed in the bottom waters at this station (Fig. 3.12a). Moving further southwest, overall, the dAl level in the bottom waters first decreased at GI-01/12 and then increased again close to the Central Indian Ridge (CIR) at ER-10 (Fig. 3.12b). On the other hand, average dAl concentrations in the deep waters showed a continuous increase from the north (2.6 nM at GI-01/11) towards the southwest and showed the highest dAl levels near the CIR (5.3 nM at GI-01/16, Fig. 3.12b). At GI-01/16, the dAl concentration gradually increased in the deeper waters (≥1500 m; Fig. 3.12b), reaching to the maximum value (5.3 nM) at the deepest

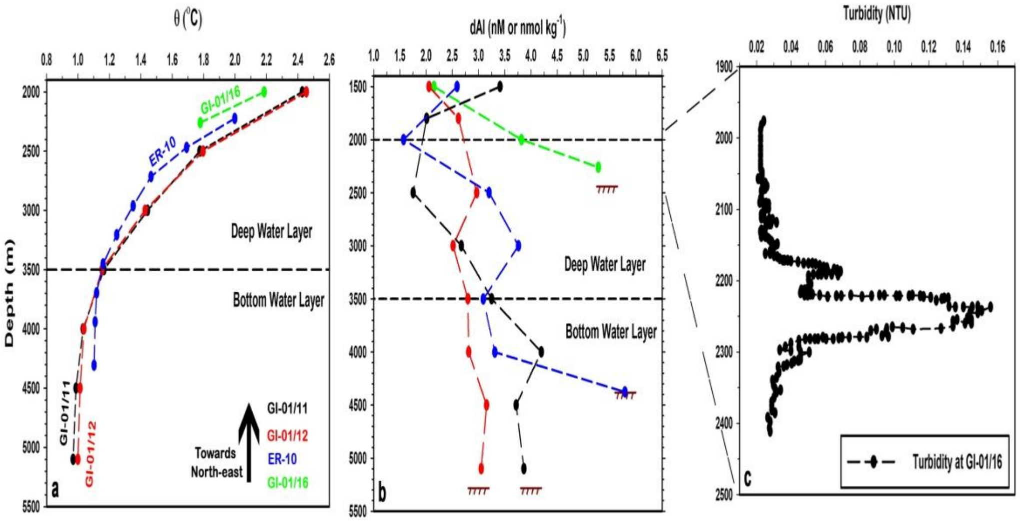

Fig. 3.12: Vertical profiles of (a) potential temperature (θ) and (b) dAl in the deep and bottom waters of stations sampled in the ITF–ISG region. The solid brown line below each dAl profile in (b) indicates the water depth of the respective sampling station. Fig. (c) shows variations in water turbidity in the deep waters of station GI-01/16; the turbidity maximum (at ~2250m) observed in the plot marks the presence of a hydrothermal plume.

sampled depth (2260 m) and coincided with the anomalously high water turbidity values around 2250 m (Fig. 3.12c).

3.4 Discussion

3.4.1 Controls on dAl distribution in the surface mixed layer and upper thermocline waters (≤300 m)

In the surface mixed layer, deposition of atmospheric mineral dust and its subsequent partial dissolution is the key process regulating the dAl distribution. However, as noted in the introductory remarks, the huge input of fluvial derived lithogenic sediments in the north-eastern Indian Ocean (the BoB and the Andaman Sea), either in the form of suspended sediments in the surface water layer and/or resuspended after deposition over the shelf, may impact the surface dAl concentrations in these regions. Moreover, the surface and upper thermocline waters in the northern and the equatorial Indian Ocean are influenced by seasonally reversing monsoonal current (Wyrtki, 1973; Schott and McCreary Jr, 2001), which may play an important role in transporting the dAl signals from one sub-basin to another. In addition to the aforementioned processes, the intrusion of Pacific waters through the Indonesian seas to the upper water column (primarily above 400 m, Schott et al., 2009) of the tropical Indian Ocean with the Indonesian Throughflow (ITF) may impact the dAl distribution.

In the following Sections 3.4.1.1–3.4.1.3, to have first-order estimates of the dAl input to the surface mixed layer, supported by the lithogenic sediments flux from atmospheric dust deposition and/or fluvial sediment discharge to the BoB, the equatorial Indian Ocean and the Arabian Sea, a 1-D box-model equation, which is a rearranged MADCOW model equation (Grand et al., 2015a) is used and given as follows:

$$\mathbf{dAl_{lith}} = \frac{\mathbf{G \times MRT \times f_{Al}^{sed} \times Sol.}}{\mathbf{A_{wt} \times MLD_c}} \times \mathbf{10^6} \qquad (3.1)$$

where **G** is the lithogenic sediment flux (in g m^{-2} yr^{-1}), **Sol.** is the fractional solubility of Al from the lithogenic sediments, $\mathbf{A_{wt}}$ is the atomic weight of Al (in g mol^{-1}), **MRT** represents the mean residence time (in years) of dAl in the surface mixed layer, $\mathbf{f_{Al}^{sed}}$, is the fraction of Al in the sediments, dAl_{lith} is the estimated lithogenic sediments supported dAl concentration (in nM) in the surface mixed layer, $\mathbf{MLD_C}$ is the annual average of mixed layer depth estimated using monthly climatological mixed layer depth data (density threshold-based; Holte et al., 2017) reported closest to the sampling locations and 10^6 is the factor to account for conversions of units.

Grand et al. (2015a) estimated the Al fractional solubility from atmospheric mineral dust deposited in the eastern Indian Ocean to be 3.6% using the observed Al solubility data from the dust deposition over the Atlantic and the Pacific surface ocean (Buck et al., 2010, 2013). The rationale behind this exercise was that the air masses carrying the mineral dust over the eastern Indian Ocean have mixed characteristics of air masses over the Atlantic (influenced by natural and anthropogenic dust) and the Pacific (from remote regions) Ocean. In the Arabian Sea, Schüßler et al. (2005) used an Al solubility of 3% with their observed surface dAl to estimate mineral dust deposition fluxes and found good agreement with the dust fluxes estimated from the direct measurements of mineral dust concentration in the ambient aerosols. Balancing the observed dAl inventory in the surface mixed layer and estimates of Al dissolution from mineral dust, Grand et al. (2015a) calculated the mean residence time of dAl in the surface mixed layer to be 1.1 years in the north-eastern Indian Ocean (north of 5°S). In the south-eastern Arabian Sea, similar estimates of the residence times, ranging from 0.5-2 years, are given by the biogeochemical modeling studies on surface dAl (Gehlen et al., 2003; Han et al., 2008).

In the following sub-sections, for consistency, we used the same Al fractional solubility and mean residence time, i.e. 3.6% and 1.1 years, respectively, to estimate the dust supported surface dAl in the BoB, the equatorial Indian Ocean and the south-eastern Arabian Sea region. Also, the fraction of Al in the atmospheric mineral dust deposited ($\mathbf{f_{Al}^{sed}}$) is assumed to be 8% (McLennan, 2001), considering the mineral dust to be originating from the upper crust.

3.4.1.1 The Bay of Bengal (BoB) and the Andaman Sea

Near uniform dAl_{ML} concentrations with significant variation in the surface water salinity in the C.BoB (GI-01/1, 3, 4 and 5; Fig. 3.7) and highly enriched

dAl_{ML} at the N.BoB (47.1 nM at GI-01/2) with comparable S_{ML} (to that observed in the C.BoB; Fig. 3.7) suggests that dAl input from the huge freshwater influx of rivers play a secondary role in controlling the dAl distribution in the surface waters of the N.BoB and the C.BoB. Apart from the dissolved Al inputs from the rivers in the BoB, Al release from the partial dissolution of and Al desorption from the lithogenic particulate matter supplied by the rivers, resuspension of sediments from continental margins (shelf and slope) and atmospheric mineral dust deposition, may also exert major controls on the dAl distribution in the upper water column of the BoB. Relative contributions of dissolved Al from river water and Al release from lithogenic sediments (atmospheric and fluvial derived) to the surface water layer of BoB may be determined if data on Al concentration in the sediments, sediment flux across surface water layer, fractional solubility of Al from the sediments, dissolved Al levels at the mouth of rivers discharging into the BoB and their water discharge are available. Al concentration in the sediments is considered to be 8% by weight, which is similar to the Al composition in the suspended sediments of Brahmaputra river [(7.9 ± 0.8)% (1SD), n = 13; Singh and France-Lanord, 2002) and the upper continental crust (8.04%; McLennan, 2001) but lower than that in the fine (<4 mm) silicate fraction of the Ganga bank sediments [(11.8 ± 0.6)% (1SD), n = 4; Singh et al., 2008).

First-order estimates for the Al fractional solubility from the sediments were obtained using the shallow depth lithogenic sediment flux data (Unger et al., 2003) in the BoB as representative of sediment input (both, from atmospheric dust deposition and fluvial sediment discharge) to the surface and considering the observed dAl_{ML} concentrations to be in steady-state with respect to the sediment derived Al input (i.e., dAl_{lith} in Eq. (3.1) equals to the observed dAl_{ML}) and first-order removal of Al by particle scavenging processes (Eq. (3.1)). In the N.BoB and the C. BoB, lithogenic sediment flux data (Unger et al., 2003) from sediment trap locations NBBT-N (flux: 14.5 g m^{-2} yr^{-1}; refer Fig. 3.1 for the location) and NBBT-S (flux: 8.7 g m^{-2} yr^{-1}; refer Fig. 3.1 for the location) and dAl_{ML} concentrations from stations GI-01/3 (28.2 nM) and GI-01/4 (26.9 nM) sampled closest to these trap locations (Fig. 3.1), respectively, were considered. In the S.BoB, lithogenic sediment flux data from sediment trap location SBBT (flux: 4.3 g m^{-2} yr^{-1}, Unger et al., 2003; Fig. 3.1) and dAl_{ML}

concentrations from stations GI-01/8 (19.0 nM) and GI-06(A)/12 (15.4 nM) close to this trap location (Fig. 3.1) were used. MLDc estimated for the stations GI-01/3, GI-01/4, GI-01/8 and GI-06(A)/12 are 19 m, 26 m, 35 m and 35 m, respectively. Using these values of parameters in Eq. (3.1), the fractional release of Al from the lithogenic sedimentary input in the N.BoB, C.BoB and S.BoB is estimated as 1.1%, 2.4% and 3.8-4.7%, respectively. In the S.BoB, the estimated Al fractional solubility range of 3.8-4.7% is relatively high compared to that in the N.BoB and the C.BoB (1.1-2.4%). Additional dAl input from the advection of dAl-rich, low salinity surface waters from the southern Andaman Sea to the S.BoB with the NMC (Fig. 3.4a) may have lead to, relatively, overestimation of Al fractional solubility in the S.BoB (i.e., at GI-01/8 and GI-06(A)/12) and therefore represent the upper limit in this region. This is also evident from relatively low surface salinity (<34) and high dAl concentrations (15.4-19.0 nM) observed at GI-01/8 and GI-06(A)/12 (Figs. 3.2a, 3.2b and 3.3b, 3.3.e).

dAl concentration measured at the mouth (salinity ≈29.4) of the Hooghly (the Ganga) estuary, during the summer monsoon of 2013, was of the order of ~57 nM and is taken as the average dAl concentration of the G-B river system to the BoB after passing through the estuary. Considering the water discharge of 10^3 km^3 yr^{-1} (Sengupta et al., 2006 and references therein), the estimated dissolved Al flux from the G-B river system to the BoB is ~5.7 x 10^7 moles yr^{-1}. To estimate the average flux of lithogenic sediments across the surface water layer of the BoB, we calculated the mean lithogenic sediment flux (9.7 ± 4.3 (1SD) g m^{-2} yr^{-1}) over 2.2 x 10^{12} m^2 area of the BoB using the shallow depth sediment traps data of Unger et al. (2003) at different sites in the BoB (Fig. 3.1).

Using our estimates of Al fractional solubility (1.1-4.7%) and mean lithogenic sediment flux (9.7 g m^{-2} yr^{-1}), Al release in the surface waters of the BoB from the sediments is estimated to be in the range: 7.0 x 10^8-3.0 x 10^9 moles yr^{-1}. This estimated Al release in the BoB is, at least, an order of magnitude larger than that estimated for the dissolved Al flux from the G-B river system (5.7 x 10^7 moles yr^{-1}) and highlights the dominance of dAl input from the large sediment flux, predominantly derived from the discharge of the Himalayan and peninsular rivers, in the BoB.

Srinivas and Sarin (2013) reported the Al flux of 0.8 ± 0.5 mg m^{-2} d^{-1} with dry deposition of the mineral dust over the BoB and observed an overall decrease in fluxes from the northern to the southern BoB during the spring–intermonsoon period (March-April). In the same study, the aerosol Al concentrations over different regions of the BoB during the winter period (January) were observed to be similar to that observed during the spring-intermonsoon period (March-April). The continental outflow of dust from the Indo-Gangetic Plain and south-east Asia to the BoB is only feasible during the late winter to spring intermonsoon period (January-April) as the wind patterns during the remaining of the year restricts the transport of dust over the BoB from the continental sources (Srinivas and Sarin, 2013). Therefore, it had been argued that the deposition fluxes of trace metals with the dust deposition observed during these four months nearly accounts for all the annual trace metal input to the BoB from the major sources of dust, i.e., the Indo-Gangetic Plains and south-east Asia, to the region (Srinivas and Sarin, 2013). Upper (1.3 mg m^{-2} d^{-1}) and lower (0.3 mg m^{-2} d^{-1}) limits of the reported Al dry deposition flux over the BoB (Srinivas and Sarin, 2013) are considered to be representative of Al flux in the N.BoB and the S.BoB, respectively, during January-April. To have lower and upper limits on the annual Al deposition fluxes over the BoB, the deposition fluxes for the rest of the year is assumed to be ranging from negligible (i.e., zero) to values similar to that during the continental outflow period (January-April). This translates to Al annual fluxes from dust deposition in the ranges of 156.0-474.5 mg m^{-2} yr^{-1} and 36.0-109.5 mg m^{-2} yr^{-1} for the N.BoB and the S.BoB, respectively. Using these estimated ranges of Al annual fluxes and estimated MLD_C values in the N.BoB (~20 m) and the S.BoB (~30 m) in Eq. (3.1), the steady-state estimates of dust input supported dAl in the N.BoB and the S.BoB are found to be 11.5-35.0 nM and 2.0-5.5 nM, respectively. These estimates are lower than the observed dAl_{ML} concentrations in the respective regions (47.1 nM at northernmost station GI-01/2 and 11.9-19.0 nM in the S.BoB) and suggest significant dAl input from the fluvial sources in the BoB, particularly through Al release from the large lithogenic sediments discharged by the rivers. If we consider the mineral dust deposition during the continental outflow period (January-April) to be a more representative estimate of the net annual atmospheric mineral dust input to the

BoB surface waters (Srinivas and Sarin, 2013), the corresponding estimates of the dust derived surface dAl in the N.BoB (~11.5 nM) and the S.BoB (~2.0 nM) accounts for only 24% and 11-17% of the total observed dAl in the surface waters of the N.BoB and the S.BoB, respectively. This would suggest that the Al release from the sediments, supplied by the fluvial discharge, is a dominant process controlling the surface dAl in the BoB. Singh et al. (2012) also highlighted the need for excess Nd released from the fluvial and/or continental margin derived lithogenic particles to account for the Nd balance in the surface waters of BoB.

Al input to the surface ocean via wet deposition may also play an important role in governing the dAl_{ML} distribution (Hand et al., 2004; Jickells, 1995; Jickells et al., 2005; Vink and Measures, 2001). However, due to the unavailability of data on wet deposition fluxes of Al and insignificant contribution of wet deposition during the continental outflow period (January to April; Srinivas and Sarin, 2013) over the BoB and the Eq.IO, we neglected the impact of wet deposition in the above (and similar calculations in Section 3.4.1.3 for the Eq.IO) calculations.

The plausible sources and processes that may induce the increase in dAl levels in the sub-surface water depths observed during the GI-01 cruise in the BoB (Fig. 3.8), include, (1) remineralization of biogenic Al-carrier phases releasing adsorbed or incorporated Al from the surface waters, (2) resuspension of continental margin sediments and subsequent release of Al from the partial dissolution of or Al desorption from the sediments and/or (3) release of dAl-rich pore waters, which could be induced by sediment resuspension. If Al removal by the biogenic particles in the surface waters and subsequent remineralization of these particles is assume to be the source of the dAl increase in the sub-surface waters, a positive correlation between the major inorganic nutrients (H_4SiO_4, NO_3^-, PO_4^{3-}) and dAl could be expected throughout the thermocline depths (100-800 m), where remineralization of biogenic debris leads to the consumption of dissolved oxygen (DO) and the release of assimilated nutrients (Anand et al., 2017). Contrary to that, dAl concentrations showed an overall decrease with increasing nutrients in the thermocline waters (Fig. 3.13), indicating particle scavenging of dAl to be dominating in the thermocline waters. Together, the absence of correlated increase of dAl and nutrients in the thermocline waters and observation of the strongest dAl influx in the sub-surface waters close to the coast (Figs. 3.2b and 3.13) suggest dAl supply from the continental margin, which fades southward due to advective mixing and scavenging.

Elevated dAl levels in the surface waters (0-50 m) near the south-east coast of India (GI-06(A)/1, Fig. 3.3d) may indicate dAl input from the dissolved and/or suspended particulate phase of peninsular rivers discharging to the Indian east coast. Resuspension of lithogenic shelf sediments, derived from and deposited by the rivers, and subsequent Al release in the surface waters may also be a source. A steep decrease in dAl_{ML} concentration from GI-06(A)/1 (23.4 nM) to GI-06(A)/2 (14.3 nM) with similar surface salinity levels at the two stations (~33.1, Fig. 3.3a) suggests that the land runoff plays an insignificant role in

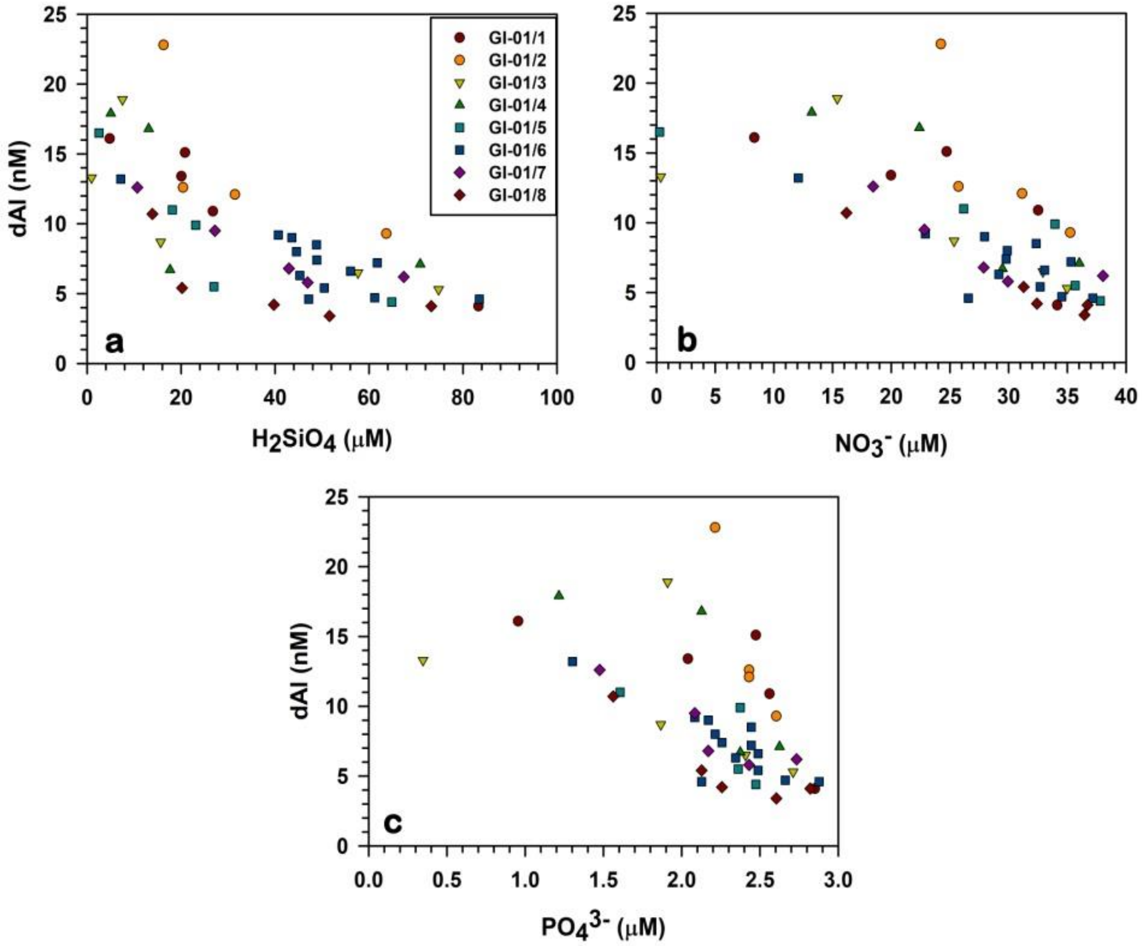

Fig. 3.13: Variation of dAl against dissolved (a) silicic acid (H_2SiO_4), (b) nitrate (NO_3^-) and (c) phosphate ($PO_4^{3-)}$ in the thermocline waters (100-800 m) of the BoB observed during the GI-01 cruise.

providing dAl to the coastal seawaters. Also, the increase in mineral dust deposition flux close to the continent (Srinivas and Sarin, 2013) may lead to an increase in surface dAl levels. In conclusion, the combined increase in sedimentary input close to the coast resulted in dAl concentration gradients from the open BoB to the south-east Indian coastal region.

Near the Nicobar Islands in the S.BoB (GI-06(A)/5 and 8) and the Andaman Sea (GI-06(A)/6 and 7), probable contributors of dAl to the surface waters include (1) freshwater and suspended sediments from the I-S and G-B river system, (2) resuspended sediments from the shelf of the Islands, which may also induce diffusion of Al from dAl enriched pore waters to ambient seawater, and (3) advection of Indonesian Water to the S.BoB and the southern Andaman Sea (Section 3.2). Surface circulation patterns (refer to Fig. 3.4a for a schematic representation) during the GI-06(A) cruise also show the freshwater influx from the I-S and G-B river system to the southern Andaman Sea and the S.BoB surface waters. Atmospheric Al deposition fluxes are low near and over the Andaman Sea (Srinivas and Sarin, 2013) and could not support the elevated dAl values in the surface waters. Comparatively, very high dAl_{ML} concentrations were observed at station GI-06(A)/7 and 8 (~43-48 nM; Fig. 3.3e). Interestingly, silicic acid concentration in the surface mixed layer also increased significantly at these stations (1.03-1.21 µM at GI-06(A)/7 and 8) compared to the adjacent stations in S.BoB (0.18-0.78 µM at GI-06(A)/4, 5 and 9) during the same period. During the winter period (December-February), the Indonesian Water makes its way to the Andaman Sea from the Strait of Malacca (SoM), which is also evident in the surface circulation pattern (refer Fig. 3.4a for a schematic representation) and discussed by Rizal et al. (2012). Indonesian Water outflow from the SoM to the southern Andaman Sea during the winter has a significant contribution from south-east South China Sea surface waters (Rizal et al., 2012). There is no available dAl data in the surface waters flowing through the SoM to the Andaman Sea. However, extremely elevated ^{228}Ra activities (625-725 dpm m^{-3}; Nozaki and Yamamoto, 2001) in the SoM demonstrate a significant interaction between the surface waters and the local sediments. Limited available dAl data in the surface waters at the center of the South China Sea (~33.7 nM; PA-11, Obata et al., 2004), the Sulu Sea (16.7 nM; PA-1, Obata et al., 2004) and the surface ITW entering to the

Indian Ocean from the south of Java and the Timor Sea (~11-12 nM, PA-2 and PA-7, Obata et al., 2004) seems inadequate to account for highly enriched dAl levels (~43-48 nM at GI-06(A)/7 and 8) near the Nicobar Islands. This could also be inferred from the dAl_{ML} concentration observed at the center of the southern Andaman Sea (24.2 nM at GI-06(A)/6), which is much lower than the dAl value at GI-06(A)/7 and 8, even though station GI-06(A)/6 also receives waters outflowing from the SoM to the Andaman Sea before it turns south towards the S.BoB and the Eq.IO (Fig. 3.4a for a schematic representation and Rizal et al. (2012)). Consequently, in addition to dAl contribution from the fluvial sources and the outflow of Indonesian Water, localized and correlated increase in dAl and silicic acid at GI-06(A)/7 and 8 suggest the dAl and dissolved Si input from the dissolution of and/or Al desorption from resuspended terrigenous sediments from the insular shelf of the Nicobar Islands. The increase in the upper water column turbidity around the Nicobar Islands (Fig. 3.14) provides further evidence for the resuspension of the shelf sediments. Recent studies (Fripiat et al., 2011; Jeandel et al., 2011; Tre´guer and De La Rocha, 2013) have also shown and suggested the release of Si from the terrigenous margin sediments as an important source of dissolved Si to the ambient seawater.

dAl concentration observed in the surface waters (17.2 nM; PA-10, Fig. 3.1, Obata et al., 2004) further north (~10°N) at the center of the Andaman Sea, during the same period, was apparently lower than at GI-06(A)/6 southward (24.2 nM; ~7.5°N) and therefore, suggest some additional contribution from the Indonesian Sea surface waters outflowing from SoM to the Andaman Sea, apart from the fluvial inputs of the I-S and G-B river systems from the north.

3.4.1.2 The Arabian Sea (AS)

Advection of low salinity BBW waters to the surface water layer of the south-eastern Arabian Sea (see Section 3.2) may carry the dAl-rich signature of the BoB surface waters to this region. It is apparent with relatively higher dAl levels and lower salinity observed in the upper 25 m at station GI-06(A)/21 (22.0-23.2 nM) compared to the other stations, GI-06(A)/22 and GI-06(A)/24 (10.0-20.5 nM), in this region (also refer to Table A1). Additionally, high atmospheric mineral dust deposition fluxes at the south-eastern Arabian Sea (Kumar et al., 2012; Measures and Vink, 1999) may also contribute to the elevated dAl_{ML} values compared to that observed in the north-western, central and southern Arabian Sea during the same season in the earlier studies (Measures and Vink, 1999; Vu and Sohrin, 2013). Deposition of mineral dust, particularly, in the southern Arabian Sea is more dominant during the winter (December–February) and the spring–intermonsoon (April–May) period compared to the rest of the year (Kumar et al., 2008; Tindale and Pease, 1999).

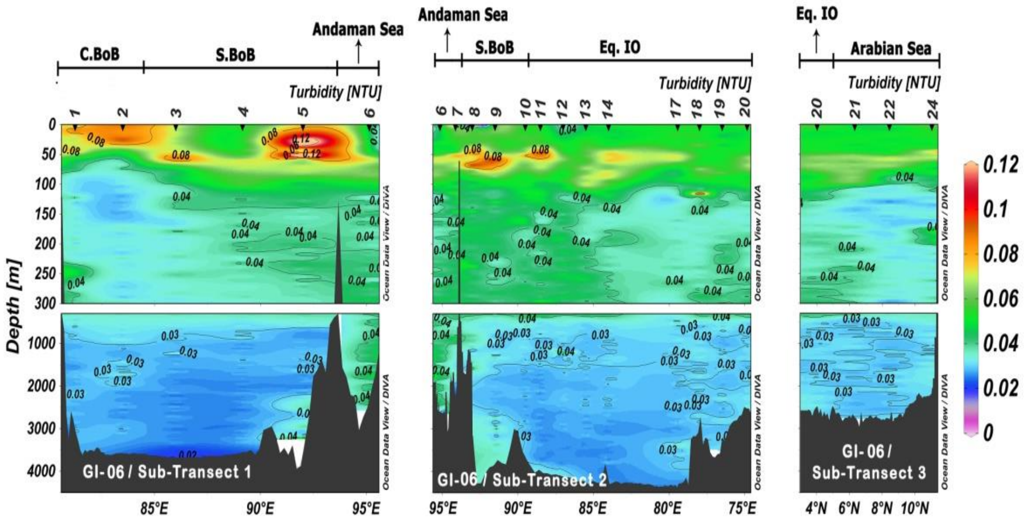

Fig. 3.14: Variation of seawater turbidity in the upper water column (0-300 m) and waters below 300 m along the sub-transects sampled during the GI-06(A) cruise. Refer to Fig. 3.3g to identify the sub-transects along the full transect of the GI-06(A) cruise.

During the winters (December 2007), Kumar et al. (2012) observed the highest Al concentrations (2.27 ± 0.98 mg m^{-3}) in aerosols collected from the atmospheric boundary layer near the eastern boundary of the Arabian Sea compared to any other season (Kumar et al., 2008; Schüßler et al., 2005 and references therein), which they attributed to: (1) transport of a large amount of mineral aerosols (13.3-50.7 mg m^{-3}) through continental outflow, under the influence of northeasterly winds, transacting a large area over the Indian subcontinent, and (2) closeness with the continent. During the spring-intermonsoon period (April-May), the mean Al concentration in aerosol from the atmospheric boundary layer in the southern Arabian Sea (8-12°N) is observed to be 1.13 mg m^{-3} (Kumar et al., 2008). Considering the above (mean) Al concentration in aerosol during the winter (December-February:

2.27 mg m^{-3}) and the spring-intermonsoon (April-May: 1.13 mg m^{-3}), annual mean Al concentration over the southern Arabian Sea is assumed to be in the range: 1.13-2.27 mg m^{-3}. This translates to Al dry deposition flux of 0.32-0.64 g m^{-2} yr^{-1} using dry-deposition velocity of 0.9 cm s^{-1} (Kumar et al., 2008). Using this range of Al flux and MLDc estimate (~25 m) near stations (GI-06(A)/21, 22 and 24) in the south-eastern Arabian Sea in Eq. (3.1), a steady-state dAl concentration of 19-38 nM is estimated in the mixed layer. This is comparable to the observed dAl_{ML} (18.6-22.7 nM) and shows that the dust derived Al is a prominent source for the surface dAl near the south-eastern Arabian Sea. The dominant impact of dust dissolution on the surface water chemistry of dissolved Nd near the eastern coast of AS was also highlighted by Goswami et al. (2014).

3.4.1.3 The Equatorial Indian Ocean

Significantly correlated variation (Fig. 3.9) between S_{ML} and dAl_{ML} in the equatorial waters suggests that the dAl_{ML} distribution in the Eq.IO is primarily controlled by the advective mixing of the dAl-rich, low salinity surface waters of the S.BoB and the Andaman Sea with relatively dAl-poor, high salinity waters of the southern Arabian Sea, under the influence of the NMC. This argument is consistent with the observed dAlML (Vu and Sohrin, 2013) in the southern Arabian Sea during the winters (December 2009), which apparently bound the lower end of the linear dAl_{ML} variations with S_{ML} in the Eq.IO region (Fig. 3.9).

The observed atmospheric dry deposition Al flux in the Eq.IO region during the winter and spring intermonsoon period was ~0.3 mg m^{-2} d^{-1}(Srinivas and Sarin, 2013). In the Eq.IO region, atmospheric models (composite model: Jickells et al., 2005; Mahowald et al., 2005 and DEAD model: Zender et al., 2003) estimate total mineral dust deposition flux on the order of 20 mg m^{-2} d^{-1}, which is about 1.5 mg m^{-2} d^{-1} of Al flux with the assumption of 8% Al in the mineral dust. This is relatively large compared to the observed Al flux (~0.3 mg m^{-2} d^{-1}) during the winter and spring intermonsoon period (January-April, Srinivas and Sarin, 2013). However, assuming a constant 8% Al in the deposited mineral dust throughout the surface dAl residence timescale of ~1 year (Grand et al., 2015a) in the region would result in overestimation of Al flux given that continental outflow is only prominent during the winter and the spring intermonsoon period (Srinivas and Sarin, 2013) and for the rest of the year winds sourced from the marine environment would be richer in sea salts. Assuming Al flux of 0.3 mg m^{-2} d^{-1} (Srinivas and Sarin, 2013) and MLD_c in the range: 30-35 m (Holte et al., 2017), the contribution of dAl to the surface mixed of the Eq.IO region from the atmospheric dust deposition will lie in the range: 4.-5.3 nM. These dust supported (and steady-state) dAl estimates are lower than those observed in the eastern equatorial region (8.3-15.4 nM at GI-06(A)/11, 12 and 13; Fig. 3.3e) and again suggest additional dAl input from advection of dAl-rich, low salinity surface waters of the S.BoB and the southern Andaman Sea. However, mixed layer dAl observed towards the western equatorial region and the southern Arabian Sea (2.7-4.3 nM at GI-06(A)/19, GI-06(A)/20 and ER-8) are relatively lower than the dust derived dAl estimates (4.6-5.3 nM). This mismatch may result from an overestimation of Al dust fluxes in the residence time scale of dAl (~1 year), particularly in the southern Arabian Sea where the seasonal variations in Al concentrations of dust are large, showing an order of magnitude lesser Al concentrations during the southwest monsoon season compared to that in northwest monsoon and spring intermonsoon period due to changes in dust source regions with changing wind patterns (Schüßler et al., 2005; Tindale and Pease, 1999).

3.4.1.4 The Indonesian Throughflow and Indian Subtropical Gyre Region

As discussed earlier, the distinct increase of dAl in the upper water column of stations GI-01/11 and 12, situated in the northern reaches of the Indian Subtropical Gyre (ISG), are consistent with the pattern observed in the earlier study (Grand et al., 2015b) in the similar latitudinal range further east at 95°E. In the previous study, this dAl increment in the surface waters at the northern end of the ISG was primarily attributed to the deposition and subsequent dissolution of mineral dust, which is emitted from the Australian continent and mostly deposited east of 90°E (Grand et al., 2015a; Mahowald et al., 2005). Here, it is argued that under the prevailing westward SEC flow (Fig. 3.4a), the dAl enriched surface waters may be advected from the zone of high dust deposition at east to our sampling sites at GI-01/11 and 12 westward and therefore imparting the high dAl_{ML} signal in this region. However, the significantly higher (1.5-2 times) dAl enrichment observed in the surface waters of the northern subtropical gyre in this study (GI-01/11 and 12) compared to that in the previous results (Grand et al., 2015b) may thus suggest inter-annual variations in the dust load, emanating from the Australian dust source regions and which finally reaches to the northern ISG, if atmospheric mineral dust deposition and its partial dissolution is considered the primary source of Al to the surface waters. Atmospheric dust emission events from the Australian sources are very episodic in nature compared to the Northern Hemisphere source regions, which emit more regularly (Mackie et al., 2008 and references therein). Mackie et al. (2008) computed the Dust Storm Index (DSI), using the dust storm frequency and visibility data, as a measure of annual dust activity and reported its variation for 46 years (1960-2005) in Australia. They found that high dust events correlate with the periods of intense drought years in the continent. After the record rainfall in most of the Australian basins with the onset of the La-Nina conditions in the Pacific Ocean during the period of 2010-12, arid conditions again started building up in Australia from 2013 (Australian Annual Climate Summary 2010, 2011, 2012 and 2013; Available at http://www.bom.gov.au/climate/current). Such a situation may increase the dust influx from Australia to the ISG before the sampling period in the subtropics (April 2014), but this still remains a speculation.

In the northern reaches of the ISG (8-15°S), advection of Indonesian Throughflow Water (ITW) may also play a major role in governing the surface dAl concentrations and, more importantly, in the depths below the surface mixed layer, where the Al release from the settling mineral dust particles is deemed negligible (Grand et al., 2015b; Maring and Duce, 1987; Measures et al., 2010). Elevated ^{228}Ra activities (>100 dpm m^{-3}; Nozaki and Yamamoto, 2001) observed in the surface waters at ~10°S, 103°E (PA-7, Fig. 3.1) and ~13°S, 117°E (PA-2, Fig. 3.1), from where the ITW enters to the tropical Indian Ocean, suggest strong interactions of the surface waters with the sediments of continental shelf surrounding the Indonesian Seas. Such a process may also result in Al release from the shelf sediment to the surface waters, therefore enriching the dAl values in these waters. dAl concentration in the ITW entering the eastern Indian Ocean should then be a function of the extent of its interaction with sediments and discharge, which may vary seasonally and inter-annually (Tomczak and Godfrey, 2003b; Liu et al., 2015; Potemra and Schneider, 2007). In their observations at the eastern Indian Ocean (~95°E), Grand et al. (2015b) also highlighted the significant contribution of dAl from the advection of ITW to the upper thermocline water depths (200-400 m) of the northern ISG region. Fig. 3.15 shows the comparison of dAl profiles, observed in the upper 500 m, between GI-01/12 (this study), receiving prominent input from the ITW, and I09N-113 (~14.6°S) sampled at similar latitude at 95°E transect of Grand et al. (2015b). Similar pattern and magnitude of dAl distribution in the upper thermocline (Fig. 3.15; $\gamma^n > 23$ kg m^{-3}, i.e., >100-500 m) observed in this study support the earlier inference of dAl input to the tropical Indian Ocean with the inflow of ITF waters and spreads further westward along the advective pathway. However, due to advective mixing and scavenging along the SEC carrying the ITW, a relatively lower dAl concentration should be expected towards the west (at GI-01/12) compared to that at I09N-113 if the ITW are considered the source of dAl in the thermocline depths. Moreover, both GI-01/12 and I09N-113 (Grand et al., 2015b) showed dAl levels in the thermocline waters much larger than that observed at station PA-2 (Fig. 3.15), sampled by Obata et al. (2004) in the year of 1997 (17 years before this study and 7 years before the study by Grand et al. (2015b)), further east near the Timor Sea (Fig. 3.1) from where the ITF waters are sourced to the tropical Indian Ocean. These observations may suggest interannual variation in dAl input with the ITW advection. Earlier studies (Liu et al., 2015; Potemra and Schneider, 2007) have confirmed that large interannual variations occur in the Indonesian Throughflow (ITF) discharge to the tropical Indian Ocean. Liu et al. (2015), using expendable bathythermograph data, showed that the mean annual ITF transport monotonously increased during 30 years of their study period, from 1984-2013, at the rate of 1 Sverdrup per 10 years. These results, therefore, underscore the need for time-series studies in the future to understand the impact of ITF discharge on dAl and other trace elements distribution.

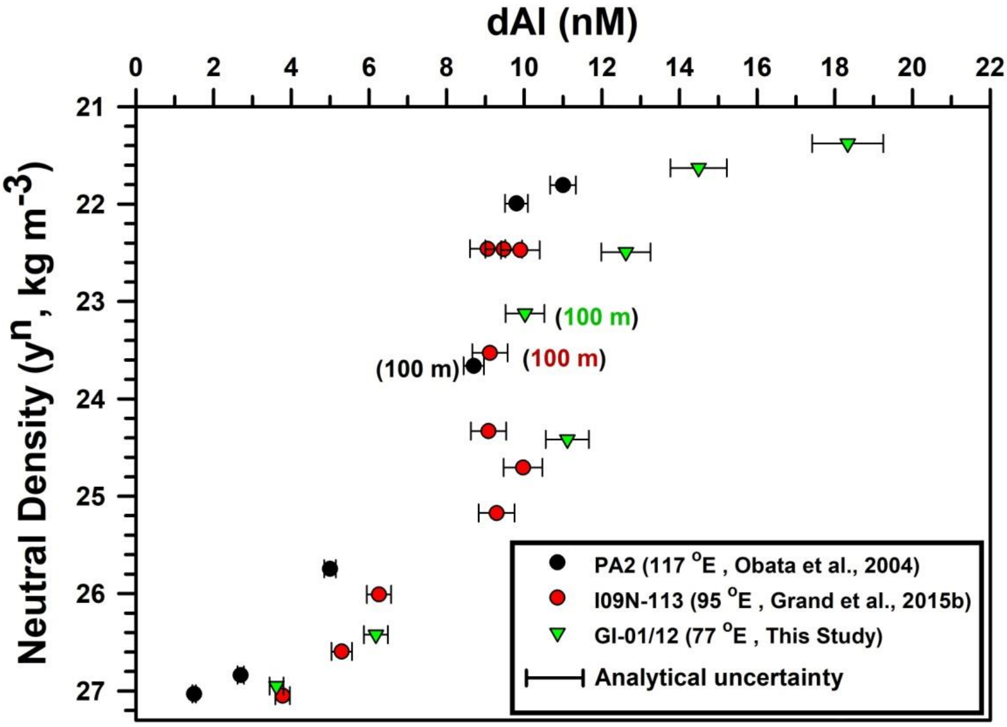

Fig. 3.15: Comparison between dAl distribution observed in the upper 500 m water column at GI–01/12, I09N–113 (Grand et al., 2015b) and PA-2 (Obata et al., 2004) sampled along the South Equatorial Current carrying the Indonesian Throughflow Water. Due to large distances between the stations, the dAl data is plotted against the neutral density. dAl observed at 100 m for each station is also highlighted to indicate the relative difference in neutral density at this depth for different stations. Analytical uncertainties indicated for the GI-01/12 and PA-2 data were that observed (5%, 1SD) after repeat analysis of in-house reference seawater, InStd-D, in this study and at 2.0 nM by Obata et al. (2004), respectively. Precision for dAl analysis for I09N cruise samples was not indicated by Grand et al. (2015b) and, therefore, considered as 5% here for comparison.

At the center of the subtropical gyre (GI-01/16), a relative decrease (to 8.6 nM) in surface dAl compared to the northern gyre region (14-18 nM) correlates with the decline in mineral dust deposition flux (Grand et al., 2015a; Mahowald et al., 2005).

3.4.2 Controls on dAl distribution in the lower thermocline and deeper waters (>300 m)

In the open ocean, most of the dissolvable Al from the mineral dust deposited on the ocean surface is released in the surface mixed layer with no significant dissolution below the mixed layer (Maring and Duce, 1987; Measures et al., 2010). Also, residence time estimates (Orians and Bruland, 1986) for dAl in the open ocean surface waters are short (4 weeks-4 years) vis-a-vis deep water residence time, which is an order of magnitude higher (50-200 years). Given the above conditions, the dAl distribution in the intermediate and deep water depths of open ocean waters is largely controlled by the water advection and reversible scavenging of Al adsorbed on the particulate phases as they sink through the water column below the surface layer. Though, this assertion may break in the regions close to the ocean boundaries (continental margins and seafloor) due to external dAl contributions from the partial dissolution of and/or Al desorption from the fluvial derived and resuspended boundary sediments, and diffusion of pore waters rich in dAl (Grand et al., 2015b; Caschetto and Wollast, 1979; Van Beueskom et al., 1997). In the next sections, the dAl distribution observed in the intermediate, deep and bottom waters of different regions sampled in the Indian Ocean are presented and the probable sources and processes leading to the observed distribution are discussed.

3.4.2.1 The Bay of Bengal (BoB) and the Andaman Sea

The sediment trap data of Unger et al. (2003) in the BoB showed higher mean lithogenic particle flux (6.0-19.5 g m^{-2} yr^{-1}) for the deep sediment traps (~2000-3000 m) compared to the lithogenic sediment flux (4.3-14.5 g m^{-2} yr^{-1}) across the shallow traps (700-1500 m). This indicates that the resuspension of sediments from the continental slope supplies additional lithogenic matter to the deeper waters of the BoB together with the fluvial and shelf derived particulate lithogenic matter. During the GI-01 cruise, the general increase in dAl levels close to the continental slope and seafloor (Fig. 3.2b) suggest that the resuspension of the slope and benthic sediments along with the probable influx of dAl enriched pore waters, upon sediment resuspension, act as sources of dAl in the deep and bottom waters of the BoB. Also, note that dAl maxima near seafloor showed a decrease in magnitude from the N.BoB to the S.BoB (Fig. 3.2b). This may result from a decrease in the fraction of lithogenic sediments settling through the BoB water column (Unger et al., 2003), providing the necessary reactive mineral phases in the form of aluminosilicates and clay minerals to the margin sediments, from which Al could be released to the water column upon their resuspension. Singh et al. (2012) estimated the particulate matter derived excess dissolved Nd (Nd_{xs}) needed, in addition to the dissolved Nd contribution resulting from the mixing of water masses, to balance the total mass of dissolved Nd observed in the BoB. Their results showed the hotspots of Nd_{xs} in the deep and bottom waters of BoB apparently, focused near the continental slope and rise. This result also suggests resuspension of sediments from the continental margin and their subsequent partial dissolution as a process of trace metal supply to the deep and bottom waters. During the late winter period (GI-06(A) cruise), the increase in dAl levels observed in the intermediate and deep waters (>500 m) towards the eastern coast of India (GI-06(A)/1, Fig. 3.3d) suggests that sediment resuspension is a ubiquitous process along the continental margins of BoB, providing additional dAl input to the deeper waters of the region.

One of the striking observations in the deeper waters of the southern Andaman Sea (at GI-06(A)/6) is the near-uniform dAl (~3.7 nM) below 1000 m (1500-2400 m, Figs. 3.3d and 3.10) in contrast to the nearby S.BoB stations (GI-06(A)/5 and 8, Fig. 3.3d and 3.3e), which show about 1 nM lower dAl levels in the similar depth range (2.5-2.7 nM at 1800-2500 m; Figs. 3.3d and 3.3e). Also, the uniform dAl composition in the deeper waters at GI-06(A)/6 was similar to that observed in the lower thermocline depth (~1200 m) at the nearby S.BoB stations (GI-06(A)/5 and 8, Figs. 3.3d and 3.3e). The deeper waters of the Andaman Sea (>1000 m) are predominantly derived from the lower thermocline waters of the BoB, entering through the Ten-degree channel and the Great Passage, as the shallow sills of the Andaman-Nicobar Ridge isolates the deep basin of the Andaman Sea from that of the BoB below ~1800 m (Dutta et al., 2007 and references therein). Apparently, rapid renewal of the deep waters (within 6 years, Okubo et al., 2004) in the Andaman Sea compared to the scavenging residence time of dAl, ensures similar dAl composition in the deep and lower thermocline waters (~1200 m) of the Andaman Sea and the BoB, respectively. Moreover, rapid vertical mixing of the Andaman deep waters (timescale: ≤5 years, Dutta et al., 2007) leads to near-uniform dAl concentrations.

Dutta et al. (2007) suggested that internal solitary waves induced by the tidal currents over rough topography of the Andaman Sea could cause rapid vertical mixing in the deep waters. This process may also induce sediment resuspension from the sea margins, which is supported by higher water turbidity observed within the deeper (>1000 m) waters of the sea compared to the surrounding waters in the BoB (Fig. 3.14). The relative increase in dAl concentrations observed below 500 m close to the Andaman-Nicobar Ridge (GI-06(A)/7, Figs. 3.3e and 3.10) may, therefore, suggest additional dAl input from the resuspended sediments due to water turbulence over the ridge within the sea.

3.4.2.2 The Arabian Sea (AS)

In the deeper waters (>1000 m) of the Arabian Sea, the observed increase in dAl towards the continental margin (at station GI-06(A)/24, refer Figs. 3.3f and 3.11) suggests an additional external source of dAl. The increase in the lithogenic sediment flux from the central Arabian Sea to the eastern Arabian Sea is evident from the deep (~3000 m) sediment trap data (Ramaswamy and Nair, 1994). This increment in lithogenic flux results from the supply of fluvial sediments from the Indus, Narmada and Tapi rivers discharging to the eastern Arabian Sea (Ramaswamy and Nair, 1994). Further, the observed discrete maximum in the thermocline waters of station GI-06(A)/24 at 600 m depth (Figs. 3.3f and 3.11) suggests Al input either due to the resuspension of margin sediments or diffusion of dAl enriched pore waters. In either of the cases, lithogenic sediments settling over the continental margin must play an important role in the supply of reactive Al mineral phases. It is important to note that the enrichment in the dAl levels observed in the deep waters near the coast of the Arabian Sea was much lower compared to that observed near the coastal region of the BoB, presumably due to much smaller fluvial (and associated sediment) discharge in the eastern Arabian Sea compared to the coastal BoB (Ramaswamy and Nair, 1994; Unger et al., 2003).

3.4.2.3 The Equatorial Indian Ocean

The dAl maximum observed at station GI-01/9 around 3000 m correlates with the increase in dissolved Fe (dFe) concentrations in similar deep waters depths at the same station (refer to Fig. 11(I) of Chinni et al., 2019). Chinni et al. (2019) proposed this increase in the dFe to be resulting from the advection of dFe-rich deeper waters (>2500 m) close to the Java Trench, which constitutes the subduction zone between the Indian and the Indonesian plate. The interaction of re-circulated seawater (through the faults) with poly-metallic nodules is suggested to be the source of dFe-rich deeper waters near the trench. In the absence of dAl data near the trench, it is unclear if such a process

may also lead to the enrichment of dAl concentrations in the deeper water. Alternatively, here, it is argued that the deep and bottom waters flowing as the western boundary currents along the eastern boundary of the NER (Tomczak and Godfrey, 2003a; You, 1999) may produce sufficient turbulence over the NER to resuspend the margin sediments, which may subsequently act as the source of dFe and dAl to the deep and bottom waters. This could be inferred from the elevated dAl concentrations and the turbidity values observed in the deep and bottom waters of the S.BoB close to the eastern margin of the NER at station GI-06(A)/9 (Figs. 3.3e and 3.14). These dAl rich deep waters (2000-3500 m) are subsequently advected from the east of the NER to the Central Indian Ocean Basin at GI-01/9 (Fig. 3.4b) and result in the observed dAl maximum. Such enrichment in dAl was not observed in the bottom waters (below 3500 m, Fig. 3.2b) at GI-01/9 due to the topographical barrier for the advection of bottom waters (>3500 m) to the region near station GI-01/9 from the east of the NER (Fig. 3.4b).

The increase in dAl towards the seafloor in the bottom waters (>3500 m) observed at the eastern Eq.IO stations (GI-06(A)/11, 12, 13 and 14, Fig. 3.3e) during the GI-06(A) cruise imply dAl flux from the bottom sediments in these regions.

3.4.2.3.1 Residence time of the dissolved Al in the deep waters of the Equatorial Indian Ocean

The residence time of dAl against removal by particle scavenging in the deep waters (2000-3500 m) of the Eq.IO using the one dimensional (1-D) scavenging-advection-diffusion model (Craig, 1974) is estimated. This model has two inherent assumptions: (1) horizontal concentration gradients in the distribution of the modeled dissolved constituent in the region of application are negligible and (2) vertical mixing is the dominant process with the absence of any significant horizontal advection of a distinct water mass in the model layer. As recognized by previous studies (Mantyla and Reid, 1995; You, 1999;

You, 2000), the Indian deep waters represent the modified Circumpolar Deep Water (CDW) and occupy the depth range 2000-3500 m. Due to significant vertical upwelling and dianeutral mixing, the northern Indian deep waters (north of 30°S) show remarkable linearity in the potential temperature-salinity plot (Fig. 3.5) and, therefore, could be treated as a 'z-diffusive layer' where the 1-D advection-diffusion model is applicable (Craig, 1969). The AABW majorly fills the water column below 3500 m as a distinct water mass (Tomczak and Godfrey, 2003a; You, 1999) and hence, dAl below 3500 is not considered for the fitting using the 1-D scavenging-advection-diffusion model. Also, we restricted the model application to the Eq.IO stations sampled during the GI-06(A) cruise as important horizontal dAl concentration gradients were observed for the deep waters of the northern Indian Ocean (the BoB, the Andaman Sea and the Arabian Sea; Sections 3.4.2.1 and 3.4.2.2), the southern end of the Eq.IO region (station GI-01/9; refer Section 3.4.2.3) and the ITW-ISG region (refer Section 3.4.2.4). Fig. 3.16 shows the best model fits (solid black lines) to the deep-water dAl profiles of the Eq.IO stations sampled during the GI-06(A) cruise, considering the conservative mixing due to vertical advection-diffusion of dAl and setting the boundary dAl concentrations to be free variables (refer to Eq. (B3) and its description in Appendix B). At stations GI-06(A)/11, 14 and 17, significant and discrete positive dAl deviations (>5%) from the conservative mixing line (denoted by arrows in Fig. 3.16) within the deep-water layer boundaries suggest the additional, non-uniform dAl input in between the model boundaries. This additional input may be produced due to horizontal advection or net *in situ* Al release from the particulate matter within the deep waters. It is particularly evident for the GI-06(A)/11, where the transport of dAl-rich deep waters from the region near the NER (GI-06(A)/10 and 9) could be seen (Fig. 3.3e). In any of the two cases, the deep-water dAl profiles at these stations could not be convincingly simulated with a 1-D scavenging-advection-diffusion model used in this study. Therefore, we applied the model to the deep-water dAl profiles of stations GI-06(A)/12, 13 and 19 (blue lines) to constrain the deep-water residence time of dAl in the region. Other stations (GI-06(A)/18 and GI-06(A)/20) are not examined due to lack of enough data points in the deep waters (≤3) compared to the number of free variables (3, i.e., C_m, C_o and ψ/ω; refer to Eq. (B2) of Appendix B) in the model. The best fits for the 1-D scavenging-advection-diffusion model (refer to Eq. (B2) of Appendix B) to the deep-water dAl at GI-06(A)/12, 13 and 19 (blue lines, Fig. 3.16) gives the ratio of the dAl scavenging rate to the vertical advection velocity (i.e., ψ/ω; refer to Table 3.1 for estimated values). From these ψ/ω estimates, the scavenging residence time ($\tau=1/\psi$) could be calculated if data on ω is available.

Srinivasan et al. (2000) estimated the mean upwelling velocity, ω, north of 30°S across the lower deep water layer boundary (~3500 m) to be 10 m yr^{-1} upward using the adjusted ^{14}C concentration profiles ('corrected for the effects of addition of particulate radiocarbon to the deep waters'; Srinivasan et al., 2000). This is relatively smaller than the upwelling velocity of ~12.5 m yr^{-1} given by Warren (1981) across ~2000 m at ~18° and the basin-mean upwelling velocity of ~14 m yr^{-1} across ~2000m north of 32°S determined by Robbins and Toole (1997) by considering, together, the hydrographic data and advective flux of the dissolved silica. Assuming ω to be varying in the range of 10-14 m yr^{-1}, the variations in the scavenging residence time of the dAl in the deep waters of the Eq.IO are reported here (Table 3.1). The estimated residence time of dAl against scavenging in the deep waters lies in the range: 92-196 yrs (Table 3.1). However, the model fit to the deep-water profile at GI-06(A)/19 was comparatively poor ($R^2 = 0.44$, Fig. 3.16) and may suggest horizontal dAl input, probably, from relatively dAl enriched deep and bottom waters near the margin of Chagos-Laccadive Ridge as also visible in the slight increase in dAl at ~1800m at GI-06(A)/20 and 21 (Fig. 3.3f). Accordingly, neglecting the residence time estimates from GI-06(A)/19, the inferred range of 92-141 yrs, using dAl profiles of stations GI-06(A)/12 and 13, is considered to be more representative. This residence time range is similar to that observed in the deep Pacific Ocean (50-200 yrs, Orians and Bruland, 1985, 1986). It is, however, relatively larger than the basin-averaged deep-water dAl replacement time (50 ± 10 yrs) calculated in the North Atlantic (Hayes et al., 2018b). Replacement time is a measure of the time needed to replace the trace element inventory for

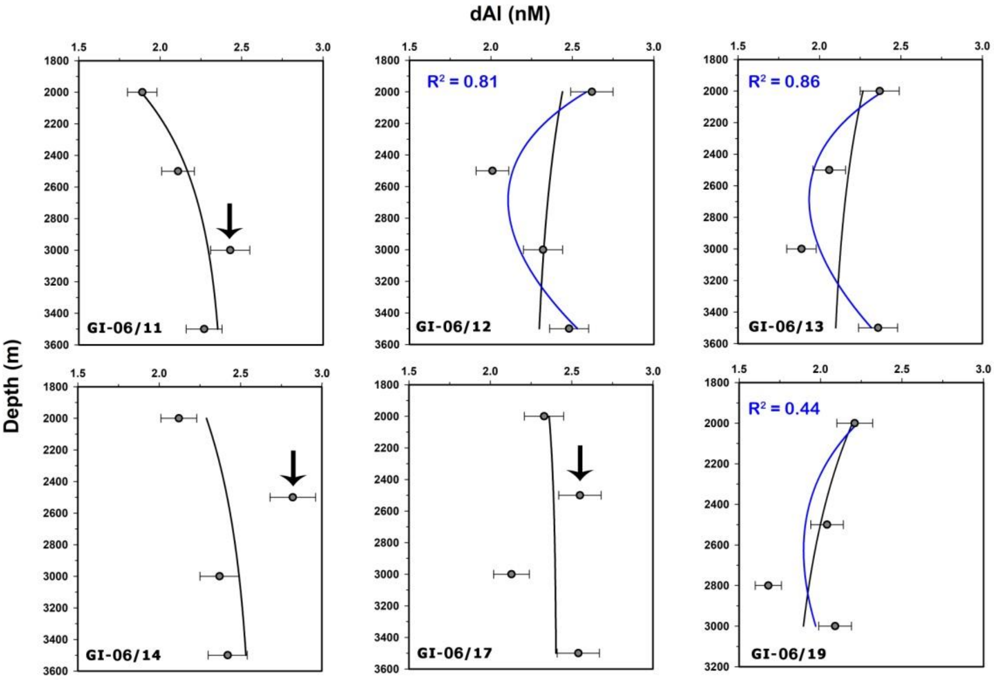

Fig. 3.16: Deep-water (2000–3500 m) dAl distribution at the selected Eq.IO stations (see text) overlain by best model fits (in the least square sense) to the distribution using 1-D advection-diffusion, i.e., vertical conservative mixing, model (solid black lines; also refer to Eq. (3) and its description in the Appendix B) and 1-D scavenging-advection-diffusion model (solid blue lines; also refer Eq. (2) and its description in the Appendix B). Horizontal bars represent the precision of analysis (_5%, see text) achieved at similar dAl concentrations. In the graph, arrows point to the dAl values within the deep-water layers showing significant dAl excess with respect to the conservative mixing line (solid black lines).

a given volume of seawater by the source(s) considered for the element. The replacement time is equal to the removal residence time only if the distribution of the element in the region of interest is in a steady-state. Considering the deep-water dAl distribution in the North Atlantic to be in a steady-state, the smaller estimate of deep-water dAl replacement time presumably results due to more intense scavenging of dAl by the particulate matter, particularly by diatoms associated with the North Atlantic spring bloom (Malviya et al., 2016). Deep-water scavenging of dAl near the ocean margins is also indicated by significant depletion (compared to that in the African dust and Bulk Continental Crust) of Ti:Al ratio in the fine particulate matter and, in general, continuous increase in the particulate Al levels in the deeper waters (>500 m) of the North Atlantic (Hayes et al., 2018a and supporting information therein; Ohnemus and Lam, 2015), more significant near the continental margins.

Table 3.1: Results estimated for ψ/ω and τ by fitting the 1-D scavenging-advection-diffusion model to the deep-water dAl profiles at the Eq.IO stations, GI-06(A)/12, 13 and 19. z* values are estimated by fitting the 1-D advection-diffusion model to the deep-water salinity distribution in the respective stations.

Station ID	z* (km)	ψ/ω (km^{-1})	$ω^1$ (km/yr)	τ (yr)
GI-10/12	1.04	0.78	0.010	128
			0.014	92
GI-10/13	0.95	0.71	0.010	141
			0.014	101
GI-10/19	0.78	0.51	0.010	196
			0.014	140

[1] Data sources: Robbins and Toole, 1997; Srinivasan et al., 2000; Warren, 1981

3.4.2.4 The Indonesian Throughflow and Indian Subtropical Gyre

Our sampling station GI-01/16, lies very close to the Kairei vent field discovered (Gamo et al., 2001) over the Central Indian Ridge (CIR) and is just north of the Rodrigues Triple Junction (RTJ). At this station, we observed anomalously high deep water turbidity values in the narrow depth range of ~2150-2300 m with turbidity maximum around 2250 m depth (Fig. 3.12c). Coinciding with this high turbidity signal, was the deep-water dAl maximum (at 2250 m; Figs. 3.12b and 3.12c). At the same station and identical depth (2250 m), Chinni et al. (2019) also observed highly enriched dissolved Fe concentration (20.86 nM), about 28 times higher than the background deep-water dissolved Fe level (~0.75 nM) and suggested it to be of hydrothermal origin. Various earlier studies have also reported the active hydrothermal venting in the vicinity of the RTJ and over the CIR, either through indirect clues from hydrothermal plume signals of prominent suspended sediment and chemical anomalies (Gamo et al., 1996; Jean-Baptiste et al., 1992; Vu and Sohrin, 2013) or direct observation of hydrothermal venting sites over the CIR (Gallant and Von Damm, 2006; Gamo et al., 2001). Therefore, dAl maximum coinciding with the turbidity and dissolved Fe maxima may suggest that the dAl input is sourced from the dAl-enriched hydrothermal fluids emanating from the active vents over the CIR. However, the gradual increase in dAl concentrations to the dAl maximum close to the seafloor at GI-01/16 (Fig. 3.12b) may also, in principle, result from the dAl flux due to the sediment resuspension and/or diffusion of dAl-rich pore water from the sea bottom as the primary source(s). Further north at ER-10, Vu and Sohrin (2013) also reported the dAl enrichment in the deep-water hydrothermal plume encountered during their study (around 3000 m, Fig. 3.12b) and, based on the relationship between ^{3}He, dAl and other trace metal data, suggested that the observed enrichment at ER-10 is probably due to resuspended sediments. To better constrain the source(s) of dAl, higher resolution sampling, both vertical and lateral, of deep waters in this region is needed for the measurement of dAl and other chemical constituents of hydrothermal origin.

The dAl distribution trend for bottom water depths in the Central Indian Ocean Basin (Fig. 3.12b) indicates the advection of dAl-rich bottom waters at GI-01/11 across the NER from the Western Australian Basin. This is also supported by the dAl maximum in the bottom waters of station GI-01/11, which is observed much above the seafloor (~1200 m above the seafloor at 4000m; Fig. 3.12b) and therefore, discards the possibility that bottom sediments were the primary source of dAl increase in the bottom waters. Again, as suggested for the southern equatorial region (station GI-01/9; see Section 3.4.2.3), the interaction of the bottom waters, flowing as the western boundary current along the eastern NER, with the sediments over the ridge may enrich the dAl concentrations in the bottom waters. More studies on dAl distribution in the deep and bottom waters along the eastern margin of NER are needed to confirm this hypothesis. Further, the dAl levels in the bottom waters decrease as they turn and move southward at GI-01/12 (Fig. 3.12b), presumably, due to mixing and scavenging loss. The mean dAl concentration in the bottom waters again increased close to the CIR at ER-10 (Fig. 3.12b); however, here, the dAl profile showed a sudden increase close to the seafloor, suggestive of external dAl input from the bottom sediments.

3.5 Conclusion

A comprehensive study on the cycling of dAl in the water columns of the northern, equatorial and subtropical gyre region of the Indian Ocean has been carried out and forms the first extensive evaluation of sources, sinks and internal cycling of dAl in the deep and bottom waters of the BoB and the equatorial Indian Ocean. The dAl distribution throughout the water column of the BoB is predominantly influenced by the lithogenic sedimentary input from fluvial and continental margin sources, enriched in reactive clay minerals. Using the estimated range of the Al fractional solubility from the lithogenic sediments in the BoB surface waters, the dAl flux to the surface waters of BoB from the dissolution of / Al desorption from the lithogenic sediments is calculated to be at least an order of magnitude higher than that supplied by the G-B river system waters. This suggests that the Al release from the sediments is a dominant process controlling the surface dAl distribution in the BoB. In the southern Andaman Sea, partial dissolution of resuspended local shelf sediments from the Nicobar Islands and the advection of Indonesian Water from the SoM results in elevated dAl levels in the surface mixed layer and the upper thermocline waters. Rapid ventilation of and vertical mixing in the deep waters of the Andaman Sea and, apparently, the lower scavenging removal rate of dAl result in near-uniform distribution of dAl in the deeper waters at the center of the southern Andaman Sea.

Overall, dAl concentrations in the surface and upper thermocline waters of the equatorial Indian Ocean region were controlled by the advective mixing of the low salinity, dAl-rich waters of the S.BoB and the Andaman Sea with the high salinity, dAl-poor waters of the southern Arabian Sea under the influence of NMC. Using the 1-D scavenging-advection-diffusion model, the scavenging residence time of dAl in the deep waters of the Eq.IO region is estimated to lie in the range: 92-141 years.

During the winter monsoon, continental outflow, predominantly from the Indian subcontinent, leads to the high atmospheric deposition of mineral aerosols close to the south-eastern boundary of the Arabian Sea; this, in turn, translates to the elevated dAl levels in the surface mixed layer. In the deeper waters of the Arabian Sea, the relative increase in the dAl levels close to the continental margin hints at the net Al release from the boundary sediments.

At the northern reaches of the subtropical gyre region, significant enrichment of dAl throughout the upper water column (<500 m) agrees with the dAl distribution pattern observed in the similar depth range further east at ~95°E

(Grand et al., 2015b) and is primarily attributed to the atmospheric dust flux from the Australian continent, which is the major dust source to the ISG region, and the advection of the ITW. However, higher (compared to the previous study) dAl levels in the surface mixed layer were observed in this study and, presumably, reflect the interannual variations in the dust deposition flux to the ISG region. The increase in dAl concentrations in the deep waters (2000-3500 m) over the eastern flank of the CIR seems to result from bottom sediment resuspension close to the ridge. This enrichment in the deep-water dAl levels dies out due to water–mass mixing and scavenging along the advective pathway of deep waters towards the north in the subtropical gyre region. The advection of the dAl enriched AABW (below 3500 m) from the Western Australian Basin to the northern Central Indian Basin across the deep saddles of the NER is observed.

Chapter 4

Distribution and cycling of dissolved aluminium in the Arabian Sea and the western equatorial Indian Ocean

4.1 Introduction

In the open ocean regions, dissolved aluminium (dAl) distribution in the surface waters has extensively been used as a proxy for the atmospheric mineral dust input to the ocean surface (Measures and Vink, 1999; Measures and Vink, 2005; Measures et al., 2015; Grand et al., 2015a). The rationale behind exploiting surface dAl to derive the mineral dust deposition flux to the ocean include (1) high abundance (~8% by weight; McLennan, 2001) and largely invariant composition of Al in the upper continental crust, a predominant source of mineral aerosols over the open ocean regions (Mahowald et al., 2005 and references therein), (2) short removal timescales of dAl in the surface ocean (~few weeks to 4 years, Orians and Bruland, 1986), (3) insensitivity of parent dAl species (i.e., $\mathrm{Al(OH)}_4^{-1}$ and $\mathrm{Al(OH)}_3^0$) to redox changes in seawater (Bruland et al., 2014 and references therein; Measures and Vink, 2000), and (4) no (known) role of Al in active biological processes. Constraints on eolian dust deposition over the marine environment are crucial to estimate for the atmospheric input of bio-essential metals (e.g., Fe, Mn, P) to the ocean surface, which set major controls on the abundance and diversity of the marine phytoplankton in the open oceanic regions (Jickells et al., 2005; Sunda, 2012 and references therein). Close to the continental margins, however, surface dAl distribution may have additional (other than dust deposition) controls due to the significant influence of ocean-continent exchange processes such as fluvial discharge, resuspension of the margin sediments (Menzel Barraqueta et al., 2018; Middag et al., 2015; Singh et al., 2020). Moreover, in the dynamic marine system, the impact of water mass advection on the dAl distribution of water column may not be neglected a priori (Baker et al., 2016). The relative importance of the advective processes on modulating the dAl distribution may be understood by comparing the scavenging rate of dAl and the water advection rate in the given oceanic region (Baker et al., 2016; van Hulten et al., 2013). Particle scavenging processes predominantly control the output flux of dAl from the seawater, where passive adsorption of Al onto the biogenic particulates and their subsequent removal out of the water column is particularly important (Middag et al., 2015; Moran and Moore, 1988; Orians and Bruland, 1986). Consequently, the residence time for dAl in seawater in a given region is significantly influenced by the biological productivity and export of biogenic particles out of the water column (Orians and Bruland, 1986). In summary, it is essential to understand and decouple the potential impacts of the processes mentioned above (other than atmospheric dust deposition) on the surface dAl distribution prior to using it as a tracer of continental mineral dust input over the oceans.

The Arabian Sea (hereafter, AS) is characterized as one of the highest dust receiving regions in the global ocean (Jickells et al., 2005; Mahowald et al., 2005). Dust emission, and its subsequent transport, from various neighboring arid (e.g., southern Arabian Peninsula, Makran Basin, Sistan Basin) and semi-arid (Thar Desert) continental regions contribute to the high net annual dust deposition observed over the AS (Pease et al., 1998; Tindale and Pease, 1999; Kumar et al., 2020). However, significant seasonal variability in dust concentrations in the surface-level aerosols over the AS is observed (Chester et al., 1984; Pease et al., 1998; Siefert et al., 1999; Tindale and Pease, 1999). This variability arises in response to the marked seasonal changes in wind stress over the AS and surrounding continents (also discussed later in the text), which influences the dust production and its transport from different neighboring continental sources (Schott and McCreary, 2001; Tindale and Pease, 1999). Moreover, the estimated scavenging residence timescales for surface dAl in the AS are relatively short (few months to ~1 year; Han et al., 2008). Together, seasonal variations in dust deposition flux and short dAl residence time result in significant temporal changes in surface water dAl concentrations in the AS (Measures and Vink, 1999; Schüβler et al., 2005). Given this seasonality, the model estimates of annual (climatological) mean surface dAl concentrations in the AS (Gehlen et al., 2003; Han et al., 2008) appear to be of limited importance and motivate to simulate the surface dAl variations in seasonal timescales. One of the objectives of this study is to model, for the first time, the seasonal variations in surface dAl concentrations in the AS using a simple 1-D, non-steady-state box model and compare them with the observed dAl variations.

Most of the labile Al from the eolian dust deposited over the open ocean gets released in the surface mixed layer (Maring and Duce, 1987). In the sub-surface depths, water mass advection and reversible scavenging of Al from suspended and sinking particulates become more important in controlling the dAl distribution. The impact of water mass advection on the sub-surface dAl distribution is observed in different oceanic regions (Measures et al., 2015; Middag et al., 2015; Singh et al., 2020; Grand et al., 2015b). In the AS, the thermocline water mass structure (200-900 m) is influenced by the outflow of high salinity water masses from the neighboring marginal seas (the Red Sea, the Persian Gulf; Shenoi et al., 1993). These shallow marginal basins receive high eolian dust input from the nearby deserts (e.g., the Rub-Al-Khali and the Nubian Desert), impacting the trace element distribution in their water column (Shriadah et al., 2004; Measures and Vink, 1999). Once these waters advect to the AS, they could entrain into the surface layer under the strong upwelling conditions that develop during the summer and winter monsoon periods (Wyrtki, 1973). The probable impact of the advection of the marginal seas waters on the dAl and other lithogenic trace metals distribution in the AS is, therefore, important to evaluate.

Earlier studies (Measures and Vink 1999; Narvekar and Singbal, 1993; Schüβler et al., 2005; Thi Dieu Vu and Sohrin; Upadhyay and SenGupta, 1994) had investigated the surface dAl concentrations in the AS. However, these studies were mostly restricted to the summer and winter monsoon periods (with minimal spatial coverage during the intermonsoon seasons). Also, full vertical depth dAl profiles in the AS are limited (Narvekar and Singbal, 1993; Schüβler et al., 2005; Thi Dieu Vu and Sohrin; Upadhyay and SenGupta, 1994). In this study, we measured full vertical water column dAl profiles across the AS along the GEOTRACES-India transect, GI-05 (Fig. 4.1), during the fall inter-monsoon period (autumn season, late September-early October) to better understand the (1) annual surface dAl cycling in response to the seasonal variations in dust deposition over the AS and (2) processes controlling the dAl distribution in the thermocline and deeper waters of the Sea. This is the first report on surface dAl distribution in the AS during the mid-fall intermonsoon period (late September to early October) and, therefore, adds to the previous understanding of surface dAl annual cycling in the Sea (Measures and Vink, 1999; Schüβler et al., 2005; Thi Dieu Vu and Sohrin, 2013). This study also forms the first comprehensive investigation of dAl cycling over the full vertical water column in the western AS and the western equatorial Indian Ocean region.

4.2 Meteorological and hydrological setting in the study area

This section discusses ancillary information on general meteorology, circulation scheme and water mass structure in the studied regions to better understand the observed dAl distribution. The AS is subjected to a strong monsoonal climatology where remarkable seasonal changes (both in direction and amplitude) in wind stress are recorded (Schott and McCreary., 2001). These changes in the meteorology show a significant impact on the hydrology, water mass circulation, primary biological production in the AS (McCreary et al., 1996; Schott and McCreary, 2001), and control the emission and transport of dust from various potential sources surrounding the Sea (Pease et al., 1998; Tindale and Pease, 1999). The development of a low-pressure zone over the north-western region of India and Tibetan Plateau during the summers season (July-August) results in the formation of a south-westerly, low-level wind jet, the Findlater Jet, in the AS (Schott and McCreary, 2001). During the same period (summers), the presence of the high-pressure zone over the eastern Mediterranean region facilitates the development of strong regional winds (the Summer Shamal and the Red Sea winds) over northeast Africa and the Arabian Peninsula, which merge into the Findlater Jet in the AS region. During the transit from the summer monsoon to the fall inter-monsoon period (sampling season of this study), a marked decrease in wind stress is usually observed over the AS and surrounding regions (Schott and McCreary, 2001; Halpern et al., 1998). This changing wind regime leads to the collapse of the Summer Shamal and the Red Sea winds during the fall intermonsoon period. Over the eastern AS, however, along with long-range transport of continental dust from the Arabian Peninsula and northeast Africa, more regional dust input from the arid/semi-arid regions of southwest Asia (e.g., Thar Desert, Makran coast, Indus River delta) is possible (Pease et al., 1998; Kumar et al., 2020).

Surface water salinity remains high (35.5-36.8) over all the sampled regions in the AS, but a gradual decrease towards the southern AS is apparent (Fig. 4.2A).

Significantly higher evaporation (E) minus precipitation (P) rate (E-P) in the northern AS (~2 m/yr) compared to that in the southern AS (~0.2-0.5 m/yr) results in the observed gradient in surface salinity and formation of the Arabian Sea High Salinity Water (ASHSW) in the northern AS surface ocean (Shetye et al., 1994). ASHSW subducts below the surface water layer as it advects towards the central and southern AS and is observed as a distinct high salinity core in the depth range of 75-100 m at the northern and central AS stations (GI-05/3-GI-05/9, Fig. 4.2A). Salinity maxima observed in the upper thermocline depths (200-300 m; Fig. 4.2A) of the northern and central AS

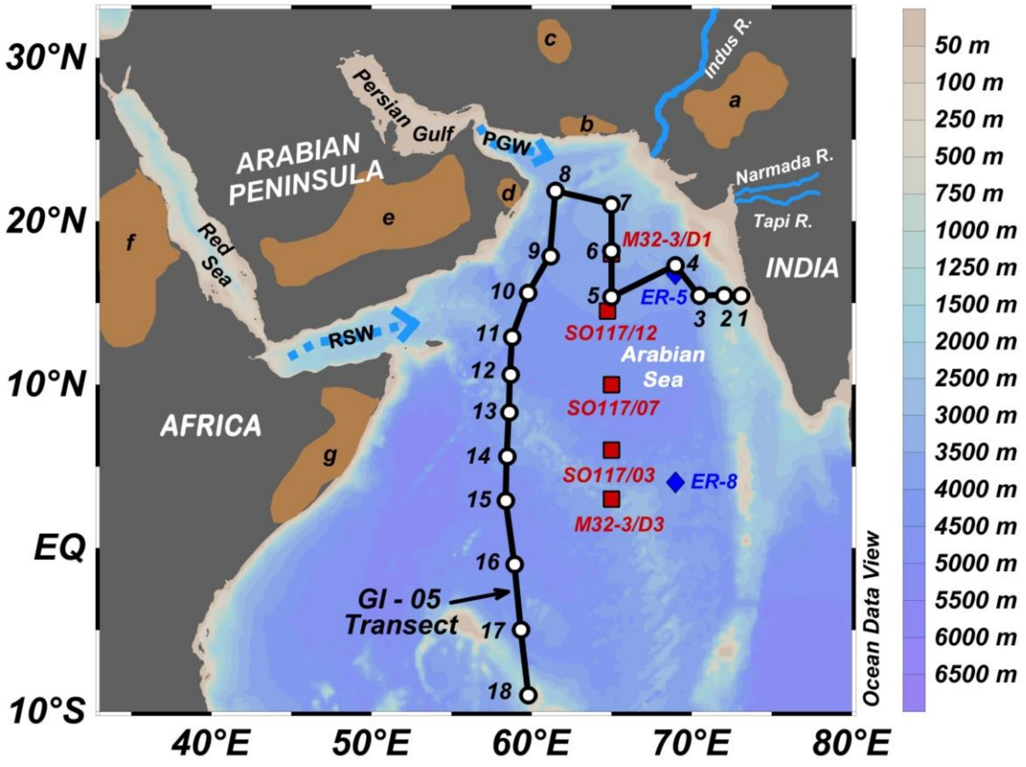

Fig. 4.1: Seawater sampling locations (white circles) occupied during the GEOTRACES-India cruise, GI-05. Major rivers (Indus, Narmada and Tapi) and marginal seas water masses (PGW: Persian Gulf Water and RSW: Red Sea Water) flowing into the Arabian Sea are highlighted. Selected sampling sites for dAl data from previous studies used in this work are also plotted. Brown patches over the surrounding landmasses are the schematic representations of some of the important dust source regions to the study area: (a) Thar Desert, (b) Makran Coast, (c) Sistan Basin, (d) Wahiba Sands, (e) Rub-Al-Khali Desert, (f) Nubian Desert, (g) Somali Coast. The map was prepared using the ODV software (version: 4.7.9, Schlitzer 2016).

stations (GI-05/5 to GI-05/9) represent the intrusion of high salinity Persian Gulf Water (PGW) from the Gulf of Oman to the open AS (Shenoi et al., 1993). The AS may also receive high salinity water (Red Sea Water) input to its lower thermocline depths (~600-800 m) from the Red Sea (Wyrtki, 1973). The absence of any strong salinity maxima in the characteristic potential density range (σ_θ: 27.0-27.4 kg m^{-3}; Shenoi et al., 1993; Fig. 4.2A) of the Red Sea Water (RSW) suggests a limited inflow of the water mass to the sampled regions during the study period (September-October). This observation agrees with the lowest estimated outflow of the Red Sea Water to the AS at the end of the summers (September-October; Maillard and Soliman, 1986).

The deep and bottom depths (>2000 m) in the AS and the western equatorial Indian Ocean are occupied by the Antarctic Bottom Water (AABW), the Modified North Atlantic Deep Water and the North Indian Deep Water (NIDW) (Kumar and Li, 1996; You, 1999, 2000; Mantyla and Reid, 1995). AABW primarily fills the bottom-most depths (>3500 m; Tomczak and Godfrey, 2003) of the regions and is sourced from the dense and cold bottom waters of the Weddell Sea (Mantyla and Reid, 1995). Advective mixing and entrainment of the North Atlantic Deep Water into the deep circumpolar waters of the Indian Ocean sector of the Southern Ocean (You, 1999) result in the formation of the MNADW (You, 2000). Relative to the MNADW in the southern and central Indian Ocean, the deep waters (~2000-3500) in the northern Indian Ocean (e.g., The AS and the Bay of Bengal) are significantly higher in salinity and dissolved nutrients and lower in dissolved oxygen content (You, 1999; Mantyla nad Reid, 1995). Due to large differences in these parameters, the deep waters in the northern Indian Ocean (predominantly in the AS and the Bay of Bengal) are considered as a different water-mass, the North Indian Deep Water (NIDW). The NIDW is shown to be representing an aged form of the MNADW (You, 2000).

The deep and bottom waters (>2000 m) enter the Somali Basin from the Mascarene Basin through the Amirante Trench and fills the deeper depths in the equatorial Indian Ocean (Mantyla and Reid, 1995; You, 2000; also refer to Fig. 4.3). In the AS, the deep and bottom waters are derived from the Somali Basin through the deep passage across the Owen Fracture Zone (Mantyla and

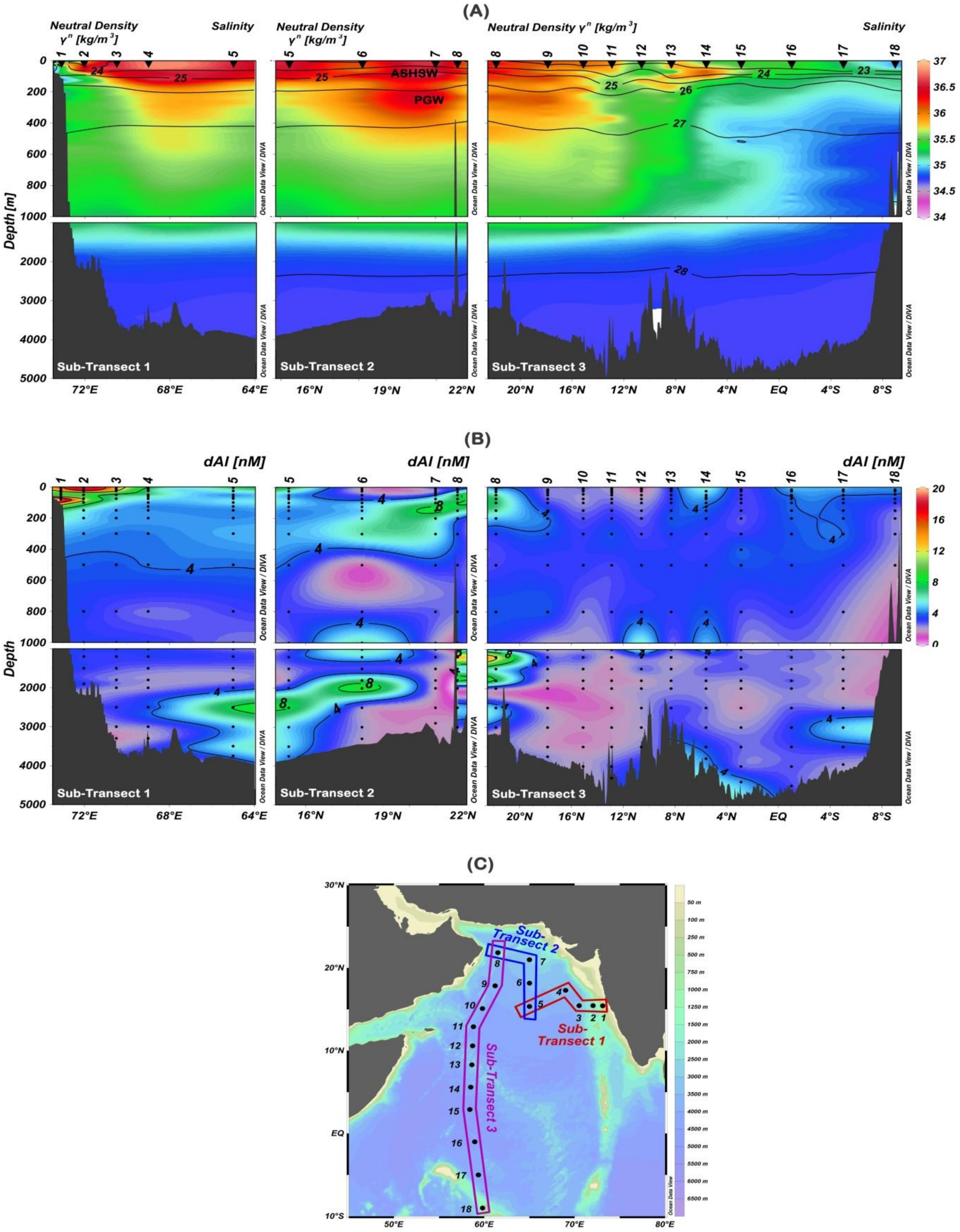

Fig. 4.2: (A) Salinity and **(B)** dAl variations in the water column along the GI-05 cruise section. Overlain contours in Fig. 4.2A and 4.2B represent the isolines for neutral density and dAl concentrations, respectively. For better understanding, the salinity and dAl data are plotted separately for the upper 1000m and the water column below. Further, for better visualization, the full GI-05 transect data is divided and plotted into three sub-transects, which are shown in Fig. 4.2**C**.

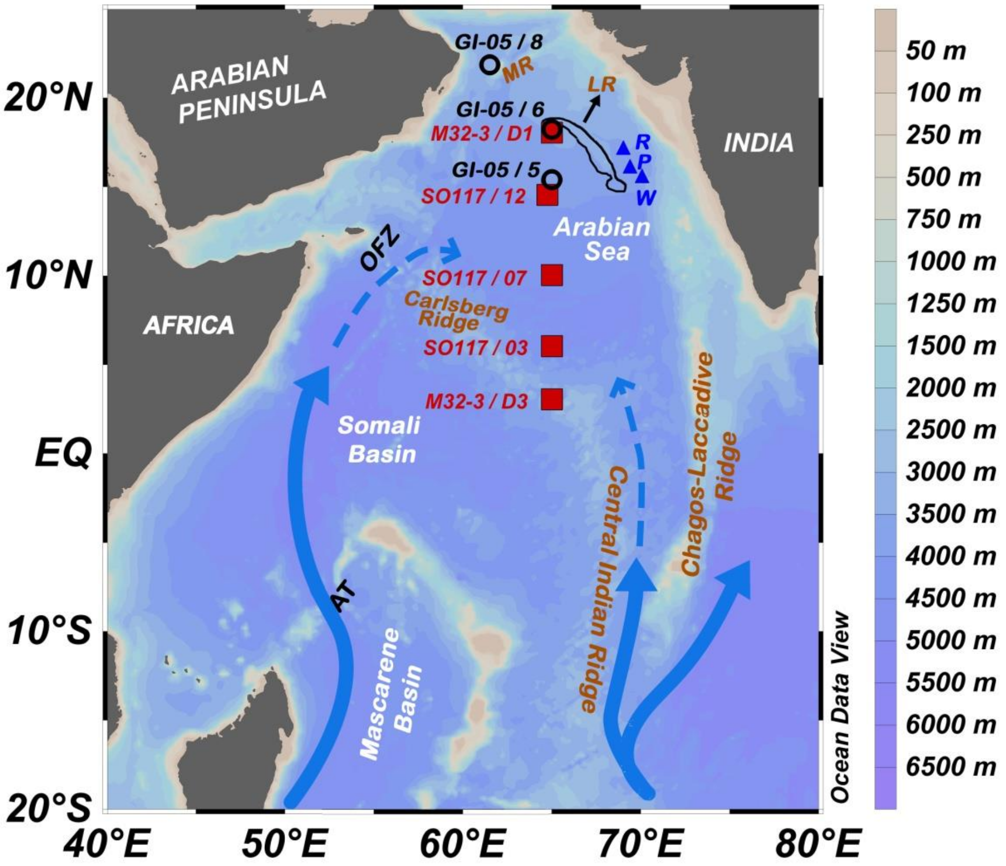

Fig. 4.3: A schematic representation of the deep-water circulation (>2000m) in the western equatorial Indian Ocean region and the Arabian Sea. Sampling stations (black open circles: this study and solid red squares; Schüβler et al., 2005) for which deep-water dAl concentrations are compared (discussed) in the text are plotted. The major ridges in the Arabian Sea and western equatorial Indian Ocean are also highlighted. LR: Laxmi Rigde, MR: Murray Ridge. Blue solid triangles mark the locations of the R:Raman Seamount, P:Panikkar Seamount and W:Wadia Guyot in the Laxmi Basin.

Reid, 1995; Fig. 4.3). Another important pathway of deep-water advection into the AS is through the deep gateway between the Chagos-Laccadive Ridge and the Central Indian Ridge at ~10°S as a boundary flow along the eastern flank of the Central Indian Ridge (You, 2000; Fig. 4.3).

4.3 Results

4.3.1 dAl in the surface mixed layer

Fig. 4.4 shows the distribution of dAl in the surface-mixed layer at all the stations sampled in this study. An overall east-west decreasing trend of dAl levels is evident in the AS (> 10°N). In the western AS (stations GI-05/8 to GI-

05/12), relatively low dAl concentrations (1.5 nM to 3.3 nM) were observed compared to that measured in the central (2.0 nM to 7.3 nM at stations GI-05/5 to GI-05/7) and the eastern regions of the sea (6.9 nM to 20.9 nM at stations GI-05/1 to GI-05/4). Also, the surface dAl concentrations observed in this study were compared with the surface Al distribution observed by Measures

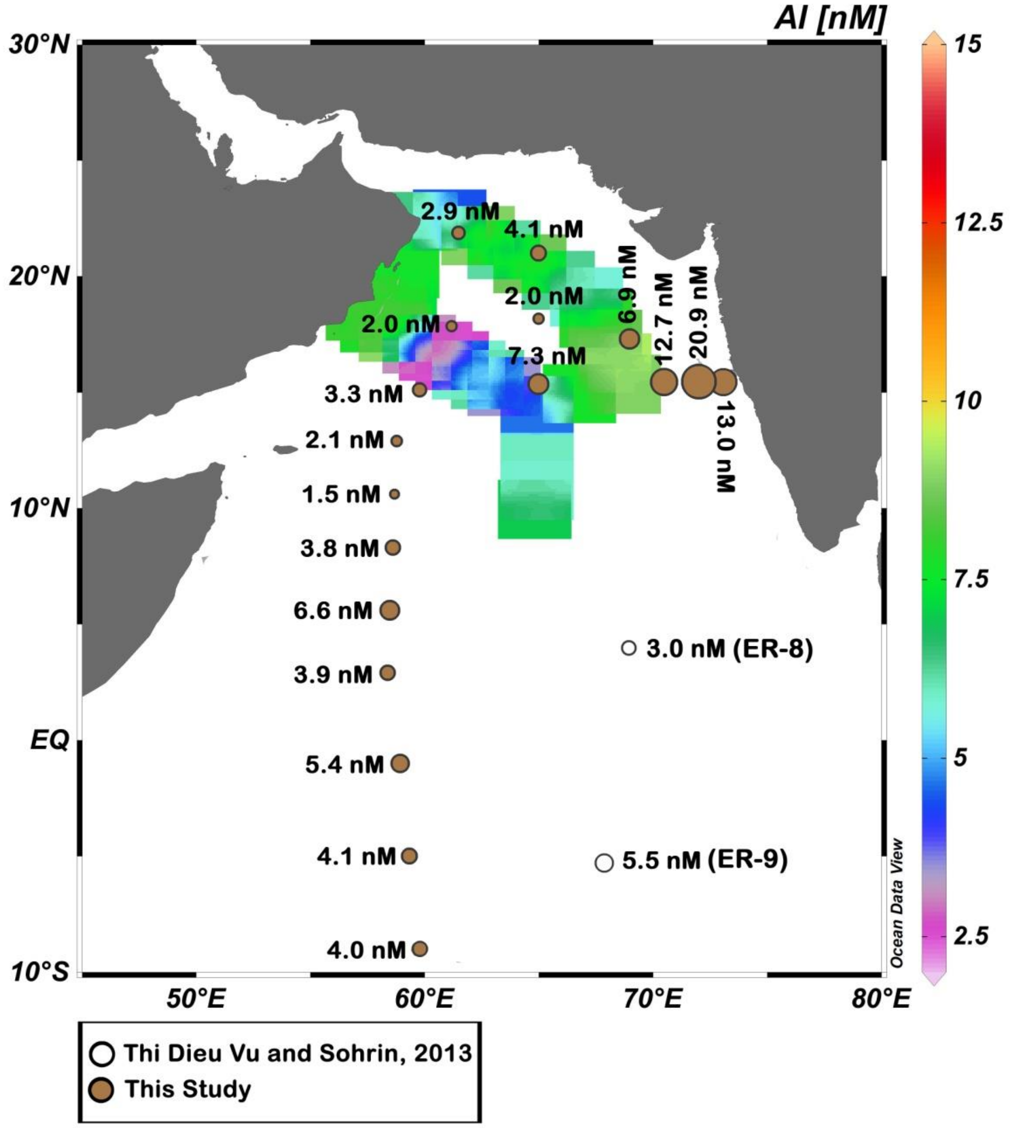

Fig. 4.4: Dissolved Al concentrations observed in the surface mixed layers during the fall inter monsoon period at the GI-05 cruise stations (brown circles). The background colored gridding in the Arabian Sea shows the surface dAl distribution observed in the late summer period (late August to early September; Measures and Vink, 1999), temporally closest (and before) to the sampling period of this study (late September to early October). Surface dAl levels (white circles) reported by Thi Dieu Vu and Sohrin (2013) in the nearby equatorial Indian Ocean regions are also plotted for comparison (see text for more details).

and Vink (1999) in the AS during the late southwest monsoon period (late August to early September), closest to (and before) the sampling season (late September to early October) of this study (Fig. 4.4). The two datasets compare well in most of the regions except in the northwest AS, where our measured surface dAl concentrations are significantly lower (Fig. 4.4). This difference probably indicates the influence of the changing meteorological setting, during the transition between the two seasons (summers to fall intermonsoon; see section 4.2 and section 4.4.1 for further discussion), on surface dAl distribution. The surface dAl levels observed by Narvekar and Singbal (1993; ~40-130 nmol kg^{-1}) and Upadhyay and SenGupta (1994; ~40-75 nmol kg^{-1}) in the eastern AS are higher by one or two orders of magnitudes than that observed (~6-20 nM) during the German and US-JGOFS (Measures and Vink, 1999; Schüβler et al., 2005), Japanese GEOTRACES (Thi Dieu Vu and Sohrin, 2013) and this study at nearby stations. Although this mismatch may arise due to probable systematic error or contaminations, the possibility of significant interannual variations in the surface dAl concentrations could not be ruled out.

Further south in the western equatorial region (5°S-10°N), a relative increase in the surface dAl concentrations (3.8-6.6 nM) was observed (Fig. 4.4). There is no previous report on dAl in the western equatorial region; however, elevated surface dAl in this region may indicate distinct dust source and/or internal cycling of dAl (refer section 4.4.1).

4.3.2 dAl in the sub-surface waters

In this section, the important dAl variations (and related changes in ancillary parameters) observed below the surface mixed layer (>50 m) in the studied regions are briefly highlighted. A sharp increase in dAl concentration (~3 times the dAl level in the water column above) is observed over the continental shelf (80 m) of the eastern AS (GI-05/1, Fig. 4.2B). This signal decreases steeply towards the open sea region (GI-05/3 and 4, Fig. 4.2B), indicating rapid removal of dAl close to the shelf region itself. The dAl variations observed in the thermocline depths (50-300 m) of the central and north-western AS regions (stations GI-05/5 to GI-05/8, Fig. 4.2B) are noteworthy. At these stations, elevated dAl levels in the depth range of 75-100 m (γ^n ~ 24.5-25.0 kg m^{-3}) correlates to the observed salinity maxima of the ASHSW (Fig. 4.2A and 4.2B). A marked dAl-high is also observed at the core depth range (200-300 m, γ^n ~ 26.2–26.8 kg m^{-3}, Fig. 4.2B) of the PGW at stations GI-05/6 and 7. Further towards the southern AS and the western equatorial Indian Ocean (GI-05/10 to GI-05/18), the dAl distribution in the thermocline water depths (100-800 m) becomes more uniform (Fig. 4.2B).

In the deeper water depths (>1000 m), dAl profiles in the AS demonstrate some interesting features. Station GI-05/8 lies adjacent to the southwest-northeast aligned Murray Ridge in the northern AS (Fig. 4.3). Highly enriched dAl levels (~5-13 nM) are observed in the deep waters close to the Murray Ridge (GI-05/8, Fig. 4.2B), focused around 1200 m and 2500 m depths. Distinct deep-water dAl maxima (~2000-2500 m) were also observed in the central AS region (GI-05/5 and 6; Fig. 4.2B). An increase in the dAl concentrations is evident close to the seafloor over the Carlsberg Ridge (GI-05/12, 13 and 14; Fig. 4.2B).

4.4 Discussion

4.4.1 dAl in the surface mixed layer

Surface dAl concentrations have shown strong seasonal and intra-basin variations in the AS (Measures and Vink; Schüβler et al., 2005; Thi Dieu Vu and Sohrin, 2013). For readers to appreciate these observed spatio-temporal variations of surface dAl in the AS, the surface dAl data from current along with previous studies have been compiled and plotted in Fig. 4.5. These variations are majorly attributed to the changes in the source regions of aerosols over the Sea and dAl scavenging rates due to seasonal changes in wind patterns and biological productivity, respectively (Measures and Vink, 1999; Schüβler et al., 2005). Seasonal variation in the surface-mixed layer thickness also plays an important role in the vertical re-distribution of the Al input from atmospheric dust deposited and/or other sources in the surface ocean layer. Significantly lower surface dAl levels observed towards the northern and in the north-western AS (GI-05/6, 7 and 8; Fig. 4.4) during the fall inter-monsoon (this study), compared to that reported during the late southwest monsoon (Measures and Vink, 1999), hints at the impact of changing meteorological, and related hydrological conditions (refer section 4.2), on the surface dAl distribution. During the southwest monsoon, the coeval development of the low-level 'Findlater' wind jet and the regional Summer Shamal and the Red Sea winds facilitates a massive emission and transport of

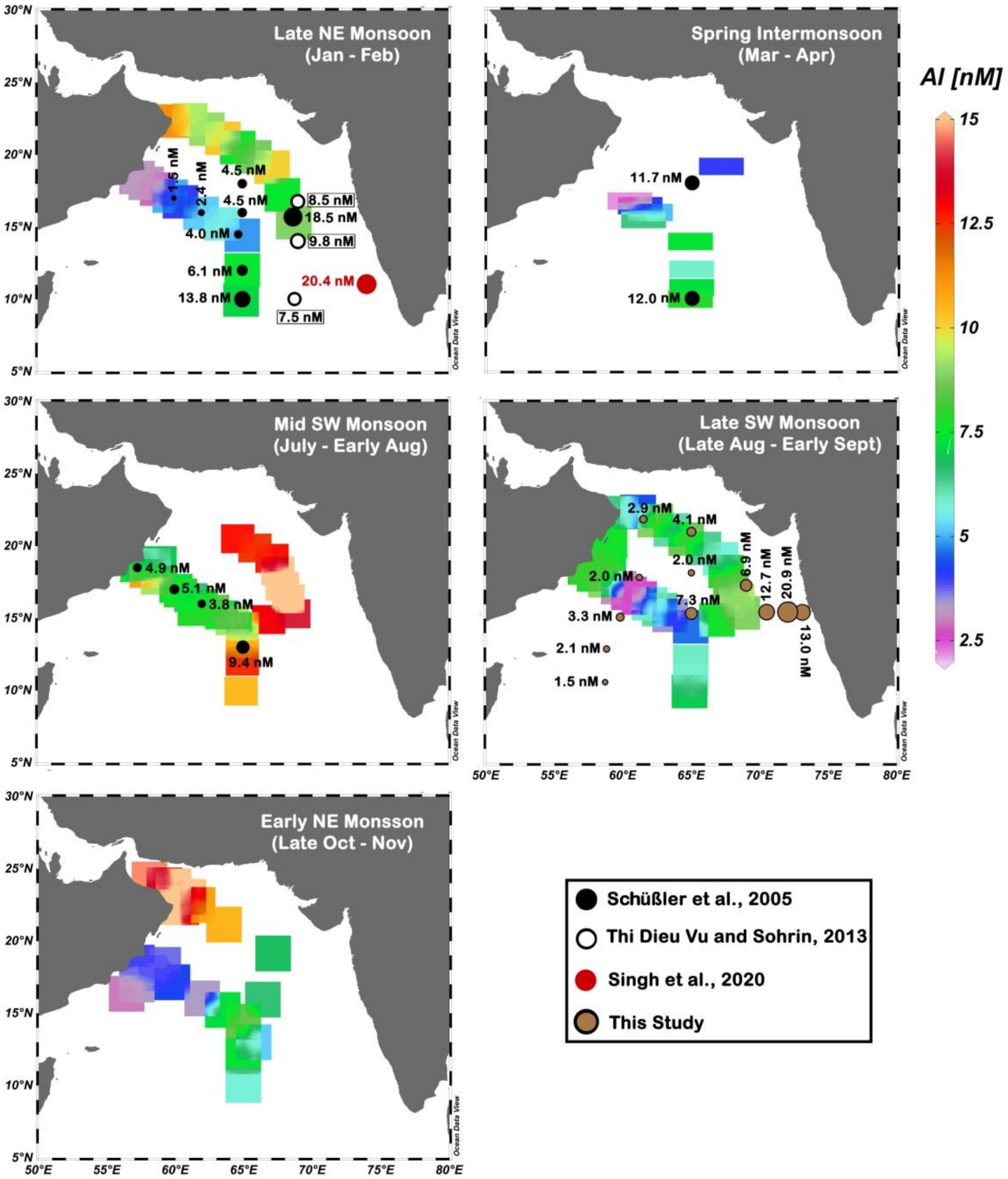

Fig. 4.5: The observed spatio-temporal variations in the surface dAl distribution in the Arabian Sea. The background colored gridding in the Arabian Sea shows the surface dAl distribution observed by Measures and Vink (1999) during different seasons. Data sources: Measures and Vink (1999), Schüβler et al. (2005), Singh et al. (2020), Thi Dieu Vu and Sohrin (2013).

mineral dust from the arid regions of the southern Arabian Peninsula and northeast Africa (Nubian Desert) to the north and north-western AS (Léon and Legrand, 2003; Ramaswamy et al., 2017). As the southwest monsoon ends, a significant decrease in the wind stress and change in wind direction occurs, which results in a reduction of the continental mineral dust emission (Léon and Legrand, 2003) and, presumably, its subsequent transport to the north and north-western AS. This reduction in the dust input may manifest as the corresponding (observed) decrease in the surface dAl concentrations during the fall inter-monsoon (this study, Fig. 4.4). Also, relatively high biological productivity in the north and north-western AS throughout the southwest monsoon, presumably, ensures effective Al removal by biogenic particles from the surface waters. This process would inhibit the high surface-dAl signal observed in the northern AS during the southwest monsoon (Measures and Vink, 1999) to sustain in the following season (fall inter-monsoon) as the atmospheric Al input in the region decreases. These arguments are also supported by the modeling results in the western AS and discussed later in the text (section 4.4.1.1). On the other hand, relatively elevated surface dAl concentrations in the eastern AS (12.7-20.9 nM at stations GI-05/1, 2 and 3; Fig. 4.4) propose a different balance between the input and removal processes. Unlike the western AS (west of 60°E), where the mean annual rainfall is very small (<0.4 m yr^{-1}, Kumar and Prasad, 1997), the eastern AS (east of 65°E) receives considerable precipitation (annual mean: ~1.0-1.5 m yr^{-1}, Kumar and Prasad, 1997; Behara et al., 2019), particularly during the summers (June-September, refer to Figure 1c and 1d of Behara et al., 2019). These circumstances favor the wet deposition of a large amount of mineral dust, derived from the Middle-East and northeast African desert regions, over the eastern AS during the summers (June-September, Ramaswamy et al., 2017; Kumar et al., 2020). Further, the relative estimates of column-integrated net primary productivity (NPP), from both the *in situ* measurements (Barber et al., 2001; Kumar et al., 2000) and satellite-based data (Behrenfeld and Falkowski, 1997; Eppley-VGPM NPP data, Custom Product; Available at the website: http://sites.science.oregonstate.edu/ocean.productivity/index.php; also refer to Fig. 4.6), show relatively lower NPP values for the eastern AS compared to that in the western AS, which may impact the surface dAl removal rate in the two regions. High surface dAl levels observed in the eastern AS in this study during the fall-intermonsoon season may therefore result due to high mineral dust deposition flux (mostly via wet deposition) in the preceding season (summer monsoon: June-September) and comparatively (to western AS) lower surface dAl removal rate owing to lower NPP during the summer and fall-intermonsoon period (July-October, Fig 4.6).

Compared to the western AS, the western equatorial (5°S-<10°N) Indian Ocean show elevated surface dAl concentrations (3.8-6.6 nM, Fig. 4.4). These values are also higher than that observed further east in the equatorial region (~3.0 nM at station ER-8, Fig. 4.4), which implies additional local Al input towards the western equatorial boundary. Earlier studies (Tindale and Pease, 1999; Clemens et al., 1991; Léon and Legrand, 2003) have recognized that arid regions of the Somali coast could be potential sources of dust to the north-western Indian Ocean under the influence of the Findlater Jet, which develops

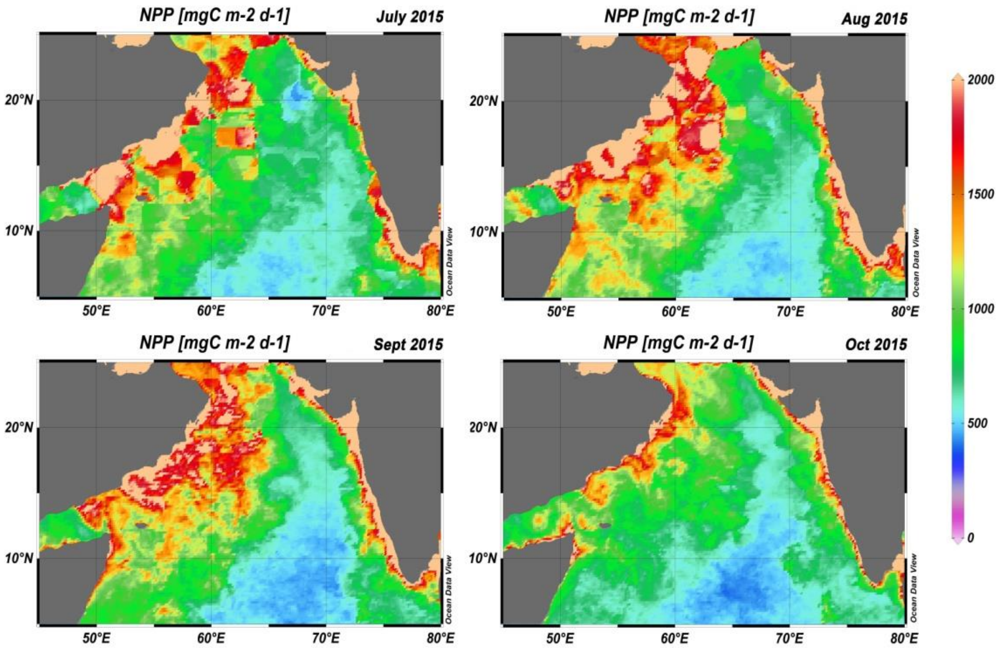

Fig. 4.6: Satellite-data (Behrenfeld and Falkowski, 1997; Eppley-VGPM NPP data, Custom Product, http://sites.science.oregonstate.edu/ocean.productivity/index.php) based variation in net primary production (in mgC m^{-2} d^{-1}) in the AS during the summers (July-September) and fall-intermonsoon period (October).

during the southwest monsoon. Pease et al. (1998), based on their study on dust concentration and its geochemistry over the AS, concluded that the dust emission from the Somali coast does not influence the aerosol composition over the AS. However, there is no such study to evaluate the presumed impact of the Somali dust transport in the western equatorial Indian Ocean (south of 5°S and west of 65°E). In this study, the observed increase in surface dAl levels in the western equatorial region may suggest the influence of dust emission from the Somali coast to be more local (restricted to the western equatorial region). Moreover, due to lower (compared to the AS) biological productivity in the equatorial and subtropical Indian Ocean, the surface dAl residence time estimates (1-2 yr; Han et al., 2008) are relatively high in these regions. Therefore, the observed surface dAl concentration would represent an integrated signal of atmospheric dust deposition over a larger span of time in these regions.

4.4.1.1 Modeling seasonal variations of surface dAl in the AS

The observed temporal changes in the measured surface dAl concentrations (this study; Measures et al., 1999; Schüβler et al., 2005; Singh et al., 2020; Thi Dieu Vu and Sohrin, 2013) in the AS suggest that surface dAl distribution in the sea is not in a steady-state, at least in seasonal time scales. Therefore, models considering the temporal variations of surface dAl in the AS would be more realistic. Global ocean model studies (e.g., Gehlen et al., 2003; Han et al., 2008) have estimated annual averaged distribution of surface dAl, which shows high relative errors compared to the observed dAl in the surface waters of the AS. In this section, the seasonal variations in surface dAl in the AS are modeled using a simple 1-D, non-steady-state formulation. The structure and assumptions used in the model are described in the following text.

Deposition (dry and wet) and subsequent partial dissolution of atmospheric dust is considered as the external source of dAl to the surface waters of the AS. Removal of Al from the water column is assumed to be first-order with respect to the dAl (i.e., the removal rate is proportional to the observed dAl). If we also take into account the influence of water advection and turbulent mixing on the dAl distribution, mathematically, the temporal changes in dAl in the surface-mixed layer can be described as follows:

$$\frac{\mathbf{d[dAl]}}{\mathbf{dt}} = \frac{\mathbf{C^{Al}_{dust}}.(\mathrm{V_d}+\mathrm{R.S_r}).\mathbf{f^{Al}_{sol}}}{\mathbf{MLD.A^{Al}_{wt}}} - \frac{\mathbf{[dAl]}}{\mathbf{\tau}} - \nabla.(\mathbf{v}[\mathbf{dAl}]) + \nabla.(\mathbf{D}\,\nabla[\mathbf{dAl}]) \qquad (4.1)$$

where **[dAl]** is the dissolved Al concentration (in µmol m^{-3} ≡ nM) in the surface mixed layer, $\mathbf{C^{Al}_{dust}}$ is the concentration of Al in the aerosol (in µg m^{-3}), $\mathbf{V_d}$ is the dry dust deposition velocity (in m d^{-1}), **R** is the precipitation rate (in m d^{-1}), $\mathbf{S_r}$ is the dust washout ratio (i.e., the ratio of Al concentration in rain and aerosol), $\mathbf{f^{Al}_{sol}}$ is the fractional Al solubility from the dust, **MLD** is the mixed layer depth (in meters), $\mathbf{A^{Al}_{wt}}$ is the atomic mass of Al (in g mol^{-1}) and $\boldsymbol{\tau}$ is the scavenging residence time (in days) of dAl in the surface ocean. The third ($\nabla.(\mathbf{v}[\mathbf{dAl}])$) and the fourth ($\nabla.(\mathbf{D}\,\nabla[\mathbf{dAl}])$) terms on the right-hand side of the Eq. (4.1) represent the effect of water advection and turbulent mixing, respectively, on the mixed layer dAl. Previous studies (Baker et al., 2016; van Hulten et al., 2013) compared the estimated residence times for dAl with respect to particle scavenging (τ_s) and water advection timescale (τ_a) in the surface waters of the AS and showed that the later is relatively very large compared to the former (i.e.,$\frac{\boldsymbol{\tau_a}}{\boldsymbol{\tau_s}}$ >>1), particularly for the northern and western regions of the sea (Baker et al., 2016). This result suggests that the relative influence of advection and diffusive mixing on surface dAl distribution in the AS could be considered negligible (Baker et al., 2016). Considering the above arguments and neglecting the advection-turbulent mixing terms, Eq. 4.1 could be simplified as follows:

$$\frac{\mathbf{d[dAl]}}{\mathbf{dt}} = \frac{\mathbf{C^{Al}_{dust}}.(\mathbf{V_d}+\mathbf{R.S}).\mathbf{f^{Al}_{sol}}}{\mathbf{MLD.A^{Al}_{wt}}} - \frac{\mathbf{[dAl]}}{\boldsymbol{\tau}} = \mathbf{dAl^{atm}_{input}(t)} - \frac{\mathbf{dAl}}{\boldsymbol{\tau}} \qquad (4.2)$$

To estimate the time-dependent atmospheric dAl input function (i.e., $\mathrm{dAl^{atm}_{input}(t)}$), knowledge of temporal variations in $\mathbf{f^{Al}_{sol}}$,$\mathbf{V_d}$, **R**, **S** , $\mathbf{C^{Al}_{dust}}$ and **MLD** is required. The data available on aerosol Al concentration $(\mathbf{C^{Al}_{dust}})$ from the earlier studies (Tindale and Pease, 1999; Siefert et al., 1999; Kumar et al., 2008, also refer to compiled data in Table C1 in Appendix C) is used to estimate the seasonal variations in $\mathbf{C^{Al}_{dust}}$. Given that the dataset available on

$\mathbf{C_{dust}^{Al}}$ for the AS is limited (refer to Fig. 4.7), it is crucial to choose the space of model application in a way such that maximum temporal variability could be defined. Seasonal studies on aerosol Al composition are more extensive for the western part of the AS (west of 65°E), as apparent from Fig. 4.7. Moreover, significant latitudinal variations in aerosol Al concentration are observed for a given time period in the AS; aerosol Al concentration is significantly high in the northern region compared to the central and southern regions (Tindale and Pease, 1999; Pease et al., 1998). Therefore, to have a better temporal resolution for $\mathbf{C_{dust}^{Al}}$, dAl distribution is modeled in the west-central part of the sea, i.e., in the region 14-20°N, 57-65°E (Fig. 4.7). The majority of the compiled data comes from the US-JGOFS study on aerosol composition over the AS (Tindale and Pease, 1999) and, therefore, seasonal mean (geometric) values for $\mathbf{C_{dust}^{Al}}$ were estimated following the temporal divisions of major seasons defined

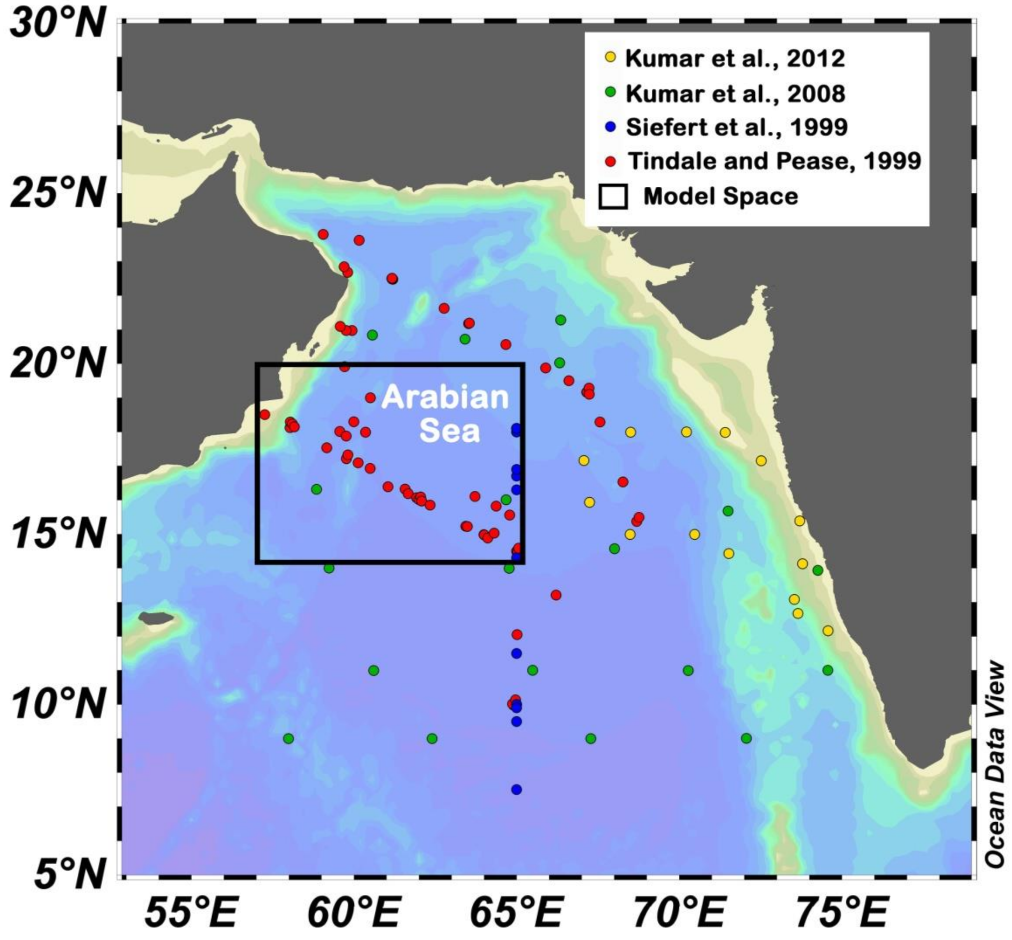

Fig. 4.7: Aerosol sampling locations from the previous studies used for the compilation of aerosol Al concentration over the AS. The model space over which the seasonal variations in surface dAl are simulated is also shown.

in that study (Table C1 in Appendix C). Note that outliers (data points outside the 2σ range of the seasonal averages) in the compiled data $\mathbf{C_{dust}^{Al}}$ were removed before calculating the seasonal means.

A dry deposition velocity ($\mathbf{V_d}$) of ~0.9 cm/sec for mineral aerosol deposition over the AS was estimated during the spring-intermonsoon period using aerosol ^{210}Pb as a tracer (Sarin et al., 1999). There are no studies on seasonal changes in the dry deposition velocities of aerosols over the AS. However, Tindale and Pease (1999) indicated that the deposition velocity of mineral dust during the summer monsoon could be relatively high. Due to limited studies on seasonal variations of dry deposition velocity, here, $\mathbf{V_d}$ is considered to be 0.9 cm/sec (≈777 m d^{-1}, Sarin et al., 1999) and constant throughout all the seasons except for the summer monsoon (discussed later in this section). Estimated and observed seasonal changes in precipitation over the AS (Kumar and Prasad, 1997; Measures and Vink, 1999; Schott et al., 2009 and references therein) indicate that rainfall events mostly occur during the summer monsoon period (June-August) and are low or negligible for rest of the seasons (2-7 times lower rainfall than the summer monsoon, Kumar and Prasad, 1997). Moreover, the central and western AS (our model space) receives the lowest rainfall throughout the year (Kumar and Prasad, 1997; Schott et al., 2009 and references therein). Also, as per our knowledge, there is no report on the wet deposition of atmospheric Al in the western AS. Therefore, due to limited rainfall and no available estimates on the wet deposition fluxes of atmospheric Al in the western AS, we considered only dry deposition of Al in our model (i.e. $(\mathbf{V_d} + \mathbf{R.S_r}) \approx \mathbf{V_d}$ in Eq. (4.2)).

As noted earlier (section 4.4.1), the development of strong surface winds (the Findlater Jet, the Summer Shamal and the Red Sea winds) during the summer monsoon aids the deflation and transport of a huge amount of mineral dust from the deserts of the southern Arabian Peninsula and northeast Africa to the western AS (Léon and Legrand, 2003; Ramaswamy et al., 2017). It is also directly or indirectly represented by the observed/estimated elevation in (1) dust activity over the southern Arabian Peninsula and northeast Africa (Léon and Legrand, 2003), (2) satellite signals of dust load over the AS (Husar et al., 1997; Ramaswamy et al., 2017), and (3) surface dAl concentrations (Measures and Vink, 1999). Contrary to these results, the lowest surface-level atmospheric mineral dust concentrations over the AS are observed during the summer monsoon (June-August; Pease et al., 1998; also refer to Table C1 in Appendix C). To resolve this apparent contradiction, Tindale and Pease (1999) suggested the mechanism of intense scavenging of continental dust by sea-salts during the summers, which is described here briefly. A large proportion of surface-level air mass over the AS during the summers is derived from the pristine marine regions of the equatorial and subtropical Indian Ocean, which bring a huge amount of sea-salts to the AS (Pease et al., 1998; Tindale and Pease, 1999). The high influx of sea-salts dilutes the mineral dust levels in the surface-level aerosols (Tindale and Pease, 1999). However, these sea-salt particulates are also observed to form large aggregates with the mineral dust particles (Tindale and Pease, 1999), which may deposit at increased settling velocities (deposition velocity). Moreover, as estimated by the satellite data, a thick layer of mineral dust resides over the surface-level, sea-salt rich aerosol layer over the AS during the summer monsoon (Ramaswamy et al., 2017), which may also contribute to the net mineral dust deposition (mainly via wet deposition during the summers; Ramaswamy et al., 2017). Therefore, the estimates of mineral dust deposition flux (and hence Al deposition flux) during the summer monsoon based on the surface-level dust concentrations and the dry deposition velocity estimated during the spring-intermonsoon (Sarin et al.,1999) may be highly underestimated. Schüβler et al. (2005) calculated the atmospheric Al dry deposition flux during the summers by using the time-averaged Al flux estimated for the non-summer monsoon periods and multiplying it with the ratio of aerosol optical thickness observed during the summer monsoon and non-summer monsoon periods. This gave an effective Al dry deposition flux of 81 µmol m^{-2} d^{-1} during the summer monsoon. Moreover, this modified estimate agrees well with the (high) deep water Al particle flux observed in the AS during the summer monsoon (Schüβler et al., 2005) and, therefore, was used to estimate the atmospheric dAl input in the model space during the summers. For the rest of the seasons, the atmospheric dAl inputs were calculated using the dry deposition velocity estimated by Sarin et al. (1999; 0.9 cm sec^{-1}) and seasonal mean (geometric) of Al concentration in the surface-level aerosols (Table 4.1). Among all the seasons, the lowest resolution on aerosol Al concentration data is for the autumn (fall intermonsoon) period (Table C1 in Appendix C).

Han et al. (2008) estimated a relatively short residence time ($\boldsymbol{\tau}$: ≤0.5 yr) for dAl in the western AS surface waters and showed an improved match between modeled and observed annual mean surface dAl levels, compared to other modeling studies (Gehlen et al. 2003; Measures and Vink, 2000). Similar estimates (0.4-0.8 yr) are also given by van Hulten et al. (2013). However, as noted earlier, the biogenic particles are the main carrier phase for the scavenged dAl in the ocean. Therefore, it is reasonable to expect a temporal variability in $\boldsymbol{\tau}$, in a given region, with seasonal changes in the net primary productivity (NPP). The AS experiences a strong seasonality in primary productivity (McCreary et al., 1996), which may impact the scavenging residence time of surface dAl. Therefore, the surface dAl were modeled considering τ to be temporally varying. The temporal variations in τ are estimated by normalizing the mean $\boldsymbol{\tau}$ (i.e., 0.5 yr) with changes in NPP in the modeled region (refer to Appendix D). SeaWiFS satellite data-based monthly averaged NPP estimates were extracted and used for normalizing the mean τ. Since the majority of the data for aerosol Al and surface dAl concentrations are taken from the US-JGOFS study carried out in the year 1995 (Tindale and Pease, 1999), it is reasonable to use NPP data from the same year. However, the oldest available SeaWiFS satellite-based NPP data is for the year 1998 and is used in the model.

An optimal fractional Al solubility from the Al minerals in the dust ($\mathbf{f_{sol}^{Al}}$) of 0.03 (i.e., 3%) has been considered by earlier studies in the AS (Gehlen et al., 2003; Schüβler et al., 2005). However, no studies on direct estimation of Al solubility by aerosol leaching experiments (with de-ionized water, seawater or buffer solution; Berger et al., 2018) are available in the AS. Therefore, Al fractional solubility was optimized by minimizing the error (root mean square) between the mean observed and modeled surface dAl during different seasons. The optimized Al fractional solubility is found to be 3.5%, which is similar to that considered by the earlier studies (3 %, Gehlen et al., 2003; Schüβler et al., 2005). Average seasonal MLD values were estimated using the monthly mean MLD (climatological and density threshold-based) data extracted from the available global database (Holte et al., 2017).

Using the above constraints on $\mathbf{f_{sol}^{Al}}$, $\mathbf{V_d}$, $\mathbf{C_{dust}^{Al}}$ **and MLD**, seasonal variability of dAl input from the atmosphere ($\text{i.e.}, \frac{\mathbf{C_{dust}^{Al}.V_d.f_{sol}^{Al}}}{\mathbf{MLD.A_{wt}^{Al}}}$ in µmol m^{-3} d^{-1}) to the model space was estimated and plotted (and tabulated) in Fig. 4.8A (Table 4.1). Further, this input function was assumed to be an annual periodic function (i.e., time period=365 days) and fitted using a finite Fourier series (Fig. 4.8A; refer

Table 4.1: Estimated seasonal means of Al concentration in surface-layer aerosols, atmospheric Al deposition flux, MLD and dAl input in the mixed layer from the atmospheric dust deposition.

Season	Al in surface-level aerosols (ug m^{-3})	Deposition Velocity (Vd) (cm s^{-1})	Atm. Al deposition flux (µmol m^{-2} d^{-1})	Fractional Al solubility	Seasonal mean MLD (m)	Seasonal mean of atm. dAl input (µmol m^{-3} d^{-1})
Late Winter	0.58	0.90	16.58	0.035	59	0.0098
Spring	0.56	0.90	16.08	0.035	21	0.0265
Summer	0.03	-	81.00*	0.035	49	0.0581
Autumn	0.37	0.90	10.64	0.035	25	0.0149
Early Winter	0.61	0.90	17.59	0.035	45	0.0136

* Corrected atmospheric Al deposition flux during the summer monsoon period estimated by Schüβler et al. (2005;see text for further explanation)

to Appendix D for details). Such a formulation helped represent the seasonal variations in the dAl input as a continuous, periodic function and derive a stable analytical solution for the Eq (4.2) (refer to Appendix D for details). The basis of assuming the annual periodicity is a small observed inter-annual variability in aerosol Al concentration over the AS (Schüβler et al., 2005 and references therein).

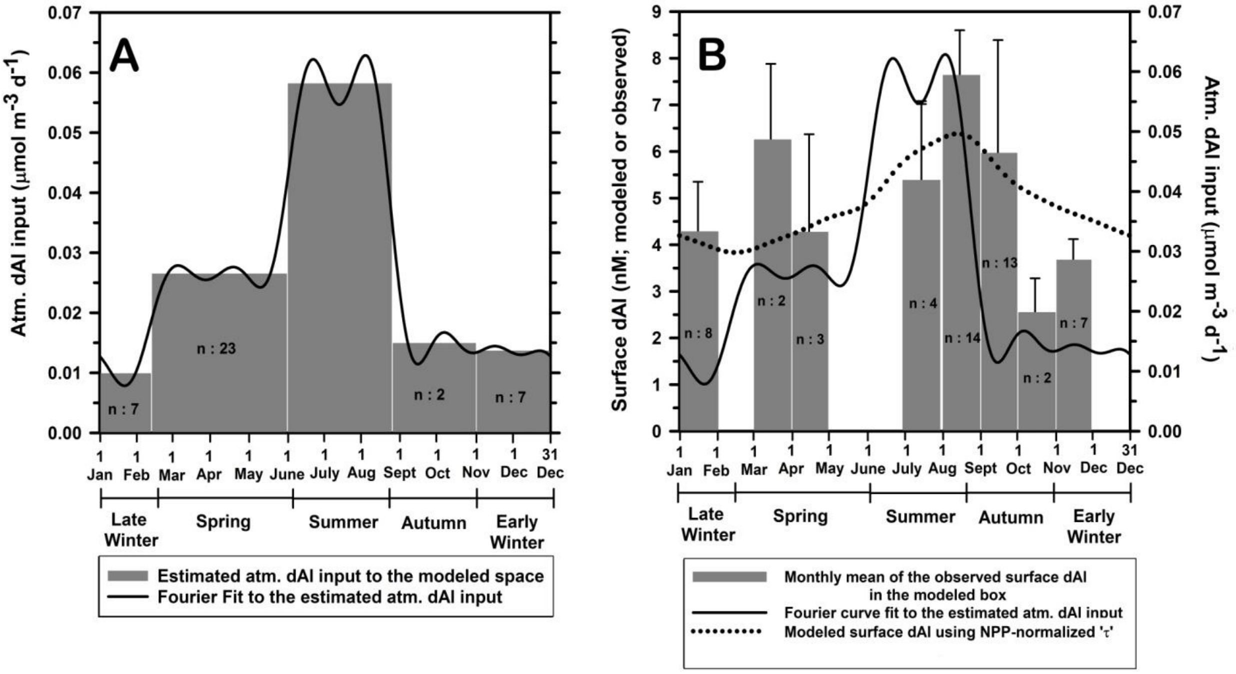

Fig. 4.8: (A) Bar plot for the estimated seasonal means of the atmospheric dAl input ($\mathbf{dAl_{input}^{atm}}$). The number of data points that are used to evaluate the seasonal mean of Al concentration in surface-level aerosols is also shown inside the bar for each season. The overlaid solid black line represents the finite Fourier series fit to the $\mathbf{dAl_{input}^{atm}}$ variation, considering it to be annual periodic (see text). Also, note that the $\mathbf{dAl_{input}^{atm}}$ for the summer season is estimated using the corrected Al atmospheric flux calculated by Schüβler et al. (2005; see text); therefore, the number of data points is not indicated for the summer season bar. (**B**) Model solutions considering the constant (dashed line) or temporally variable, NPP-normalized (dotted line) dAl residence time ($\boldsymbol{\tau}$). Bar plot shows the observed surface dAl concentrations in different months. For reference, the estimated (Fourier curve fit) $\mathbf{dAl_{input}^{atm}}$ (solid line) is also plotted.

Fig. 4.8B shows the comparison between the observed and modeled temporal dAl variations in the model space. The observed temporal changes in the surface dAl concentrations were estimated from the available data (this study; Measures and Vink, 1999; refer to Table C2 in Appendix C). Model solution is compared to the observed surface dAl distribution in the modeled region (Fig. 4.8B). Overall, the model results are able to capture the general seasonal trend observed for surface dAl in the modeled region of the AS. The modeled surface dAl levels are also of the same order as measured (Fig. 4.8B). Similar to the observed trend, the model dAl concentrations show an increase after the winter period during the spring season and peak in the summers (Fig. 4.8B). Subsequent decrease, from the peak levels, in the modeled dAl levels is seen during the transition from the summer monsoon to the fall inter-monsoon (autumn) period; in agreement with the observed surface dAl trend (Fig. 4.8B). Also, note that the model surface dAl distribution follows the variations in the estimated dAl input from the atmosphere with a time lag, which depends on the dAl residence time (Fig. 4.8B).

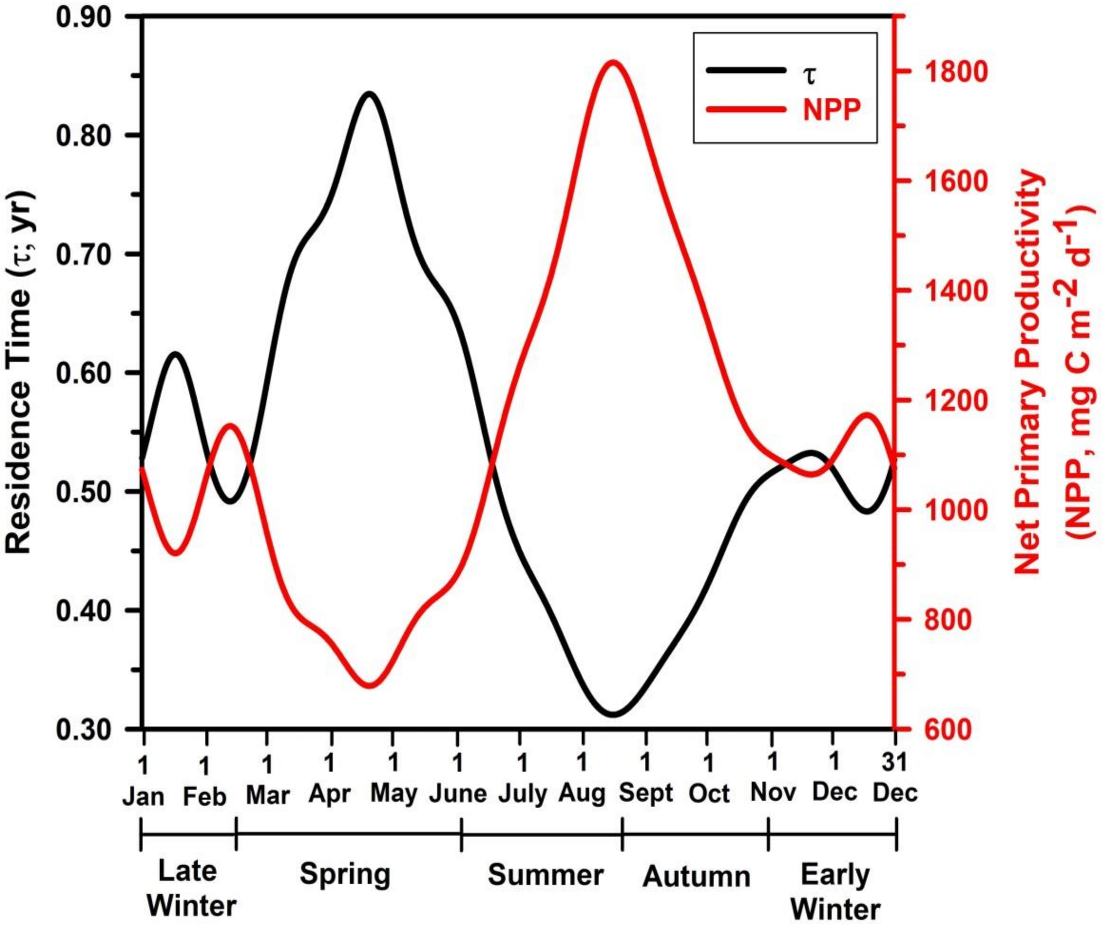

Fig. 4.9: Estimated temporal variations in the net primary productivity (NPP) and dAl residence time (also refer to the Appendix D for more details).

continuous increase in modeled dAl is derived under the increasing atmospheric dAl input towards the summers (Fig. 4.8B). In contrast, the lowest estimated **τ** during the summers (due to the highest estimated NPP values, Fig.

4.9) led to rapid removal (and decline) of modeled surface dAl and, relatively, lower (but closer to observed values) estimated dAl levels during the autumn compared to the constant **τ** model solution (Fig. 4.8B). It should also be noted that the resolution of observed dAl is lowest during the inter monsoon seasons (spring and autumn, Fig. 4.8B). More data on surface dAl in these seasons is needed to bring out a better picture of dAl seasonal variations and a stricter validation of the model.

4.4.2 Influence of intrusion of the ASHSW and marginal seas water masses on the dAl distribution in the AS

Formation of the high salinity waters in the marginal seas (the Persian Gulf and the Red Sea) and the northern AS, and their spread into the sub-surface depths (~25-1000m) of the open AS regions are well documented (Shenoi et al., 1993; Wyrtki, 1973; Shetye et al., 1994; Schott and McCreary, 2001). In the intermediate and deep waters, the dAl scavenging removal timescales are relatively large than the surface layer (few weeks to 4 yrs in surface vis-á-vis 50-200 yrs in deep waters, Orians and Bruland, 1986) owing to change in marine particulate matter abundance in the water column, particularly biogenic phases, which act as carriers of the scavenged Al. Therefore, the preformed (i.e., source region) dAl signals of the marginal seas and northern AS water masses (ASHSW, PGW and RSW) may be transported to regional (or intra-basin) distances as they intrude into the thermocline depths and influence the dAl distribution in the open AS.

Both the Red Sea and the Persian Gulf receive a high atmospheric dust input (on the order of 10-20 g m^{-2} yr^{-1}) sourced from the surrounding arid regions of the Arabian Peninsula and North Africa (Chen et al., 2008; Hamza et al., 2011; Torfstein et al., 2017). Elevated levels of crustally-derived elements (such as Al, Fe, Mn) in the aerosols and their subsequent deposition over (or close to) the marginal seas lead to the enrichment of these elements in the water column (Shriadah et al., 2004; Measures and Vink, 1999). The northern AS, where the ASHSW forms, also show a similar level of enrichment of Al in the aerosols compared to that observed over the Red Sea and the Gulf of Oman (Chester et al., 1985 and references therein; Chen et al., 2008). Relatively, elevated dAl concentrations observed at the core depth ranges of the ASHSW (50-100 m) and the PGW (200-300 m) at the central and north-western region of the AS (stations GI-05/5 to 8; Fig. 4.2A and 4.2B) indicate the impact of advection of these waters on the dAl distribution in the AS. However, this signal fades out, moving away from the water mass source region (the northern AS) towards the southern AS region (Fig. 4.2B), presumably due to the advective mixing and scavenging processes. Another interesting observation is the relative freshening of the PGW core salinity (~250m) at station GI-05/8, which is sampled closest to the source region, i.e., the Persian Gulf, compared to station GI-05/7, where the highest PGW core salinity (~250m, Fig. 4.2A) is measured. The high salinity at GI-05/7 is also correlated with the highest dAl enrichment observed at the PGW core depths (Fig. 4.2). Studies (Prasad et al., 2001; Wyrtki, 1971) have shown that this freshening of the PGW along the western AS occurs via the advection of relatively low-salinity equatorial thermocline waters (observe thermocline salinity distribution at stations south of GI-05/14, Fig. 4.2A) by the northward-flowing Somali Current and vertical mixing at the Somalia and Arabia coast due to upwelling, during the summer monsoon. This signal is still seemed to be preserved during the transition from the summer monsoon to the fall-intermonsoon (study period of this study). The low-salinity thermocline equatorial waters are, relatively, depleted in dAl concentrations (Fig. 4.2B) and, therefore, their mixing with the PGW waters dilutes its preformed dAl signal.

No enrichment in dAl concentrations is apparent in the potential density range (~27.0–27.4 kg m^{-3}, ~500–800 m, Shenoi et al., 1993) for the RSW. This may result from significantly diminished outflow (by ~30% from the mean annual outflow, Maillard and Soliman, 1986; Siedler, 1969) of the RSW to the AS during the summers and autumn period (July to October). Additionally, the possibility of dAl loss from the RSW along the advective pathway due to water mass mixing and scavenging is also there. Nevertheless, more studies are needed to better understand the relative influence of the advection of the high salinity water masses (ASHSW, PGW and RSW) on the dAl distribution in the thermocline water depths of the AS during different seasons.

4.4.3 Controls on dAl distribution in the deeper waters (>1000 m)

One of the highlights from the deep water dAl distribution in the studied regions is the highly enriched dAl levels observed close to the Murray Ridge (GI-05/8, Fig. 4.2B) in the intermediate (1200-1800 m) and deep waters (2500m). There are no previously reported dAl data around the ridge for comparison. The station GI-05/7 (this study, Fig. 4.2B), sampled at a similar latitude to the east (of the station GI-05/8), however, shows no such dAl anomalies. Moreover, similar water mass structures observed in the deeper depths (>1000m) of GI-05/8 and the adjacent station (GI-05/7, Fig. 4.2A) eliminates the possibility of an advective dAl source. These observations are suggestive of a localized source of dAl at GI-05/8, probably from the margin of the ridge. Partial dissolution of resuspended sediment and/or benthic flux of dAl-rich pore waters from the ridge margin may support the observed elevated levels of dAl. An essential prerequisite for the margin sediments to be a source of dAl is the availability of reactive Al phases, which may release (by dissolution or Al desorption) Al in the pore waters during sediment diagenesis or to the ambient seawater upon resuspension. Sediments deposited over the Murray Ridge show relatively high detritus proportion (42%; Weijden and Weijden, 2002), comparable to the average lithogenic fraction reported in the northern Bay of Bengal from the deep sediment trap data (39%, Unger et al., 2003). Reactive clay minerals (e.g., kaolinite, illite) in the lithogenic sediments may rapidly release Al on their interaction with the ambient seawater (Mackin and Swider, 1987; Köhler et al., 2003). Another sedimentary phase that may act as a potential source of dAl in the ambient waters to the sediment-water interface is the biogenic silica or opal. Biogenic opal is a major sink for dAl in the ocean water (Dixit and Van Cappellen, 2002; Dymond et al., 1997; Moran and Moore, 1988) and post-deposition to the seafloor, act as a nucleus for the rapid formation of authigenic aluminosilicate when exposed to Al-rich pore waters conditions (Koning et al., 2007). Al released due to opal dissolution or Al desorption from the sedimentary opal surface may also contribute to the dAl flux from the ridge margin to the ambient seawater. This hypothesis is supported by the fact that the highest opal reactivity (in terms of the opal dissolution rate constant) in the northern AS is estimated for those deposited over the Murray Ridge (Weijden and Weijden, 2002).

Another important observation is the presence of deep water (2000-2500m) dAl maxima in the central AS region (GI-05/5 and 6). For better understanding, the deeper water (≥1500 m) dAl data was compared with that reported earlier in the AS by the German-JGOFS study (Schüβler et al., 2005; Fig. 4.10). In the earlier study (Schüβler et al., 2005), deep-water (2000-3000m) dAl enrichment was observed close to the Carlsberg Ridge (at the stations M32-3/D3 and SO117/3; Fig. 4.10), which is comparable to that found in this study at the central AS (GI-05/5 and 6). Schüβler et al. (2015) suggested it to be originating

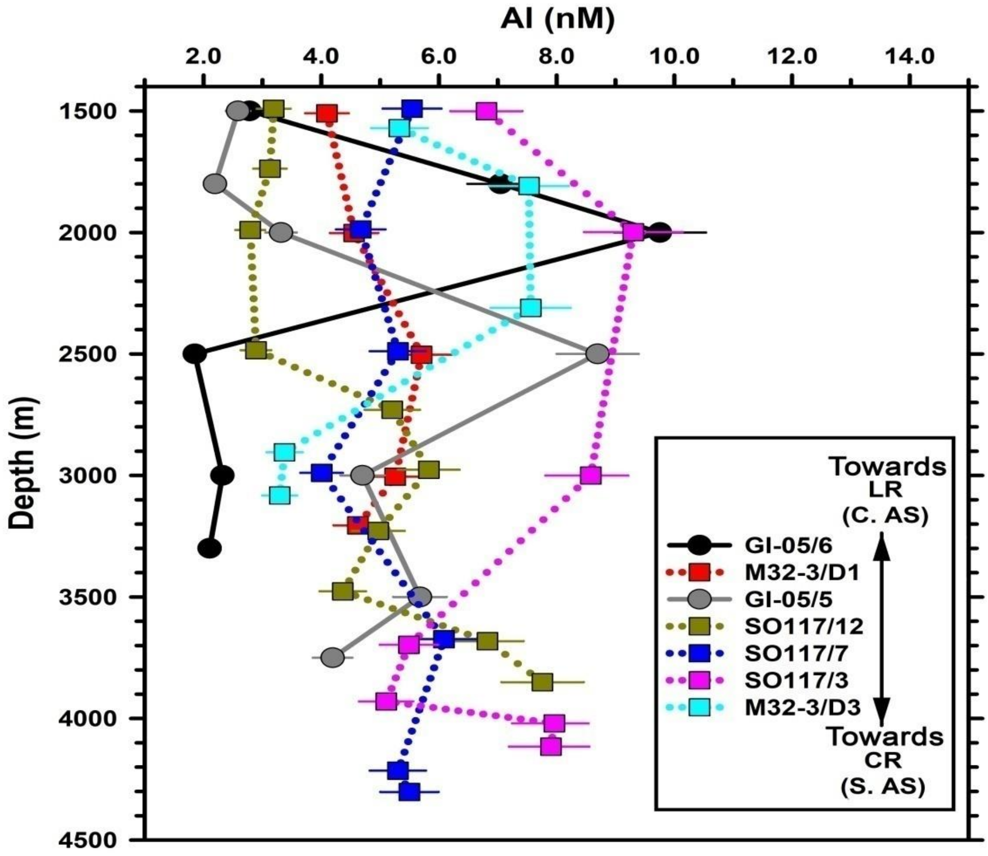

Fig. 4.10: Deep-water dAl distribution observed during this (solid line and circles) and German-JGOFS study (dashed line and solid squares; Schüβler et al., 2005) in the southern and central Arabian Sea. The relative spatial locations of the stations are indicated in the Legend. CR: Carlsberg Ridge, LR: Laxmi Ridge, S.AS: Southern Arabian Sea, C.AS: Central Arabian Sea.

due to the Al dissolution from the Carlsberg Ridge sediments. Away from the Carsberg Ridge, towards the central AS, the dAl concentrations in the deep-waters (>1500m) sampled during the German-JGOFS cruises, overall, show a significant decrease (at the stations SO117/7, SO117/12, M32-3/D1; Fig. 4.10), probably, indicating advective loss (due to mixing and scavenging) of the dAl signal. Such a trend may suggest that the advection of high dAl signal over the Carlsberg Ridge is not the primary source of dAl enrichment observed at the central AS in this study. Close to the Laxmi Ridge (station M32-3/D1, Fig. 4.3), a distinct deep-water dAl maximum was observed around 3000m (Fig. 4.10) during the German-JGOFS study, suggesting a local deep-water dAl source. The deep dAl maxima (around 2000-3000m) observed in the central AS (at stations M32-3/D1, GI-05/5 and GI-05/6; Fig. 4.10) may be sourced from the dAl input from the margin sediments of the nearby Laxmi Ridge that rises 1000-1500m above the adjacent abyssal plains. Apart from the ridge, several seamounts and guyot (e.g., the Raman Seamount, the Panikkar Seamount, Wadia Guyot) are also discovered in the nearby Laxmi Basin (Fig. 4.3). Deep-water interaction with the sediments over these seamounts may also result in the increase of dAl levels in the ambient waters that may advect to the stations where deep dAl maxima are observed. You (1999, 2000) has shown that significant dianeutral upwelling occurs across the deep-water layers (mostly above 3000m) in the central AS. One possible process leading to the deep-water interaction with the sediments over the Laxmi Ridge and other seafloor structures (seamounts and guyot) in the Laxmi Basin is the dianeutral upwelling of the deep-waters due to significant vertical turbulent flow (refer to Fig.7-10 of You, 1999) in relatively narrow Laxmi Basin, and subsequent overflow (of the deep-waters) across the ridge to the west in the central AS. However, this explanation remains speculative and requires high-resolution deep-water dAl investigations near the ridge regions to be validated.

4.5 Summary

Dissolved Al distribution in the surface waters of the AS shows strong seasonality and this study adds to the limited understanding of surface dAl cycling in the sea during the inter monsoon periods. A relative decrease observed in surface dAl levels in the western AS during the fall intermonsoon period (autumn, this study) compared to the summer monsoon is concluded to be resulting from a decrease in the mineral dust input from the surrounding sources in response to weakened monsoonal winds. This study presents the first attempt to simulate the temporal variations in surface dAl distribution in the AS (specifically, the western AS) using a simple 1D, non-steady-state model. Overall, our model results match well with the observed seasonal changes in the surface dAl concentration. Relatively, elevated surface dAl levels in the western equatorial Indian Ocean region suggest the influence of the dust emission from the Somali coast.

The outflows of the dAl-rich, high salinity water masses from the marginal sea (Persian Gulf) and the northern AS (ASHSW) are observed to carry their signature to the thermocline depths of the open AS. However, the spatial extent of the influence (on dAl distribution) of these water masses is found to be mostly restricted to the northern AS region during the sampling season (autumn or fall intermonsoon). The outflows of these water masses to the AS are highly seasonal; therefore, more studies are needed to investigate probable seasonal variability in the advective dAl input to the sea.

In the deeper waters (>1000 m) ambient to the Murray Ridge, a significant local input of dAl is observed, presumably, due to the Al release from the resuspended margin sediments. The deep-water dAl maxima (2000-2500m) observed in the central AS is hypothesized to be resulting from the deep-water interaction with the sediments over the nearby Laxmi Ridge, and seamounts and guyots present in the Laxmi Basin.

Chapter 5

The biogeochemical cycling of dissolved manganese in the Arabian Sea

5.1 Introduction

Mn is utilized as a trace nutrient by phytoplankton (Coale, 1991; Raven, 1990; Sunda, 2012). Major biological roles of Mn in phytoplankton are realized (1) in the water oxidizing component of the protein complex, photosystem-II (Raven, 1990), and (2) as an activator for the enzyme superoxide dismutase, required for the removal of reactive oxygen species that are produced during photosynthesis (Peers and Price, 2004). The relative abundance of bioavailable Mn in surface waters is observed to impact the biological production of and diversity in phytoplankton (Buma et al., 1991; Coale, 1991; Pausch et al., 2019). Redox cycling of Mn in the marine system set major controls on dissolved Mn distribution in the ocean water column (Klinkhammer and Bender, 1980; Lewis and Luther, 2000; Sunda and Huntsman, 1988). Mn may exit as Mn(II), Mn(III) or Mn(IV) across different phases (dissolved or particulate) in the marine system. Mn(III) and Mn(IV) are the stable redox forms in the oxygenated seawater and exist as insoluble Mn-oxides and oxyhydroxides (Sunda, 2012 and references therein). On the other hand, Mn(II) is more soluble but thermodynamically unstable in the oxygen-rich seawater and susceptible to get oxidized to Mn(III) and Mn(IV) by reacting with dissolved O_2 (Morgan, 2005). Kinetics of Mn(II) conversion to oxidized forms via homogeneous oxidation is, however, very slow (half-life ~500 yrs; Morgan, 1997). Mn(II) may also be transformed to insoluble Mn-oxides and oxyhydroxides through heterogeneous (on metal surfaces) or biotically-mediated oxidation (by extracellular proteins present in certain bacteria and fungi; Morgan, 2005; Tebo et al., 2005 and references therein), which proceed significantly faster (Morgan, 2005). In well-lit surface ocean waters, however, Mn-oxides and oxyhydroxides phases may prominently be reduced to Mn(II) through photo-reduction (Sunda and Huntsman, 1994). Moreover, biotically-mediated oxidation of Mn(II) is significantly inhibited in the presence of sunlight (Moffett, 1997; Sunda and Huntsman, 1988). In conclusion, the redox conditions and solar insolation over the ocean water column have prominent control on the partitioning of Mn into insoluble Mn(III) and Mn(IV) and more soluble Mn(II) oxidation states (Lewis and Luther, 2000; Johnson et al., 1996; Sunda and Huntsman, 1988; Sunda and Huntsman, 1994).

External sources of dissolved Mn (dMn) to the ocean include (1) atmospheric mineral dust (Baker et al., 2016), (2) rivers (Aguilar-Islas and Bruland, 2006), (3) reducing sediments of continental margins (Homoky et al., 2016; Lewis and Luther, 2000; Saager et al., 1989) and (4) hydrothermal fluids (Middag et al., 2011; Resing et al., 2015). Removal of dMn from the water column majorly proceeds through (1) heterogeneous and biotically-mediated Mn-oxidation (Sunda and Huntsman, 1988), and (2) bio-assimilation of Mn, and subsequent organic matter export (Johnson et al., 1996). The *in situ* produced Mn-oxide and oxyhydroxide phase also act as an important sink of other trace metals, including micro-nutrients such as Fe, Ni, Co, Zn (van Hulten et al., 2017 and references therein), in seawater and therefore, influence their cycling.

The Arabian Sea receives a large annual influx of atmospheric mineral dust (~5-17 g m^{-2} yr^{-1}; Schüβler et al., 2005) from the surrounding arid/semi-arid continental sources. Therefore, atmospheric dust deposition may act as a prominent source of dMn in the Arabian Sea surface waters. One of the objectives of this chapter is to estimate the dMn input fluxes across the Arabian Sea from the atmospheric dust deposition. The Arabian Sea is also characterized as a region of high primary production (Kumar et al., 2000; Marra and Barber, 2005). The relative role of bio-assimilation in removing surface dMn vis-á-vis removal through Mn-oxidation is crucial to estimate for better understanding of biogeochemical cycling of Mn and other trace-nutrients in the Arabian Sea water column. High primary production and subsequent export of organic matter out of the surface waters fuel the bacterial degradation (remineralization) of organic matter in the Arabian Sea sub-surface waters. Consumption of dissolved oxygen during the remineralization of organic matter results in the formation of an oxygen-deficit (suboxic, dissolved oxygen < 5µM) zone in the thermocline waters (~200-1000 m) of most of the Arabian Sea (Morrison et al., 1999; McCreary et al., 2013). Intense organic matter remineralization and inadequate ventilation of thermocline waters lead to the development of a perennial denitrification zone in the east-central region of the Arabian Sea (Naqvi,1991; Fig. 5.1). Redox changes in the upper water column (0-1000m) may play significant role in the internal cycling of dMn in the Arabian Sea and remobilization of Mn from the continental shelf and slope sediments to the ambient ocean water column. Further, the presence of several hydrothermally active sites over the spreading ridges in the Arabian Sea and adjacent marginal seas (Gamo et al., 2015; Jean-Baptiste et al., 1990; Ray et al., 2012) could influence the deep-water dMn distribution through the injection of hydrothermal fluids

5.2 Hydrography

The circulation pattern and the water mass structure of the upper water column (0-1000 m) in the Arabian Sea are significantly affected by the seasonally reversing monsoon meteorology over the sea during the summers (June-August) and winters (November-February). Seawater samples for this study were collected during the late winter period (January-February) when strong north-easterly wind stress is generally in effect over the Arabian Sea (Schott and McCreary, 2001). The presence of the westward flowing North Monsoon Current (NMC) is evident during the study period along the southern Arabian Sea, which bifurcates into another northward branch flowing along the west coast of India (Fig. 5.1 and 5.2). The NMC transports the low-salinity Bay of Bengal (BoB) surface waters to the south-eastern Arabian Sea (Kumar et al., 2004; Schott et al., 2009) as apparent from the relatively lower surface salinity (34.31-34.71) observed at stations GI-06(B)/4 and 5 (Fig. 5.3a). Another important physical feature captured along the southern Arabian Sea is the presence of westward drifting anti-cyclonic, mesoscale eddies (Fig. 5.1 and 5.2) originating near the south-eastern boundary of the Arabian Sea. Formation and evolution of these eddies during the winter period were described in detail in the earlier studies (Bruce et al., 1998; McCreary et al., 1993; Shanker and Shetye, 1997; Rao et al., 2013). Rao et al. (2013) suggested that the development of intense zonal baroclinic instability near the south-eastern tip of India, due to the transport of low-salinity BoB surface waters, contributes to the meandering of the NMC and, thus, the formation of eddies. These eddies may further play a role in the dispersal of the low-salinity BoB surface waters across the Arabian Sea as they advect westward. Such a possibility is recognized at stations GI-06(B)/11 and 12, where a sudden decrease in the surface salinity (from ~35.45 at GI-06(B)/10 to ~35.16 at GI-06(B)/11), along with the shoaling of the potential density anomaly isolines, indicating the presence of a warm-core (anti-cyclonic) eddy (Fig. 5.2c and Fig. 5.3a), was observed. A similar phenomenon was also noted in the BoB where mesoscale eddies were found to impact the spatial dispersal of the huge freshwater influx, dominantly sourced from the Himalayan rivers (the Ganga and the Brahmaputra; Lekha et al., 2018). The surface salinity increases towards the north-western Arabian Sea region (~35.51 at GI-06(B)/14 to 36.53 at GI-06(B)/18, Fig. 5.3a). In the sub-surface depths (75-100 m), the presence of the Arabian Sea High Salinity Water (ASHSW) is ubiquitous in the southern region (GI-06(B)/3 to GI-06(B)/14, Fig. 5.3a).

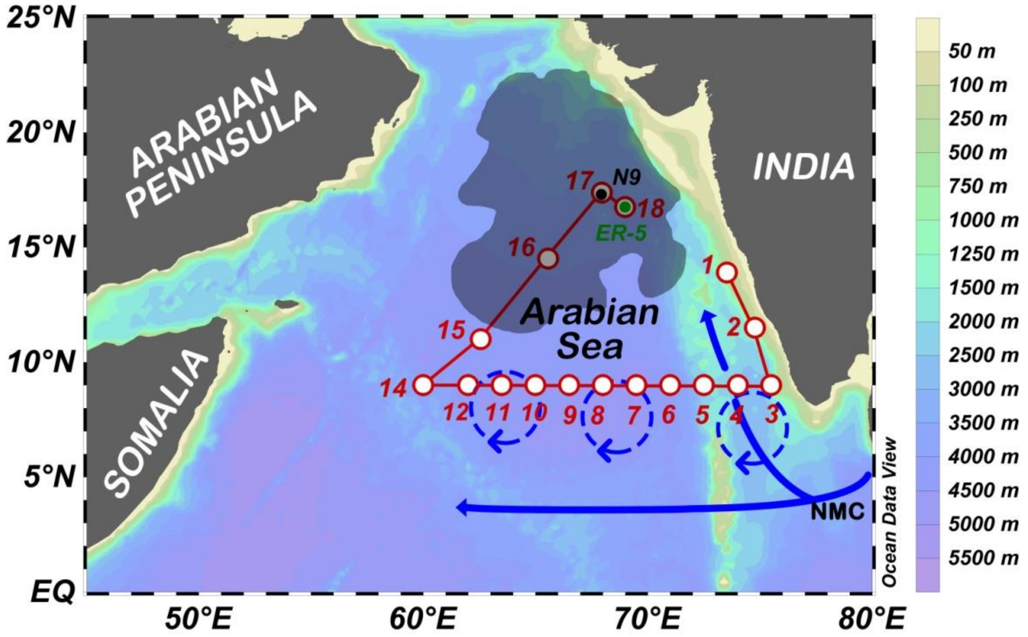

Fig. 5.1: Sampling locations (red outlines circles) along the GEOTRACES-India cruise transect GI-06(Leg B) for the measurement of dissolved Mn. Crossover stations, N9 (black circle; Lewis and Luther, 2000) and ER-5 (green circle; Thi Dieu Vu and Sohrin, 2013) are also plotted. The black patch in the map represents the perennial denitrification zone in the Arabian Sea (Naqvi, 1991). Solid blue arrows show the general surface water circulation pattern in the southern and along the eastern Arabian Sea coast, under the influence of Northeast Monsoon Current (NMC). Dashed blue circles highlight the presence of anti-cyclonic eddies in the southern Arabian Sea (also refer to Fig. 5.2).

In the thermocline depths (200-800 m), advection of the high salinity Persian Gulf Water (~300m) and the Red Sea Water (500-800m) from the Arabian marginal seas (the Persian Gulf and the Red Sea, respectively) are apparent at the central region (GI-06(B)/16, 17 and 18, Fig. 5.3a) of the Arabian Sea. The presence of these waters become feeble in the southern Arabian Sea region as evident from, relatively, more uniform salinity distribution observed in the thermocline waters along the zonal transect (Fig. 5.3a).

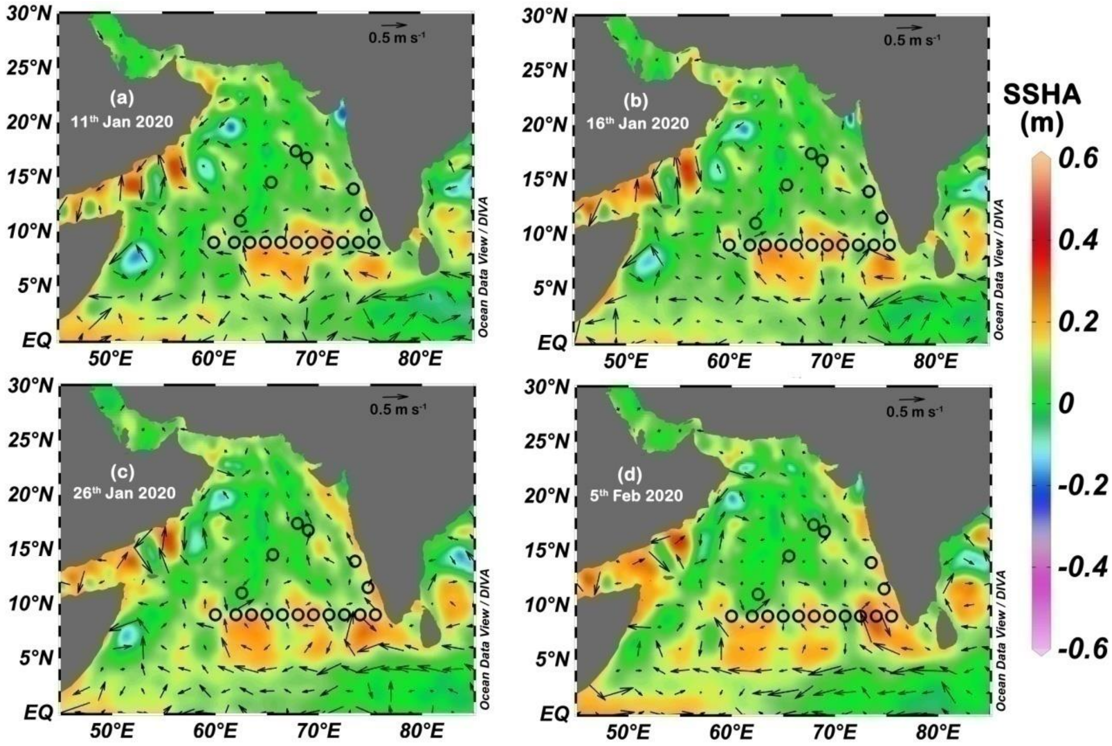

Fig. 5.2: Satellite-data based surface water circulation (black arrows; ESR. 2009) and sea surface height anomaly (SSHA; background-color gridding) in the Arabian Sea. The altimeter products (SSHA) were produced by Ssalto/Duacs and distributed by Aviso+, with support from Cnes (https://www.aviso.altimetry.fr)

5.3 Results and Discussion

5.3.1 Surface dMn distribution

dMn concentration in the surface waters varies from 1.41 nmol kg^{-1} to 4.19 nmol kg^{-1}, including all the sampled stations. The highest levels of surface dMn (3.74-4.19 nmol kg^{-1}) were observed for the coastal stations (GI-06(B)/1 and 2, Fig. 5.3b) in the south-eastern Arabian Sea. An increase in the atmospheric mineral dust deposition flux towards the coastal region (Kumar et al., 2012; Aswini et al. 2020), compared to the open Arabian Sea (Tindale and Pease, 1999), may explain the observed elevated dMn levels over the continental shelf. dMn input from the resuspension and reductive/non-reductive dissolution of the shelf sediments could also contribute to the surface dMn inventory (Kadko et al., 2019; Middag et al., 2011; Morton et al., 2019). However, no distinct increase in dMn concentrations was observed close to the sediment-water interface (~20-30 m above the margin) over the shelf region (GI-06(B)/1 and 2, Fig. 5.3b), apparently suggesting insignificant dMn flux from the shelf sediments to the ambient seawater. Oxic water column conditions

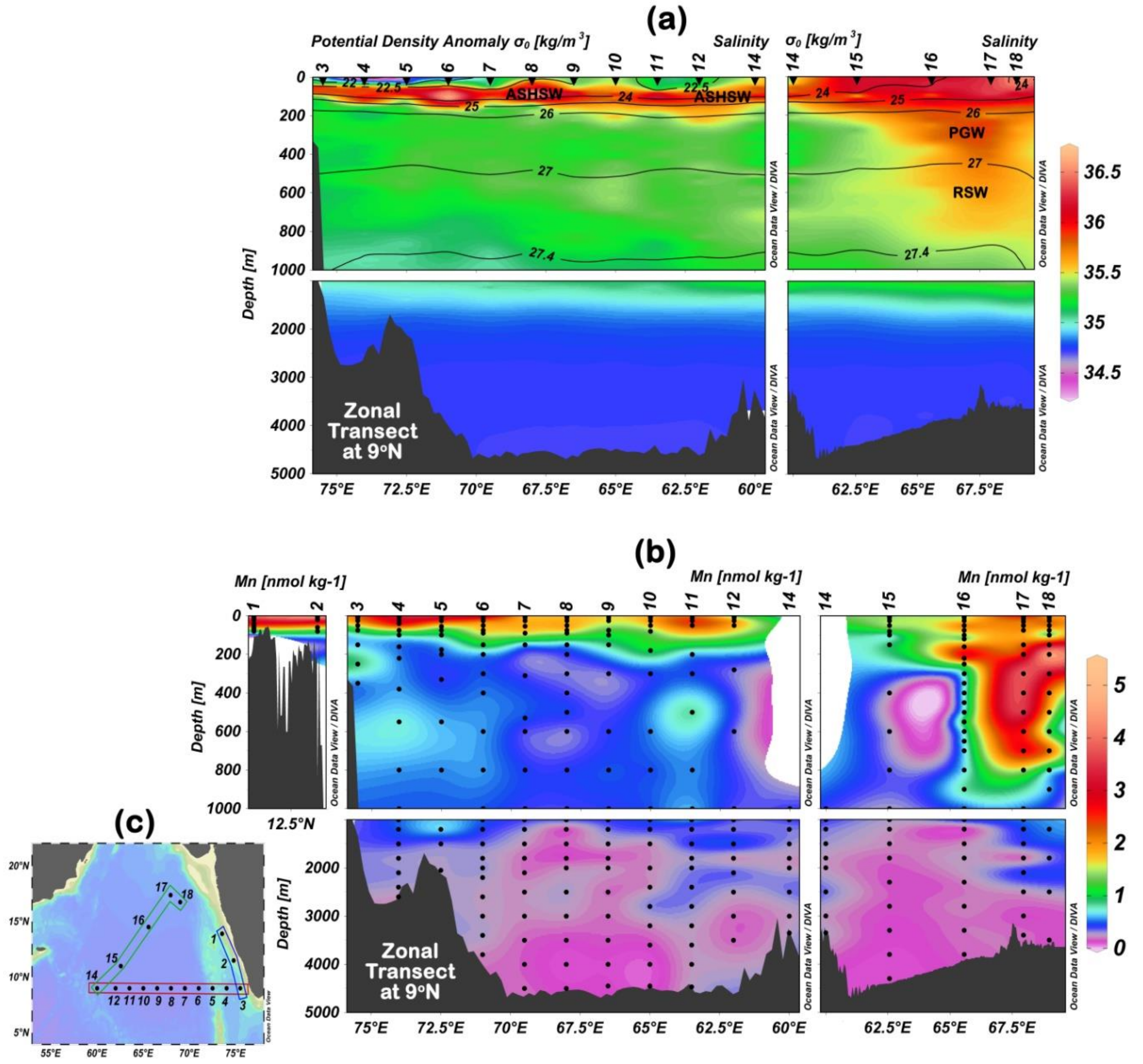

Fig. 5.3: (a) Salinity and **(b)** dMn distribution along the GI-06(B) transect. For better understanding, salinity and dMn data are plotted separately for the upper 1000m and deeper (>1000m)water column. To facilitate data visualization, salinity and dMn distributions along the GI-06(B) transect are divided into sub-transects, as indicated in Fig. **5.3c**. The overlaid contours in the salinity plot represent the potential density anomaly isolines.

(dissolved oxygen level ~180µM) in the ambient waters to sediment-water interface in the shelf region may inhibit the buildup of the soluble and reduced Mn (Mn(II), Morgan, 2005) released from the shelf sediments. The possibility of dMn input with the continental run-off to the surface waters may also be eliminated considering the negligible contribution of the freshwater influx (from the Indian Peninsular rivers) to the sea-salt budget in the south-eastern Arabian Sea during the winters (Sandeep et al., 2018). Moving off-shore along the zonal sub-transect in the southern Arabian Sea, a marked increase in the surface dMn concentrations (by ~0.70-1.00 nmol kg^{-1}) was observed in the low-salinity BoB surface water plume at stations GI-06(B)/4, 5 and 6 (Fig. 5.3b and Fig. 5.4). The Northeast Monsoon Current (NMC) transporting the low-salinity BoB surface waters to the Arabian Sea is fed by the East Indian Coastal Current (Kumar et al., 2004), which carries highly dMn-enriched (~13-133 nmol kg^{-1}, Srichandan et al., 2016 and references therein) coastal surface waters of the western BoB region (Kumar et al., 2004; Schott et al., 2009). Therefore, the advective input of dMn with the NMC carrying the dMn-rich coastal BoB surface waters may explain the surface dMn increase in the low-salinity plume at the south-eastern Arabian Sea. West of the low-salinity plume, surface dMn show more uniform and lower levels (1.64-1.80 nmol kg^{-1}) except at station GI-06(B)/11, where relatively elevated concentration (2.40 nmol kg^{-1}) was observed. Interestingly, the relative increase in dMn concentration at this station is accompanied by a significant decrease in surface salinity (from ~35.45 at GI-06(B)/10 to ~35.16 at GI-06(B)/11; also refer to Fig. 5.4). Further, surface circulation pattern, significant positive sea-surface

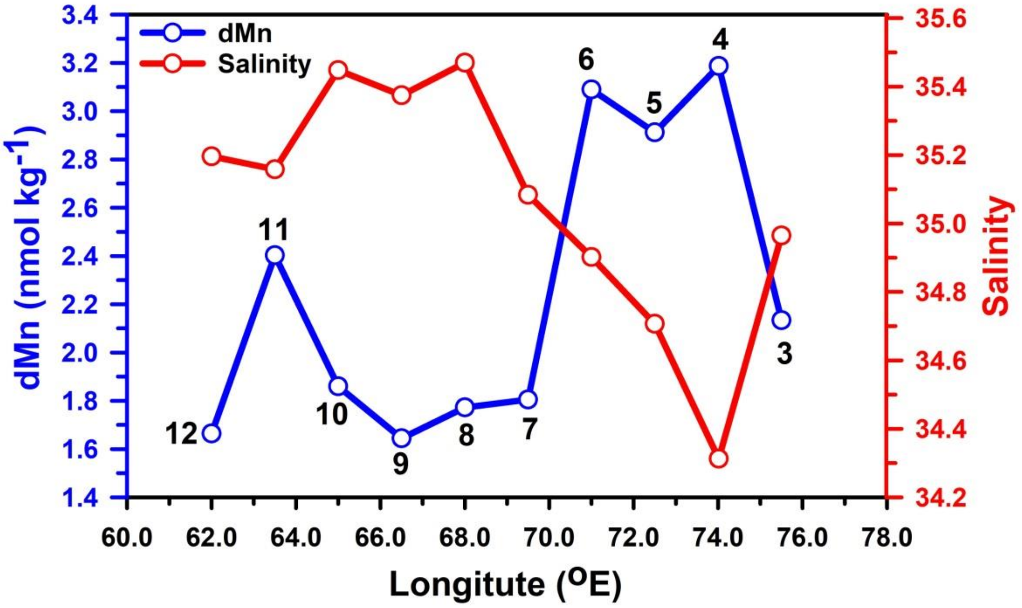

Fig. 5.4: Variation in mixed layer salinity (red line) and dMn along the zonal transect (GI-06(B)/3 to GI-06(B)/12) in the southern Arabian Sea

height anomaly (Fig. 5.2c) and deepening of potential density anomaly isolines (Fig. 5.3a) observed at the station GI-06(B)/11 during the sampling period indicate the presence of an anti-cyclonic (warm core), mesoscale eddy. As discussed before (refer to section 5.2), the formation of mesoscale eddies in the south-eastern Arabian Sea could affect the dispersal pattern of low-salinity and, relatively, dMn-rich BoB surface waters advected in this region during the winters with the NMC.

5.3.1.1 Atmospheric input, removal flux and steady-state residence timescales of dMn in the Arabian Sea surface waters

This section attempts to estimate the (1) surface dMn input fluxes from the dry deposition of atmospheric dust and (2) surface dMn removal fluxes concerning different probable removal mechanisms in the Arabian Sea. Using these estimates and observed dMn inventory in the surface mixed layer, we also aim to determine and compare the steady-state residence timescales of dMn with respect to the atmospheric input. Data on Mn concentrations in the surface-level aerosols over the Arabian Sea was extracted from the US-JGOFS Arabian Sea field program data server (Tindale, 1997) and used for estimating the Mn deposition flux from the atmosphere. Several studies (Pease et al., 1998; Tindale and Pease, 1999; Schüβler et al., 2005; Siefert et al., 1999) have shown that the Arabian Sea is subjected to significant spatio-temporal variations in the atmospheric mineral dust deposition fluxes. Here, we seek to evaluate the annual mean of the dMn input to and removal fluxes from the surface waters. Therefore, to estimate the annual mean of the dMn input flux to the sea and the steady-state residence time (with respect to the atmospheric input), we focused on the regions where the data on seasonal variations in aerosol-Mn concentrations and surface dMn data are available (such that annual mean could be estimated). These regions are represented as different zones and are shown in Fig. 5.5. The aerosol-Mn data points available in each zone were sub-divided into different seasons (early and late winter, spring, summer; Fig. 5.5) according to the seasonal divisions followed in Pease et al. (1998; also refer to Table 1), and used to calculate the seasonal mean aerosol-Mn concentration. In

Table 5.1: Estimation of dissolved Mn (dMn) input fluxes from the atmospheric dust deposition in the different studied zones/regions of the Arabian Sea.

	Season (Time interval[a])	**Seasonal mean of aerosol-Mn (ug m^{-3})**	**Non-summer mean of aerosol-Mn[b] (ug m^{-3})**	**Corrected Summer aerosol-Mn[c] (ug m^{-3})**	**Annual mean of aerosol-Mn 1[d] (ug m^{-3})**	**Annual mean of aerosol-Mn 2[e] (ug m^{-3})**	**Mn Solubility**	**Vd (m d^{-1})**	**dMn flux 1[f] (nmol m^{-2} d^{-1})**	**dMn flux 2[g] (nmol m^{-2} d^{-1})**	**Range of dMn flux (nmol m^{-2} d^{-1})**
Zone 1	LW (1 Jan - 10 Feb)	0.059	0.026	0.066	0.019	0.038	0.27	777.6	72.6	143.6	72.6 - 239.4
	Sp (11 Feb - 31 May)	0.018					0.45		121.0	239.4	
	Su (1 Jun - 24 Aug)	0.0007									
	EW (1 Nov - 31 Nov)	0.019									
Zone 2	LW	0.041	0.020	0.050	0.015	0.029	0.27	777.6	56.1	109.6	56.1 - 182.7
	Sp	0.0091					0.45		93.5	182.7	
	Su	0.0011									
	EW	0.026									
Zone 3	LW	0.0049	0.0088	0.022	0.0075	0.013	0.27	777.6	28.6	48.1	28.6 - 80.1
	Sp	0.0052					0.45		47.7	80.1	
	Su	0.0042									
	EW	0.018									
Zone 4	LW	0.032	0.018	0.046	0.0190	0.026	0.27	777.6	72.7	99.5	72.7 - 165.9
	Sp	0.0045					0.45		121.2	165.9	
	Su	0.021									
	EW	0.034									

a: Time interval of different seasons as per Pease et al., 1998. LW: Late Winter; Sp: Spring; Su: Summer; EW: Early Winter; **b:** Time-averaged aerosol-Mn concentration considering all the non-summer monsoon seasons (i.e., LW, Sp and EW); **c:** Corrected-summer aerosol-Mn concentration estimated by multiplying the non-summer aerosol-Mn with a factor of 2.5 (see text); **d:** Annual time-average aerosol-Mn estimated using the non-corrected summer aerosol-Mn values; **e:** Annual time-average aerosol-Mn estimated using the corrected summer aerosol-Mn values; **f:** Lower limit of the dissolved Mn input flux from the atmospheric deposition to the surface waters estimated using the Annual aerosol-Mn 1 values; **g:** Upper limit of the dissolved Mn input flux from the atmospheric deposition to the surface waters estimated using the Annual aerosol-Mn 2 values a zone, if more than one data point of aerosol-Mn for a season is available (refer to Table E1 in Appendix E), the geometric mean of the data points is considered as the seasonal mean for further calculations. The mean annual aerosol-Mn concentration in a zone is then estimated as the time-averaged value of the seasonal aerosol-Mn mean concentrations in that zone (Table 5.1).

As noted in the earlier studies (Tindale and Pease, 1999; Schubler et al., 2005), aluminium (Al) (and thus, continental dust) concentration in the surface-level aerosols over the Arabian Sea is the lowest during the summer monsoon season. This is attributed to the dilution (of continental dust) by sea-salts transported in a huge amount by the strong south-westerly monsoonal winds from the remote marine regions of the equatorial and southern Indian Ocean (Tindale and Pease, 1999). However, other (proportionally) related (to aerosol

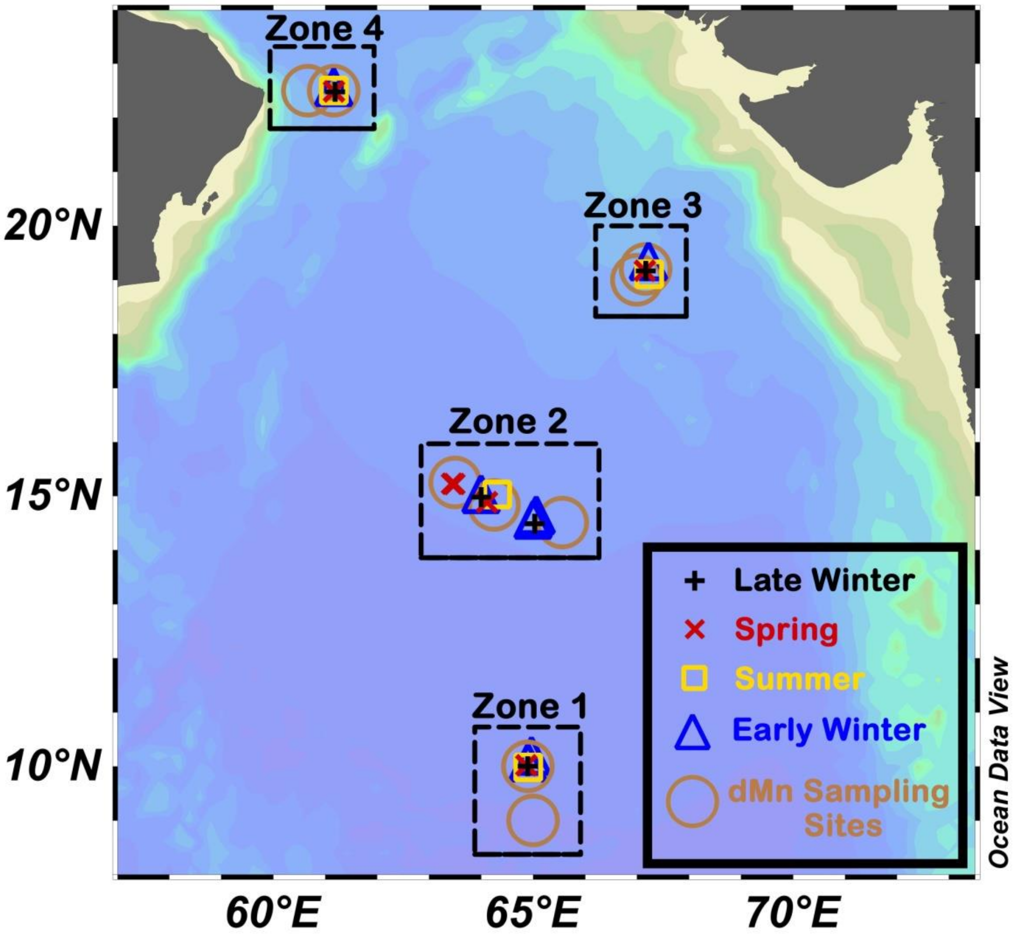

Fig. 5.5: Map showing different regions (zones, see text) where seasonal variations in aerosol Mn and dMn concentrations data from this and previous studies are used to estimate the atmospheric input flux of dMn and its residence time in the Arabian Sea surface waters.

continental dust concentration) chemical and physical parameters such as surface dissolve aluminium, lithogenic sediment flux and satellite-based dust loading show elevated values during the summer-monsoon compared to the non-summer monsoon seasons. These observations advocate for high concentration and deposition flux of continental dust over the Arabian Sea (Husar et al., 1997; Schüβler et al., 2005; Tindale and Pease, 1999) during the summer monsoon. To explain this apparent mismatch (between low surface-level dust concentration and, relatively, elevated values of other proportionally related parameters), studies (Tindale and Pease, 1999; Ramaswamy et al., 2017) have suggested (1) the contribution of the highly continental dust-rich layers, observed above the sea-salt-rich surface level aerosols during the summers, to the net mineral dust deposition (mainly through wet deposition) and (2) a relative increase in the aerosol dry deposition velocity over the Arabian Sea during the summer monsoon, due to the formation of sea-salt and dust particles aggregates. Schüβler et al. (2005) determined the corrected-Al deposition flux during the summer monsoon by multiplying the time-averaged, non-summer monsoon Al flux with the ratio of aerosol optical thicknesses estimated during the summer and non-summer monsoon seasons (Husar et al., 1997). Such estimates provided ~2.5 times higher Al-flux during the summer monsoon compared to that estimated for the non-summer monsoon seasons. The corrected-Al flux estimate also matched well with the deep sediment trap Al-flux in the Arabian Sea (Schüβler et al., 2005). Considering aerosol-Mn over the Arabian Sea to be predominantly sourced from the crustal sources, the corrected-Mn deposition flux during the summer monsoon was estimated following the Schüβler et al. (2005) corrections methodology/factor (as for Al) and considered it to be the upper limit. This exercise seems reasonable given that the Mn/Al ratios observed in the aerosols over the Arabian Sea during the spring and summer monsoon period are similar to that for the upper continental crust (Siefert et al., 1999), which suggests the aerosol-Mn to be, dominantly, of the crustal origin. The lower limit of the mean annual Mn deposition flux was estimated by considering the observed surface-level aerosol-Mn concentration during the summer monsoon season (Table 5.1; Tindale, 1997). The mean dry deposition velocity (V_d) of aerosols was taken as the effective deposition velocity (0.9 cm $sec^{-1} \approx 777.6$ m d^{-1}) of the bulk aerosol estimated by Sarin et al. (1999) in the Arabian Sea.

To determine the dMn input to the surface waters from the atmospheric dust deposition, the fractional solubility of Mn ($\mathbf{Sol_{Mn}}$) from the deposited dust needs to be constrained. The observed $\mathbf{Sol_{Mn}}$ shows large variability over the global oceans (~10-90%, Baker et al., 2006; Buck et al., 2010; Buck et al., 2013; Guieu et al., 1994). The highest estimates (>50%) are generally associated with the aerosols derived from the anthropogenic sources (Baker et al., 2006; Guieu et al., 1994; van Hulten et al., 2017). Median values of $\mathbf{Sol_{Mn}}$ estimated by different studies (Baker et al., 2006; Buck et al., 2010; Guieu et al., 1994) for the aerosols predominantly derived from the Saharan Deserts (rich in continental dust) lie in the range: 30-55%. $\mathbf{Sol_{Mn}}$ values are also relatively high in the north and north-western Pacific Ocean regions (median ~45%), where the continental dust input from the Asian mainland is significant (Buck et al., 2013). The lowest $\mathbf{Sol_{Mn}}$ estimates were obtained for the aerosols having a significant contribution from the remote marine air-mass (Baker et al., 2006; Guieu et al., 1994). For example, relatively lower median $\mathbf{Sol_{Mn}}$ (27%) were determined for the aerosols samples collected over the remote south-eastern Pacific Ocean region (along the CLIVAR cruise sub-transect, P16S) compared to that in the north and north-western region (~45%, along the CLIVAR cruise sub-transect P16N and transect P02; Buck et al., 2013). There are no estimates on $\mathbf{Sol_{Mn}}$ from the dust deposition over the Arabian Sea. The predominant sources of aerosols over the Arabian Sea are the surrounding arid/semi-arid continental regions (e.g., southern Arabian Peninsula, Makran Basin, Sistan Basin, Thar Desert) for most of the year (Tindale and Pease, 1999; Kumar et al., 2020). However, as discussed above, during the summers, sea-salts constitute a significant proportion of the atmospheric mineral aerosol, which may impact (lower down) the effective $\mathbf{Sol_{Mn}}$ from the mineral dust deposited (Guieu et al., 1994). To accommodate all the probable estimates, we considered the $\mathbf{Sol_{Mn}}$ from the mineral dust deposited over the Arabian Sea to vary in the range of 27-45% (Table 5.1). Using the above constraints on annual mean aerosol-Mn ($\mathbf{Mn_{atm}}$), depositional velocity (**Vd**), and $\mathbf{Sol_{Mn}}$, the dMn input flux from the atmospheric dust deposition ($\mathbf{I_{atm}^{Mn}}$) was calculated as follows

$$\mathbf{I_{atm}^{Mn}} = \frac{\mathbf{Mn_{atm} \cdot Vd \cdot Sol_{Mn}}}{\mathbf{M_{wt}^{Mn}}} \qquad \mathbf{(5.1)}$$

and found to lie in the range of 28.6-239.4 nmol m^{-2} d^{-1}, including all the zones (Table 5.1). These annual estimates compare well with that determined earlier by van Hulten et al. (2017) using the mineral dust deposition estimates of Interaction with Chemistry and Aerosols (INCA) model (refer to Figure 4 of van Hulten et al., 2017). The uncertainty associated with the calculation of the dMn input fluxes majorly arises from the variations considered in $\mathbf{Sol_{Mn}}$ (~1.5 fold) and annual atmospheric Mn flux (1.4-2.0 fold; considering uncorrected and corrected summer monsoon Mn flux, Tabel 5.1). Therefore, the total variation in the dMn flux calculation in a zone range from ~3.0-3.5 fold (as also apparent in the results, refer to Table 5.1); compared to this, the analytical error in the measured aerosol Mn concentration is negligible (mean error: 18%; Tindale, 1997). The steady-state residence time of surface dMn (with respect to the atmospheric input) was also estimated by dividing the observed mean of the surface mixed layer dMn inventory (i.e., dMn times the mixed layer depth; in µmol m^{-2}) with the estimated atmospheric dMn fluxes (in µmol m^{-2} d^{-1}) in different zones (Fig. 5.5). The dMn data from different sampling stations (Fig. 5.5 and Table 5.2), used for the calculation of the surface mixed layer dMn inventory in each zone (Table 5.2), is taken from the present and previous studies (Lewis and Luther, 2000; Saager et al., 1989). The annual mean of the surface mixed layer depth (MLD) at different dMn data locations was estimated by extracting the (climatological) monthly MLD dataset available at the nearby regions (Holte et al., 2017; refer to Table 5.2). The estimated residence times lie in the range of 1.0-9.3 years, including all the zones (Table 5.2). These estimates of residence times are comparable to those evaluated in the Northeast Atlantic Ocean (1.0-3.8 yr, de Jong et al., 2007) and near the productive coastal regions of the eastern North Pacific (0.22-11.0 yr, Landing and Bruland, 1987; Martin and Knauer, 1980). Residence time estimates for surface dMn in the Arabian are, however, relatively lower than that calculated for the oligotrophic, open Pacific Ocean waters (5-74 yrs, Landing and Bruland, 1987; Klinkhammer and Bender, 1980).

As noted in the introductory remarks, the major pathways for the removal of dMn from the seawater include (1) biotically-mediated Mn-oxidation to insoluble Mn-oxides (Morgan, 2005 and references therein; Sunda and Huntsman, 1988; Tebo et al., 2005), (2) heterogenous Mn-oxidation on metal oxide surfaces (Davies and Morgan, 1989; Morgan, 2005 and references therein), (3) passive adsorption of dMn onto the particles with organic coatings and/or biogenic particles (Balistrieri et al., 1981; Martin and Knauer, 1980), and (4) biological uptake of dMn by the phytoplankton in the surface waters (Coale et al., 1991). Although biotically-mediated Mn-oxidation (and subsequent removal of Mn-oxides) is the most prominent pathway for the net removal of dMn over the vertical ocean water column (Sunda, 2012 and references therein; Sunda and Huntsman, 1988), it is significantly inhibited by light (photo-inhibition) in the well-lit surface waters (Sunda and Huntsman, 1988; Moffett, 1997). Therefore, other *in situ* removal processes (heterogenous Mn-oxidation, passive adsorption and biological uptake) become more important in the surface waters (Moffett, 1997). Active uptake of Mn by phytoplankton as a bio-essential trace metal and subsequent removal of the assimilated-Mn from the surface waters, directly by vertical settling of dead

Table 5.2: Estimation of the surface water dissolved Mn (dMn) inventory and residence time, with respect to the atmospheric input, in the different studied zones/regions of the Arabian Sea.

	Sampling Station	**dMn (μmol m^{-3})**	**MLD (m)**	**dMn inventory (μmol m^{-2})**	**Mean dMn inventory (μmol m^{-2})**	**Range of atm. dMn input flux (nmol m^{-2} d^{-1})**	**Range of estimated residence time (yr)**
Zone 1	S15[a]	3.1	43	133	104	72.6 - 239.4	1.2-3.9
	GI-06(B)/10	1.9	40	74			
Zone 2	S9[a]	1.5	44	66	65	56.1 - 182.7	1.0-3.2
	S10[a]	1.3	44	57			
	GI-06(B)/16	1.5	46	71			
Zone 3	N6[a]	1.9	38	72	97	28.6 -80.1	3.3-9.3
	N7[a]	3.3	38	125			
	Sa6[b]	2.4	38	92			
Zone 4	N2[a]	2.5	30	75	72	72.7 - 165.9	1.2-2.7
	Sa8[b]	2.5	28	69			

a: Sampling locations from Lewis and Luther (2000)
b: Sampling locations from Saager et al. (1989)

phytoplankton detritus or indirectly by settling of zooplankton fecal pellets after phytoplankton grazing, forms one of the removal pathways for dMn. The removal flux of Mn via phytoplankton assimilation ($\mathbf{R_{phy}^{Mn}}$) is estimated by considering the effective carbon normalized Mn quota ($\mathbf{(Mn{:}C)_{phy}}$) for the

Table 5.3: Estimated dMn removal fluxes from the surface waters at different Arabian Sea locations (refer to Fig. 5.6) via bio-assimilation.

	Station	**Reported or Estimated Annual POC Flux ($\mathbf{F_{POC}}$) (mmol m^{-2} d^{-1})**	**$\mathbf{(Mn{:}C)_{phy}}$ (nmol mmol^{-1})**	**Range of dMn removal flux (nmol m^{-2} d^{-1})**	**Range of atm. dMn input flux at the nearby zone (nmol m^{-2} d^{-1})**
Open Ocean					
	N4	5.39[a]	1.6	8.6 - 13.5	
			2.5		
	N6	4.53[a]	1.6	7.2 - 11.3	28.6 - 80.1 (Zone 3)
			2.5		
	N7	2.88[a]	1.6	4.6 - 7.2	28.6 - 80.1 (Zone 3)
			2.5		
	N11	3.08[a]	1.6	4.9 - 7.7	
			2.5		
	S3	8.04[b]	1.6	12.9 – 20.1	
			2.5		
	S4	6.75[b]	1.6	10.8 - 16.9	
			2.5		
	S7	5.54[b]	1.6	8.9 – 13.9	
			2.5		
	S11	5.38[a]	1.6	8.6 - 13.5	56.1 - 182.7 (Zone 2)
			2.5		
	S13	3.35[a]	1.6	5.4 - 8.4	
			2.5		
	S15	2.72[b]	1.6	4.4 - 6.8	72.6 -239.4 (Zone 1)
			2.5		
Coastal Region					
	N2	4.34[a]	2.7	11.7 - 24.3	72.7 -165.9 (Zone 4)
			5.6		
	S2	9.45[a]	2.7	25.5 - 52.9	
			5.6		

a: Mean annual POC flux at 100m estimated using the seasonal POC data given by Buesseler et al., 1998.

b: Mean annual POC flux at 100m given by Lee et al., 1998.

phytoplankton community in the Arabian Sea and multiplying the $\mathbf{(Mn{:}C)_{phy}}$ with the POC export flux out of the euphotic zone ($\mathbf{F_{POC}}$). Here, the POC export flux at 100m is taken as the measure of the fraction of the primary production exported out of the surface waters (euphotic zone). Mathematically, using the above-described formulation, the removal flux due to biological assimilation of Mn can be described as

$$\mathbf{R_{phy}^{Mn}} = (\mathbf{Mn:C})_{\mathbf{phy}} . \mathbf{F_{POC}} \tag{5.2}$$

Mn:C ratio may vary for different phytoplankton species (Ho et al., 2000; Twining et al., 2013) and, therefore, the effective carbon normalized Mn quota, i.e., **$(\mathbf{Mn:C})_{\mathbf{phy}}$**, for a phytoplankton community would depend on the relative abundance of different constituting species. Tarren et al. (1999) studied the phytoplankton community structure in the Arabian Sea during the highly productive late summer monsoon and the relatively low productive season of the fall-intermonsoon. They also compared the seasonal changes in the phytoplankton community at the western coastal region (near the Oman coast) and in the open waters of the western and central Arabian Sea. Their results show that except for the coastal upwelling regions during the summer monsoon, picoplankton (Synechococcus and/or Prochlorococcus) dominate the total biomass of the primary producers across the studied ocean regions (open and coastal) and seasons. However, during the summer monsoon and in the coastal waters, diatoms also contributed significantly to the total biomass, reaching as high as 80% (by mass; Tarren et al., 1999). Therefore, in the open waters, it is reasonable to consider **$(\mathbf{Mn:C})_{\mathbf{phy}}$** similar to that observed for the autotrophic picoplankton; however, for the coastal regions, diatom contribution to the **$(\mathbf{Mn:C})_{\mathbf{phy}}$** should be taken into account. To our knowledge, no estimates on Mn:C ratios are available for phytoplankton in the Arabian Sea. Twining and Baines (2013) recently reviewed the observed variations in trace metal (micro-nutrient) quotas across the dominant phytoplankton groups found in the global oceans and different oceanic regions. The mean Mn:C ratio for the autotropic picoplankton in the equatorial and temperate Pacific Ocean region is estimated to be ~1.6 and 2.5 nmol mmol^{-1}, respectively, from the previously published data (King et al., 2012; Twining et al., 2011; Twining et al., 2013 and references therein). These ratios are estimated by using the observed mean P-normalized Mn quota (i.e., Mn:P; King et al., 2012; Twining et al., 2011; Twining et al., 2013 and references therein) and the mean C:P ratio found in the autotrophic picoplankton (Twining et al. 2011) and surface bulk particulate matter (King et al., 2012) in the equatorial and temperate Pacific Ocean, respectively. The reported/estimated mean Mn:C for diatoms in the equatorial and temperate regions of the Pacific Ocean and Pacific Ocean sector of the Southern Ocean is relatively higher (compared to the picoplankton) and lie in the range of 3.0-3.9 nmol mmol^{-1} (King et al., 2012; Twining et al., 2004; Twining et al., 2011; Twining et al., 2013 and references therein). Twining et al. (2004) also observed that their estimated mean C:P ratio (104 mol mol^{-1}) for diatoms in the Southern Ocean is about two-fold higher than that estimated by Cullen et al. (2003) in the nearby region (66 mol mol^{-1}), where diatom dominated the biomass. To have an upper estimate of Mn:C ratio for diatoms, the mean Mn:P ratio (0.42 mmol mol^{-1}) observed by Twining et al. (2004) in the Southern Ocean was used and converted to Mn:C by using the C:P ratio (66 mol mol^{-1}) given by Cullen et al. (2003). This provided an upper estimate to Mn:C for diatoms (6.4 nmol mmol^{-1}). To summarize, $\mathbf{(Mn{:}C)_{phy}}$ is considered (in Eq. 5.2) to be in the range of 1.6-2.5 nmol mmol^{-1} for the open waters (picoplankton dominated) and 2.7-5.6 nmol mmol^{-1} in the coastal waters (considering 80% diatom plus 20% picoplankton) of the Arabian Sea. The mean annual POC vertical export flux ($\mathbf{F_{POC}}$) data for different regions in the Arabian Sea (Fig. 5.6 and Table 5.3) was either taken from Lee et al. (1998) or estimated by time-averaging the available seasonal POC export flux data (Buesseler et al., 1998). Finally, the range of mean annual surface dMn removal flux by biological assimilation ($\mathbf{R_{phy}^{Mn}}$) was evaluated by using the constraints òn $\mathbf{(Mn{:}C)_{phy}}$ and $\mathbf{F_{POC}}$ (for different regions stations) in Eq. (5.2). The estimated annual removal flux for the open ocean and coastal regions varies in the range of 4.2-23.3 nmol m^{-2} d^{-1} and 11.7-52.9 nmol m^{-2} d^{-1}, respectively, including all the regions (stations; Table 5.3). These estimated fluxes are significantly (~3-10 times) less than the lower estimate of the atmospheric dMn input at the nearby region/zone (Fig. 5.6 and Table 5.3) and, therefore, suggest that the bio-assimilation, and subsequent removal, exert secondary control on the dMn removal out of the surface waters.

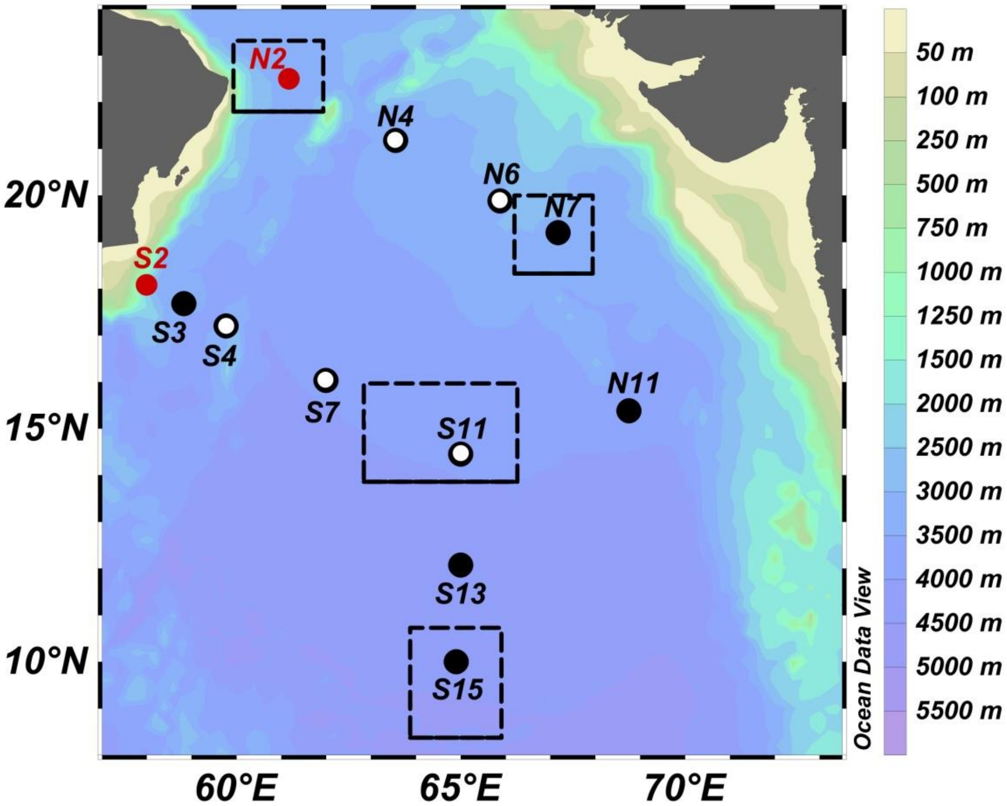

Fig. 5.6: Solid black (open ocean) and red (coastal region) symbols mark the locations where surface dMn removal by active biological uptake is estimated. White circles represent stations where surface dMn removal fluxes by both bio-assimilation, and oxidation and passive scavenging of Mn are estimated. The dashed rectangles represent different zones where the atmospheric input fluxes of dMn are calculated.

Removal of Mn from the water column by *in situ* oxidation and passive adsorption results in the formation of reactive particulate Mn (i.e., amorphous Mn-oxyhydroxides and adsorbed-Mn on the surfaces of particles, Landing and Lewis, 1987; Sunda and Huntsman, 1988). The relative abundance of these reactive phases have been estimated (Berger et al., 2008; Jensen et al., 2020; Landing and Bruland, 1987; Lewis and Luther, 2000; Martin and Knauer, 1984; Sunda and Huntsman, 1988; Whitemore et al., 2019) by measuring the weak acid (e.g., acetic acid, ascorbic acid) leachable fraction of the total particulate Mn (weak acid leachable + refractory). The reported (Lewis and Luther, 2000) reactive particulate Mn (pMn_R, i.e., acetic acid leachable particulate Mn from the bulk suspended particulates) data in the surface waters (~50 m) of the Arabian Sea is used as the measure of surface dMn removed to particulate form via *in situ* oxidation and passive scavenging. Next, we calculated the relative abundance of the pMn_R with respect to particulate organic carbon (i.e., pMn_R/POC; Table 5.4) using the POC data reported at the same station, season and similar depth (Ducklow, 1997). Finally, the mean annual surface dMn removal flux ($\mathbf{R_{abio}^{Mn}}$) was estimated by multiplying the calculated pMn_R/POC ratio with the annual mean of the vertical POC export flux across the 100m depth (used as a measure of the POC export out of the euphotic zone). Mathematically, it can be represented as

$$\mathbf{R_{abio}^{Mn} = pMn_R/POC\ .\ F_{POC}} \tag{5.3}$$

The inherent assumptions in this calculation are that the pMn_R/POC remains the same throughout the year and POC export flux across the 100m is similar to that across the shallower depth, i.e., 50m, where the pMn_R/POC is determined. The dMn removal flux is evaluated for the stations (Fig. 5.6) where the data on all the required parameters, i.e., pMn_R, POC and POC export flux, are available (Ducklow, 1997; Buesseler et al., 1998; Lewis and Luther, 2000; Lee et al., 1998). The reference depth for the pMn_R and POC data, and calculation of the pMn_R/POC ratio was taken as 50m because it is closest to the annual mixed layer depths (36-45m) and where pMn_R data is available. The estimated surface dMn removal flux (using Eq. (5.3)) for all the stations are given in Table 5.4 and lie in the range of 51.9-276.0 nmol m^{-2} d^{-1}. These removal flux

Table 5.4: Estimation of the cumulative dMn removal fluxes from the surface waters at different locations (refer to Fig. 5.6) the Arabian Sea via heterogeneous and biotically-mediated oxidation, and passive particle adsorption.

Station	pMn_R (nM)	POC (µM)	pMn_R/POC (µmol/mmol)	POC flux (mmol m^{-2} d^{-1})	Estimated dMn removal Flux (nmol m^{-2} d^{-1})	Range of atm. dMn input flux at the nearby zone (nmol m^{-2} d^{-1})
N4	0.093	5.92	0.0157	5.39	84.6	
N6	0.064	3.99	0.0160	4.53	72.7	28.6 - 80.1 (Zone 3)
S11	0.061	3.15	0.0194	5.38	104.2	56.1 - 182.7 (Zone 2)
S7	0.037	3.95	0.0094	5.54	51.9	
S4	0.222	5.43	0.0409	6.75	276.0	

estimates for different stations are similar or within the estimated range of dMn input flux from the atmospheric mineral dust deposition in the nearby zone (Table 5.4), suggesting the dominant role of dMn removal by *in situ* Mn oxidation and passive particle scavenging. It is also important to note that these estimates do not distinguish between the Mn removal by biotically mediatied oxidation or heterogeneous oxidation or passive particle scavenging; these are cumulative removal flux estimates for all these removal mechanisms.

5.3.2 Sub-surface dMn distribution

5.3.2.1 Thermocline waters

Below the surface mixed layer (i.e., below ~20-50 m), dMn levels, in general, show a steep decrease with depth in the upper thermocline waters (up to 150-200m, Fig. 5.3b). The photo-inhibition effect on the biotically-mediated *in situ* Mn oxidation subsides in the sub-surface waters due to the decrease in the total incident solar radiation, and it becomes a prominent removal process for dMn (Sunda and Huntsman, 1988). Moreover, the initial dissolution rate (upon deposition) of atmospheric dust-associated Mn phases in seawater is significantly faster (Mendez et al., 2010), which implies that the dMn input flux from the atmospheric dust dissolution is much larger in the surface layer and decrease in the sub-surface waters as the dust particles sink. Together, the increased *in situ* Mn-oxidation rates due to biotical-mediation and decreased dMn input flux from the dissolution of dust particles led to the steep decline in the sub-surface dMn concentrations.

In the lower thermocline waters (between 500-800 m or σ_θ ~ 27.1-27.3 kg m^{-3}, Fig. 5.3b), dMn maxima were observed along the zonal section towards the western coast of India (station GI-06(B)/4 to GI-06(B)/6). The depths of the dMn maxima, interestingly, lie in the observed potential density range of the Red Sea Water (RSW) intrusion into the Arabian Sea (σ_θ: 27.0-27.4, Shenoi et al., 1993). Further west of the station GI-06(B)/6, along the zonal transect, the observed dMn concentrations in similar depths decrease and become more uniform (~0.5 nmol kg^{-1} at stations GI-06(B)/7 to GI-06(B)/10 and GI-06(B)/12); however, an anomalous increase in the dMn concentration is observed at station GI-06(B)/11 (~0.9 nmol kg^{-1}, Fig. 5.3b). Earlier studies

(Lewis and Luther, 2000; Saager et al., 1989) have also reported dMn anomalies associated with the RSW advection in the Arabian Sea. Combining all the observed data (from this and the previous studies), a spatial pattern on the magnitude of these anomalies could be inferred. The highest positive dMn anomalies (~4-6 nmol kg^{-1} with respect to the background level) are recorded in the north and north-western Arabian Sea regions (Lewis and Luther, 2000; Saager et al., 1989). Relatively moderate levels of dMn enrichment (~1-2 nmol kg^{-1}; Lewis and Luther, 2000) are observed near the Oman coast in the western Arabian Sea. The lowest dMn anomaly levels (~0.2-0.5 nmol kg^{-1}) are found in the southern Arabian Sea region (along the zonal transect at 9°N in this study; also refer to dMn data at stations M1 and S9 in Fig. 3 of Lewis and Luther, 2000). This pattern also hints at the probable source(s) of the observed anomalies and the dispersal of the source signal in the Arabian Sea. Lewis and Luther (2000) suggested the reductive dissolution of reactive Mn phases in the

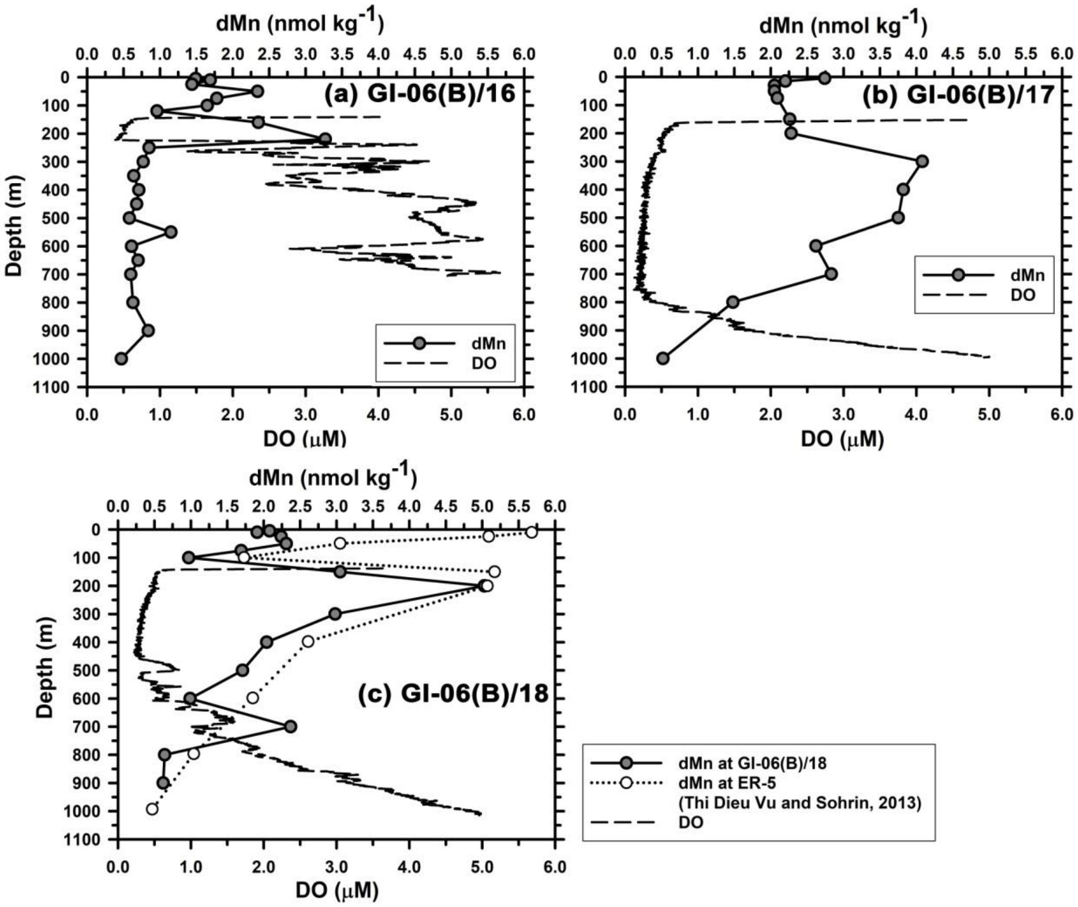

Fig. 5.7: dMn variations in the oxygen deficit depths (dissolved O_2 <6μM) at the stations sampled in the perennial denitrification zone of the Arabian Sea

extremely reducing sediments (showing significant reduction of sulfate; Lewis and Luther, 2000 and references therein) of the Pakistan Margin (at the northern Arabian Sea boundary) and subsequent advective-diffusive transport of reduced Mn, as the dominant mechanism resulting in high positive dMn anomalies in the lower thermocline waters (σ_θ ~27.1-27.3 kg m^{-3}) of the north-northwestern Arabian Sea. dMn input flux from the Oman slope sediments in the western Arabian Sea is considered to be moderate owing to a relatively lower degree of sediment reduction (compared to the Pakistan Margin sediments) and, therefore, probably lower enrichment of dMn in the pore water (Lewis and Luther, 2000 and references therein). Elevated dMn concentrations observed in the lower thermocline depths towards the coast along the zonal transect in the southern Arabian Sea (this study) may also suggest the western margin of India to be a dMn source; this possibility was pitched earlier (Lewis and Luther, 2000) as well considering the high dMn input flux estimated from the western Indian margin sediments (Yadav, 1996). The relative contribution of each of the suggested margin sources to the observed dMn anomalies could be evaluated once the estimates on dMn input flux from the reducing margin sediments, scavenging and horizontal water advection rate become available.

Another highlight was the significant increase in dMn concentrations observed over the thermocline waters depths in the intense oxygen depletion and denitrification zone of the Arabian Sea (station GI-06(B)/16, 17 and 18, Fig. 5.3b and Fig. 5.7). The observed dMn enrichment in the oxygen minimum zone (OMZ; ~150-1000 m, Dissolved Oxygen <5 µM) at station GI-06(B)/18 compares well with that reported at respective crossover stations (i.e., ER-5; Vu and Sohrin, 2013; refer to Fig. 5.7c). It is interesting to note that the maximum dMn concentrations are observed over the depths of highest DO depletion (≤0.5 µM) within the OMZ (Fig. 5.7; also refer to Fig. 3 and 4 of Lewis and Luther, 2000). Also, dMn maxima reported earlier are found correlated to the secondary nitrite maxima in the Arabian Sea OMZ (Lewis and Luther, 2000; Saager et al., 1989). dMn maxima observed in this study also correlates well with the depths of nitrite maxima found in the nearby (or crossover) stations (Lewis and Luther, 2000; Thi Dieu Vu and Sohrin, 2013). On the basis of these observations, studies have suggested the observed dMn maxima in the OMZ to result from the (*in situ*) reductive dissolution of Mn oxyhydroxides in the extremely DO depleted, denitrification depths. This is also supported by the observed correlated minima in the particulate Mn to particulate Al ratio (and reactive particulate Mn concentration) with the dMn maxima in the OMZ (Lewis and Luther, 2000), indicating the dissolution of Mn oxyhydroxides in the water column. The *in situ* Mn oxyhydroxides reduction is suggested to occur through the biotically mediated oxidation of organic carbon, where oxidized Mn particulate phases may act as the terminal electron-accepting species (Lewis and Luther, 2000 and references therein). The assimilated Mn released from the remineralization of organic matter may also contribute to the dMn input in the OMZ (Johnson et al., 1996). However, our calculation of dMn removal flux from the surface waters suggested that the proportion of dMn removed via biological assimilation is much smaller compared to that via Mn-oxidation (see section 5.3.1.1).

5.3.2.2 dMn in the deeper waters (>1500m)

dMn concentrations in the deeper waters (below 1500m) are relatively low (generally less than 0.3 nmol kg^{-1} and reaching as low as 80 pmol kg^{-1}), in agreement with the previously reported data (Lewis and Luther, 2000; Thi Dieu Vu and Sohrin, 2013) and those observed in large part of the deep global ocean (0.10-0.15 nM, van Hulten et al., 2017 and references therein). However, on a closer look into the deep water dMn distribution, subtle changes could be observed. West of 70°E along the zonal transect at 9°N (GI-06(B)/07 to GI-06(B)/14), a slight dMn increase within the 2000-3000 m (compared to the background level) is observable (Fig. 5.8a). The probable mechanisms that may result in the observed deep-water dMn maxima at these stations include (1) advection of dMn-rich deep waters and (2) dMn input from the nearby margin(s), over the similar isopycnal depths, due to partial dissolution of resuspended, reactive Mn-rich sediments and/or diffusion of dMn-rich pore waters (Middag et al., 2015). The deep-water dMn maxima levels observed at stations GI-06(B)/7, 8, 9 (0.23-0.28 nmol kg^{-1}, Fig. 5.8a) are similar to those observed close to the Chagos-Laccadive Ridge (0.25-0.31 nmol kg^{-1} at stations GI-06(B)/5 and 6) throughout the deep-water depth range (2000-3000m; Fig. 5.3b and Fig. 5.8a). The advection of relatively dMn-rich deep-waters close to the Chagos-Laccadive Ridge may, therefore, result in the observed deep-water dMn maxima at stations GI-06(B)/7, 8 and 9. However, moving further west, to stations GI-06(B)/ 10, 11, 12 and 14, the dMn levels in the deep-water maxima are significantly higher (0.34-0.37 nmol kg^{-1}, Fig. 5.8a), which may not be explained by the advection of deep-waters ambient to the Chagos-Laccadive Ridge. The Arabian Sea and the adjoining Gulf of Aden host active seafloor spreading systems (The West and the East Sheba Ridge, the Carlsberg Ridge) over which several active hydrothermal venting regions have been discovered (Gamo et al., 2015; Jean-Baptiste et al., 1990; Murton et al., 2006; Ray et al., 2012; Srinivasan et al., 2004). Based on the observation of strong anomalies in chemical and physical properties (e.g., light transmission, δ^{3}He, Mn, Fe, CH_4), previous studies (Gamo et al., 2015; Srinivasan et al., 2004) have recognized the spread of deep-water hydrothermal plumes (1500-3000m) to the western Arabian Sea region, sourced from the West Sheba Ridge in the Gulf of Aden. In the western Arabian Sea, these deep hydrothermal plumes are observed to spread at the core depth of ~2200-2500m (refer to Figure 5a and 5b of Srinivasan et al., 2004), which is in general agreement with the depth range

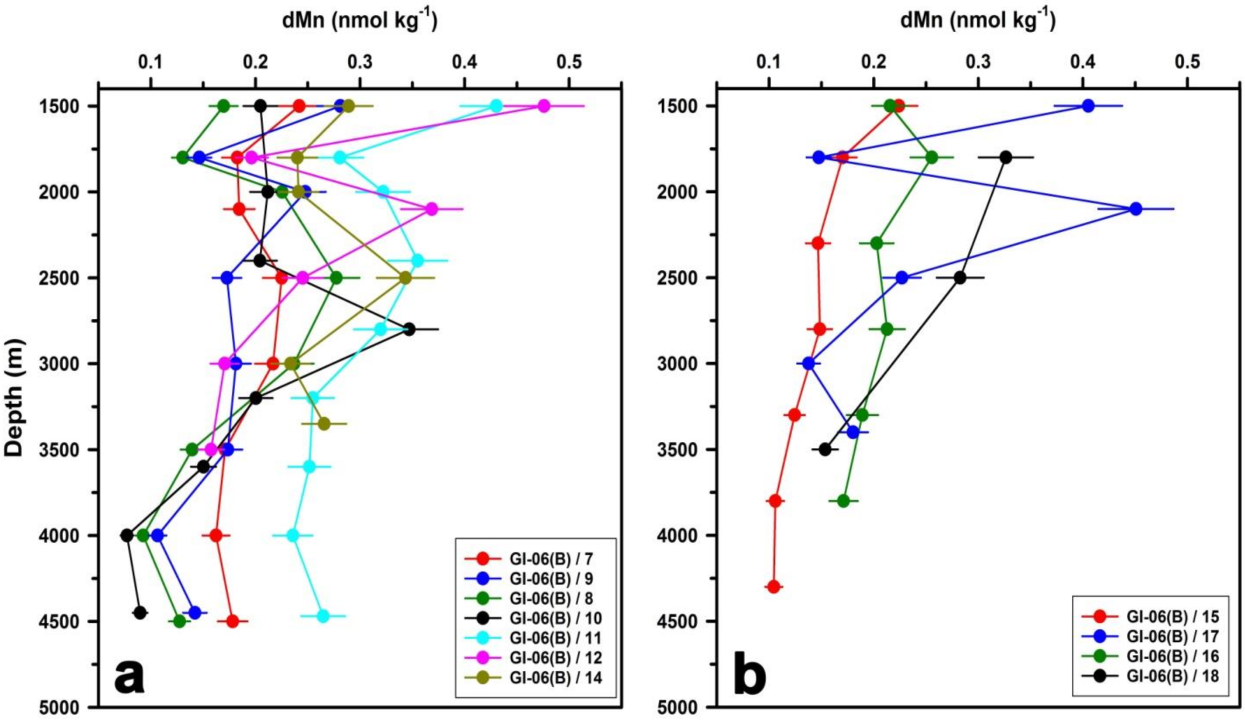

Fig. 5.8: (a) Deep-water (≥1500m) dMn distribution in the western part of the zonal transect (GI-06(B)/7 to GI-06(B)/14) in the southern Arabian Sea. **(b)** Deep-water dMn distribution in the central Arabian Sea (at stations GI-06(B)/15, 16, 17 and 18)

(2000-3000m) of observed dMn maxima along the central and western region of the zonal transect (stations GI-06(B)/7 to GI-06(B)/14 at 9°N, Fig. 5.8a). Deep-water dMn maximum concentration of ~3nM (at ~2200m) was observed at the exit of the Gulf of Aden (~13°N, 49°E, Gamo et al., 2015). The advection of these dMn-rich deep waters to the Arabian Sea could also explain the dMn maxima (0.23-0.37 nmol kg^{-1}) observed along the zonal transect. Relatively, high dMn anomalies at the western stations (GI-06(B)/10 to 14) compared to that in the central region (GI-06(B)/7 to 9) also agrees with the observed trend of the advective loss (due to water mass mixing) of plume signal (as seen in the δ^3He variations) towards the central Arabian Sea from the Gulf of Aden (Srinivasan et al., 2004).

Deep-water dMn concentration maximum (0.45 nmol kg^{-1}), ~3 fold compared to the background dMn levels (~0.16 nmol kg^{-1}), was observed (at 2100 m, Fig. 5.8b) at the station GI-06(B)/17, situated close to the Laxmi Ridge (Fig. 1). This increase in dMn levels does not seem to originate from the advection of the deep hydrothermal plume waters from southern to the central Arabian Sea since no such dMn anomalies were observed at stations further south, i.e., GI-06(B)/15 and 16 (Fig. 5.8b). Interestingly, the deep-water dMn maxima observed at GI-06(B)/17 correlates to the deep-water (at 2000m) dissolved Al maxima observed at a nearby station, GI-05/6, sampled during the Indian Geotraces cruise, GI-05 (refer to Fig. 4.3 of Chapter 4). This correlated increase in the dMn and dissolved Al concentrations strengthens the hypothesis pitched earlier (see section 4.5.3 of Chapter 4) of deep-water dissolved trace metal input from the margin sediments of the nearby Laxmi Ridge, which advects to the adjacent deep-water column.

5.4 Conclusion

Dissolved Mn data reported in this study enhances the limited full vertical water column data in the Arabian Sea and improves our understandings of the dMn cycling in the sea. The major findings of this study are listed below:

1) The relatively elevated surface dMn concentrations close to the western Indian coast correlates with the increase in the atmospheric mineral dust deposition towards the coast.

2) The dMn input fluxes from the deposition of atmospheric mineral dust to the surface waters are estimated, using the (earlier) observed aerosol-Mn concentration data, across different regions of the Arabian Sea and found to lie between 28.6-239.4 nmol m^{-2} d^{-1}. These estimates compare well with earlier (van Hulten et al., 2017) estimates based on the mineral dust deposition data of the Interaction with Chemistry and Aerosols (INCA) model.

3) The residence time of surface dMn in the Arabian Sea is constrained using the atmospheric dMn input and surface mixed layer dMn inventory, and assuming steady-stade condition. The residence time is found to vary in the range of 1.0-9.3 yr across the Arabian Sea.

3) Estimates on the dMn removal fluxes from the surface waters in the Arabian Sea suggest that the dMn is predominantly removed via *in situ* Mn-oxidation and passive particle scavenging, while removal by bio-assimilation plays a secondary role.

4) Significantly elevated dMn concentrations are observed in the oxygen-deficit thermocline depths in the denitrification zone of the Arabian Sea, resulting from the Mn release from the reductive dissolution of Mn-oxyhydroxides and/or remineralization of bio-assimilated Mn in the organic matter.

Chapter 6

Summary and future research perspectives

This thesis focuses on understanding the relative impact of diverse biogeochemical processes on the distribution of dAl and dMn in the Indian Ocean basins. Comprehensive understanding of the cycling of dAl and dMn in the seawater is an essential prerequisite for establishing the sensitivity of their distributions to different biogeochemical processes and thus, utilizing them as proxies for these processes. Towards the same, trace metal clean seawater sampling protocols and different analytical methodologies are established for the precise and accurate measurements of dAl and dMn over full vertical water column profiles along the GEOTRACES-India cruise transects in the northern (i.e., the Bay of Bengal, the Andaman Sea and the Arabian Sea), equatorial and subtropical gyre regions of the Indian Ocean. The major outcomes of all the studies carried out are summarized in the following sections.

6.1 Establishment of dAl and dMn analytical systems

Flow injection analysis systems are established in-house for the measurements of sub-nanomolar to nanomolar levels of dAl (Al-FIAS) and dMn (Mn-FIAS) in seawater. These portable systems offer an opportunity to carry out rapid onboard analysis of dAl and dMn and avoid the chances of sample contamination associated with transport and storage. Shore-based measurements of dMn (and other trace metals) were made using the seaFAST-integrated HR-ICP-MS system. Seawater reference samples (SAFe-S and GEOTRACES-GS and GD) were also analyzed for their dAl and dMn levels using these analytical systems. Good agreement between the measured and consensus values of dAl and dMn in these reference samples ensured the analytical accuracy. Further, comparable results for dAl and dMn vertical distributions at the crossover stations provided additional confidence in the seawater sampling and processing protocols.

6.2 Dissolved Al cycling in the Indian Ocean basins

6.2.1 The Bay of Bengal and the Andaman Sea

Dissolved Al (dAl) distribution throughout the vertical water column in the Bay of Bengal (BoB), particularly in the northern and central BoB, is predominantly controlled by the huge lithogenic sedimentary input from fluvial discharge and continental margins, followed by the subsequent release of labile Al from the sediments as they sink through the water column. The fractional Al solubility from the lithogenic sediment input in the BoB surface waters is estimated to lie in the range of 1.1-4.7%. Using these solubility estimates, the dAl input flux from the lithogenic sediment (atmospheric and fluvial) supply to the BoB surface waters is calculated to be 7.0 x 10^8-3.0 x 10^9 moles yr^{-1}, which is at least an order of magnitude larger than that estimated from Ganga-Brahmaputra freshwater supply. dAl input from the partial dissolution of resuspended insular shelf sediments of the Nicobar Islands and the advection of Indonesian Water from the Strait of Malacca control the dAl distribution in the surface mixed layer and the upper thermocline waters in the southern Andaman Sea. Near-uniform dAl distribution in the deeper waters (>1000m) at the center of the southern Andaman Sea indicate rapid ventilation of and vertical mixing in the deep waters compared to the scavenging removal of dAl.

6.2.2 The Arabian Sea

Surface water dAl distribution in the Arabian Sea (AS) exhibits significant seasonal variability. A strong east-west surface dAl concentration gradient is observed in the AS during the fall-intermonsoon sampling period. This gradient results from the relative changes in atmospheric dust deposition and primary production in the eastern and western AS during the transition from the summer monsoon to the fall-intermonsoon season. During the winter monsoon, the Northeast Monsoon Current is observed to transport the dAl-rich, low-salinity BoB surface waters to the southwest AS.

A simple non-steady-state model is constructed to simulate seasonal variations in surface dAl, for the first time, in a highly meteorological dynamic Arabian Sea basin. The model involves balancing the (annual) periodic variations in dAl input from the atmospheric Al deposition flux, estimated using the observed data on Al concentration in the marine boundary layer, and removal by passive scavenging, modeled considering first-order dAl removal. The solutions from the model have been obtained under both constant and variable (net primary production normalized) residence time (τ) conditions and are compared to the observed surface dAl distribution in the modeled region.

Overall, the model solutions explained the general trend and order of magnitude of the observed seasonal variations in the surface dAl concentrations. Such a model could be utilized as a first-order tool to estimate the seasonal variations in dust deposition flux using the surface dAl variations, and vice-versa.

The intrusion of the Persian Gulf Water and the Arabian Sea High Salinity Water is observed to influence the thermocline dAl distribution in the open AS by transporting the dAl-rich signature of their formation regions. However, the impact of these water masses is observed to be limited to the northern AS region during the sampling season of fall-intermonsoon. The advective input of dAl from the Arabian marginal seas (i.e., the Persian Gulf and the Red Sea) has implications for the possible supply of other lithogenic elements, including trace nutrients such as Fe and Mn, to the sub-surface depths of the AS and later to the euphotic layers via upwelling or convective mixing during the monsoon seasons. High-resolution sampling, both in space and time, in the marginal seas and the thermocline depths of the AS (e.g., Fe, Mn) is needed to better quantify the advective supply of dissolved Al and other lithogenic elements to the AS and its possible impact on the primary production.

6.2.3 The equatorial and subtropical gyre regions of the Indian Ocean

Surface dAl distribution in the eastern and central equatorial Indian Ocean region during the winter season is controlled by the advective mixing between the dAl-rich BoB surface waters and, relatively, dAl-poor surface waters of the southern Arabian Sea, under the influence of the strong Northeast Monsoon Current. This result implies that the correction for advective dAl supply is needed prior to exploiting the surface dAl distribution in these regions as the proxy of atmospheric mineral dust deposition. Close to the western Equatorial Indian Ocean boundary, a relative increase in the surface dAl levels suggests localized input of atmospheric mineral dust, sourced from the Somali coast.

Elevated surface dAl concentrations observed at the north-western reaches of the subtropical gyre are consistent with that reported earlier (Grand et al., 2015a) and represent the impact of the deposition of atmospheric mineral dust derived from the Australian continent. However, surface dAl enrichment observed in the present study (~14-18 nM) is about 1.5-2 times higher than that found during the previous investigation (~9-12 nM; Grand et al., 2015a). The apparent mismatch is suggested to arise due to inter-annual variation in the atmospheric dust input from the Australian sources. This hypothesis is supported by the estimated annual changes in dust storm event frequency over the Australian continent (Mackie et al., 2008). The advection of Indonesian Throughflow Water (ITW) is observed to bring dAl-rich waters (~5-10 nM) to the upper thermocline (100-500 m) depths in the northern subtropical gyre region. Such a pattern was also observed during the earlier studies (Grand et al., 2015b; Obata et al., 2004). Moreover, a comparison between the dAl data from the present and previous studies reveals an overall increasing trend in dAl concentrations over the depths of ITW intrusion with progressing sampling years. This trend is also consistent with the estimated overall increase in the ITW mean annual discharge (by 1 Sverdrup per decade) to the northern subtropical gyre region of the Indian Ocean.

The deep-water (>1500m) dAl concentrations in the Equatorial Indian Ocean are generally low and more uniform (~2-3 nM). A one-dimensional vertical advection-diffusion-scavenging model is used to constrain the deep-water dAl residence time and found to lie between the range of 92-141 yr. These estimates are comparable to those reported in the Pacific Ocean (50-200 yr; Orians and Bruland, 1986). Residence time estimates are essential to understand the relative role of different local or regional deep-water processes, operating at varying timescales, in governing the dAl distribution. Particularly, the interaction of deep waters with the margin sediments of different ridge systems, including the Ninety East Ridge, the Central Indian Ridge and the Carlsberg Ridge, in the equatorial and subtropical gyre regions of the Indian Ocean, and subsequent advection of these deep waters, are observed to influence the dAl distribution, at least, at the intra-basin scale.

6.3 Dissolved Mn cycling in the Arabian Sea

Dissolved Mn (dMn) concentrations are measured along the GEOTRACES-India cruise transect, GI-06(Leg B), in the southern and central Arabian Sea to understand the controls of different biogeochemical processes on dMn distribution. Surface dMn maxima are observed throughout the sampling transect and the highest surface dMn levels are found close to the south-western coast of India (3.8-4.2 nmol kg^{-1}) and in the low-salinity BoB surface water plume, encountered in the south-eastern Arabian Sea (~3.2 nmol kg^{-1}). Generally, dMn profiles show scavenged-type distribution, exhibiting a steep decrease in concentrations below the surface mixed layer (~50-200 m) and become low and more uniform (~0.1-0.3 nmol kg^{-1}) in the deeper waters (>1500 m). Exceptional to this general trend, dMn maxima are observed in the oxygen-deficit thermocline waters depths (~200-600 m) at the stations sampled close to the Indian coastal margin and in the perennial denitrification zone of the Arabian Sea. Diffusive dMn flux from the reducing sediments of the western Indian continental margin (Yadav, 1996) may explain the elevated dMn levels in the thermocline depths close to the margin. In the perennial denitrification zone of the Arabian Sea, highly elevated dMn concentrations (~3.2-5.0 nmol kg^{-1}) are found correlated with the depths of extreme dissolved oxygen depletion (<0.5 µM) in the thermocline waters. These dMn enrichments presumably result from the *in situ* reductive dissolution of Mn-oxyhydroxides over the thermocline water column. However, the degradation of biogenic matter in the thermocline waters may also contribute to the dMn input through the remineralization of assimilated Mn. A thorough investigation is needed to apportion the contributions from the reductive dissolution of Mn-oxyhydroxides and organic matter degradation.

The annual dMn input flux to the surface waters across the Arabian Sea from the dry deposition of atmospheric mineral dust is estimated to vary in the range of 28.6-239.4 nmol m^{-2} d^{-1}. Using these fluxes and integrated dMn inventory in the surface mixed layer, and considering the steady-state condition, the residence time of dMn in the surface waters of the Arabian Sea is estimated to be ranging from 1.0-9.3 yr. Output fluxes for surface dMn in the Arabian Sea are determined for different possible pathways, including removal via (1) bio-assimilation and (2) heterogeneous and/or biotically-mediated Mn-oxidation. The output fluxes calculations show that the removal through bio-assimilation (4.4-24.3 nmol m^{-2} d^{-1}) plays a secondary role. The estimated removal fluxes for surface dMn via Mn-oxidation (51.9-276.0 nmol m^{-2} d^{-1}) are comparable to the atmospheric input fluxes (28.6-239.4 nmol m^{-2} d^{-1}).

6.4 Future research perspectives

In this thesis, extensive measurements and studies along some of the strategic GEOTRACES-India sections have significantly improved the understanding of the biogeochemical cycling of dissolved Al and Mn in the Indian Ocean basins. The results from these studies have also brought out some interesting research problems to be addressed in the future and the same are listed below:

(1) The first-order balance between dAl input and removal fluxes in the surface waters of the BoB indicates that the lithogenic sediment supply by the G-B river system sets prominent control on the surface dAl distribution. In this regard, dAl measurements across the G-B river system estuaries are needed to better constrain the riverine fluxes and understand the role of estuarine processes (solute-particle interaction, biological cycling) in controlling the dAl distribution in the BoB water column.

(2) In this thesis, a simple non-steady-state model was constructed to simulate the seasonal changes in surface dAl concentrations over the western Arabian Sea. The model solves for the seasonal variations in surface dAl by computing the temporal changes in the rate of dAl input flux from the atmospheric dust deposition and first-order output rate. With constraints on the composition of Fe in aerosols over the Arabian Sea and the fractional solubility of Fe from dust deposition, such a model could be utilized to estimate the seasonal changes in atmospheric Fe input to the Arabian Sea. These estimates are crucial to study the influence of natural variations in the supply of micro-nutrients on primary production and its diversity.

(3) dMn input from the riverine (freshwater and sediment) discharge and diffusive Mn flux from the shelf sediments may play an essential role in governing dMn distribution in the surface ocean (Aguilar-Islas and Bruland, 2006; Homoky et al., 2016). Poor constraints on riverine dMn fluxes at the western Indian continental margin and the unavailability of dMn data over the shallow shelf (water depth <100m) region restricts the evaluation of the

relative contributions from fluvial discharge and shelf sediments to surface dMn inventory in the Arabian Sea. Data on dMn concentrations across the western Indian estuaries (particularly of the major rivers such as Indus, Krishna and Tapi) and at the sediment-water interface over the shallow shelf region are needed to explain the surface dMn budget in the Arabian Sea comprehensively.

(4) A significant increase in the dMn levels over the oxygen-deficit and denitrification thermocline depths is observed in the Arabian Sea. However, quantitative estimates on the relative dMn supply from *in situ* degradation of organic matter, reductive dissolution of Mn-oxyhydroxide particulate phases and lateral advective input from the reducing shelf and slope sediments are uncertain. Measurements of (1) particulate organic matter (carbon) export from the euphotic zone to the thermocline depths, (2) particulate Mn levels over the oxygen minimum depths and (3) dMn concentrations in the pore-waters of the reducing slope sediments are essential to constraint the inputs from different sources.

APPENDIX

Appendix A

Table A1: dAl data observed at different sampling depths for all the stations occupied during the GI-01, GI-05 and the GI-06(A)(A) cruises

Cruise	Station	Latitude (°N)	Longitude (°E)	Depth (m)	dAl (nM)
GI-01	1	16.53	83.57	2	26.0
GI-01	1	16.53	83.57	10	26.3
GI-01	1	16.53	83.57	25	15.5
GI-01	1	16.53	83.57	50	14.7
GI-01	1	16.53	83.57	75	10.9
GI-01	1	16.53	83.57	100	16.1
GI-01	1	16.53	83.57	150	13.4
GI-01	1	16.53	83.57	200	15.1
GI-01	1	16.53	83.57	300	10.9
GI-01	1	16.53	83.57	800	4.1
GI-01	1	16.53	83.57	1200	3.8
GI-01	1	16.53	83.57	1500	3.5
GI-01	1	16.53	83.57	2000	10.4
GI-01	2	19.94	87.30	2	47.1
GI-01	2	19.94	87.30	10	36.0
GI-01	2	19.94	87.30	25	18.7
GI-01	2	19.94	87.30	50	22.3
GI-01	2	19.94	87.30	75	13.3
GI-01	2	19.94	87.30	100	22.8
GI-01	2	19.94	87.30	150	12.6
GI-01	2	19.94	87.30	200	12.1
GI-01	2	19.94	87.30	500	9.3
GI-01	2	19.94	87.30	800	4.2
GI-01	2	19.94	87.30	1000	4.6
GI-01	3	18.01	87.00	2	28.2
GI-01	3	18.01	87.00	25	19.8
GI-01	3	18.01	87.00	50	24.6

GI-01	3	18.01	87.00	75	13.1
GI-01	3	18.01	87.00	100	13.3
GI-01	3	18.01	87.00	150	18.9
GI-01	3	18.01	87.00	200	8.7
GI-01	3	18.01	87.00	500	6.5
GI-01	3	18.01	87.00	800	5.3
GI-01	3	18.01	87.00	1200	3.7
GI-01	3	18.01	87.00	1600	6.0
GI-01	3	18.01	87.00	2400	13.7
GI-01	4	16.00	87.00	2	26.9
GI-01	4	16.00	87.00	10	28.5
GI-01	4	16.00	87.00	25	24.3
GI-01	4	16.00	87.00	50	12.3
GI-01	4	16.00	87.00	75	7.3
GI-01	4	16.00	87.00	100	17.9
GI-01	4	16.00	87.00	150	16.8
GI-01	4	16.00	87.00	200	6.7
GI-01	4	16.00	87.00	800	7.1
GI-01	4	16.00	87.00	1200	5.1
GI-01	4	16.00	87.00	1800	5.7
GI-01	4	16.00	87.00	2000	3.6
GI-01	4	16.00	87.00	2400	3.0
GI-01	4	16.00	87.00	2700	14.8
GI-01	5	14.00	87.00	2	27.8
GI-01	5	14.00	87.00	10	25.8
GI-01	5	14.00	87.00	25	27.8
GI-01	5	14.00	87.00	50	27.2
GI-01	5	14.00	87.00	75	10.0
GI-01	5	14.00	87.00	100	16.5
GI-01	5	14.00	87.00	150	11.0
GI-01	5	14.00	87.00	200	9.9
GI-01	5	14.00	87.00	300	5.5
GI-01	5	14.00	87.00	500	4.4
GI-01	5	14.00	87.00	1200	5.0

GI-01	5	14.00	87.00	1500	5.0
GI-01	5	14.00	87.00	2000	5.6
GI-01	5	14.00	87.00	2500	2.7
GI-01	5	14.00	87.00	3000	4.9
GI-01	6	11.01	87.00	2	23.0
GI-01	6	11.01	87.00	10	21.2
GI-01	6	11.01	87.00	25	16.6
GI-01	6	11.01	87.00	50	16.8
GI-01	6	11.01	87.00	75	12.7
GI-01	6	11.01	87.00	100	13.2
GI-01	6	11.01	87.00	150	9.2
GI-01	6	11.01	87.00	200	9.0
GI-01	6	11.01	87.00	225	4.6
GI-01	6	11.01	87.00	250	6.3
GI-01	6	11.01	87.00	275	8.0
GI-01	6	11.01	87.00	300	7.4
GI-01	6	11.01	87.00	325	8.5
GI-01	6	11.01	87.00	350	5.4
GI-01	6	11.01	87.00	450	6.6
GI-01	6	11.01	87.00	475	4.7
GI-01	6	11.01	87.00	500	7.2
GI-01	6	11.01	87.00	800	4.6
GI-01	6	11.01	87.00	1000	4.0
GI-01	6	11.01	87.00	1200	5.3
GI-01	6	11.01	87.00	1500	4.8
GI-01	6	11.01	87.00	2000	2.5
GI-01	6	11.01	87.00	3000	2.9
GI-01	6	11.01	87.00	3350	9.7
GI-01	7	8.02	87.00	2	13.2
GI-01	7	8.02	87.00	10	10.6
GI-01	7	8.02	87.00	25	11.2
GI-01	7	8.02	87.00	50	10.1
GI-01	7	8.02	87.00	75	8.6
GI-01	7	8.02	87.00	100	12.6

GI-01	7	8.02	87.00	150	9.5
GI-01	7	8.02	87.00	200	6.8
GI-01	7	8.02	87.00	300	5.8
GI-01	7	8.02	87.00	800	6.2
GI-01	7	8.02	87.00	1000	4.2
GI-01	7	8.02	87.00	1200	3.4
GI-01	7	8.02	87.00	1500	2.7
GI-01	7	8.02	87.00	2000	1.9
GI-01	7	8.02	87.00	3000	3.0
GI-01	7	8.02	87.00	3400	2.9
GI-01	7	8.02	87.00	3650	3.1
GI-01	8	5.01	87.00	2	19.2
GI-01	8	5.01	87.00	10	18.9
GI-01	8	5.01	87.00	25	10.6
GI-01	8	5.01	87.00	50	10.1
GI-01	8	5.01	87.00	75	5.9
GI-01	8	5.01	87.00	100	10.7
GI-01	8	5.01	87.00	150	5.4
GI-01	8	5.01	87.00	200	4.2
GI-01	8	5.01	87.00	500	3.4
GI-01	8	5.01	87.00	800	4.1
GI-01	8	5.01	87.00	1000	4.7
GI-01	8	5.01	87.00	2000	3.4
GI-01	8	5.01	87.00	2500	1.9
GI-01	8	5.01	87.00	2950	2.7
GI-01	8	5.01	87.00	3500	2.2
GI-01	8	5.01	87.00	4000	3.8
GI-01	9	2.01	87.00	2	11.3
GI-01	9	2.01	87.00	10	10.3
GI-01	9	2.01	87.00	25	10.6
GI-01	9	2.01	87.00	50	6.1
GI-01	9	2.01	87.00	75	2.8
GI-01	9	2.01	87.00	100	4.5
GI-01	9	2.01	87.00	150	3.8

GI-01	9	2.01	87.00	200	4.9
GI-01	9	2.01	87.00	300	3.7
GI-01	9	2.01	87.00	500	2.8
GI-01	9	2.01	87.00	800	3.0
GI-01	9	2.01	87.00	1000	2.8
GI-01	9	2.01	87.00	1200	2.4
GI-01	9	2.01	87.00	1500	2.2
GI-01	9	2.01	87.00	2500	3.5
GI-01	9	2.01	87.00	3000	4.7
GI-01	9	2.01	87.00	4000	2.3
GI-01	9	2.01	87.00	4300	3.1
GI-01	10	-3.50	84.00	2	14.0
GI-01	10	-3.50	84.00	10	13.4
GI-01	10	-3.50	84.00	25	7.0
GI-01	10	-3.50	84.00	50	3.5
GI-01	10	-3.50	84.00	75	2.7
GI-01	10	-3.50	84.00	100	3.9
GI-01	10	-3.50	84.00	150	3.1
GI-01	10	-3.50	84.00	200	2.8
GI-01	10	-3.50	84.00	500	3.0
GI-01	10	-3.50	84.00	1000	4.1
GI-01	10	-3.50	84.00	1200	2.8
GI-01	10	-3.50	84.00	1500	2.1
GI-01	10	-3.50	84.00	2500	2.4
GI-01	10	-3.50	84.00	3000	2.5
GI-01	10	-3.50	84.00	3500	2.5
GI-01	10	-3.50	84.00	4000	3.6
GI-01	10	-3.50	84.00	4500	2.6
GI-01	10	-3.50	84.00	4800	3.4
GI-01	11	-8.50	80.80	2	13.7
GI-01	11	-8.50	80.80	10	13.9
GI-01	11	-8.50	80.80	25	7.9
GI-01	11	-8.50	80.80	50	9.5
GI-01	11	-8.50	80.80	150	5.4

GI-01	11	-8.50	80.80	200	5.9
GI-01	11	-8.50	80.80	300	4.6
GI-01	11	-8.50	80.80	500	3.8
GI-01	11	-8.50	80.80	1000	2.2
GI-01	11	-8.50	80.80	1200	2.5
GI-01	11	-8.50	80.80	1500	3.4
GI-01	11	-8.50	80.80	1800	2.0
GI-01	11	-8.50	80.80	2500	1.8
GI-01	11	-8.50	80.80	3000	2.7
GI-01	11	-8.50	80.80	3500	3.2
GI-01	11	-8.50	80.80	4000	4.2
GI-01	11	-8.50	80.80	4500	3.7
GI-01	11	-8.50	80.80	5100	3.9
GI-01	12	-14.49	77.00	10	18.3
GI-01	12	-14.49	77.00	50	14.5
GI-01	12	-14.49	77.00	75	12.6
GI-01	12	-14.49	77.00	100	10.0
GI-01	12	-14.49	77.00	150	11.1
GI-01	12	-14.49	77.00	300	6.2
GI-01	12	-14.49	77.00	500	3.6
GI-01	12	-14.49	77.00	800	2.8
GI-01	12	-14.49	77.00	1000	3.0
GI-01	12	-14.49	77.00	1200	1.9
GI-01	12	-14.49	77.00	1500	2.1
GI-01	12	-14.49	77.00	1800	2.6
GI-01	12	-14.49	77.00	2500	3.0
GI-01	12	-14.49	77.00	3000	2.5
GI-01	12	-14.49	77.00	3500	2.8
GI-01	12	-14.49	77.00	4000	2.8
GI-01	12	-14.49	77.00	4500	3.2
GI-01	12	-14.49	77.00	5100	3.1
GI-01	16	-25.32	70.04	10	8.6
GI-01	16	-25.32	70.04	25	7.5
GI-01	16	-25.32	70.04	50	6.7

GI-01	16	-25.32	70.04	75	5.5
GI-01	16	-25.32	70.04	100	8.1
GI-01	16	-25.32	70.04	150	4.7
GI-01	16	-25.32	70.04	200	5.8
GI-01	16	-25.32	70.04	300	6.1
GI-01	16	-25.32	70.04	500	5.2
GI-01	16	-25.32	70.04	800	4.1
GI-01	16	-25.32	70.04	1200	3.4
GI-01	16	-25.32	70.04	1500	2.1
GI-01	16	-25.32	70.04	2000	3.8
GI-01	16	-25.32	70.04	2260	5.3

Cruise	**Station**	**Latitude (°N)**	**Longitude (°E)**	**Depth (m)**	**dAl (nM)**
GI-06(A)	1	12.27	81.25	2	23.3
GI-06(A)	1	12.27	81.25	10	26.8
GI-06(A)	1	12.27	81.25	25	14.7
GI-06(A)	1	12.27	81.25	50	10.6
GI-06(A)	1	12.27	81.25	75	10.0
GI-06(A)	1	12.27	81.25	100	9.9
GI-06(A)	1	12.27	81.25	200	6.0
GI-06(A)	1	12.27	81.25	300	5.9
GI-06(A)	1	12.27	81.25	600	4.7
GI-06(A)	1	12.27	81.25	800	4.2
GI-06(A)	1	12.27	81.25	1000	3.5
GI-06(A)	1	12.27	81.25	1200	4.1
GI-06(A)	1	12.27	81.25	1500	5.6
GI-06(A)	1	12.27	81.25	2000	4.0
GI-06(A)	1	12.27	81.25	2400	5.9
GI-06(A)	1	12.27	81.25	2800	5.2
GI-06(A)	1	12.27	81.25	3200	5.8
GI-06(A)	2	10.48	83.50	2	14.6
GI-06(A)	2	10.48	83.50	10	14.2
GI-06(A)	2	10.48	83.50	20	14.0

GI-06(A)	2	10.48	83.50	30	13.0
GI-06(A)	2	10.48	83.50	50	8.1
GI-06(A)	2	10.48	83.50	75	7.2
GI-06(A)	2	10.48	83.50	100	6.5
GI-06(A)	2	10.48	83.50	150	5.5
GI-06(A)	2	10.48	83.50	200	4.8
GI-06(A)	2	10.48	83.50	300	4.2
GI-06(A)	2	10.48	83.50	500	3.5
GI-06(A)	2	10.48	83.50	800	3.6
GI-06(A)	2	10.48	83.50	1000	3.0
GI-06(A)	2	10.48	83.50	1200	2.6
GI-06(A)	2	10.48	83.50	1500	2.4
GI-06(A)	2	10.48	83.50	1800	2.1
GI-06(A)	2	10.48	83.50	2000	1.8
GI-06(A)	2	10.48	83.50	2400	1.9
GI-06(A)	2	10.48	83.50	2800	2.5
GI-06(A)	2	10.48	83.50	3200	1.8
GI-06(A)	3	8.50	86.00	5	10.7
GI-06(A)	3	8.50	86.00	15	8.7
GI-06(A)	3	8.50	86.00	50	8.3
GI-06(A)	3	8.50	86.00	75	10.6
GI-06(A)	3	8.50	86.00	100	8.7
GI-06(A)	3	8.50	86.00	150	8.0
GI-06(A)	3	8.50	86.00	200	4.3
GI-06(A)	3	8.50	86.00	300	4.8
GI-06(A)	3	8.50	86.00	500	2.4
GI-06(A)	3	8.50	86.00	800	3.0
GI-06(A)	3	8.50	86.00	1000	2.7
GI-06(A)	3	8.50	86.00	1200	3.0
GI-06(A)	3	8.50	86.00	1800	1.5
GI-06(A)	3	8.50	86.00	2500	2.5
GI-06(A)	3	8.50	86.00	3000	2.7
GI-06(A)	4	8.15	89.15	5	13.8
GI-06(A)	4	8.15	89.15	10	13.6

GI-06(A)	4	8.15	89.15	20	13.4
GI-06(A)	4	8.15	89.15	50	11.9
GI-06(A)	4	8.15	89.15	60	11.8
GI-06(A)	4	8.15	89.15	70	12.1
GI-06(A)	4	8.15	89.15	100	11.6
GI-06(A)	4	8.15	89.15	150	8.8
GI-06(A)	4	8.15	89.15	200	6.3
GI-06(A)	4	8.15	89.15	300	3.9
GI-06(A)	4	8.15	89.15	500	3.4
GI-06(A)	4	8.15	89.15	800	3.0
GI-06(A)	4	8.15	89.15	1000	2.7
GI-06(A)	4	8.15	89.15	1200	2.2
GI-06(A)	4	8.15	89.15	1500	2.2
GI-06(A)	4	8.15	89.15	1800	1.9
GI-06(A)	4	8.15	89.15	2000	2.0
GI-06(A)	4	8.15	89.15	2500	2.3
GI-06(A)	4	8.15	89.15	2800	1.8
GI-06(A)	4	8.15	89.15	3100	1.8
GI-06(A)	4	8.15	89.15	3350	2.2
GI-06(A)	5	7.83	92.00	5	24.5
GI-06(A)	5	7.83	92.00	15	23.5
GI-06(A)	5	7.83	92.00	25	19.6
GI-06(A)	5	7.83	92.00	50	12.1
GI-06(A)	5	7.83	92.00	75	9.4
GI-06(A)	5	7.83	92.00	100	8.3
GI-06(A)	5	7.83	92.00	150	7.0
GI-06(A)	5	7.83	92.00	200	7.6
GI-06(A)	5	7.83	92.00	300	5.2
GI-06(A)	5	7.83	92.00	500	4.7
GI-06(A)	5	7.83	92.00	1200	3.8
GI-06(A)	5	7.83	92.00	1500	4.1
GI-06(A)	5	7.83	92.00	1800	2.7
GI-06(A)	5	7.83	92.00	2000	2.5
GI-06(A)	5	7.83	92.00	2500	2.6

GI-06(A)	5	7.83	92.00	3000	3.3
GI-06(A)	5	7.83	92.00	3300	4.4
GI-06(A)	6	7.49	95.13	2	26.3
GI-06(A)	6	7.49	95.13	10	22.1
GI-06(A)	6	7.49	95.13	25	23.8
GI-06(A)	6	7.49	95.13	50	18.2
GI-06(A)	6	7.49	95.13	100	10.0
GI-06(A)	6	7.49	95.13	150	6.5
GI-06(A)	6	7.49	95.13	200	6.1
GI-06(A)	6	7.49	95.13	300	5.2
GI-06(A)	6	7.49	95.13	600	4.1
GI-06(A)	6	7.49	95.13	800	4.0
GI-06(A)	6	7.49	95.13	1000	3.4
GI-06(A)	6	7.49	95.13	1500	3.7
GI-06(A)	6	7.49	95.13	1800	3.7
GI-06(A)	6	7.49	95.13	2000	3.4
GI-06(A)	6	7.49	95.13	2400	3.7
GI-06(A)	7	6.65	94.11	5	43.0
GI-06(A)	7	6.65	94.11	10	46.4
GI-06(A)	7	6.65	94.11	25	48.6
GI-06(A)	7	6.65	94.11	50	15.6
GI-06(A)	7	6.65	94.11	75	17.6
GI-06(A)	7	6.65	94.11	100	13.9
GI-06(A)	7	6.65	94.11	150	7.3
GI-06(A)	7	6.65	94.11	200	4.8
GI-06(A)	7	6.65	94.11	300	4.5
GI-06(A)	7	6.65	94.11	500	3.7
GI-06(A)	7	6.65	94.11	800	4.9
GI-06(A)	7	6.65	94.11	1000	5.2
GI-06(A)	8	6.28	93.00	5	46.2
GI-06(A)	8	6.28	93.00	10	51.2
GI-06(A)	8	6.28	93.00	25	47.6
GI-06(A)	8	6.28	93.00	50	21.1
GI-06(A)	8	6.28	93.00	75	16.2

GI-06(A)	8	6.28	93.00	100	10.4
GI-06(A)	8	6.28	93.00	150	6.5
GI-06(A)	8	6.28	93.00	200	5.4
GI-06(A)	8	6.28	93.00	300	6.2
GI-06(A)	8	6.28	93.00	600	4.2
GI-06(A)	8	6.28	93.00	800	4.1
GI-06(A)	8	6.28	93.00	1000	3.6
GI-06(A)	8	6.28	93.00	1200	3.1
GI-06(A)	8	6.28	93.00	1400	3.1
GI-06(A)	8	6.28	93.00	1600	2.5
GI-06(A)	9	5.78	91.50	5	21.5
GI-06(A)	9	5.78	91.50	10	23.0
GI-06(A)	9	5.78	91.50	25	21.3
GI-06(A)	9	5.78	91.50	50	13.0
GI-06(A)	9	5.78	91.50	75	12.9
GI-06(A)	9	5.78	91.50	100	11.3
GI-06(A)	9	5.78	91.50	150	7.3
GI-06(A)	9	5.78	91.50	200	5.3
GI-06(A)	9	5.78	91.50	300	4.7
GI-06(A)	9	5.78	91.50	500	4.5
GI-06(A)	9	5.78	91.50	800	4.7
GI-06(A)	9	5.78	91.50	1000	4.9
GI-06(A)	9	5.78	91.50	1200	3.1
GI-06(A)	9	5.78	91.50	1500	3.5
GI-06(A)	9	5.78	91.50	1800	3.0
GI-06(A)	9	5.78	91.50	2000	2.5
GI-06(A)	9	5.78	91.50	2500	2.1
GI-06(A)	9	5.78	91.50	3000	2.5
GI-06(A)	9	5.78	91.50	3300	3.1
GI-06(A)	9	5.78	91.50	3600	3.1
GI-06(A)	10	5.08	89.50	5	7.3
GI-06(A)	10	5.08	89.50	10	7.4
GI-06(A)	10	5.08	89.50	25	7.3
GI-06(A)	10	5.08	89.50	50	7.3

GI-06(A)	10	5.08	89.50	75	7.0
GI-06(A)	10	5.08	89.50	100	6.9
GI-06(A)	10	5.08	89.50	200	5.5
GI-06(A)	10	5.08	89.50	300	5.3
GI-06(A)	10	5.08	89.50	600	3.9
GI-06(A)	10	5.08	89.50	800	3.9
GI-06(A)	10	5.08	89.50	1000	3.9
GI-06(A)	10	5.08	89.50	1200	2.7
GI-06(A)	10	5.08	89.50	1500	3.3
GI-06(A)	10	5.08	89.50	1800	2.9
GI-06(A)	10	5.08	89.50	2000	2.5
GI-06(A)	10	5.08	89.50	2500	2.3
GI-06(A)	10	5.08	89.50	3000	3.3
GI-06(A)	10	5.08	89.50	3200	3.1
GI-06(A)	11	4.70	88.50	5	13.5
GI-06(A)	11	4.70	88.50	10	12.9
GI-06(A)	11	4.70	88.50	25	13.8
GI-06(A)	11	4.70	88.50	50	10.2
GI-06(A)	11	4.70	88.50	75	6.1
GI-06(A)	11	4.70	88.50	100	7.5
GI-06(A)	11	4.70	88.50	150	5.6
GI-06(A)	11	4.70	88.50	200	5.1
GI-06(A)	11	4.70	88.50	300	5.1
GI-06(A)	11	4.70	88.50	500	5.0
GI-06(A)	11	4.70	88.50	800	4.8
GI-06(A)	11	4.70	88.50	1000	4.7
GI-06(A)	11	4.70	88.50	1200	3.6
GI-06(A)	11	4.70	88.50	1500	2.3
GI-06(A)	11	4.70	88.50	1800	2.4
GI-06(A)	11	4.70	88.50	2000	1.9
GI-06(A)	11	4.70	88.50	2500	2.1
GI-06(A)	11	4.70	88.50	3000	2.4
GI-06(A)	11	4.70	88.50	3500	2.3
GI-06(A)	11	4.70	88.50	3800	2.4

GI-06(A)	12	4.15	87.00	5	15.0
GI-06(A)	12	4.15	87.00	10	15.7
GI-06(A)	12	4.15	87.00	25	11.9
GI-06(A)	12	4.15	87.00	50	5.4
GI-06(A)	12	4.15	87.00	75	8.0
GI-06(A)	12	4.15	87.00	100	9.8
GI-06(A)	12	4.15	87.00	150	6.2
GI-06(A)	12	4.15	87.00	200	5.8
GI-06(A)	12	4.15	87.00	300	4.9
GI-06(A)	12	4.15	87.00	500	3.8
GI-06(A)	12	4.15	87.00	800	3.2
GI-06(A)	12	4.15	87.00	1000	3.4
GI-06(A)	12	4.15	87.00	1200	2.8
GI-06(A)	12	4.15	87.00	1500	2.3
GI-06(A)	12	4.15	87.00	1800	2.2
GI-06(A)	12	4.15	87.00	2000	2.6
GI-06(A)	12	4.15	87.00	2500	2.0
GI-06(A)	12	4.15	87.00	3000	2.3
GI-06(A)	12	4.15	87.00	3500	2.5
GI-06(A)	12	4.15	87.00	3900	4.2
GI-06(A)	13	3.60	85.50	5	8.4
GI-06(A)	13	3.60	85.50	10	8.1
GI-06(A)	13	3.60	85.50	25	4.7
GI-06(A)	13	3.60	85.50	50	3.3
GI-06(A)	13	3.60	85.50	75	3.4
GI-06(A)	13	3.60	85.50	100	5.1
GI-06(A)	13	3.60	85.50	150	4.8
GI-06(A)	13	3.60	85.50	200	4.6
GI-06(A)	13	3.60	85.50	300	3.5
GI-06(A)	13	3.60	85.50	600	3.4
GI-06(A)	13	3.60	85.50	800	2.8
GI-06(A)	13	3.60	85.50	1000	3.7
GI-06(A)	13	3.60	85.50	1200	3.2
GI-06(A)	13	3.60	85.50	1500	2.3

GI-06(A)	13	3.60	85.50	1800	2.2
GI-06(A)	13	3.60	85.50	2000	2.4
GI-06(A)	13	3.60	85.50	2500	2.1
GI-06(A)	13	3.60	85.50	3000	1.9
GI-06(A)	13	3.60	85.50	3500	2.4
GI-06(A)	13	3.60	85.50	4000	3.0
GI-06(A)	14	3.00	84.00	5	5.8
GI-06(A)	14	3.00	84.00	10	6.2
GI-06(A)	14	3.00	84.00	25	5.5
GI-06(A)	14	3.00	84.00	40	5.4
GI-06(A)	14	3.00	84.00	50	5.1
GI-06(A)	14	3.00	84.00	60	4.8
GI-06(A)	14	3.00	84.00	75	5.5
GI-06(A)	14	3.00	84.00	100	7.0
GI-06(A)	14	3.00	84.00	200	4.5
GI-06(A)	14	3.00	84.00	300	5.0
GI-06(A)	14	3.00	84.00	500	4.9
GI-06(A)	14	3.00	84.00	800	2.8
GI-06(A)	14	3.00	84.00	1000	3.3
GI-06(A)	14	3.00	84.00	1200	2.9
GI-06(A)	14	3.00	84.00	1500	2.3
GI-06(A)	14	3.00	84.00	1800	2.5
GI-06(A)	14	3.00	84.00	2000	2.1
GI-06(A)	14	3.00	84.00	2500	2.8
GI-06(A)	14	3.00	84.00	3000	2.4
GI-06(A)	14	3.00	84.00	3500	2.4
GI-06(A)	14	3.00	84.00	3800	2.1
GI-06(A)	14	3.00	84.00	4150	3.3
GI-06(A)	17	3.97	79.43	5	5.4
GI-06(A)	17	3.97	79.43	10	4.3
GI-06(A)	17	3.97	79.43	25	4.3
GI-06(A)	17	3.97	79.43	50	4.1
GI-06(A)	17	3.97	79.43	75	2.6
GI-06(A)	17	3.97	79.43	100	4.1

GI-06(A)	17	3.97	79.43	150	4.6
GI-06(A)	17	3.97	79.43	200	3.4
GI-06(A)	17	3.97	79.43	300	4.3
GI-06(A)	17	3.97	79.43	500	3.7
GI-06(A)	17	3.97	79.43	800	2.7
GI-06(A)	17	3.97	79.43	1000	2.7
GI-06(A)	17	3.97	79.43	1200	2.7
GI-06(A)	17	3.97	79.43	1500	1.9
GI-06(A)	17	3.97	79.43	1800	3.7
GI-06(A)	17	3.97	79.43	2000	2.3
GI-06(A)	17	3.97	79.43	2500	2.6
GI-06(A)	17	3.97	79.43	3000	2.1
GI-06(A)	17	3.97	79.43	3500	2.5
GI-06(A)	17	3.97	79.43	3800	2.4
GI-06(A)	17	3.97	79.43	4100	2.3
GI-06(A)	18	4.00	77.99	5	4.6
GI-06(A)	18	4.00	77.99	10	4.7
GI-06(A)	18	4.00	77.99	25	5.3
GI-06(A)	18	4.00	77.99	50	4.4
GI-06(A)	18	4.00	77.99	75	2.4
GI-06(A)	18	4.00	77.99	100	3.8
GI-06(A)	18	4.00	77.99	150	4.4
GI-06(A)	18	4.00	77.99	200	3.8
GI-06(A)	18	4.00	77.99	300	3.5
GI-06(A)	18	4.00	77.99	500	2.7
GI-06(A)	18	4.00	77.99	1000	2.1
GI-06(A)	18	4.00	77.99	1200	2.0
GI-06(A)	18	4.00	77.99	1500	2.0
GI-06(A)	18	4.00	77.99	1800	2.4
GI-06(A)	18	4.00	77.99	2000	1.8
GI-06(A)	18	4.00	77.99	2500	2.0
GI-06(A)	18	4.00	77.99	2800	2.2
GI-06(A)	19	4.00	76.49	5	2.6
GI-06(A)	19	4.00	76.49	10	2.9

GI-06(A)	19	4.00	76.49	25	2.6
GI-06(A)	19	4.00	76.49	50	2.2
GI-06(A)	19	4.00	76.49	75	3.1
GI-06(A)	19	4.00	76.49	100	4.8
GI-06(A)	19	4.00	76.49	150	4.7
GI-06(A)	19	4.00	76.49	200	3.8
GI-06(A)	19	4.00	76.49	300	3.3
GI-06(A)	19	4.00	76.49	500	3.4
GI-06(A)	19	4.00	76.49	800	3.2
GI-06(A)	19	4.00	76.49	1000	3.1
GI-06(A)	19	4.00	76.49	1200	2.4
GI-06(A)	19	4.00	76.49	1500	2.5
GI-06(A)	19	4.00	76.49	1800	2.5
GI-06(A)	19	4.00	76.49	2000	2.2
GI-06(A)	19	4.00	76.49	2500	2.0
GI-06(A)	19	4.00	76.49	2800	1.7
GI-06(A)	19	4.00	76.49	3000	2.1
GI-06(A)	20	4.03	74.84	2	4.8
GI-06(A)	20	4.03	74.84	10	3.9
GI-06(A)	20	4.03	74.84	25	4.4
GI-06(A)	20	4.03	74.84	50	3.3
GI-06(A)	20	4.03	74.84	75	2.7
GI-06(A)	20	4.03	74.84	100	4.0
GI-06(A)	20	4.03	74.84	150	4.5
GI-06(A)	20	4.03	74.84	200	4.3
GI-06(A)	20	4.03	74.84	300	3.6
GI-06(A)	20	4.03	74.84	600	3.8
GI-06(A)	20	4.03	74.84	800	4.4
GI-06(A)	20	4.03	74.84	1000	3.2
GI-06(A)	20	4.03	74.84	1200	2.5
GI-06(A)	20	4.03	74.84	1500	2.8
GI-06(A)	20	4.03	74.84	1800	3.1
GI-06(A)	20	4.03	74.84	2000	2.2
GI-06(A)	20	4.03	74.84	2500	2.6

GI-06(A)	21	6.32	74.47	5	22.2
GI-06(A)	21	6.32	74.47	10	23.2
GI-06(A)	21	6.32	74.47	25	22.0
GI-06(A)	21	6.32	74.47	50	9.9
GI-06(A)	21	6.32	74.47	75	11.0
GI-06(A)	21	6.32	74.47	100	6.3
GI-06(A)	21	6.32	74.47	150	4.5
GI-06(A)	21	6.32	74.47	200	4.3
GI-06(A)	21	6.32	74.47	300	3.6
GI-06(A)	21	6.32	74.47	500	3.7
GI-06(A)	21	6.32	74.47	800	4.0
GI-06(A)	21	6.32	74.47	1000	3.0
GI-06(A)	21	6.32	74.47	1200	2.8
GI-06(A)	21	6.32	74.47	1500	2.8
GI-06(A)	21	6.32	74.47	1800	3.0
GI-06(A)	21	6.32	74.47	2200	2.3
GI-06(A)	21	6.32	74.47	2600	2.5
GI-06(A)	22	8.44	74.10	5	18.4
GI-06(A)	22	8.44	74.10	10	18.9
GI-06(A)	22	8.44	74.10	25	14.6
GI-06(A)	22	8.44	74.10	50	10.0
GI-06(A)	22	8.44	74.10	75	7.9
GI-06(A)	22	8.44	74.10	100	6.5
GI-06(A)	22	8.44	74.10	150	4.5
GI-06(A)	22	8.44	74.10	200	4.0
GI-06(A)	22	8.44	74.10	300	4.4
GI-06(A)	22	8.44	74.10	500	4.3
GI-06(A)	22	8.44	74.10	800	3.2
GI-06(A)	22	8.44	74.10	1000	3.5
GI-06(A)	22	8.44	74.10	1200	3.0
GI-06(A)	22	8.44	74.10	1500	2.6
GI-06(A)	22	8.44	74.10	1800	2.5
GI-06(A)	22	8.44	74.10	2200	2.5
GI-06(A)	22	8.44	74.10	2600	2.4

GI-06(A)	24	11.03	74.03	5	20.4
GI-06(A)	24	11.03	74.03	10	20.5
GI-06(A)	24	11.03	74.03	25	10.0
GI-06(A)	24	11.03	74.03	50	8.6
GI-06(A)	24	11.03	74.03	75	7.2
GI-06(A)	24	11.03	74.03	100	7.0
GI-06(A)	24	11.03	74.03	150	6.0
GI-06(A)	24	11.03	74.03	200	4.8
GI-06(A)	24	11.03	74.03	300	5.2
GI-06(A)	24	11.03	74.03	500	4.4
GI-06(A)	24	11.03	74.03	600	5.4
GI-06(A)	24	11.03	74.03	800	3.6
GI-06(A)	24	11.03	74.03	1000	3.6
GI-06(A)	24	11.03	74.03	1200	3.5
GI-06(A)	24	11.03	74.03	1400	3.5
GI-06(A)	24	11.03	74.03	1600	3.5
GI-06(A)	24	11.03	74.03	1800	3.3

Cruise	Station	Longitude (°E)	Latitude (°N)	Depth (m)	dAl (nM)
GI-05	1	73.10	15.43	5	13.0
				20	9.9
				35	9.4
				50	7.5
				65	10.0
				80	28.1
GI-05	2	72.03	15.46	5	20.9
				15	22.3
				25	21.0
				50	9.5
				75	9.3
				100	7.0
				150	5.2
				200	5.6
				300	4.5
				500	4.0
				800	3.6
				1000	3.3
				1200	3.4

				1500	3.5
				1900	3.7
GI-05	3	70.50	15.45	5	12.7
				15	12.4
				25	11.9
				50	5.7
				75	5.9
				150	4.6
				200	3.8
				300	3.9
				500	3.3
				800	2.8
				1000	3.4
				1200	2.8
				1500	2.7
				1800	2.1
				2000	2.2
				2500	3.8
				3000	2.6
				3300	1.8
GI-05	4	69.00	17.30	5	6.9
				15	6.1
				25	5.6
				50	9.2
				60	5.2
				75	6.1
				100	4.9
				125	4.4
				150	4.7
				200	5.0
				300	4.2
				500	4.5
				800	2.5
				1000	3.4
				1200	3.6
				1500	2.7
				1800	2.7
				2000	2.3
				2500	2.6
				3000	2.2
				3300	1.8
GI-05	5	65.00	15.35	5	7.3

				25	6.5
				50	3.7
				65	4.2
				75	5.6
				100	5.8
				125	4.4
				150	4.2
				200	4.3
				300	4.8
				500	4.0
				800	3.1
				1000	2.6
				1200	3.3
				1500	2.6
				1800	2.2
				2000	3.3
				2500	8.7
				3000	4.7
				3500	5.7
				3750	4.2
GI-05	6	65.00	18.17	5	2.0
				15	2.1
				25	1.4
				50	3.3
				75	2.9
				100	5.3
				125	5.5
				150	4.4
				200	5.4
				300	6.7
				500	0.9
				800	2.9
				1000	6.4
				1200	5.1
				1500	2.8
				1800	7.0
				2000	9.8
				2500	1.8
				3000	2.3
				3300	2.1
GI-05	7	65.00	21.00	5	4.1
				15	2.1

				25	1.8
				35	2.1
				50	3.6
				75	6.1
				100	6.0
				150	10.1
				200	5.9
				300	6.1
				500	3.8
				800	2.8
				1000	2.1
				1200	3.0
				1500	2.1
				1800	1.8
				2000	1.6
				2500	1.6
				2900	1.9
GI-05	8	61.50	21.85	5	2.9
				15	4.2
				30	4.4
				50	9.7
				75	5.9
				100	8.7
				150	6.4
				200	3.8
				300	3.4
				500	3.1
				800	3.8
				1000	3.3
				1200	13.1
				1500	5.2
				1800	8.4
				2000	2.1
				2500	4.9
				3000	2.9
GI-05	9	61.20	17.85	5	2.0
				15	3.8
				25	2.0
				35	2.2
				50	2.2
				75	2.3
				100	2.8
				150	4.3
				200	4.5

				300	3.6
				500	3.0
				800	4.0
				1000	1.9
				1200	2.6
				1500	2.2
				1800	1.9
				2000	1.3
				2500	1.9
				3000	2.1
				3500	1.8
				3750	2.5
GI-05	10	59.80	15.61	5	3.3
				15	2.8
				25	1.9
				45	2.4
				75	1.7
				100	2.1
				150	3.1
				200	2.7
				300	3.1
				500	3.3
				800	2.4
				1000	2.3
				1200	3.2
				1500	2.3
				1800	2.0
				2000	1.7
				2500	10.4
				3000	1.7
				3500	1.7
				4000	2.0
GI-05	11	58.80	12.90	5	2.1
				15	2.4
				25	1.9
				35	2.1
				50	2.9
				75	2.1
				100	2.7
				150	3.5
				200	2.9
				300	4.0
				500	2.8
				800	3.1

				1000	2.6
				1200	1.7
				1500	1.5
				1800	1.6
				2000	2.0
				2500	1.6
				3000	1.9
				3500	1.9
				4000	2.9
				4300	2.4
GI-05	12	58.67	10.60	5	1.5
				15	1.6
				25	1.1
				50	1.8
				75	2.5
				100	2.5
				150	2.4
				200	2.8
				300	2.9
				500	3.6
				800	3.3
				1000	6.1
				1200	2.8
				1500	3.0
				1800	1.8
				2000	2.2
				2500	2.2
				3000	2.1
				3500	2.5
GI-05	13	58.63	8.30	5	3.8
				15	4.2
				25	2.2
				50	3.0
				75	3.5
				100	3.3
				150	3.4
				200	4.4
				300	3.2
				500	3.4
				800	3.3
				1000	2.5
				1200	2.3
				1500	2.1
				1800	2.4

				2000	2.4
				2500	3.0
GI-05	14	58.50	5.60	25	6.6
				50	3.6
				65	5.8
				75	2.8
				100	4.4
				125	4.2
				150	3.6
				200	4.0
				300	2.9
				500	3.4
				800	3.7
				1000	4.9
				1200	2.6
				1500	2.9
				1800	2.4
				2000	2.4
				2500	2.7
				3000	2.7
				3500	3.7
				3800	4.3
GI-05	15	58.40	2.90	5	3.9
				15	3.1
				25	3.2
				50	2.6
				75	3.7
				100	2.5
				150	3.4
				200	2.6
				300	2.9
				400	4.4
				500	3.5
				800	2.9
				1000	2.5
				1200	2.7
				1500	2.8
				1800	2.3
				2000	2.0
				2500	1.7
				3000	2.3
				3500	2.8
				4000	2.6
				4400	4.6

GI-05	16	58.95	-1.00	5	5.7
				15	5.1
				25	5.0
				50	3.7
				60	3.0
				75	3.3
				100	4.8
				150	4.0
				200	3.8
				300	3.7
				500	3.6
				800	3.3
				1000	2.7
				1200	2.8
				1500	2.4
				1800	2.8
				2000	2.6
				2500	2.8
				3000	3.3
				3500	3.1
				4000	2.9
				4500	3.0
GI-05	17	59.35	-5.00	5	4.1
				15	5.2
				25	4.2
				50	4.2
				75	2.8
				100	3.4
				150	4.4
				200	3.6
				300	4.2
				500	3.2
				800	2.4
				1000	2.0
				1200	2.3
				1500	2.1
				1800	2.1
				2000	1.9
				2500	2.5
				3000	5.2
				3500	3.4
				3950	2.3
GI-05	18	59.81	-9.00	5	4.0
				15	4.3

25	3.9
45	4.2
75	4.7
100	2.0
150	2.7
200	2.5
300	2.5
500	2.0
750	2.3

Appendix B

The dAl distribution in the deep waters is modeled using steady-state, 1-D scavenging- advection-diffusion model for a stable and non-conservative (SNC) tracer, considering no *in situ* production (Craig, 1974). The model equation is given as

$$\boldsymbol{K}.\frac{\partial^2 \boldsymbol{C_z}}{\partial \boldsymbol{z}^2} - \boldsymbol{\omega}.\frac{\partial \boldsymbol{C_z}}{\partial \boldsymbol{z}} - \psi.\boldsymbol{C_z} = 0 \qquad \text{(B1)}$$

which has a general solution

$$\boldsymbol{C_z} = \{\boldsymbol{C_m} \times \left[\boldsymbol{exp}\frac{-(z_m - z)}{2z^*}\right] \times \boldsymbol{sinh}\left(\frac{Az}{2z^*}\right) + \boldsymbol{C_o} \times \left[\boldsymbol{exp}\frac{z}{2z^*}\right] \times \boldsymbol{sinh}\left[\frac{A(z_m - z)}{2z^*}\right]\} \times \{\boldsymbol{sinh}\left[\frac{Az_m}{2z^*}\right]\}^{-1} \qquad \text{(B2)}$$

where, **z*= K/ω** is the mixing parameter and **A= [1 + 4z*(ψ/ω)]**$^{\mathbf{1/2}}$.

In the above equations, **K** denotes the vertical diffusivity; **ω** represents the vertical advection velocity; **ψ** is the scavenging rate; and $\mathbf{C_z}$ is the dAl concentration at the vertical depth '**z**', taken positive towards the ocean surface. $\mathbf{C_m}$ and $\mathbf{C_o}$ are the dAl concentrations at the model's upper ($\mathbf{z = z_m}$) and lower ($\mathbf{z = z_o}$) boundaries. The lower model boundary $\mathbf{z = z_o}$ is also considered as the point of reference, i.e., $\mathbf{z_o = 0}$. The value of the mixing parameter, **z***, is estimated by fitting the general solution of the steady-state, 1-D advection-diffusion model for the stable and conservative (SC) tracer (Craig, 1974) to the salinity distribution in the deep waters. The general solution of the steady-state, 1-D advection-diffusion model for the SC tracer is given as

$$\boldsymbol{C_z} = \boldsymbol{C_o} + (\boldsymbol{C_m} - \boldsymbol{C_o}) \times \left[\boldsymbol{exp}\frac{z}{z^*} - 1\right] \times \left[\boldsymbol{exp}\frac{z_m}{z^*} - 1\right]^{-1} \qquad \text{(B3)}$$

Next, we find the best fit for the dAl distribution in the deep waters to Eq. (B2) with $\mathbf{C_m}$, $\mathbf{C_o}$ and **ψ/ω** as free variables.

Appendix C

Table C1: Data on Al concentration in the surface-level aerosols in the model space, compiled from the previous studies.

Sampling Season	Data Source Study	Sampling Day	Nominal Sampling Latitude (°N)	Nominal Sampling Longitude (°E)	Aerosol Al (ug m^{-3})
Late Winter: 1st Jan. to 10th Feb.	Tindale and Pease, 1999	22-01-1995	14.98	64.00	0.66
	Tindale and Pease, 1999	23-01-1995	15.97	62.08	0.43
	Tindale and Pease, 1999	24-01-1995	16.09	62.05	0.56
	Tindale and Pease, 1999	25-01-1995	16.01	62.00	0.54
	Tindale and Pease, 1999	27-01-1995	17.33	59.81	0.85
	Tindale and Pease, 1999	30-01-1995	18.12	58.03	1.02
	Tindale and Pease, 1999	10-02-1995	18.23	58.11	0.28
Spring: 11th Feb. to 31th May	Tindale and Pease, 1999	12-02-1995	16.93	60.50	0.9
	Tindale and Pease, 1999	15-02-1995	15.22	63.49	0.61
	Tindale and Pease, 1999	16-02-1995	14.88	64.11	0.85
	Tindale and Pease, 1999	19-02-1995	17.53	59.16	0.98
	Tindale and Pease, 1999	28-03-1995	15.23	63.44	1.06
	Kumar et al., 2008	30-04-2006	14.00	64.77	0.21
	Kumar et al., 2008	01-05-2006	14.00	59.23	0.69
	Kumar et al., 2008	02-05-2006	16.32	58.85	0.65
	Kumar et al., 2008	06-05-2006	16.01	64.68	0.58
	Seifert et al., 1999	09-05-1995	16.30	65.00	0.27
	Seifert et al., 1999	09-05-1995	16.70	65.00	0.19
	Seifert et al., 1999	10-05-1995	18.00	65.00	0.29
	Seifert et al., 1999	10-05-1995	18.00	65.00	0.28
	Seifert et al., 1999	11-05-1995	18.00	65.00	0.28
	Seifert et al., 1999	11-05-1995	18.10	65.00	0.48
	Seifert et al., 1999	12-05-1995	18.10	65.00	0.54
	Seifert et al., 1999	13-05-1995	18.10	65.00	0.83
	Seifert et al., 1999	14-05-1995	18.10	65.00	0.77

	Seifert et al., 1999	15-05-1995	18.10	65.00	0.94
	Seifert et al., 1999	16-05-1995	18.10	65.00	1.12
	Seifert et al., 1999	17-05-1995	18.10	65.00	0.82
	Seifert et al., 1999	18-05-1995	16.90	65.00	0.54
	Seifert et al., 1999	19-05-1995	14.30	65.00	0.61
Summer: 1st June to 24th Aug.	Tindale and Pease, 1999	23-06-1995	19.91	59.71	0.08
	Tindale and Pease, 1999	27-06-1995	17.99	60.35	0.02
	Tindale and Pease, 1999	02-07-1995	15.82	64.37	0.04
	Tindale and Pease, 1999	04-07-1995	16.39	61.04	0.01
	Tindale and Pease, 1999	25-07-1995	15.56	64.79	0.04
	Tindale and Pease, 1999	27-07-1995	15.03	64.31	0.06
	Tindale and Pease, 1999	04-08-1995	16.33	61.57	0.02
	Tindale and Pease, 1999	06-08-1995	17.09	60.12	0.04
Autumn: 25th Aug. to 31th Oct.	Tindale and Pease, 1999	02-09-1995	16.19	61.66	0.29
	Tindale and Pease, 1999	25-09-1995	18.01	59.56	0.47
Early Winter: 1st Nov. to 31th Dec.	Tindale and Pease, 1999	10-11-1995	14.50	65.00	0.68
	Tindale and Pease, 1999	15-11-1995	18.50	57.26	1.42
	Tindale and Pease, 1999	13-12-1995	14.59	65.06	0.72
	Tindale and Pease, 1999	16-12-1995	14.98	64.00	0.78
	Tindale and Pease, 1999	17-12-1995	15.85	62.34	0.66
	Tindale and Pease, 1999	19-12-1995	17.21	59.77	0.44
	Tindale and Pease, 1999	22-12-1995	18.15	58.16	0.20

Table C2: Data on surface water Al concentration in the model space, compiled from this and previous studies.

Sampling Month	Data Source Study	Latitude(°N)	Longitude (°E)	Al (nM)
January	Measures and Vink, 1999	18.45	57.30	3.3
January	Measures and Vink, 1999	18.08	58.00	3.2
January	Measures and Vink, 1999	17.68	58.84	2.9
January	Measures and Vink, 1999	17.20	59.77	5.0
January	Measures and Vink, 1999	16.80	60.50	4.0
January	Measures and Vink, 1999	16.02	62.01	5.3
January	Measures and Vink, 1999	15.25	63.50	5.7
January	Measures and Vink, 1999	14.45	65.00	4.9
March	Measures and Vink, 1999	16.02	61.96	5.1
March	Measures and Vink, 1999	14.01	64.89	7.4
April	Measures and Vink, 1999	16.82	60.50	2.2
April	Measures and Vink, 1999	16.43	61.25	4.2
April	Measures and Vink, 1999	15.51	61.50	6.4
July	Measures and Vink, 1999	14.45	65.00	7.8
July	Schüβler et al., 2005	16.00	62.00	3.8
July	Schüβler et al., 2005	17.00	60.00	5.1
July	Schüβler et al., 2005	18.50	57.30	4.9
August	Measures and Vink, 1999	18.50	57.30	7.5
August	Measures and Vink, 1999	18.65	57.75	6.1
August	Measures and Vink, 1999	18.77	58.17	6.4
August	Measures and Vink, 1999	17.68	58.84	9.3
August	Measures and Vink, 1999	19.00	59.00	7.0
August	Measures and Vink, 1999	17.09	60.12	7.4
August	Measures and Vink, 1999	16.80	60.50	8.0
August	Measures and Vink, 1999	16.43	61.25	6.6
August	Measures and Vink, 1999	15.53	61.50	7.9
August	Measures and Vink, 1999	15.77	61.74	7.9
August	Measures and Vink, 1999	16.03	62.00	7.4

August	Measures and Vink, 1999	15.64	62.80	8.5
August	Measures and Vink, 1999	15.25	63.50	7.6
August	Measures and Vink, 1999	14.83	64.25	9.3
September	Measures and Vink, 1999	18.50	57.30	8.1
September	Measures and Vink, 1999	18.63	57.75	8.1
September	Measures and Vink, 1999	18.08	58.00	7.9
September	Measures and Vink, 1999	18.88	58.59	8.8
September	Measures and Vink, 1999	17.68	58.83	9.0
September	Measures and Vink, 1999	19.00	59.00	7.2
September	Measures and Vink, 1999	17.18	59.77	3.1
September	Measures and Vink, 1999	16.80	60.50	2.5
September	Measures and Vink, 1999	16.43	61.25	2.6
September	Measures and Vink, 1999	16.03	62.00	5.9
September	Measures and Vink, 1999	15.63	62.77	6.2
September	Measures and Vink, 1999	15.25	63.50	3.5
September	Measures and Vink, 1999	14.45	65.00	4.7
October	This study	15.10	59.80	3.1
October	This study	17.85	61.20	2.0
November	Measures and Vink, 1999	16.42	56.50	3.0
November	Measures and Vink, 1999	17.00	57.23	3.4
November	Measures and Vink, 1999	18.50	57.26	4.0
November	Measures and Vink, 1999	17.79	58.67	4.0
November	Measures and Vink, 1999	18.36	59.14	3.7
November	Measures and Vink, 1999	17.18	59.82	4.3
November	Measures and Vink, 1999	16.03	62.00	3.3

Appendix D

The temporal variations in the atmospheric dAl input (estimated in terms of seasonal variations; see section 4.4.1.1 and Fig. 4.8A of Chapter 4) over the model space are considered to be annually periodic. With this assumption, the estimated seasonal variations in the dAl input (refer to Fig. 4.8A of Chapter 4) are fitted (approximated) with a truncated Fourier series, which can be mathematically described as follows:

$$\mathbf{dAl^{atm}_{input}(t) = a_0 + \sum_{i=1}^{n} a_i \cos(iwt) + \sum_{i=1}^{n} b_i \sin(iwt)} \qquad \text{(D1)}$$

where, **n** is the number of terms up to which the Fourier series approximation is considered; **i**=1, 2, 3,…, n; $\mathbf{a_0, a_i}$ and $\mathbf{b_i}$ are the estimated coefficients for the truncated Fourier series approximation. Also, note that under the annual periodicity assumption for the atmospheric dAl input function (i.e., $\mathbf{dAl^{atm}_{input}(t)}$ in Eq. (D1)), **w** becomes equal to $2\pi/365$ d^{-1} (≈0.0172 d^{-1}). Substituting Eq. (D1) in Eq. (4.2) of Chapter 4, we get

$$\mathbf{\frac{d[dAl]}{dt} = \left(a_0 + \sum_{i=1}^{n} a_i \cos(iwt) + \sum_{i=1}^{n} b_i \sin(iwt)\right) - \frac{dAl}{\tau}} \qquad \text{(D2)}$$

Eq. (D2) is a first-order differential equation of the form

$$\mathbf{\frac{d(y(t))}{dt} + P(t).y(t) = Q(t)} \qquad \text{(D3)}$$

where, **y(t)=dAl (t)** (i.e., surface dAl as a function of time); **P(t)=** $\mathbf{\frac{1}{\tau}}$ and **Q(t) =** $\mathbf{dAl^{atm}_{input}\ (t)}$

For simplicity, let’s consider

$$\mathbf{dAl^{atm}_{input}\ (t) = a_o + b.\sin(wt)} \qquad \text{(D4)}$$

where, $\mathbf{a_o}$ and **b** are arbitrary constants.

Substituting Eq. (D4) in Eq. (D3), we have

$$\mathbf{\frac{dy}{dt} + \frac{y}{\tau} = a_o + b.\sin(wt)} \qquad \text{(D5)}$$

The general solution of Eq. (D5) is given as

$$\mathbf{y} = \mathbf{a_o}.\boldsymbol{\tau} + \frac{\mathbf{b.sin\,(wt-\varphi)}}{\sqrt{\mathbf{w^2+(1/\tau)^2}}} + \mathbf{C.e^{-t/\tau}} \tag{D6}$$

where, '**C**' is an integration constant and $\mathbf{tan(\varphi) = w.\tau}$

With time, the solution in Eq. (D6) converges to the following stable form (as $\mathbf{C.e^{-t/\tau}}$ converges to zero)

$$\mathbf{y} = \mathbf{a_o}.\boldsymbol{\tau} + \frac{\mathbf{b.sin\,(wt-\varphi)}}{\sqrt{\mathbf{w^2+(1/\tau)^2}}} \tag{D7}$$

The relative importance of the term $\mathbf{C.e^{-t/\tau}}$ depends on the value of **C**, which also gives a measure of the initial dAl levels (dAl$_o$), i.e., the dAl concentration at t=0. dAl$_o$ may be visualized as the dAl level before the model space was subjected to temporal (here, periodic) changes in dAl input. The solution given in Eq. (A6) converges to the stable form, i.e., to Eq. (A7) quickly, if dAl$_o$ is comparable to the magnitude of periodic dAl variations (i.e., the second term in the RHS of Eq. (A7)) solved against the periodic changes in dAl input.

Similarly, if we consider $\mathbf{dAl^{atm}_{input}\,(t) = a_o + b.sin(wt) + a.cos(wt)}$ and substitute it in Eq. (D3), the stable analytical solution is given as

$$\mathbf{y} = \mathbf{a_o}.\boldsymbol{\tau} + \frac{\mathbf{b.sin(wt-\varphi)}}{\sqrt{\mathbf{w^2+(1/\tau)^2}}} + \frac{\mathbf{a.cos(wt-\varphi)}}{\sqrt{\mathbf{w^2+(1/\tau)^2}}} \tag{D8}$$

Finally, if we consider the general form of $\mathbf{dAl^{atm}_{input}(t)}$ given in Eq. (D1) and substitute it in Eq. (D3), it can easily be shown (using the forms of the solutions derived in Eq. (D7) and (D8)) that the stable analytical solution to Eq. (D3) is given as

$$\mathbf{y(t)} = \mathbf{a_o}.\boldsymbol{\tau} + \sum_{\mathbf{i=1}}^{\mathbf{n}} \frac{\mathbf{b_i.sin(iwt-\varphi_i)}}{\sqrt{\mathbf{(iw)^2+(1/\tau)^2}}} + \sum_{\mathbf{i=1}}^{\mathbf{n}} \frac{\mathbf{a_i.cos(iwt-\varphi_i)}}{\sqrt{\mathbf{(iw)^2+(1/\tau)^2}}} = \mathbf{dAl(t)} \tag{D9}$$

Note that the Eq. (D3) was also solved numerically by considering an arbitrary initial condition (i.e., y(0)=y$_o$) and using the 4th order Runge-Kutta method.

The numerical solution converges to the stable analytical solution given in Eq. (D9).

The Eq. (D3) was also (numerically) solved considering the temporal variations in surface dAl residence time, $\boldsymbol{\tau}$**.** The temporally varying surface dAl residence time, $\boldsymbol{\tau}$, is estimated as follows

$$\boldsymbol{\tau}(\mathbf{t}) = \boldsymbol{\tau}_{\mathbf{0}} . \frac{\mathbf{NPP_0}}{\mathbf{NPP(t)}} \tag{D10}$$

where, $\boldsymbol{\tau}_{\mathbf{0}}$ and $\mathbf{NPP_0}$ are the annual mean of the residence time and net primary productivity in the model space, respectively. The time-varying function, **NPP(t)** is also considered as an annually periodic function and determined using the SeaWiFS satellite data-based monthly averaged NPP estimates and fitting these estimates using the truncated Fourier series, in a similar way used for approximating the function $\mathbf{dAl_{input}^{atm}}$ (Eq. D1).

Appendix E

Table E1: Data on Mn concentration in the surface-level aerosols (Tindale, 1997) over different zones.

	Season	Latitude	Longitude	Mn (ug m^{-3})
Zone 1	LW	10.01	64.90	0.059
	SP	10.02	64.87	0.018
	SU	9.98	64.90	0.00067
	EW	10.13	64.97	0.02
	EW	10.01	64.90	0.019
Zone 2	LW	14.98	64.00	0.0084
	LW	14.49	65.03	0.2
	SP	15.22	63.49	0.0064
	SP	14.88	64.11	0.009
	SP	15.23	63.44	0.013
	SU	15.03	64.31	0.0011
	EW	14.50	65.00	0.029
	EW	14.59	65.06	0.051
	EW	14.98	64.00	0.012
Zone 3	LW	19.17	67.17	0.0049
	SP	19.17	67.15	0.0052

	SU	19.10	67.23	0.0042
	EW	19.28	67.22	0.018
Zone 4	LW	22.48	61.19	0.032
	SP	22.48	61.17	0.0045
	SU	22.51	61.17	0.021
	EW	22.50	61.17	0.034

Table E2: dMn distribution along the GEOTRACES-India cruise transect, GI-06(B).

Cruise	Station	Latitude	Longitude	Depth (m)	dMn (nmol kg^{-1})
GI-06(B)	1	13.905	73.528	5	4.19
GI-06(B)	1	13.905	73.528	10	3.66
GI-06(B)	1	13.905	73.528	20	3.42
GI-06(B)	1	13.905	73.528	40	2.61
GI-06(B)	1	13.905	73.528	50	2.75
GI-06(B)	1	13.905	73.528	60	2.01
GI-06(B)	1	13.905	73.528	70	1.18
GI-06(B)	1	13.905	73.528	80	1.13
GI-06(B)	2	11.500	74.780	5	3.74
GI-06(B)	2	11.500	74.780	10	5.22
GI-06(B)	2	11.500	74.780	20	3.33
GI-06(B)	2	11.500	74.780	60	1.73
GI-06(B)	2	11.500	74.780	80	1.17
GI-06(B)	3	9.000	75.501	5	2.21
GI-06(B)	3	9.000	75.501	10	2.05
GI-06(B)	3	9.000	75.501	25	2.23
GI-06(B)	3	9.000	75.501	50	1.55
GI-06(B)	3	9.000	75.501	75	1.02
GI-06(B)	3	9.000	75.501	150	0.63
GI-06(B)	3	9.000	75.501	250	0.94
GI-06(B)	3	9.000	75.501	350	0.51
GI-06(B)	4	9.000	74.017	8	3.19
GI-06(B)	4	9.000	74.017	25	2.72
GI-06(B)	4	9.000	74.017	40	3.21
GI-06(B)	4	9.000	74.017	75	1.45
GI-06(B)	4	9.000	74.017	100	0.74
GI-06(B)	4	9.000	74.017	160	0.54
GI-06(B)	4	9.000	74.017	220	0.54
GI-06(B)	4	9.000	74.017	380	0.58
GI-06(B)	4	9.000	74.017	550	0.72
GI-06(B)	4	9.000	74.017	800	0.56

GI-06(B)	4	9.000	74.017	1000	0.49
GI-06(B)	4	9.000	74.017	1200	0.47
GI-06(B)	4	9.000	74.017	1500	0.39
GI-06(B)	4	9.000	74.017	1800	0.29
GI-06(B)	4	9.000	74.017	2100	0.31
GI-06(B)	4	9.000	74.017	2400	0.28
GI-06(B)	4	9.000	74.017	2600	0.23
GI-06(B)	5	9.000	72.500	7	3.29
GI-06(B)	5	9.000	72.500	25	2.54
GI-06(B)	5	9.000	72.500	55	1.45
GI-06(B)	5	9.000	72.500	75	1.18
GI-06(B)	5	9.000	72.500	100	0.91
GI-06(B)	5	9.000	72.500	175	0.50
GI-06(B)	5	9.000	72.500	200	0.54
GI-06(B)	5	9.000	72.500	330	0.40
GI-06(B)	5	9.000	72.500	550	0.59
GI-06(B)	5	9.000	72.500	800	0.54
GI-06(B)	5	9.000	72.500	1200	0.67
GI-06(B)	5	9.000	72.500	1500	0.32
GI-06(B)	5	9.000	72.500	2050	0.27
GI-06(B)	6	9.000	71.000	10	3.09
GI-06(B)	6	9.000	71.000	25	1.92
GI-06(B)	6	9.000	71.000	50	1.67
GI-06(B)	6	9.000	71.000	75	1.97
GI-06(B)	6	9.000	71.000	90	1.49
GI-06(B)	6	9.000	71.000	150	1.12
GI-06(B)	6	9.000	71.000	200	0.51
GI-06(B)	6	9.000	71.000	300	0.50
GI-06(B)	6	9.000	71.000	400	0.53
GI-06(B)	6	9.000	71.000	600	0.57
GI-06(B)	6	9.000	71.000	800	0.57
GI-06(B)	6	9.000	71.000	1000	0.48
GI-06(B)	6	9.000	71.000	1200	0.42
GI-06(B)	6	9.000	71.000	1500	0.34
GI-06(B)	6	9.000	71.000	1800	0.28
GI-06(B)	6	9.000	71.000	2000	0.31
GI-06(B)	6	9.000	71.000	2200	0.27
GI-06(B)	6	9.000	71.000	2600	0.25
GI-06(B)	6	9.000	71.000	3000	0.25
GI-06(B)	6	9.000	71.000	3400	0.29
GI-06(B)	6	9.000	71.000	3800	0.20
GI-06(B)	7	9.000	69.500	5	1.72
GI-06(B)	7	9.000	69.500	10	1.87
GI-06(B)	7	9.000	69.500	25	1.83
GI-06(B)	7	9.000	69.500	54	1.81
GI-06(B)	7	9.000	69.500	90	1.76

GI-06(B)	7	9.000	69.500	150	0.51
GI-06(B)	7	9.000	69.500	310	0.40
GI-06(B)	7	9.000	69.500	530	0.50
GI-06(B)	7	9.000	69.500	600	0.34
GI-06(B)	7	9.000	69.500	800	0.44
GI-06(B)	7	9.000	69.500	1000	0.40
GI-06(B)	7	9.000	69.500	1200	0.32
GI-06(B)	7	9.000	69.500	1500	0.24
GI-06(B)	7	9.000	69.500	1800	0.18
GI-06(B)	7	9.000	69.500	2100	0.18
GI-06(B)	7	9.000	69.500	2500	0.23
GI-06(B)	7	9.000	69.500	3000	0.22
GI-06(B)	7	9.000	69.500	3500	0.17
GI-06(B)	7	9.000	69.500	4000	0.16
GI-06(B)	7	9.000	69.500	4500	0.18
GI-06(B)	8	9.000	68.000	5	1.69
GI-06(B)	8	9.000	68.000	10	1.86
GI-06(B)	8	9.000	68.000	25	1.77
GI-06(B)	8	9.000	68.000	50	1.84
GI-06(B)	8	9.000	68.000	75	1.91
GI-06(B)	8	9.000	68.000	90	1.38
GI-06(B)	8	9.000	68.000	150	0.51
GI-06(B)	8	9.000	68.000	200	0.45
GI-06(B)	8	9.000	68.000	300	0.33
GI-06(B)	8	9.000	68.000	400	0.37
GI-06(B)	8	9.000	68.000	500	0.49
GI-06(B)	8	9.000	68.000	600	0.29
GI-06(B)	8	9.000	68.000	800	0.43
GI-06(B)	8	9.000	68.000	1000	0.39
GI-06(B)	8	9.000	68.000	1200	0.13
GI-06(B)	8	9.000	68.000	1500	0.17
GI-06(B)	8	9.000	68.000	1800	0.13
GI-06(B)	8	9.000	68.000	2000	0.23
GI-06(B)	8	9.000	68.000	2500	0.28
GI-06(B)	8	9.000	68.000	3000	0.24
GI-06(B)	8	9.000	68.000	3500	0.14
GI-06(B)	8	9.000	68.000	4000	0.09
GI-06(B)	8	9.000	68.000	4500	0.13
GI-06(B)	9	9.000	66.500	10	1.60
GI-06(B)	9	9.000	66.500	25	1.69
GI-06(B)	9	9.000	66.500	75	1.22
GI-06(B)	9	9.000	66.500	100	1.07
GI-06(B)	9	9.000	66.500	150	0.88
GI-06(B)	9	9.000	66.500	300	0.31
GI-06(B)	9	9.000	66.500	600	0.42
GI-06(B)	9	9.000	66.500	800	0.48

GI-06(B)	9	9.000	66.500	1000	0.42
GI-06(B)	9	9.000	66.500	1200	0.35
GI-06(B)	9	9.000	66.500	1500	0.28
GI-06(B)	9	9.000	66.500	1800	0.15
GI-06(B)	9	9.000	66.500	2000	0.25
GI-06(B)	9	9.000	66.500	2500	0.17
GI-06(B)	9	9.000	66.500	3000	0.18
GI-06(B)	9	9.000	66.500	3500	0.17
GI-06(B)	9	9.000	66.500	4000	0.11
GI-06(B)	9	9.000	66.500	4450	0.14
GI-06(B)	10	9.000	65.000	5	1.82
GI-06(B)	10	9.000	65.000	10	1.91
GI-06(B)	10	9.000	65.000	25	1.85
GI-06(B)	10	9.000	65.000	50	1.77
GI-06(B)	10	9.000	65.000	80	1.28
GI-06(B)	10	9.000	65.000	180	1.13
GI-06(B)	10	9.000	65.000	300	0.40
GI-06(B)	10	9.000	65.000	600	0.52
GI-06(B)	10	9.000	65.000	800	0.45
GI-06(B)	10	9.000	65.000	1000	0.47
GI-06(B)	10	9.000	65.000	1200	0.39
GI-06(B)	10	9.000	65.000	1500	0.20
GI-06(B)	10	9.000	65.000	2000	0.21
GI-06(B)	10	9.000	65.000	2400	0.20
GI-06(B)	10	9.000	65.000	2800	0.35
GI-06(B)	10	9.000	65.000	3200	0.20
GI-06(B)	10	9.000	65.000	3600	0.15
GI-06(B)	10	9.000	65.000	4000	0.08
GI-06(B)	10	9.000	65.000	4450	0.09
GI-06(B)	11	9.000	63.500	10	2.12
GI-06(B)	11	9.000	63.500	25	2.74
GI-06(B)	11	9.000	63.500	50	2.35
GI-06(B)	11	9.000	63.500	200	0.54
GI-06(B)	11	9.000	63.500	300	0.46
GI-06(B)	11	9.000	63.500	500	0.88
GI-06(B)	11	9.000	63.500	800	0.56
GI-06(B)	11	9.000	63.500	1000	0.60
GI-06(B)	11	9.000	63.500	1200	0.34
GI-06(B)	11	9.000	63.500	1500	0.43
GI-06(B)	11	9.000	63.500	1800	0.28
GI-06(B)	11	9.000	63.500	2000	0.32
GI-06(B)	11	9.000	63.500	2400	0.36
GI-06(B)	11	9.000	63.500	2800	0.32
GI-06(B)	11	9.000	63.500	3200	0.25
GI-06(B)	11	9.000	63.500	3600	0.25
GI-06(B)	11	9.000	63.500	4000	0.24

GI-06(B)	11	9.000	63.500	4470	0.26
GI-06(B)	12	9.000	62.000	5	1.41
GI-06(B)	12	9.000	62.000	10	1.27
GI-06(B)	12	9.000	62.000	25	2.22
GI-06(B)	12	9.000	62.000	50	1.76
GI-06(B)	12	9.000	62.000	280	0.33
GI-06(B)	12	9.000	62.000	600	0.32
GI-06(B)	12	9.000	62.000	1000	0.36
GI-06(B)	12	9.000	62.000	1200	0.33
GI-06(B)	12	9.000	62.000	1500	0.48
GI-06(B)	12	9.000	62.000	1800	0.20
GI-06(B)	12	9.000	62.000	2100	0.37
GI-06(B)	12	9.000	62.000	2500	0.25
GI-06(B)	12	9.000	62.000	3000	0.17
GI-06(B)	12	9.000	62.000	3500	0.16
GI-06(B)	14	9.000	60.000	1000	0.40
GI-06(B)	14	9.000	60.000	1200	0.33
GI-06(B)	14	9.000	60.000	1500	0.29
GI-06(B)	14	9.000	60.000	1800	0.24
GI-06(B)	14	9.000	60.000	2000	0.24
GI-06(B)	14	9.000	60.000	2500	0.34
GI-06(B)	14	9.000	60.000	3000	0.23
GI-06(B)	14	9.000	60.000	3350	0.27
GI-06(B)	15	11.000	62.563	5	1.52
GI-06(B)	15	11.000	62.563	10	1.30
GI-06(B)	15	11.000	62.563	25	1.51
GI-06(B)	15	11.000	62.563	50	1.47
GI-06(B)	15	11.000	62.563	80	1.34
GI-06(B)	15	11.000	62.563	100	0.49
GI-06(B)	15	11.000	62.563	150	0.97
GI-06(B)	15	11.000	62.563	400	0.28
GI-06(B)	15	11.000	62.563	600	0.29
GI-06(B)	15	11.000	62.563	800	0.36
GI-06(B)	15	11.000	62.563	1000	0.28
GI-06(B)	15	11.000	62.563	1200	0.24
GI-06(B)	15	11.000	62.563	1500	0.22
GI-06(B)	15	11.000	62.563	1800	0.17
GI-06(B)	15	11.000	62.563	2300	0.15
GI-06(B)	15	11.000	62.563	2800	0.15
GI-06(B)	15	11.000	62.563	3300	0.12
GI-06(B)	15	11.000	62.563	3800	0.11
GI-06(B)	15	11.000	62.563	4300	0.10
GI-06(B)	16	14.510	65.566	5	1.49
GI-06(B)	16	14.510	65.566	10	1.69
GI-06(B)	16	14.510	65.566	25	1.44
GI-06(B)	16	14.510	65.566	50	2.34

GI-06(B)	16	14.510	65.566	75	1.78
GI-06(B)	16	14.510	65.566	100	1.65
GI-06(B)	16	14.510	65.566	120	0.96
GI-06(B)	16	14.510	65.566	160	2.35
GI-06(B)	16	14.510	65.566	220	3.27
GI-06(B)	16	14.510	65.566	250	0.85
GI-06(B)	16	14.510	65.566	300	0.77
GI-06(B)	16	14.510	65.566	350	0.64
GI-06(B)	16	14.510	65.566	400	0.71
GI-06(B)	16	14.510	65.566	450	0.68
GI-06(B)	16	14.510	65.566	500	0.58
GI-06(B)	16	14.510	65.566	550	1.15
GI-06(B)	16	14.510	65.566	600	0.61
GI-06(B)	16	14.510	65.566	650	0.70
GI-06(B)	16	14.510	65.566	700	0.60
GI-06(B)	16	14.510	65.566	800	0.63
GI-06(B)	16	14.510	65.566	900	0.84
GI-06(B)	16	14.510	65.566	1000	0.47
GI-06(B)	16	14.510	65.566	1200	0.11
GI-06(B)	16	14.510	65.566	1500	0.22
GI-06(B)	16	14.510	65.566	1800	0.26
GI-06(B)	16	14.510	65.566	2300	0.20
GI-06(B)	16	14.510	65.566	2800	0.21
GI-06(B)	16	14.510	65.566	3300	0.19
GI-06(B)	16	14.510	65.566	3800	0.17
GI-06(B)	17	17.380	67.955	5	2.74
GI-06(B)	17	17.380	67.955	15	2.20
GI-06(B)	17	17.380	67.955	30	2.05
GI-06(B)	17	17.380	67.955	50	2.05
GI-06(B)	17	17.380	67.955	75	2.09
GI-06(B)	17	17.380	67.955	150	2.26
GI-06(B)	17	17.380	67.955	200	2.28
GI-06(B)	17	17.380	67.955	300	4.08
GI-06(B)	17	17.380	67.955	400	3.82
GI-06(B)	17	17.380	67.955	500	3.75
GI-06(B)	17	17.380	67.955	600	2.62
GI-06(B)	17	17.380	67.955	700	2.83
GI-06(B)	17	17.380	67.955	800	1.48
GI-06(B)	17	17.380	67.955	1000	0.52
GI-06(B)	17	17.380	67.955	1200	0.46
GI-06(B)	17	17.380	67.955	1500	0.41
GI-06(B)	17	17.380	67.955	1800	0.15
GI-06(B)	17	17.380	67.955	2100	0.45
GI-06(B)	17	17.380	67.955	2500	0.23
GI-06(B)	17	17.380	67.955	3000	0.14
GI-06(B)	17	17.380	67.955	3400	0.18

GI-06(B)	18	16.751	68.994	5	2.08
GI-06(B)	18	16.751	68.994	10	1.91
GI-06(B)	18	16.751	68.994	25	2.24
GI-06(B)	18	16.751	68.994	50	2.31
GI-06(B)	18	16.751	68.994	75	1.69
GI-06(B)	18	16.751	68.994	100	0.97
GI-06(B)	18	16.751	68.994	150	3.05
GI-06(B)	18	16.751	68.994	200	5.03
GI-06(B)	18	16.751	68.994	300	2.98
GI-06(B)	18	16.751	68.994	400	2.04
GI-06(B)	18	16.751	68.994	500	1.71
GI-06(B)	18	16.751	68.994	600	0.99
GI-06(B)	18	16.751	68.994	700	2.37
GI-06(B)	18	16.751	68.994	800	0.64
GI-06(B)	18	16.751	68.994	900	0.62
GI-06(B)	18	16.751	68.994	1200	0.54
GI-06(B)	18	16.751	68.994	1800	0.33
GI-06(B)	18	16.751	68.994	2500	0.28
GI-06(B)	18	16.751	68.994	3500	0.15

References

Aguilar-Islas A. M. and Bruland K. W. (2006) Dissolved manganese and silicic acid in the Columbia River plume: A major source to the California current and coastal waters off Washington and Oregon. *Marine Chemistry* **101**, 233–247. Available at: 10.1016/j.marchem.2006.03.005.

Aswini M. A., Kumar A. and Das S. K. (2020) Quantification of long-range transported aeolian dust towards the Indian peninsular region using satellite and ground-based data - A case study during a dust storm over the Arabian Sea. *Atmospheric Research* **239**, 104910. Available at: 10.1016/j.atmosres.2020.104910.

Aguilar-Islas A. M., Resing J. A. and Bruland K. W. (2006) Catalytically enhanced spectrophotometric determination of manganese in seawater by flow-injection analysis with a commercially available resin for on-line preconcentration. *Limnol. Oceanogr. Methods* **4**, 105–113. Available at: 10.4319/lom.2006.4.105.

Anand S. S., Rengarajan R., Sarma V. V. S. S., Sudheer A. K., Bhushan R. and Singh S. K. (2017) Spatial variability of upper ocean POC export in the Bay of Bengal and the Indian Ocean determined using particle-reactive 234Th. *J.Geophys. Res. Oceans* **122**, 3753-3770. Available at: http://dx.doi.org/10.1002/2016jc012639.

Balistrieri L., Brewer P. G. and Murray J. W. (1981) Scavenging residence times of trace metals and surface chemistry of sinking particles in the deep ocean. *Deep Sea Research Part A. Oceanographic Research Papers* **28**, 101–121. Available at: 10.1016/0198-0149(81)90085-6.

Baker A. R., Jickells T. D., Witt M. and Linge K. L. (2006) Trends in the solubility of iron, aluminium, manganese and phosphorus in aerosol collected over the Atlantic Ocean. *Marine Chemistry* **98**, 43–58. Available at: 10.1016/j.marchem.2005.06.004.

Baker A. R., Landing W. M., Bucciarelli E., Cheize M., Fietz S., Hayes C. T., Kadko D., Morton P. L., Rogan N. and Sarthou G. (2016) Trace element and isotope deposition across the air–sea interface: progress and research needs. *Phil. Trans. R. Soc. A* **374**, 20160190. Available at: 10.1098/rsta.2016.0190.

Behara A., Vinayachandran P. N. and Shankar D. (2019) Influence of Rainfall Over Eastern Arabian Sea on Its Salinity. J. Geophys. Res. Oceans 124, 5003–5020. Available at: 10.1029/2019jc014999.

Behrenfeld M. J. and Falkowski P. G. (1997) Photosynthetic rates derived from satellite-based chlorophyll concentration. Limnol. Oceanogr. 42, 1–20. Available at: 10.4319/lo.1997.42.1.0001.

Berger, C. J. M., Lippiatt, S. M., Lawrence, M. G., and Bruland, K. W. (2008). Application of a chemical leach technique for estimating labile particulate aluminum, iron, and manganese in the Columbia River plume and coastal waters off Oregon and Washington. *J. Geophys. Res.* 113, C00B01. doi:10.1029/2007JC004703.

Bower A. S., Hunt H. D. and Price J. F. (2000) Character and dynamics of the Red Sea and Persian Gulf outflows. *J. Geophys. Res.* **105**, 6387–6414. Available at: 10.1029/1999jc900297.

Brown M. T. and Bruland K. W. (2008) An improved flow-injection analysis method for the determination of dissolved aluminum in seawater. *Limnol. Oceanogr. Methods* **6**, 87-95. Available at: http://dx.doi.org/10.4319/lom.2008.6.87.

Bruce J. G., Kindle J. C., Kantha L. H., Kerling J. L. and Bailey J. F. (1998) Recent observations and modeling in the Arabian Sea Laccadive High region. *J. Geophys. Res.* **103**, 7593–7600. Available at: 10.1029/97jc03219.

Bruland K. W., Middag R. and Lohan M. C. (2014) Controls of Trace Metals in Seawater. , 19–51. Available at: 10.1016/b978-0-08-095975-7.00602-1.

Buesseler K., Ball L., Andrews J., Benitez-Nelson C., Belastock R., Chai F. and Chao Y. (1998) Upper ocean export of particulate organic carbon in the Arabian Sea derived from thorium-234. *Deep Sea Research Part II: Topical Studies in Oceanography* **45**, 2461–2487. Available at: 10.1016/s0967-0645(98)80022-2.

Buma A. G. J., de Baar H. J. W., Nolting R. F. and van Bennekom A. J. (1991) Metal enrichment experiments in the Weddell-Scotia Seas: Effects of iron and manganese on various plankton communities. *Limnol. Oceanogr.* **36**, 1865–1878. Available at: 10.4319/lo.1991.36.8.1865.

Buck C. S., Landing W. M., Resing J. A. and Measures C. I. (2010) The solubility and deposition of aerosol Fe and other trace elements in the North Atlantic Ocean: Observations from the A16N CLIVAR/CO2 repeat hydrography section. *Mar. Chem.* **120**, 57-70.
Available at: http://dx.doi.org/10.1016/j.marchem.2008.08.003.

Buck C. S., Landing W. M. and Resing J. (2013) Pacific Ocean aerosols: Deposition and solubility of iron, aluminum, and other trace elements. *Mar. Chem.* **157**, 117-130. Available at: http://dx.doi.org/10.1016/j.marchem.2013.09.005.

Caschetto S. and Wollast R. (1979) Dissolved aluminium in interstitial waters of recent marine sediments. Geochimica et Cosmochimica Acta 43, 425-428. Available at: 10.1016/0016 7037(79)90207-2.

Chen Y., Paytan A., Chase Z., Measures C., Beck A. J., Sañudo-Wilhelmy S. A. and Post A. F. (2008) Sources and fluxes of atmospheric trace elements to the Gulf of Aqaba, Red Sea. *J. Geophys. Res.* **113**, D05306. Available at: 10.1029/2007jd009110.

Chester R., Sharples E. J. J. and Sanders G. S. (1985) The concentration of particulate aluminum and clay minerals in aerosols from the northern Arabian Sea. *Journal of Sedimentary Research* **55**, 37–41. Available at: 10.1306/212f85f8-2b24-11d7-8648000102c1865d.

Chinni V. (2018) Ph.D. Thesis: Distributions of dissolved Iron and Zinc in the Indian Ocean Implications to their sources sinks and internal cycling. Available at: http://hdl.handle.net/10603/287238.

Chinni V., Singh S. K., Bhushan R., Rengarajan R. and Sarma V. (2019) Spatial variability in dissolved iron concentrations in the marginal and open waters of the Indian Ocean.

Available at: http://dx.doi.org/10.1016/j.marchem.2018.11.007.

Chou L. and Wollast R. (1997) Biogeochemical behavior and mass balance of dissolved aluminum in the western Mediterranean Sea. **44**, 741-768. *Deep Sea Res. Part II Top. Stud. Oceanogr.* Available at: http://dx.doi.org/10.1016/s0967-0645(96)00092-6.

Clemens S., Prell W., Murray D., Shimmield G. and Weedon G. (1991) Forcing mechanisms of the Indian Ocean monsoon. *Nature* **353**, 720–725. Available at: 10.1038/353720a0.

Coale K. H. (1991) Effects of iron, manganese, copper, and zinc enrichments on productivity and biomass in the subarctic Pacific. *Limnol. Oceanogr.* **36**, 1851–1864. Available at: 10.4319/lo.1991.36.8.1851.

Craig H. (1969) Abyssal carbon and radiocarbon in the Pacific. *J. Geophys. Res.* **74**, 5491-5506. Available at: http://dx.doi.org/10.1029/jc074i023p05491.

Craig H. (1974) A scavenging model for trace elements in the deep sea. *Earth Planet. Sci. Lett.* **23**, 149-159. Available at: http://dx.doi.org/10.1016/0012-821x(74)90042-9.

Cullen J. T., Chase Z., Coale K. H., Fitzwater S. E. and Sherrell R. M. (2003) Effect of iron limitation on the cadmium to phosphorus ratio of natural phytoplankton assemblages from the Southern Ocean. *Limnol. Oceanogr.* **48**, 1079–1087. Available at: 10.4319/lo.2003.48.3.1079.

Dammshäuser A., Wagener T. and Croot P. L. (2011) Surface water dissolved aluminum and titanium: Tracers for specific time scales of dust deposition to the Atlantic? *Geophys. Res. Lett.* **38**. Available at: 10.1029/2011gl049847.

Damodararao K., Singh S. K., Rai V. K., Ramaswamy V. and Rao P. S. Lithology, Monsoon and Sea Surface Current Control on Provenance, Dispersal and Deposition of Sediments over the Andaman Continental Shelf. Front. Mar. Sci. **3**. Available at: http://dx.doi.org/10.3389/fmars.2016.00118.

Davies S. H. R. and Morgan J. J. (1989) Manganese(II) oxidation kinetics on metal oxide surfaces. *Journal of Colloid and Interface Science* **129**, 63–77. Available at: 10.1016/0021-9797(89)90416-5.

Dileep Kumar M. and Li Y.-H. (1996) Spreading of water masses and regeneration of silica and 226Ra in the Indian Ocean. *Deep Sea Research Part II: Topical Studies in Oceanography* **43**, 83–110. Available at: 10.1016/0967-0645(95)00084-4.

Dixit S. and Van Cappellen P. (2002) Surface chemistry and reactivity of biogenic silica. *Geochimica et Cosmochimica Acta* **66**, 2559–2568. Available at: 10.1016/s0016-7037(02)00854-2.

Duce R. A., Liss P. S., Merrill J. T., Atlas E. L., Buat-Menard P., Hicks B. B., Miller J. M., Prospero J. M., Arimoto R. and Church T. M. (1991) The atmospheric input of trace species to the world ocean. *Global Biogeochem. Cycles* **5**, 193–259. Available at: 10.1029/91gb01778.

Ducklow, Hugh. "Particulate Organic Carbon and Particulate Organic Nitrogen". United States JGOFS Data Server. Woods Hole Oceanographic Institution, USA: U.S. JGOFS Data Management Office, iPub: "June 3, 1997". Accessed: 'August 31, 2020'. http://usjgofs.whoi.edu/jg/serv/jgofs/arabian/ttn-045/poc_pon.html0%7Bdir=usjgofs.whoi.edu/jg/dir/jgofs/arabian/ttn-045/,info=usjgofs.whoi.edu/jg/info/jgofs/arabian/ttn-045/poc_pon%7D

Dutta K., Bhushan R. and Somayajulu B. (2007) Rapid vertical mixing rates in deep waters of the Andaman Basin. *Sci. Total Environ.* **384**, 401-408. Available at: http://dx.doi.org/10.1016/j.scitotenv.2007.04.041.

Dymond J., Collier R., McManus J., Honjo S. and Manganini S. (1997) Can the aluminum and titanium contents of ocean sediments be used to determine the paleoproductivity of the oceans? *Paleoceanography* **12**, 586–593. Available at: 10.1029/97pa01135.

ESR. 2009. OSCAR third degree resolution ocean surface currents. Ver. 1. PO.DAAC, CA, USA. Dataset accessed [2018-04-20] at http://dx.doi.org/10.5067/OSCAR-03D01.

Falkowski P., Scholes R. J., Boyle E., Canadell J., Canfield D., Elser J., Gruber N., Hubbard K., et al. (2000) The Global Carbon Cycle: A Test of Our Knowledge of Earth as a System. **290**, 291–296. Available at: 10.1126/science.290.5490.291.

Field C. B. (1998) Primary Production of the Biosphere: Integrating Terrestrial and Oceanic Components. **281**, 237–240. Available at: 10.1126/science.281.5374.237.

Fripiat F., Cavagna A.-J., Savoye N., Dehairs F., André L. and Cardinal D. (2011) Isotopic constraints on the Si-biogeochemical cycle of the Antarctic Zone in the Kerguelen area (KEOPS). Marine Chemistry 123, 11-22. Available at: https://doi.org/10.1016/j.marchem.2010.08.005.

Gaillardet J., Viers J. and Dupré B. (2014) Trace Elements in River Waters. In *Treatise on Geochemistry* Elsevier. pp. 195-235. Available at: http://dx.doi.org/10.1016/b978-0-08-095975 7.00507-6.

Gallant R. M. and Von Damm K. L. (2006) Geochemical controls on hydrothermal fluids from the Kairei and Edmond Vent Fields, 23°-25°S, Central Indian Ridge. *Geochemistry, Geophys. Geosystems* **7**. Available at: http://dx.doi.org/10.1029/2005gc001067.

Galy A. and France-Lanord C. (2001) Higher erosion rates in the Himalaya: Geochemical constraints on riverine fluxes. *Geology* **29**, 23. Available at: https://doi.org/10.1130/0091-7613(2001)029%3C0023:HERITH%3E2.0.CO;2.

Gamo T., Chiba H., Yamanaka T., Okudaira T., Hashimoto J., Tsuchida S., Ishibashi J.- ichiro, Kataoka S., Tsunogai U. and Okamura K. (2001) Chemical characteristics of newly discovered black smoker fluids and associated hydrothermal plumes at the Rodriguez Triple Junction, Central Indian Ridge. *Earth Planet. Sci. Lett.* **193**, 371-379. Available at: http://dx.doi.org/10.1016/s0012-821x(01)00511-8.

Gamo T., Nakayama E., Shitashima K., Isshiki K., Obata H., Okamura K., Kanayama S., Oomori T., Koizumi T. and Matsumoto S. (1996) Hydrothermal plumes at the Rodriguez triple junction, Indian ridge. *Earth Planet. Sci. Lett.* **142**, 261-270. Available at: http://dx.doi.org/10.1016/0012-821x(96)00087-8.

Gamo T., Okamura K., Hatanaka H., Hasumoto H., Komatsu D., Chinen M., Mori M., Tanaka J., Hirota A. and Tsunogai U. (2015) Hydrothermal plumes in the Gulf of Aden, as characterized by light transmission, Mn, Fe, CH4 and δ13C–CH4 anomalies. *Deep Sea Research Part II: Topical Studies in Oceanography* **121**, 62–70. Available at: 10.1016/j.dsr2.2015.06.004.

Gehlen M., Beck L., Calas G., Flank A.-M., Van Bennekom A. and Van Beusekom J. (2002) Unraveling the atomic structure of biogenic silica: evidence of the structural association of Al and Si in diatom frustules. *Geochim. Cosmochim. Acta* **66**, 1601-1609. Available at: http://dx.doi.org/10.1016/s0016-7037(01)00877-8.

Gehlen M., Heinze C., Maier-Reimer E. and Measures C. I. (2003) Coupled Al-Si geochemistry in an ocean general circulation model: A tool for the validation of oceanic dust deposition fields? *Global Biogeochem. Cycles* **17**. Available at: 10.1029/2001gb001549.

GEOTRACES Planning G. (2006) *GEOTRACES Science Plan. Baltimore, Maryland: Scientific Committee on Oceanic Research.*

Goswami V., Singh S. K. and Bhushan R. (2014) Impact of water mass mixing and dust deposition on Nd concentration and εNd of the Arabian Sea water column. *Geochim. Cosmochim. Acta* **145**, 30-49.
Available at: http://dx.doi.org/10.1016/j.gca.2014.09.006.

Grand M. M., Measures C. I., Hatta M., Hiscock W. T., Buck C. S. and Landing W. M. (2015a) Dust deposition in the eastern Indian Ocean: The ocean perspective from Antarctica to the Bay of Bengal. *Global Biogeochem. Cycles* **29**, 357–374. Available at: 10.1002/2014gb004898.

Grand M. M., Measures C. I., Hatta M., Hiscock W. T., Landing W. M., Morton P. L., Buck C. S., Barrett P. M. and Resing J. A. (2015b) Dissolved Fe and Al in the upper 1000 m of the eastern Indian Ocean: A high-resolution transect along 95°E from the Antarctic margin to the Bay of Bengal. *Global Biogeochem. Cycles* **29**, 375–396. Available at: 10.1002/2014gb004920.

Grand M. M., Measures C. I., Hatta M., Morton P. L., Barrett P., Milne A., Resing J. A. and Landing W. M. (2015c) The impact of circulation and dust deposition in controlling the distributions of dissolved Fe and Al in the south Indian subtropical gyre. *Mar. Chem.* **176**, 110-125.
Available at: http://dx.doi.org/10.1016/j.marchem.2015.08.002.

Guieu C., Duce R. and Arimoto R. (1994) Dissolved input of manganese to the ocean: Aerosol source. *J. Geophys. Res.* **99**, 18789. Available at: 10.1029/94jd01120.

Halpern D., Freilich M. H. and Weller R. A. (1998) Arabian Sea surface winds and ocean transports determined from ERS-1 scatterometer. *J. Geophys. Res.* **103**, 7799–7805. Available at: 10.1029/97jc02572.

Hamza W., Enan M. R., Al-Hassini H., Stuut J.-B. and de-Beer D. (2011) Dust storms over the Arabian Gulf: a possible indicator of climate changes consequences. *Aquatic Ecosystem Health & Management* **14**, 260–268. Available at: 10.1080/14634988.2011.601274.

Han Q., Moore J. K., Zender C., Measures C. and Hydes D. (2008) Constraining oceanic dust deposition using surface ocean dissolved Al. *Global Biogeochem. Cycles* **22**. Available at: 10.1029/2007gb002975.

Hand J. L., Mahowald N. M., Chen Y., Siefert R. L., Luo C., Subramaniam A. and Fun I. (2004) Estimates of atmospheric- processed soluble iron from observations and a global mineral aerosol model: Biogeochemical implications. *J. Geophys. Res.* **109**. Available at: http://dx.doi.org/10.1029/2004jd004574.

Hansen H. P. and Koroleff F. (1999) Determination of nutrients. In *Methods of seawater analysis 3rd edn.(eds. Grasshoff K., Kremling K. And Ehrhardt M.).* pp. 159-228. Available at: http://dx.doi.org/10.1002/9783527613984.ch10.

Hayes C. T., Black E. E., Anderson R. F., Baskaran M., Buesseler K. O., Charette M. A., Cheng H., Cochran J. K., Edwards R. L. and Fitzgerald P. (2018a) Flux of Particulate Elements in the North Atlantic Ocean Constrained by Multiple Radionuclides. Global Biogeochem. Cycles 32, 1738-1758. https://doi.org/10.1016/j.marchem.2010.08.00510.1029/2018GB005994.

Hayes C. T., Anderson R. F., Cheng H., Conway T. M., Edwards R. L., Fleisher M. Q., Ho P., Huang K.-F., John S. G. and Landing W. M. (2018) Replacement Times of a Spectrum of Elements in the North Atlantic Based on Thorium Supply. Global Biogeochem. Cycles 32, 1294-1311. Available at: https://doi.org/10.1029/2017GB005839.

Heimburger A., Losno R. and Triquet S. (2013) Solubility of iron and other trace elements in rainwater collected on the Kerguelen Islands (South Indian Ocean). *Biogeosciences* **10**, 6617–6628. Available at: 10.5194/bg-10-6617-2013.

Holte J. and Talley L. (2009) A New Algorithm for Finding Mixed Layer Depths with Applications to Argo Data and Subantarctic Mode Water Formation*. *J. Atmos. Ocean. Technol.* **26**, 1920-1939.
Available at: http://dx.doi.org/10.1175/2009jtecho543.1.

Holte J., Talley L. D., Gilson J. and Roemmich D. (2017) An Argo mixed layer climatology and database. *Geophys. Res. Lett.* **44**, 5618–5626. Available at: 10.1002/2017gl073426.

Ho T.-Y., Quigg A., Finkel Z. V., Milligan A. J., Wyman K., Falkowski P. G. and Morel F. M. M. (2003) THE ELEMENTAL COMPOSITION OF SOME

MARINE PHYTOPLANKTON1. *J Phycol* **39**, 1145–1159. Available at: 10.1111/j.0022-3646.2003.03-090.x.

Homoky W. B., Weber T., Berelson W. M., Conway T. M., Henderson G. M., van Hulten M., Jeandel C., Severmann S. and Tagliabue A. (2016) Quantifying trace element and isotope fluxes at the ocean–sediment boundary: a review. *Phil. Trans. R. Soc. A.* **374**, 20160246. Available at: 10.1098/rsta.2016.0246.

Husar R. B., Prospero J. M. and Stowe L. L. (1997) Characterization of tropospheric aerosols over the oceans with the NOAA advanced very high resolution radiometer optical thickness operational product. *J. Geophys. Res.* **102**, 16889–16909. Available at: 10.1029/96jd04009.

Hydes D. J. (1979) Aluminum in Seawater: Control by Inorganic Processes. *Science* **205**, 1260-1262. Available at: http://dx.doi.org/10.1126/science.205.4412.1260.

Jean-Baptiste P., Belviso S., Alaux G., Nguyen B. C. and Mihalopoulos N. (1990) 3He and methane in the Gulf of Aden. *Geochimica et Cosmochimica Acta* **54**, 111–116. Available at: 10.1016/0016-7037(90)90199-u.

Jean-Baptiste P., Mantisi F., Pauwells H., Grimaud D. and Patriat P. (1992) Hydrothermal3He and manganese plumes at 19°29′S on the Central Indian Ridge. *Geophys. Res. Lett.* **19**, 1787-1790. Available at: http://dx.doi.org/10.1029/92gl00577.

Jeandel C., Peucker-Ehrenbrink B., Jones M. T., Pearce C. R., Oelkers E. H., Godderis Y., Lacan F., Aumont O. and Arsouze T. (2011) Ocean margins: The missing term in oceanic element budgets?. Eos Trans. AGU 92, 217-218. Available at: https://doi.org/10.1029/2011eo260001.

Jensen, L. T., Morton, P., Twining, B. S., Heller, M. I., Hatta, M., Measures, C. I., et al. (2020). A comparison of marine Fe and Mn cycling: U.S. GEOTRACES GN01 Western Arctic case study. *Geochim. Cosmochim. Acta* 288, 138–160. doi:10.1016/j.gca.2020.08.006.

Jickells T. (1995) Atmospheric inputs of metals and nutrients to the oceans: their magnitude and effects. *Mar. Chem.* **48**, 199-214. Available at: http://dx.doi.org/10.1016/0304-4203(95)92784 p.

Jickells T. D., An Z. S., Andersen K. K., Baker A. R., Bergametti G., Brooks N., Can J. J., Boyd P. W., Duce R. A., Hunter K. A. and Kawahata H. (2005) Global Iron Connections Between Desert Dust, Ocean Biogeochemistry, and Climate. *Science* **308**, 67-71. Available at: http://dx.doi.org/10.1126/science.1105959.

Johnson K. S., Coale K. H., Berelson W. M. and Michael Gordon R. (1996) On the formation of the manganese maximum in the oxygen minimum. *Geochimica et Cosmochimica Acta* **60**, 1291–1299. Available at: 10.1016/0016-7037(96)00005-1.

Kadko D., Aguilar-Islas A., Bolt C., Buck C. S., Fitzsimmons J. N., Jensen L. T., Landing W. M., Marsay C. M., Rember R. and Shiller A. M. (2019) The residence times of trace elements determined in the surface Arctic Ocean during the 2015 US Arctic GEOTRACES expedition. *Marine Chemistry* **208**, 56–69. Available at: 10.1016/j.marchem.2018.10.011.

Klinkhammer G. P. and Bender M. L. (1980) The distribution of manganese in the Pacific Ocean. *Earth and Planetary Science Letters* **46**, 361–384. Available at: 10.1016/0012-821X(80)90051-5.

King A. L., Sañudo-Wilhelmy S. A., Boyd P. W., Twining B. S., Wilhelm S. W., Breene C., Ellwood M. J. and Hutchins D. A. (2012) A comparison of biogenic iron quotas during a diatom spring bloom using multiple approaches. *Biogeosciences* **9**, 667–687. Available at: 10.5194/bg-9-667-2012.

Köhler S. J., Dufaud F. and Oelkers E. H. (2003) An experimental study of illite dissolution kinetics as a function of ph from 1.4 to 12.4 and temperature from 5 to 50°C. *Geochimica et Cosmochimica Acta* **67**, 3583–3594. Available at: 10.1016/s0016-7037(03)00163-7.

Koning E., Gehlen M., Flank A.-M., Calas G. and Epping E. (2007) Rapid post-mortem incorporation of aluminum in diatom frustules: Evidence from chemical and structural analyses. *Mar. Chem.* **106**, 208-222. Available at: http://dx.doi.org/10.1016/j.marchem.2006.06.009.

Kumar A., Sudheer A. K., Goswami V. and Bhushan R. (2012) Influence of continental outflow on aerosol chemical characteristics over the Arabian Sea during winter. *Atmospheric Environment* **50**, 182–191. Available at: 10.1016/j.atmosenv.2011.12.040.

Kumar A., Sarin M. and Sudheer A. (2008) Mineral and anthropogenic aerosols in Arabian Sea–atmospheric boundary layer: Sources and spatial variability. *Atmos. Environ.* **42**, 5169-5181. Available at: http://dx.doi.org/10.1016/j.atmosenv.2008.03.004.

Kumar A., Suresh K. and Rahaman W. (2020) Geochemical characterization of modern aeolian dust over the Northeastern Arabian Sea: Implication for dust transport in the Arabian Sea. *Science of The Total Environment* **729**, 138576. Available at: 10.1016/j.scitotenv.2020.138576.

Kumar M. R. and Prasad T. G. (1997) Annual and interannual variation of precipitation over the tropical Indian Ocean. J. Geophys. Res. 102, 18519–18527. Available at: 10.1029/97jc00979.Léon J.-F. and Legrand M. (2003) Mineral dust sources in the surroundings of the north Indian Ocean. *Geophys. Res. Lett.* **30**. Available at: 10.1029/2002gl016690.

Kumar S. P., Madhupratap M., Kumar M. D., Gauns M., Muraleedharan P. M., Sarma V. V. S. S. and De Souza S. N. (2000) Physical control of primary productivity on a seasonal scale in central and eastern Arabian Sea. J Earth Syst Sci 109, 433–441. Available at: 10.1007/bf02708331.

Kumar S. P., Narvekar J., Kumar A., Shaji C., Anand P., Sabu P., Rijomon G., Jose J., Jayaraj K. A., Radhika A. and Nai K. K. C. (2004) Intrusion of the Bay of Bengal water into the Arabian Sea during winter monsoon and associated chemical and biological response. **31**, 4-7. Available at: http://dx.doi.org/10.1029/2004gl020247.

Landing W. M. and Bruland K. W. (1987) The contrasting biogeochemistry of iron and manganese in the Pacific Ocean. *Geochimica et Cosmochimica Acta* **51**, 29–43. Available at: 10.1016/0016-7037(87)90004-4.

Lee C., Murray D. W., Barber R. T., Buesseler K. O., Dymond J., Hedges J. I., Honjo S., Manganini S. J., Marra J. and Moser C. (1998) Particulate organic carbon fluxes: compilation of results from the 1995 US JGOFS Arabian Sea Process Study. *Deep Sea Research Part II: Topical Studies in Oceanography* **45**, 2489–2501. Available at: 10.1016/s0967-0645(98)00079-4.

Lewis B. L. and Luther III G. W. (2000) Processes controlling the distribution and cycling of manganese in the oxygen minimum zone of the Arabian Sea. *Deep Sea Research Part II: Topical Studies in Oceanography* **47**, 1541–1561. Available at: 10.1016/s0967-0645(99)00153-8.

Liu Q.-Y., Feng M., Wang D. and Wijffels S. (2015) Interannual variability of the Indonesian Throughflow transport: A revisit based on 30 year expendable bathythermograph data. J. Geophys. Res. Oceans **120**, 8270-8282. Available at: http://dx.doi.org/10.1002/2015jc011351.

Locarnini R. A., Mishonov A. V., Antonov J. I., Boyer T. P., Garcia H. E., Baranova O. K., Zweng M. M., Paver C. R., Reagan J. R., Johnson D. R., Hamilton M., and Seidov D. (2013) *World Ocean Atlas 2013, Volume 1: Temperature*. S. Levitus, Ed., A. Mishonov Technical Ed.; NOAA Atlas NESDIS 73, 40 pp.

Lunel T., Rudnicki M., Elderfield H. and Hydes D. (1990) Aluminium as a depth-sensitive tracer of entrainment in submarine hydrothermal plumes. *Nature* **344**, 137-139. Available at: http://dx.doi.org/10.1038/344137a0.

Mackie D. S., Boyd P. W., McTainsh G. H., Tindale N. W., Westberry T. K. and Hunter K. A. (2008) Biogeochemistry of iron in Australian dust: From eolian uplift to marine uptake. Geochem. Geophys. Geosyst.**9**. Available at: http://dx.doi.org/10.1029/2007gc001813.

Mackin J. E. and Aller R. C. (1984) Processes affecting the behavior of dissolved aluminum in estuarine waters. *Mar. Chem.* **14**, 213-232. Available at: http://dx.doi.org/10.1016/0304-4203(84)90043-4.

Mackin J. E. and Aller R. C. (1986) The effects of clay mineral reactions on dissolved Al distributions in sediments and waters of the Amazon continental shelf. *Cont. Shelf Res.* **6**, 245-262. Available at: http://dx.doi.org/10.1016/0278-4343(86)90063-4.

Mackin J. E. and Swider K. T. (1987) Modeling the dissolution behavior of standard clays in seawater. *Geochimica et Cosmochimica Acta* **51**, 2947–2964. Available at: 10.1016/0016-7037(87)90369-3.

Mahowald N. M., Baker A. R., Bergametti G., Brooks N., Duce R. A., Jickells T. D., Kubilay N., Prospero J. M. and Tegen I. (2005) Atmospheric global dust cycle and iron inputs to the ocean. *Global Biogeochem. Cycles* **19**. Available at: 10.1029/2004gb002402.

Malviya S., Scalco E., Audic S., Vincent F., Veluchamy A., Poulain J., Wincker P., Iudicone D., de Vargas C. and Bittner L. (2016) Insights into global diatom distribution and diversity in the world's ocean. Proc Natl Acad Sci USA 113, E1516-E1525. Available at: http://dx.doi.org/10.1073/pnas.1509523113.

Maillard C. and Soliman G. (1986) Hydrography of the Red Sea and exchanges with the Indian Ocean In summer. *OCEANOLOGICA ACTA* **9**.

Mantyla A. W. and Reid J. L. (1995) On the origins of deep and bottom waters of the Indian Ocean. *J. Geophys. Res.* **100**, 2417. Available at: 10.1029/94jc02564.

Maring H. B. and Duce R. A. (1987) The impact of atmospheric aerosols on trace metal chemistry in open ocean surface seawater, 1. Aluminum. *Earth and Planetary Science Letters* **84**, 381–392. Available at: 10.1016/0012-821x(87)90003-3.

Marra J. and Barber R. T. (2005) Primary productivity in the Arabian Sea: A synthesis of JGOFS data. *Progress in Oceanography* **65**, 159–175. Available at: 10.1016/j.pocean.2005.03.004.

Martin J. H. and Knauer G. A. (1980) Manganese cycling in northeast Pacific waters. *Earth and Planetary Science Letters* **51**, 266–274. Available at: 10.1016/0012-821x(80)90209-5.

Martin J. H. and Fitzwater S. E. (1988) Iron deficiency limits phytoplankton growth in the north-east Pacific subarctic. *Nature* **331**, 341–343. Available at: 10.1038/331341a0.

Martin J. H., Fitzwater S. E. and Gordon R. M. (1990) Iron deficiency limits phytoplankton growth in Antarctic waters. *Global Biogeochem. Cycles* **4**, 5–12. Available at: 10.1029/gb004i001p00005.

McCreary J. P., Kundu P. K. and Molinari R. L. (1993) A numerical investigation of dynamics, thermodynamics and mixed-layer processes in the Indian Ocean. *Progress in Oceanography* **31**, 181–244. Available at: 10.1016/0079-6611(93)90002-u.

McCreary J. P., Kohler K. E., Hood R. R. and Olson D. B. (1996) A four-component ecosystem model of biological activity in the Arabian Sea. *Progress in Oceanography* **37**, 193–240. Available at: 10.1016/s0079-6611(96)00005-5.

McCreary J. P., Yu Z., Hood R. R., Vinaychandran P. N., Furue R., Ishida A. and Richards K. J. (2013) Dynamics of the Indian-Ocean oxygen minimum zones. *Progress in Oceanography* **112–113**, 15–37. Available at: 10.1016/j.pocean.2013.03.002.

McLennan S. M. (2001) Relationships between the trace element composition of sedimentary rocks and upper continental crust. *Geochem. Geophys. Geosyst.* **2**. Available at: 10.1029/2000gc000109.

Measures C. I. and Edmond J. M. (1988) Aluminium as a tracer of the deep outflow from the Mediterranean. J. Geophys. Res. 93, 591-595. Available at: 10.1029/jc093ic01p00591.

Measures C. I. and Edmond J. M. (1990) Aluminium in the South Atlantic: Steady state distribution of a short residence time element. *J. Geophys. Res.* **95**, 5331. Available at: http://dx.doi.org/10.1029/jc095ic04p05331.

Measures C., Hatta M., Fitzsimmons J. and Morton P. (2015) Dissolved Al in the zonal N Atlantic section of the US GEOTRACES 2010/2011 cruises and the importance of hydrothermal inputs. *Deep Sea Research Part II: Topical Studies in Oceanography* **116**, 176–186. Available at: 10.1016/j.dsr2.2014.07.006

Measures C., Sato T., Vink S., Howell S. and Li Y. (2010) The fractional solubility of aluminium from mineral aerosols collected in Hawaii and implications for atmospheric deposition of biogeochemically important trace elements. *Mar. Chem.* **120**, 144-153.
Available at: http://dx.doi.org/10.1016/j.marchem.2009.01.014.

Measures C. I., Brown M. T. and Vink S. (2005) Dust deposition to the surface waters of the western and central North Pacific inferred from surface water dissolved aluminum concentrations. *Geochem. Geophys. Geosyst.* **6**. Available at: 10.1029/2005gc000922.

Measures C. I. and Vink S. (2000) On the use of dissolved aluminum in surface waters to estimate dust deposition to the ocean. *Global Biogeochem. Cycles* **14**, 317–327. Available at: 10.1029/1999gb001188.

Measures C. I. and Vink S. (1999) Seasonal variations in the distribution of Fe and Al in the surface waters of the Arabian Sea. *Deep Sea Research Part II: Topical Studies in Oceanography* **46**, 1597–1622. Available at: 10.1016/s0967-0645(99)00037-5.

Mendez J., Guieu C. and Adkins J. (2010) Atmospheric input of manganese and iron to the ocean: Seawater dissolution experiments with Saharan and North American dusts. *Marine Chemistry* **120**, 34–43.
Available at: 10.1016/j.marchem.2008.08.006.

Menzel Barraqueta J.-L. (2018) Aluminium in the North Atlantic Ocean and the Labrador Sea (GEOTRACES GA01 section): roles of continental inputs and biogenic particle removal. *Biogeosciences* **15**, 5271–5286. Available at: 10.5194/bg-15-5271-2018.

Middag R., de Baar H., Laan P. and Bakker K. (2009) Dissolved aluminium and the silicon cycle in the Arctic Ocean. *Mar. Chem.* **115**, 176-195. Available at: http://dx.doi.org/10.1016/j.marchem.2009.08.002.

Middag R., de Baar H. J. W., Laan P. and Klunder M. B. (2011) Fluvial and hydrothermal input of manganese into the Arctic Ocean. *Geochimica et Cosmochimica Acta* **75**, 2393–2408. Available at: 10.1016/j.gca.2011.02.011.

Middag R., de Baar H. J. W., Laan P. and Huhn O. (2012) The effects of continental margins and water mass circulation on the distribution of dissolved aluminum and manganese in Drake Passage. *J. Geophys. Res. Ocean.* **117**, 1-19. Available at: http://dx.doi.org/10.1029/2011jc007434.

Middag R., van Hulten M. M. P., Van Aken H. M., Rijkenberg M. J. A., Gerringa L. J. A., Laan P. and de Baar H. J. W. (2015) Dissolved aluminium in the ocean conveyor of the West Atlantic Ocean: Effects of the biological cycle, scavenging, sediment resuspension and hydrography. *Marine Chemistry* **177**, 69–86. Available at: 10.1016/j.marchem.2015.02.015.

Moffett J. W. (1997) The importance of microbial Mn oxidation in the upper ocean: a comparison of the Sargasso Sea and equatorial Pacific. *Deep Sea Research Part I: Oceanographic Research Papers* **44**, 1277–1291. Available at: 10.1016/s0967-0637(97)00032-0.

Moore W. S. (1984) Review of the geosecs project. *Nuclear Instruments and Methods in Physics Research* **223**, 459–465. Available at: 10.1016/0167-5087(84)90692-6.

Moran S. B. and Moore R. M. (1988) Evidence from mesocosm studies for biological removal of dissolved aluminium from sea water. *Nature* **335**, 706-708. Available at: http://dx.doi.org/10.1038/335706a0.

Moran S. B. and Moore R. M. (1988) Temporal variations in dissolved and particulate aluminum during a spring bloom. *Estuarine, Coastal and Shelf Science* **27**, 205–215. Available at: 10.1016/0272-7714(88)90090-x.

Moran S. B. and Moore R. M. (1991) The potential source of dissolved aluminum from resuspended sediments to the North Atlantic Deep Water. *Geochim. Cosmochim. Acta* **55**, 2745-2751. Available at: http://dx.doi.org/10.1016/0016-7037(91)90441-7.

Morgan J. J. (2005) Kinetics of reaction between O2 and Mn(II) species in aqueous solutions. *Geochimica et Cosmochimica Acta* **69**, 35–48. Available at: 10.1016/j.gca.2004.06.013.

Morgan J. J. (1967) Chemical equilibria and kinetic properties of manganese in natural waters. In *Principles and Applications ofWater Chemistry* (eds. S. D. Faust and J. V. Hunter). pp. 561–620.

Morrison J. M., Codispoti L. A., Smith S. L., Wishner K., Flagg C., Gardner W. D., Gaurin S., Naqvi S. W. A., Manghnani V. and Prosperie L. (1999) The oxygen minimum zone in the Arabian Sea during 1995. *Deep Sea Research Part II: Topical Studies in Oceanography* **46**, 1903–1931. Available at: 10.1016/S0967-0645(99)00048-X.

Morton P. L., Landing W. M., Shiller A. M., Moody A., Kelly T. D., Bizimis M., Donat J. R., De Carlo E. H. and Shacat J. (2019) Shelf Inputs and Lateral Transport of Mn, Co, and Ce in the Western North Pacific Ocean. *Front. Mar. Sci.* **6**. Available at: 10.3389/fmars.2019.00591.

Murton B. J., Baker E. T., Sands C. M. and German C. R. (2006) Detection of an unusually large hydrothermal event plume above the slow-spreading Carlsberg Ridge: NW Indian Ocean. *Geophys. Res. Lett.* **33**. Available at: 10.1029/2006gl026048.

Narvekar P. V. and Singbal S. Y. S. (1993) Dissolved aluminium in the surface microlayer of the eastern Arabian sea. Marine Chemistry 42, 85–94. Available at: 10.1016/0304-4203(93)90239-k.

Nozaki Y. and Alibo D. S. (2003) Importance of vertical geochemical processes in controlling the oceanic profiles of dissolved rare earth elements in the northeastern Indian Ocean. *Earth Planet. Sci. Lett.* **205**, 155-172. Available at: http://dx.doi.org/10.1016/s0012-821x(02)01027-0.

Nozaki Y. and Yamamoto Y. (2001) Radium 228 based nitrate fluxes in the eastern Indian Ocean and the South China Sea and a silicon-induced “alkalinity pump” hypothesis. *Global Biogeochem. Cycles* **15**, 555-567. Available at: http://dx.doi.org/10.1029/2000gb001309.

Obata H., Nozaki Y., Alibo D. S. and Yamamoto Y. (2004) Dissolved Al, In, and Ce in the eastern Indian Ocean and the Southeast Asian Seas in comparison with the radionuclides 210Pb and 210Po. *Geochim. Cosmochim. Acta* **68**, 1035-1048. Available at: http://dx.doi.org/10.1016/j.gca.2003.07.021.

Ohnemus D. C. and Lam P. J. (2015) Cycling of lithogenic marine particles in the US GEOTRACES North Atlantic transect. Deep Sea Research Part II: Topical Studies in Oceanography 116, 283-302. Available at: http://dx.doi.org/10.1016/j.dsr2.2014.11.019.

Okubo A., Obata H., Nozaki Y., Yamamoto Y. and Minami H. (2004) 230Th in the Andaman Sea: Rapid deep-sea renewal. Geophys. Res. Lett. **31**, 1-5. Available at: http://dx.doi.org/10.1029/2004gl020226.

Orians K. J. and Bruland K. W. (1985) Dissolved aluminium in the central North Pacific. *Nature* **316**, 427-429. Available at: http://dx.doi.org/10.1038/316427a0.

Orians K. J. and Bruland K. W. (1986) The biogeochemistry of aluminum in the Pacific Ocean. *Earth and Planetary Science Letters* **78**, 397–410. Available at: 10.1016/0012-821x(86)90006-3.

Orians K. J. and Bruland K. W. (1988) The marine geochemistry of dissolved gallium: A comparison with dissolved aluminum. *Geochimica et Cosmochimica Acta* **52**, 2955–2962. Available at: 10.1016/0016-7037(88)90160-3.

Pausch F., Bischof K. and Trimborn S. (2019) Iron and manganese co-limit growth of the Southern Ocean diatom Chaetoceros debilis. *PLoS ONE* **14**, e0221959. Available at: 10.1371/journal.pone.0221959.

Pease P. P., Tchakerian V. P. and Tindale N. W. (1998) Aerosols over the Arabian Sea: geochemistry and source areas for aeolian desert dust. *Journal of Arid Environments* **39**, 477–496. Available at: 10.1006/jare.1997.0368.

Peers G. and Price N. M. (2004) A role for manganese in superoxide dismutases and growth of iron-deficient diatoms. *Limnol. Oceanogr.* **49**, 1774–1783. Available at: 10.4319/lo.2004.49.5.1774.

Pokhrel S., Rahaman H., Parekh A., Saha S. K., Dhakate A., Chaudhari H. S. and Gairola R. M. (2012) Evaporation-precipitation variability over Indian Ocean and its assessment in NCEP Climate Forecast System (CFSv2). *Clim Dyn* **39**, 2585–2608. Available at: 10.1007/s00382-012-1542-6.

Potemra J. T. and Schneider N. (2007) Interannual variations of the Indonesian throughflow. J. Geophys. Res. 112.

Prasad T. G., Ikeda M. and Kumar S. P. (2001) Seasonal spreading of the Persian Gulf Water mass in the Arabian Sea. *J. Geophys. Res.* **106**, 17059–17071. Available at: 10.1029/2000jc000480.

Ramaswamy V. And Nair R. R. (1994) Fluxes of material in the Arabian Sea and Bay of Bengal — Sediment trap studies. *Proc. Indian Acad. Sci. (Earth Planet Sci.)* **103**, 189-210. Available at: https://link.springer.com/article/10.1007/BF02839536

Ramaswamy V., Muraleedharan P. M. and Babu C. P. (2017) Mid-troposphere transport of Middle-East dust over the Arabian Sea and its effect on rainwater composition and sensitive ecosystems over India. *Sci Rep* **7**. Available at: 10.1038/s41598-017-13652-1.

Rao A. R., Rao G. N., Sreenivas P. and Kumar P. V. H. (2013) Role of Meso-Scale Eddies on Circulation in the South Eastern Arabian Sea in 2009. *Marine Geodesy* **36**, 319–333. Available at: 10.1080/01490419.2013.811448.

RAVEN J. A. (1990) Predictions of Mn and Fe use efficiencies of phototrophic growth as a function of light availability for growth and of C assimilation pathway. *New Phytol* **116**, 1–18. Available at: 10.1111/j.1469-8137.1990.tb00505.x.

Ray D., Kamesh Raju K. A., Baker E. T., Srinivas Rao A., Mudholkar A. V., Lupton J. E., Surya Prakash L., Gawas R. B. and Vijaya Kumar T. (2012) Hydrothermal plumes over the Carlsberg Ridge, Indian Ocean. *Geochem. Geophys. Geosyst.* **13**. Available at: 10.1029/2011gc003888.

Resing J. A. and Measures C. I. (1994) Fluorometric Determination of Al in Seawater by Flow Injection Analysis with In-Line Preconcentration. *Anal. Chem.* **66**, 4105-4111. Available at: http://dx.doi.org/10.1021/ac00094a039.

Resing J. A., Sedwick P. N., German C. R., Jenkins W. J., Moffett J. W., Sohst B. M. and Tagliabue A. (2015) Basin-scale transport of hydrothermal dissolved metals across the South Pacific Ocean. *Nature* **523**, 200-203. Available at: http://dx.doi.org/10.1038/nature14577.

Rizal S., Damm P., Wahid M. A., Sundermann J., Ilhamsyah Y. and Iskandar T. (2012) General circulation in the Malacca Strait and Andaman Sea: A numerical model study. *Am. J. Environ. Sci.* **8**, 479-488. Available at: http://dx.doi.org/10.3844/ajessp.2012.479.488.

Robbins P. E. and Toole J. M. (1997) The dissolved silica budget as a constraint on the meridional overturning circulation of the Indian Ocean. *Deep Sea Res. Part I Oceanogr. Res. Pap.* **44**, 879-906. Available at: http://dx.doi.org/10.1016/s0967-0637(96)00126-4.

Robinson R., Bird M., Oo N., Hoey T., Aye M., Higgitt D., X. X. L., Swe A., Tun T. and Win S. (2007) The Irrawaddy River Sediment Flux to the Indian Ocean: The Original Nineteenth‐Century Data Revisited. *J. Geol.* **115**, 629-640. Available at: http://dx.doi.org/10.1086/521607.

Saager P. M., De Baar H. J. W. and Burkill P. H. (1989) Manganese and iron in Indian Ocean waters. *Geochimica et Cosmochimica Acta* **53**, 2259–2267. Available at: 10.1016/0016-7037(89)90348-7.

Sandeep K. K., Pant V., Girishkumar M. S. and Rao A. D. (2018) Impact of riverine freshwater forcing on the sea surface salinity simulations in the Indian Ocean. *Journal of Marine Systems* **185**, 40–58. Available at: 10.1016/j.jmarsys.2018.05.002.

SARIN M. M., RENGARAJAN R. and KRISHNASWAMI S. (1999) Aerosol NO-3 and 210Pb distribution over the central-eastern Arabian Sea and their air-sea deposition fluxes. *Tellus B* **51**, 749–758. Available at: 10.1034/j.1600-0889.1999.t01-3-00001.x.

Sarma V. V. S. S. and Dalabehera H. B. (2019) New and primary production in the western Indian Ocean during fall monsoon. *Marine Chemistry* **215**, 103687. Available at: 10.1016/j.marchem.2019.103687.

Schlitzer, R., 2016. Ocean Data View. Available at: https://odv.awi.de.

Schott F. A. and McCreary J. P. (2001) The monsoon circulation of the Indian Ocean. *Progress in Oceanography* **51**, 1–123. Available at: 10.1016/s0079-6611(01)00083-0.

Schott F. A., Xie S.-P. and McCreary J. P. (2009) Indian Ocean circulation and climate variability. *Rev. Geophys.* **47**. Available at: 10.1029/2007rg000245.

Schüßler U., Balzer W. and Deeken A. (2005) Dissolved Al distribution, particulate Al fluxes and coupling to atmospheric Al and dust deposition in the Arabian Sea. *Deep Sea Research Part II: Topical Studies in Oceanography* **52**, 1862–1878. Available at: 10.1016/j.dsr2.2005.06.005.

Selavka C. M., Jiao K. S. and Krull I. S. (1987) Construction and comparison of open tubular reactors for post-column reaction detection in liquid chromatography. Anal. Chem. **59**, 2221-2224.
Available at: http://dx.doi.org/10.1021/ac00144a048.

Sengupta D., Bharath Raj G. N. and Shenoi S. S. C. (2006) Surface freshwater from Bay of Bengal runoff and Indonesian Throughflow in the tropical Indian Ocean. *Geophys. Res. Lett.* **33**. Available at: http://dx.doi.org/10.1029/2006gl027573.

Shankar D. and Shetye S. R. (1997) On the dynamics of the Lakshadweep high and low in the southeastern Arabian Sea. *J. Geophys. Res.* **102**, 12551–12562. Available at: 10.1029/97jc00465.

Shenoi S. S. C., Shetye S. R., Gouveia A. D. and Michael G. S. (1993) Salinity Extrema in the Arabian Sea. Mitt. Geol.-Palaeont. Inst. Univ. Hamburg SCOPE/UNEP Sonderband **76**, 37–49.

Shetye S. R., Gouveia A. D. and Shenoi S. S. C. (1994) Circulation and water masses of the Arabian Sea. **103**, 107–123.
Available at: https://doi.org/10.1007/BF02839532.

Shriadah M. A., Okbah M. A. and El-Deek M. S. (2004) Trace Metals in the Water Columns of the Red Sea and the Gulf of Aqaba, Egypt. *Water, Air, & Soil Pollution* **153**, 115–124. Available at: 10.1023/b:wate.0000019938.57041.21.

Siedler G. (1969) General Circulation of Water Masses in the Red Sea. In *Hot brines and recent heavy metal deposits in the Red Sea* (eds. E. T. Degens and D. A. Ross). Springer-Verlag, New York. pp. 131–137.

Siefert R. L., Johansen A. M. and Hoffmann M. R. (1999) Chemical characterization of ambient aerosol collected during the southwest monsoon and intermonsoon seasons over the Arabian Sea: Labile-Fe(II) and other trace metals. *J. Geophys. Res.* **104**, 3511–3526. Available at: 10.1029/1998jd100067.

Singh S. K. and France-Lanord C. (2002) Tracing the distribution of erosion in the Brahmaputra watershed from isotopic compositions of stream sediments. *Earth Planet. Sci. Lett.* **202**, 645-662. Available at: http://dx.doi.org/10.1016/s0012-821x(02)00822-1.

Singh S. K., Rai S. K. and Krishnaswami S. (2008) Sr and Nd isotopes in river sediments from the Ganga Basin: Sediment provenance and spatial variability in physical erosion. *J. Geophys. Res.* **113**. Available at: http://dx.doi.org/10.1029/2007jf000909.

Singh S. P., Singh S. K., Goswami V., Bhushan R. and Rai V. K. (2012) Spatial distribution of dissolved neodymium and εNd in the Bay of Bengal: Role of particulate matter and mixing of water masses. *Geochim. Cosmochim. Acta* **94**, 38-56. Available at: http://dx.doi.org/10.1016/j.gca.2012.07.017.

Singh N. D., Chinni V. and Singh S. K. (2020) Dissolved aluminium cycling in the northern, equatorial and subtropical gyre region of the Indian Ocean. *Geochimica et Cosmochimica Acta* **268**, 160–185. Available at: 10.1016/j.gca.2019.09.028.

Sree Lekha J., Buckley J. M., Tandon A. and Sengupta D. (2018) Subseasonal Dispersal of Freshwater in the Northern Bay of Bengal in the 2013 Summer Monsoon Season. *J. Geophys. Res. Oceans* **123**, 6330–6348. Available at: 10.1029/2018jc014181.

Srinivas B. and Sarin M. (2013) Atmospheric dry-deposition of mineral dust and anthropogenic trace metals to the Bay of Bengal. *J. Mar. Syst.* **126**, 56-68. Available at: http://dx.doi.org/10.1016/j.jmarsys.2012.11.004.

Srichandan S., Panigrahy R. C., Baliarsingh S. K., Rao B. S., Pati P., Sahu B. K. and Sahu K. C. (2016) Distribution of trace metals in surface seawater and zooplankton of the Bay of Bengal, off Rushikulya estuary, East Coast of India. *Marine Pollution Bulletin* **111**, 468–475. Available at: 10.1016/j.marpolbul.2016.06.099.

Srinivasan A., Rooth C. G. H., Top Z. and Olson D. B. (2000) Abyssal upwelling in the Indian Ocean: Radiocarbon diagnostics. *J. Mar. Res.* **58**, 755-778. Available at: http://dx.doi.org/10.1357/002224000321358891.

Srinivasan A., Top Z., Schlosser P., Hohmann R., Iskandarani M., Olson D. B., Lupton J. E., Jenkins W. L. (2004) Mantle 3He distribution and deep circulation in the Indian Ocean. *J. Geophys. Res.* **109**. Available at: 10.1029/2003jc002028.

Sunda W. G. and Huntsman S. A. (1988) Effect of sunlight on redox cycles of manganese in the southwestern Sargasso Sea. *Deep Sea Research Part A. Oceanographic Research Papers* **35**, 1297–1317. Available at: 10.1016/0198-0149(88)90084-2.

Sunda W. G. (1989) Trace metal interactions with marine phytoplankton. *Biological Oceanography* **6**, 411–442.

Sunda W. G. and Huntsman S. A. (1994) Photoreduction of manganese oxides in seawater. *Marine Chemistry* **46**, 133–152. Available at: 10.1016/0304-4203(94)90051-5.

Sunda W. G. (2012) Feedback Interactions between Trace Metal Nutrients and Phytoplankton in the Ocean. *Front. Microbio.* **3**. Available at: 10.3389/fmicb.2012.00204.

Tarran G. A., Burkill P. H., Edwards E. S. and Woodward E. M. S. (1999) Phytoplankton community structure in the Arabian Sea during and after the SW monsoon, 1994. *Deep Sea Research Part II: Topical Studies in Oceanography* **46**, 655–676. Available at: 10.1016/s0967-0645(98)00122-2.

Tebo B. M., Johnson H. A., McCarthy J. K. and Templeton A. S. (2005) Geomicrobiology of manganese(II) oxidation. *Trends in Microbiology* **13**, 421–428. Available at: 10.1016/j.tim.2005.07.009.

Thi Dieu Vu H. and Sohrin Y. (2013) Diverse stoichiometry of dissolved trace metals in the Indian Ocean. *Sci Rep* **3**. Available at: 10.1038/srep01745.

Tindale, Neil. "Aerosol, Al data". United States JGOFS Data Server. Woods Hole Oceanographic Institution, USA: U.S. JGOFS Data Management Office, iPub: "June 30, 1997". Accessed: 'March 20, 2020'. http://usjgofs.whoi.edu/jg/serv/jgofs/arabian/aerosols_short.html0%7Bdir=usjgofs.whoi.edu/jg/dir/jgofs/arabian/,info=usjgofs.whoi.edu/jg/info/jgofs/arabian/aerosols_short%7D

Tindale N. W. and Pease P. P. (1999) Aerosols over the Arabian Sea: Atmospheric transport pathways and concentrations of dust and sea salt. *Deep Sea Research Part II: Topical Studies in Oceanography* **46**, 1577–1595. Available at: 10.1016/s0967-0645(99)00036-3.

Tomczak M. and Large D. G. B. (1989) Optimum multiparameter analysis of mixing in the thermocline of the eastern Indian Ocean. *J. Geophys. Res.* **94**, 16141. Available at: http://dx.doi.org/10.1029/jc094ic11p16141.

Tomczak, M. and Godfrey, J.S., 2003a. Chapter 12-Hydrology of the Indian Ocean. In *Regional oceanography: an introduction 2nd edn.*. pp. 199-213. Available at: https://www.mt-oceanography.info/regoc/pdfversion.html.

Tomczak, M. and Godfrey, J.S., 2003b. Chapter 13-Adjacent seas of the Indian Ocean and the Australasian Mediterranean Sea (the Indonesian throughflow). In *Regional oceanography: an introduction 2nd edn.* pp. 215-228. Available at: https://www.mt-oceanography.info/regoc/pdfversion.html.

Toole J. M. and Warren B. A. (1993) A hydrographic section across the subtropical South Indian Ocean. *Deep Sea Research Part I: Oceanographic Research Papers* **40**, 1973–2019. Available at: 10.1016/0967-0637(93)90042-2.

Torfstein A., Teutsch N., Tirosh O., Shaked Y., Rivlin T., Zipori A., Stein M., Lazar B. and Erel Y. (2017) Chemical characterization of atmospheric dust from a weekly time series in the north Red Sea between 2006 and 2010. *Geochimica et Cosmochimica Acta* **211**, 373–393. Available at: 10.1016/j.gca.2017.06.007.

Tréguer P. J. and De La Rocha C. L. (2013) The World Ocean Silica Cycle. Annu. Rev. Mar. Sci. 5, 477-501. Available at: http://dx.doi.org/10.1146/annurev-marine-121211-172346.

Twining B. S. and Baines S. B. (2013) The Trace Metal Composition of Marine Phytoplankton. *Annu. Rev. Mar. Sci.* **5**, 191–215. Available at: 10.1146/annurev-marine-121211-172322.

Twining B. S., Baines S. B., Bozard J. B., Vogt S., Walker E. A. and Nelson D. M. (2011) Metal quotas of plankton in the equatorial Pacific Ocean. *Deep Sea Research Part II: Topical Studies in Oceanography* **58**, 325–341. Available at: 10.1016/j.dsr2.2010.08.018.

Twining B. S., Baines S. B. and Fisher N. S. (2004) Element stoichiometries of individual plankton cells collected during the Southern Ocean Iron Experiment (SOFeX). *Limnol. Oceanogr.* **49**, 2115–2128. Available at: 10.4319/lo.2004.49.6.2115.

Unger D., Ittekkot V., Schäfer P., Tiemann J. and Reschke S. (2003) Seasonality and interannual variability of particle fluxes to the deep Bay of Bengal: influence of riverine input and oceanographic processes. *Deep Sea Research Part II: Topical Studies in Oceanography* **50**, 897–923. Available at: 10.1016/s0967-0645(02)00612-4.

Upadhyay S. and Sen Gupta R. (1994) Aluminium in the north-western Indian Ocean (Arabian Sea). Marine Chemistry 47, 203–214. Available at: 10.1016/0304-4203(94)90020-5.

Van Beueskom J., Van Bennekom A., Tréguer P. and Morvan J. (1997) Aluminium and silicic acid in water and sediments of the Enderby and Crozet Basins. *Deep. Res. Part II Top. Stud. Oceanogr.* **44**, 987-1003. Available at: http://dx.doi.org/10.1016/s0967-0645(96)00105-1.

van der Weijden A. J. and van der Weijden C. H. (2002) Silica fluxes and opal dissolution rates in the northern Arabian Sea. *Deep Sea Research Part I: Oceanographic Research Papers* **49**, 157–173. Available at: 10.1016/s0967-0637(01)00050-4.

van Hulten M. M. P., Sterl A., Tagliabue A., Dutay J.-C., Gehlen M., de Baar H. J. W. and Middag R. (2013) Aluminium in an ocean general circulation model compared with the West Atlantic Geotraces cruises. *Journal of Marine Systems* **126**, 3–23. Available at: 10.1016/j.jmarsys.2012.05.005.

van Hulten M. M. P., Sterl A., Middag R., de Baar H. J. W., Gehlen M., Dutay J.-C. and Tagliabue A (2014). On the effects of circulation, sediment resuspension and biological incorporation by diatoms in an ocean model of aluminium*. *Biogeosciences* **11**, 3757-3779. Available at: http://dx.doi.org/10.5194/bg-11-3757-2014.

van Hulten M., Middag R., Dutay J.-C., de Baar H., Roy-Barman M., Gehlen M., Tagliabue A. and Sterl A. (2017) Manganese in the west Atlantic Ocean in the context of the first global ocean circulation model of manganese. *Biogeosciences* **14**, 1123–1152. Available at: 10.5194/bg-14-1123-2017.

Vink S. and Measures C. (2001) The role of dust deposition in determining surface water distributions of Al and Fe in the South West Atlantic. *Deep Sea Res. Part II Top. Stud. Oceanogr.* **48**, 2787-2809. Available at: http://dx.doi.org/10.1016/s0967-0645(01)00018-2.

Warren B. A. (1981) Transindian hydrographic section at Lat. 18°S: Property distributions and circulation in the South Indian Ocean. *Deep Sea Res. Part A. Oceanogr. Res. Pap.* **28**, 759-788. Available at: http://dx.doi.org/10.1016/s0198-0149(81)80001-5.

Whitmore, L. M., Morton, P. L., Twining, B. S., and Shiller, A. M. (2019). Vanadium cycling in the Western Arctic Ocean is influenced by shelf-basin connectivity. *Mar. Chem.* 216, 103701. doi:10.1016/j.marchem.2019.103701.

Wyrtki K. (1971) Oceanographic Atlas of the International Indian Ocean Expedition., National Science Foundation, Washington, D.C.

Wyrtki K. (1973) Physical oceanography of the Indian Ocean. In *The Biology of the Indian Ocean* (ed. B. Zeitschel). Springer-Verlag, Berlin. pp. 18–36.

Yadav D. N. (1996) Manganese remobilization from the Western Continental Margin of India. *Current Science* **71**, 900–905.

YAMAGATA N. and IWASHIMA K. (1963) Monitoring of Sea-Water for Important Radioisotopes Released by Nuclear Reactors. *Nature* **200**, 52–52. Available at: 10.1038/200052a0.

You Y. and Tomczak M. (1993) Thermocline circulation and ventilation in the Indian Ocean derived from water mass analysis. *Deep Sea Res. Part I Oceanogr. Res. Pap.* **40**, 13-56. Available at: http://dx.doi.org/10.1016/0967-0637(93)90052-5.

You Y. (1997) Seasonal variations of thermocline circulation and ventilation in the Indian Ocean. *J. Geophys. Res.* **102**, 10391–10422. Available at: 10.1029/96jc03600.

You Y. (1999) Dianeutral mixing, transformation and transport of the deep water of the Indian Ocean. *Deep Sea Research Part I: Oceanographic Research Papers* **46**, 109–148. Available at: 10.1016/s0967-0637(98)00058-2.

You Y. (2000) Implications of the deep circulation and ventilation of the Indian Ocean on the renewal mechanism of North Atlantic Deep Water. *J. Geophys. Res.* **105**, 23895–23926. Available at: 10.1029/2000jc900105.

Zender C. S., Bian H. and Newman D. (2003) Mineral Dust Entrainment and Deposition (DEAD) model: Description and 1990s dust climatology. J. Geophys. Res. 108.

Zweng, M.M, Reagan J.R., Antonov J.I., Locarnini R.A.,. Mishonov A.V, Boyer T.P.,. Garcia H.E, Baranova O.K., Johnson D.R. and Seidov D., Biddle M.M. (2013) *World Ocean Atlas 2013, Volume 2: Salinity*. S. Levitus, Ed., A. Mishonov Technical Ed.; NOAA Atlas NESDIS 74, 39 pp.

Research Articles (published/in preparation)

1. **Singh N. D.**, Chinni V. and Singh S. K. (2020) Dissolved aluminium cycling in the northern, equatorial and subtropical gyre region of the Indian Ocean. *Geochimica et Cosmochimica Acta* **268**, 160–185. Available at: 10.1016/j.gca.2019.09.028

2. **Singh N. D.** and Singh S. K. Distribution and cycling of dissolved aluminium in the Arabian Sea and the western equatorial Indian Ocean. (in preparation)

3. **Singh N. D**., Singh S. K., Malla N., Chinni V. The biogeochemical cycling of dissolved manganese in the Arabian Sea. (in preparation)

Conferences/ workshops

1. **Singh N. D.**, Chinni V. and Singh S. K. Poster presentation on "Dissolved Aluminium in the Bay of Bengal, Equatorial and Subtropical Indian Ocean: Sources, Sinks and Internal Cycling**"** during training workshop on "Metal Speciation and Isotopes in the Ocean" at the State Key Laboratory of Marine Environmental Science, Xiamen University, Xiamen, China Xiamen, China during the period May 12-17, 2018.

2. **Singh N. D**., Chinni V. and Singh S. K. Poster presentation on the topic "Dissolved Aluminium Cycling in the Northern, Equatorial and Subtropical Gyre region of the Indian Ocean" at Goldschmidt Conference-2019 in Barcelona, Spain.

3. **Singh N. D** and Singh S. K. Oral presentation on the topic "Biogeochemical cycling of dissolved manganese in the Arabian Sea" at online national research meet on "Low Temperature Geochemistry in Rivers, Oceans and at their Boundaries" organised by CSIR-NIO, Goa, India, on November 1, 2020.

Available online at www.sciencedirect.com

ScienceDirect

Geochimica et Cosmochimica Acta 268 (2020) 160–185

Geochimica et Cosmochimica Acta

www.elsevier.com/locate/gca

Dissolved aluminium cycling in the northern, equatorial and subtropical gyre region of the Indian Ocean

Naman Deep Singh [a,b], Venkatesh Chinni [a,1], Sunil Kumar Singh [a,*]

[a] *Geosciences Division, Physical Research Laboratory, Ahmedabad 380009, Gujarat, India*
[b] *Indian Institute of Technology Gandhinagar, Gandhinagar 382355, Gujarat, India*

Received 14 November 2018; accepted in revised form 13 September 2019; Available online 27 September 2019

Abstract

Dissolved aluminium (hereafter, dAl) concentrations have been determined on 34 full vertical water column profiles, sampled along the two separate GEOTRACES-India transects (GI-01 and GI-06) to understand the biogeochemical controls on dAl distribution in the northern (the Bay of Bengal, the Andaman Sea and the Arabian Sea), equatorial and subtropical gyre region of the Indian Ocean. Al released due to the partial dissolution of and/or Al desorption from the suspended lithogenic sediments, supplied in a huge amount to the Bay of Bengal (BoB) waters by the Ganga-Brahmaputra (G-B) river system, Indian peninsular rivers and sediment resuspension from the continental shelf and slope, predominantly controls the dAl distribution in the BoB and results in an overall increase in the dAl concentrations throughout the water column towards the northern BoB and the eastern coast of India. Considering the steady-state balance between the dAl input from the lithogenic sediment flux in the upper water column and first-order scavenging removal of dAl, the fractional solubility of Al from the lithogenic sediments in the BoB surface waters is estimated to be in the range of 1.1–4.7%. Advection of Indonesian Sea surface waters through the Strait of Malacca and dAl input from the partial dissolution of resuspended terrigenous sediments, sourced from the insular shelf of the Nicobar Islands, set major controls on the dAl distribution in the surface and upper thermocline waters of the southern Andaman Sea and the southern BoB region near the Nicobar Islands. Rapid renewal of and vertical mixing in the deeper waters (>1000 m) relative to scavenging removal of dAl results in near-uniform dAl concentrations (~3.7 nM) in the deeper waters at the center of the southern Andaman Sea. In the south-eastern Arabian Sea, the continental outflow of mineral dust and advection of dAl enriched Bay of Bengal surface waters control the dAl distribution in the surface water layer. dAl in the surface waters of the equatorial Indian Ocean, during the late winter sampling period of the GI-06 cruise, is predominantly determined by the mixing between dAl-rich surface waters of the southern BoB and relatively, dAl-depleted surface waters of the southern Arabian Sea under the influence of the Northeast Monsoon Current. The scavenging residence time of dAl in the deep waters of the equatorial Indian Ocean is estimated using a 1-D scavenging-advection–diffusion model and found to be in the range of 92–141 years. Deposition of Australian dust and advection of Indonesian Throughflow Water translates to the dAl enrichment in the upper water column (<500 m) at the northern end of the Indian Subtropical Gyre. Sediment resuspension near the Central Indian Ridge probably enrich the dAl in the ambient deep water depth (2000–3500 m) and this signal dampens as the deep waters progress north-westward in the Central Indian Ocean Basin. The bottom water (>3500 m) advects across the Ninety East Ridge from the Western Australian Basin to bring the dAl-rich waters to the northern end of the Central Indian Ocean Basin.

Keywords: Dissolved aluminium; Indian Ocean; GEOTRACES; Particle-water interaction; Bay of Bengal

---

[*] Corresponding author at: CSIR-National Institute of Oceanography, Dona Paula, Goa 403004, India.
E-mail addresses: sunil@prl.res.in, sunil@nio.org (S.K. Singh).

[1] Present address: CSIR-National Institute of Oceanography, Dona Paula, Goa 403004, India.

https://doi.org/10.1016/j.gca.2019.09.028
0016-7037/

1. INTRODUCTION

Dissolved aluminium concentrations in the global ocean have shown large inter-oceanic fractionation due to varying nature and strength of its external sources and internal cycling in different oceanic basins (Chou and Wollast, 1997; Grand et al., 2015b; Measures and Vink, 1999; Middag et al., 2012; Orians and Bruland, 1986). Deposition and partial dissolution of continental crust derived atmospheric mineral dust is considered as the major source of dAl to the surface ocean waters, particularly in remote ocean regions (Grand et al., 2015b; Hydes, 1979; Measures and Edmond, 1990). Al released from the resuspended sediments over continental margin and seafloor may also act as an important source of dAl to the ambient seawaters (Mackin and Aller, 1984, 1986; Middag et al., 2009, 2015; Moran and Moore, 1991). However, the relative contribution of Al released from suspended particulate matter (due to particle dissolution and/or Al desorption) and diffusive Al flux from dAl enriched sediment pore waters to the water column near sediment-water interface is uncertain due to limited knowledge on particulate Al levels of the resuspended sediments, dAl concentrations of pore waters and diffusivity across the sediment-water interface (Orians and Bruland, 1986). The extent of Al release from sediments near ocean margins depends on the intensity of water turbulence leading to sediment remobilization and availability of reactive Al in the margin sediments (Measures et al., 2015; Middag et al., 2015; Moran and Moore, 1991). Concentration of dissolved silicic acid in ambient ocean waters at sediment-water interface and biogenic silica accumulation rates in margin sediments are observed to control the Al dissolution/desorption from the resuspended sediments in the water column and dAl diffusive flux from the sediment pore waters, respectively (Koning et al., 2007; Mackin and Aller, 1984; Middag et al., 2015; Van Beueskom et al., 1997). Stoichiometric interaction of Al, released from resuspended sediments, with ambient dissolved Si may result in the precipitation of authigenic aluminosilicates and inhibits the build-up of dAl in the dissolved Si-rich ambient seawater (Mackin and Aller, 1984, 1986).

Al is also one of the most concentrated dissolved trace metals in river waters (Gaillardet et al., 2014) but estuarine processes filter out the majority of the dAl before river water discharges to the ocean (Mackin and Aller, 1984). Al released from the atmospheric mineral dust and/or resuspended sediments in the formation regions and/or along the advective pathways of water masses and their subsequent movement to other oceanic regions may also provide a significant share to the total dAl inventory in the water column, at least at basin scale (Measures and Edmond, 1988; Measures et al., 2015; Middag et al., 2009, 2015). Elevated dAl signals in the deep water hydrothermal plumes, emanating from hydrothermal vents along the mid-oceanic ridges, have been reported in the Atlantic (Lunel et al., 1990; Measures et al., 2015) and the Pacific (Resing et al., 2015) Ocean. From these studies it could be summarized that the magnitude of the dAl input from the hydrothermal processes to the deep waters is largely controlled by the composition of hydrothermal fluids, dAl content of the deep waters entrained by the hydrothermal plumes near the vents and topographical constraints around the vents (Lunel et al., 1990; Measures et al., 2015; Resing et al., 2015). The topography around the vents is also observed to play a crucial role in controlling the dispersal of the dAl-rich hydrothermal plume (Measures et al., 2015; Resing et al., 2015). However, in view of the limited observations of dAl near active hydrothermal vents and seafloor spreading sites, the relative contribution of hydrothermal dAl input to the global deep waters dAl budget is still debatable and is specifically neglected in simulations by the modeling studies done to date (Gehlen et al., 2003; van Hulten et al., 2013, 2014).

Dominant controls on output flux of dAl from the water column are set by particle scavenging processes (Hydes, 1979; Orians and Bruland, 1985). Biogenic silica particles are one of the main carrier phases of scavenged Al, given the Al chemical affinity (to get adsorbed) towards high negative surface charge density of siliceous particles (Dixit and Van Cappellen, 2002; Dymond et al., 1997; Moran and Moore, 1988). Along with passive scavenging, active uptake of Al by the living diatoms during biosynthesis of frustules is also possible, which has been shown experimentally (Gehlen et al., 2002). This has implications for export and remineralization of biogenic silica (bSi) and its regeneration since Al integration in the silicate framework has been shown to reduce the solubility of bSi in the seawater (Koning et al., 2007).

Previous studies (Grand et al., 2015a; Measures et al., 2015; Measures et al., 2005; Measures and Vink, 2000) have exploited the surface ocean dAl concentrations to estimate the atmospheric mineral dust fluxes over different ocean basins, considering the steady-state balance between Al input from partial dissolution of mineral aerosols and output via scavenging by particles and their subsequent removal out of the surface. In general, the order of error associated with this steady-state, 1-D approach is about a factor of 3 due to the uncertainties in Al solubility from mineral dust and dAl scavenging rates (Grand et al., 2015a; Measures and Vink, 1999). Compared to this, the estimates of dust deposition fluxes from atmospheric models have uncertainty on the order of a factor of 10 (Mahowald et al., 2005). Also, in the regions where advective processes and other sedimentary (e.g. continental margin sediments) sources/sinks of Al play a major role in controlling the dAl concentrations, surface dAl-based atmospheric dust fluxes may be over or underestimated using the 1-D, steady-state model (Grand et al., 2015a).

Indian Ocean basins, having distinct biogeochemical dynamics, offer a unique opportunity to understand the controls of different ocean processes on dAl and other trace metal cycling. In the north-eastern Indian Ocean (i.e. the Bay of Bengal and the Andaman Sea), the huge fluvial input, in the form of freshwater and suspended sediments (Robinson et al., 2007; Sengupta et al., 2006), may influence the biogeochemistry of the lithogenic trace metals throughout the water column (Chinni et al., 2019; Nozaki and Alibo, 2003; Nozaki and Yamamoto, 2001; Singh et al., 2012), a process which is not accounted for by the modeling studies on dAl cycling (Gehlen et al., 2003; Han et al., 2008; van Hulten et al., 2013, 2014). The Arabian Sea (north-western Indian Ocean) is subjected to large spatio-temporal variations in dust input and productivity, which may impact the distribution and cycling of Al and other trace elements in the surface and thermocline waters (Measures and Vink, 1999; Vu and Sohrin, 2013). Under the influence of summer and winter monsoon currents, enormous exchange of surface and thermocline waters takes place between the Arabian Sea and the BoB (Kumar et al., 2004; Schott et al., 2009), where the equatorial Indian Ocean region acts as a connecting pathway between the two basins. In the equatorial Indian Ocean region, south of Sri Lanka (~5 °N), mean transport in the upper water column (~60–100 m) of about 8 Sverdrup eastward (towards the Bay of Bengal) and 12 Sverdrup westward (towards the Arabian Sea) is estimated during the south-west and the northeast monsoon period, respectively (Schott et al., 2009 and references therein; also see Figs. 8, 9, 10 and 11 in Schott et al., 2009). For this reason, the dAl distribution in the surface and thermocline waters of the equatorial Indian Ocean region will be indirectly influenced by the Al cycling in the northern Indian Ocean basins.

In the Indian Ocean, relatively few measurements of dAl have been reported and thus our understanding of Al cycling in this ocean basin is quite limited. Grand et al. (2015b,c) have recently reported high (spatial) resolution dissolved Al concentrations data in the eastern Indian Ocean and across the southern end of the Indian Subtropical Gyre but their measurements were restricted to the upper water column (<1000 m). Studies reporting full vertical water column profiles for dAl in the Indian Ocean are sparse (Obata et al., 2004; Vu and Sohrin, 2013). In this study we have measured 34 full vertical profiles of dAl in the northern (the BoB, the Andaman Sea and the Arabian Sea), equatorial and subtropical gyre region of the Indian Ocean to constrain the probable sources, sinks and processes that may control the dAl distribution in these regions. This study greatly increases the spatial density of Al measurements, especially in the deep waters of the Indian Ocean.

2. MATERIAL AND METHODS

2.1. Sampling and storage

A total of 34 stations were sampled for seawater on two separate GEOTRACES India cruises (GI-01 and GI-06) onboard ORV Sagar Kanya, covering the Bay of Bengal (BoB), the southern Andaman Sea, the central and eastern equatorial Indian Ocean, the south-eastern Arabian Sea, and the north to central Indian Subtropical Gyre region. The GI–01 cruise (Fig. 1) was carried out during the spring-intermonsoon period (26th March to 19th April) of 2014. During this cruise, samples were collected offshore Vishakhapatnam (GI-01/1, Fig. 1) followed by a meridional transect near 87°E (GI–01/2 to GI–01/9; Fig. 1) through the BoB and the equatorial Indian Ocean. The cruise continued southwest through the equatorial and Indian Subtropical Gyre region for further sampling. The GI-06 cruise (Fig. 1) took place during the late winter monsoon period (29th January to 1st March) of 2017. Sampling during this cruise was carried out across the central and southern BoB, and the equatorial Indian Ocean (Fig. 1). Additional stations were sampled in the southern Andaman Sea and the south-eastern Arabian Sea (Fig. 1).

An assembly of 24, 12 L Niskin–X bottles (Teflon coated, level–action type, General Oceanics), mounted on a rosette-based sampler with epoxy coated Al frame, were deployed using a 8 km Kevlar hydrowire for the collection of seawater from surface (~2–5 m) to the ocean bottom (~50–200 m above the sediment-water interface) at each station. The seawater sampling rosette system was equipped with a CTD sensor (SBE–911plus, Sea-Bird Scientific, USA) for continuous measurements of conductivity, temperature and pressure throughout the water column. An ECO–NTU (WET Labs, Sea-Bird Scientific, USA), was added to the package for continuous measurement of seawater turbidity during the GI-06 cruise. Immediately after recovery from the ocean, Niskin–X bottles were transferred to a clean room container for further sub-sampling. From the 12 L Niskin bottles, ~1 L aliquots of seawater were collected in acid-cleaned LDPE bottles (Tarsons Products Pvt. Ltd.) after filtration using 0.2 μm filter capsules (AcroPak™ 500 with Supor® Membrane, PALL Life Sciences; rinse volume: 30 ml) under filtered and pressurized air. After filtration, all the aliquots were acidified to pH ~ 1.7 (0.024 M HCl) using HCl (Optima™, Fisher Scientific) and stored for later shore-based analysis of dissolved aluminium and other trace elements. From these stored seawater samples, ~30 ml aliquots were transferred to 60 mL wide-mouth LDPE bottles (Tarsons Products Pvt. Ltd.) for dissolved aluminium analysis using a flow injection system (described in Section 2.2). Before use, the 60 mL wide-mouth bottles were thoroughly and sequentially cleaned with 2% alkaline solution (Extran® MA 01, Merck), 4 M HCl prepared using concentrated quartz distilled (from 37% HCl, EMPARTA®, Merck) HCl and 1 M ultrapure HNO_3 (Optima™, Fisher Scientific). During acid cleaning, the bottles were soaked for, at least, 1 day at 60 °C in a hot air oven and between each cleaning step, the bottles were thoroughly rinsed 2–3 times with ultra-high pure water (resistivity: 18.2 MΩ cm; hereafter, MQ water), which was prepared using Millipore Milli–Q® Element System.

2.2. Analysis

dAl in the seawater samples was analyzed following the automated inline flow injection analytical technique of Brown and Bruland (2008) and is discussed here briefly. The seawater samples were buffered offline to pH 5.5 ± 0.2 using ammonium acetate buffer (2 M NH_4Ac, hereafter, sample buffer) prior to inline analysis of dAl. The sample buffer was prepared using commercially available 25% high purity ammonia solution (Suprapur®, Merck) and 99% high purity glacial acetic acid (Optima™, Fisher Scientific) and the pH of the buffer was adjusted to 9.0 ± 0.1 using 25% high purity ammonia solution. The cycle of each sample analysis starts with the conditioning of pre-concentration column, which was prepared by packing the

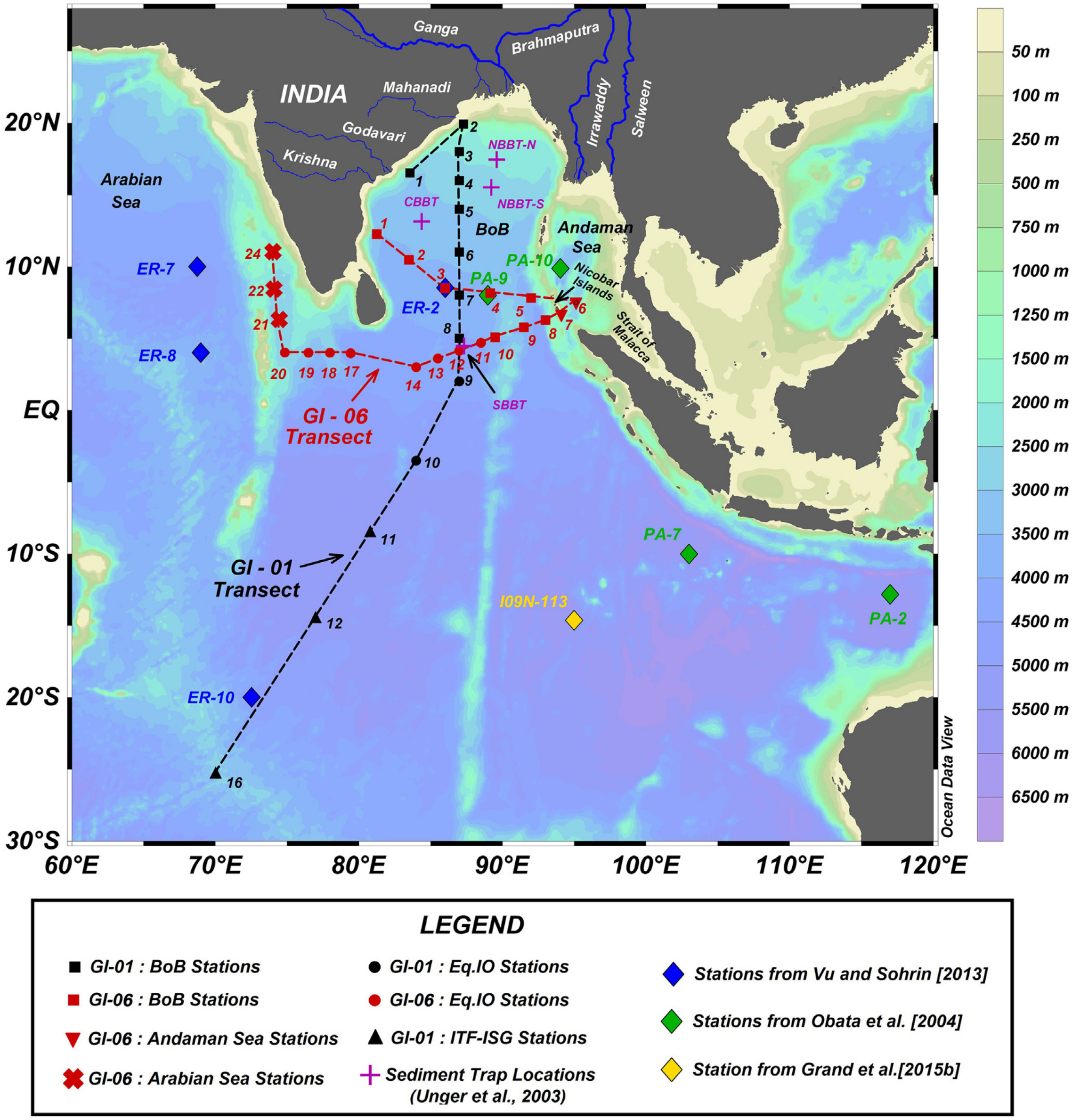

Fig. 1. Map showing the stations occupied for clean seawater sampling during the GI–01 (black symbols) and GI–06 (red symbols) cruises. Tracks of various major rivers flowing through India and Indo–Myanmar regions to the BoB and the Andaman Sea are shown. Sampling locations for dAl and other ancillary data from earlier studies used during the discussions in the text are also plotted. This map was prepared using ODV 4.7.9 software (Schlitzer, 2016). (For interpretation of the references to colour in this figure legend, the reader is referred to the web version of this article.)

iminodiacetic acid resin (TOYOPEARL® AF–Chelate–650 M, Tosoh Bioscience) in a 2 cm mini-column with internal volume of 27 µl (Global FIA, USA), for 30 s using a column conditioning solution (0.1 M NH_4Ac buffer; pH ~ 5.5). The column conditioning solution was prepared by diluting sample buffer with MQ water and adjusting the pH with 99% high purity glacial acetic acid. Next, the buffered sample was loaded onto the column for 120–300 s. Generally, samples with (expected) dAl concentration below 15 nM (open ocean samples) and >15 nM (coastal surface waters) were preconcentrated on the column for 300 s and 120–180 s, respectively. Thereafter, the column was rinsed again with the column conditioning solution for 30 s to remove the excess and interfering seawater salts. The Al was then eluted from the column with 0.1 M HCl, prepared using concentrated high purity HCl (32–35%, Optima™, Fisher Scientific), for 600 s. The eluent then mixed with lumogallion reaction solution to form a fluorescent Al–lumogallion complex. The lumogallion reaction solution is made by adding 2.5 ml of lumogallion stock solution (4.8 mM; 50 mg lumogallion (>98.0%, TCI, Japan) in 30 ml MQ water] to 250 ml of pH adjusted (to 6.3 ± 0.1), 4 M NH_4Ac buffer solution, which was prepared with 25% high purity ammonia solution and 99% high purity glacial acetic acid. Complete mixing of the Al-lumogallion complex in the reaction stream was achieved by passing it through a 10 m knitted coil (Selavka et al., 1987), kept completely submerged in a 2 L water bath (StableTemp, Cole-Parmer) at 50 °C (±0.2 °C). Brij-35 solution (5% Brij® L23 solution; Sigma-Aldrich) was then added to the reaction stream and their mixture was passed through a 4 m knitted reaction coil into the fluorescence detector (RF-20A Shimadzu). The Brij-35 solution increases the total intensity of fluorescence from the Al–lumogallion complexes formed (Resing and Measures, 1994). Before every batch of analysis (50–60 combined runs of samples, standards and blanks), the preconcentration column was thoroughly cleaned by passing ~0.5 M high purity HCl (Optima™, Fisher Scientific) through the column for several hours.

For preparing external calibration standards and estimation of procedural blank, a low-Al, column-cleaned seawater (CCSW) was made by passing buffered (pH ~ 5.5) deep seawater sample (collected in bulk during GEOTRACES cruise, GI–02, in the Indian Ocean from 4450 m depth) through the preconcentration column similar to that used for the sample analysis. For each batch of analysis, the standards for external calibration were made using freshly prepared CCSW and spiking it with different proportions of primary standard (~240 nM), which was prepared by serial dilution of commercially available, single element, Al ICP standard (1000 mg/L, CertiPUR®, Merck). Batches of analysis having different sample loading time, as discussed earlier, were run with separate external calibration curves determined for each batch. Procedural blank estimation for the dAl analysis was made by running the CCSW as a sample, generally 2–3 times in one batch of analysis. The mean of signal counts recorded for all the CCSW runs in one batch of analysis was set as the intercept of the calibration curve for the batch. The blank of the analysis was then estimated by dividing the mean signal counts for CCSW runs with the slope of the calibration curve. Mean blank determined in this study at different days of analysis for 300 s sample loading time was 0.4 ± 0.1 nM (1SD, n = 55). The detection limit, defined as three times the standard deviation of the blank, was also determined for different batches. The mean of the detection limits observed at different days of measurements in this study was 0.1 nM.

During the GI-06 and GI–01 cruises, major nutrients (H_2SiO_4, PO_4^{3-} and NO_3^-) in seawater samples were analyzed onboard based on colorimetric detection method (Hansen and Koroleff, 1999) using an automated continuous flow analyser (Skalar San^{++}) and a UV–Vis spectrophotometer (UV–1800, Shimadzu), respectively. The precision of H_2SiO_4, PO_4^{3-} and NO_3^- measurements, during the GI-01 cruise, were ±0.02 µM, ±0.01 µM and ±0.02 µM respectively (Chinni et al., 2019). During the GI-06 cruise, H_2SiO_4, PO_4^{3-} and NO_3^- were measured with percentage relative standard deviation (% RSD) better than 6%, 2% and 5%, respectively, for repeat analysis.

2.3. Data quality check

A combined total of 585 samples were analyzed for the dAl concentrations. SAFe and GEOTRACES reference seawater samples were analyzed for their dAl concentrations. The measured dAl concentrations for the North Atlantic GEOTRACES reference standards (GS and GD) showed very good agreement with their reported consensus values (Table 1). However, the dAl values for the SAFe reference standards (SAFe D1 and D2) are ~1.5–2 times higher than the reported consensus values (Table 1). The values determined here are similar to the values recently reported (Table 1) by Resing et al. (2015). We also carried out multiple analyses of two in-house reference samples (InStd–D: 2.2 nM ± 5% (1SD), n = 42 and InStd–T: 3.8 nM ± 8% (1SD), n = 49) with batches of seawater samples. InStd–D and InStd–T were sub-samples of acidified, bulk seawater samples (~20 L) collected from 4000 m and 200 m water depths, respectively, during a separate Indian GEOTRACES cruise (GI-02) in the western equatorial Indian Ocean region.

Japanese GEOTRACES station, ER-2, (Fig. 1, Vu and Sohrin, 2013) in the BoB was reoccupied (as GI-06/3) during the GI-06 cruise. To directly compare the data sets, we converted our dAl data from nM to nmol kg^{-1} (concentration unit used by Vu and Sohrin (2013)) using the potential density of the seawater samples. Though the broad distribution patterns are similar for GI-06/3 and ER-2, the absolute values show slight differences in the thermocline and deep waters (>100 m, i.e., $\gamma^n > 25$ kg m^{-3}, Fig. 2a) but mostly

Table 1
Comparison of measured dAl concentrations (this study) and their consensus values in SAFe and GEOTRACES reference samples. Results from Resing et al. (2015) for SAFe reference samples are also presented.

Reference Sample	Batch No.	Al Concentration*		
		This Study	Resing et al. (2015)**	Consensus Value**
SAFe D1	D1 #242	1.28 ± 0.12 (1SD, n = 4)	1.26 ± 0.11 (1SD, n = 32)	0.62 ± 0.03 (1SD)
SAFe D2	D2 #361	1.63 ± 0.08 (1SD, n = 3)	1.63 ± 0.13 (1SD, n = 26)	1.03 ± 0.09 (1SD)
GEOTRACES GD	GD #163	17.7 ± 0.8 (1SD, n = 4)	-	17.7 ± 0.2 (1SD)
	GD #31	17.4 ± 0.2 (1SD, n = 3)		
GEOTRACES GS	GS #101	28.6 ± 0.4 (1SD, n = 4)	-	27.5 ± 0.2 (1SD)

[*] The consensus values for the SAFe and GEOTRACES reference samples are in nmol kg^{-1} while their reported values in this study and Resing et al. (2015) are in nM.

[**] Given values represent the mean and one standard deviation of all the SAFe reference samples analyzed by Resing et al. (2015) and consensus values (as of May 2013) with one standard deviation after inter-laboratory calibration of SAFe and GEOTRACES references samples.

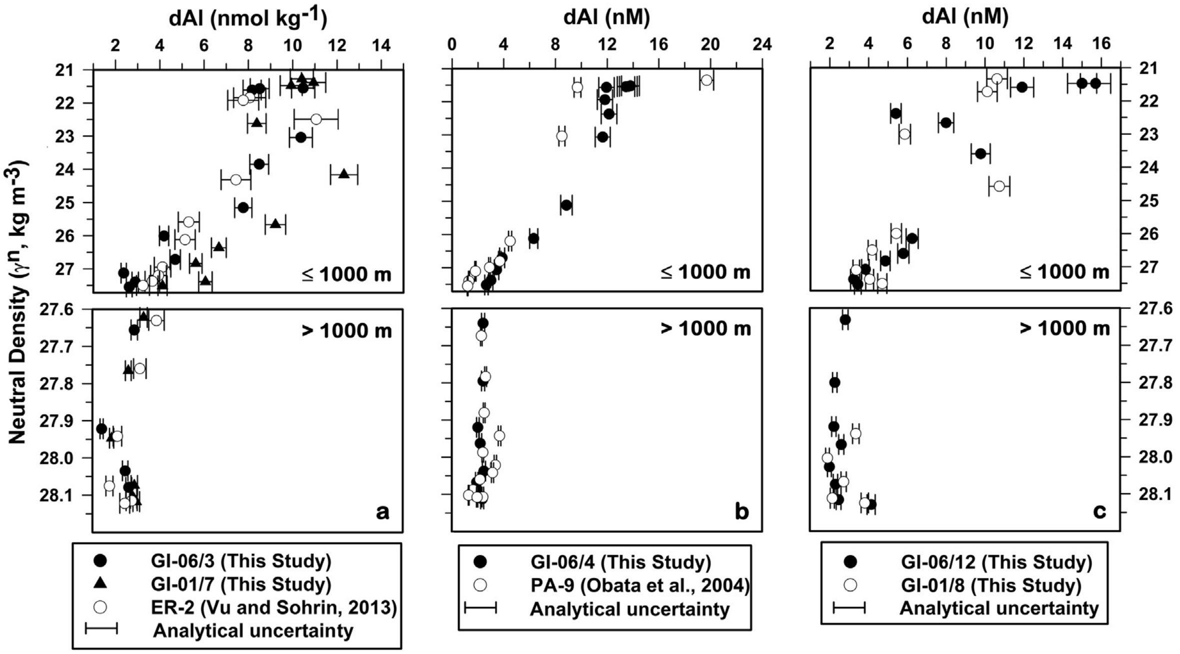

Fig. 2. Comparison of dAl vertical profiles at (a) GI–06/3 and the corresponding crossed over station, ER-2, of the Japanese GEOTRACES cruise; the results from station GI–01/7 sampled close to the cross–over stations (GI–06/3 and ER–2) are also plotted, (b) stations GI–06/4 and PA–9 (Obata et al., 2004), apparently overlapping each other in space (see text and Fig. 1), and (c) nearby stations GI–01/8 and GI–06/12. Analytical uncertainty estimates: (i) ER-2: precision achieved (~9%, 1SD; Vu and Sohrin, 2013) after repeat analysis of SAFe deep water reference seawater, (ii) PA-9: precision achieved (2.7%, 1SD; Obata et al., 2004) at 2.0 nM and (iii) This study: precision achieved (5%, 1SD) after repeat analysis of in-house reference seawater, InStd-D (see text).

overlap within 20% of the dAl observed at similar neutral densities of the two stations. Such differences were also evident when the dissolved Fe data at ER-2 and nearby station GI–01/7 (Fig. 1) were compared, particularly below 500 m (refer Fig. 2C of Chinni et al., 2019). Given the long time span (7 years) between occupations of the two stations, these differences may result from interannual variations in lithogenic sediment fluxes to the BoB (Unger et al., 2003), which predominantly controls the dissolved Fe (Chinni et al., 2019) and dAl (discussed later in Section 5.1.1 and 5.2.1) in the region. dAl concentrations in the deeper waters (>1000 m) at stations GI-01/7 and GI-06/3, sampled within 130 km (Fig. 1), compare better (Fig. 2a). Station GI-06/4 (8.148°N, 89.148°) is within 25 km of station PA-9 (8.0° N, 89.0°E, Fig. 1, Obata et al., 2004) with dAl below 1000 m being comparable or low relative to that at PA-9 (Fig. 2b). The dAl distributions at nearby stations GI-01/8 and GI-06/12 also showed comparable results (Fig. 2c). In general, the dAl concentrations at crossover or nearby stations show, relatively, large differences in the upper water column (≤1000 m, Fig. 2) presumably due to smaller residence time of dAl compared to that in the deeper waters (Orians and Bruland, 1986), and therefore, showing more sensitivity towards seasonal and interannual variations in the dAl input from sources in the BoB.

3. GENERAL CIRCULATION AND WATER MASS STRUCTURE

Several studies (Kumar and Li, 1996; Mantyla and Reid, 1995; Schott et al., 2009; Tomczak and Godfrey, 2003a,b; You and Tomczak, 1993; You, 1997, 2000; Shetye et al., 1994; Singh et al., 2012; Wyrtki, 1973) have discussed the circulation and structure of the water masses present in the Indian Ocean basins. Here, we shall describe the circulation patterns and water-mass structure observed during the study period, mostly restricting to the studied regions. To facilitate data interpretation and discussion, the study area has been sub-divided into different sub-basins in the Indian Ocean: (1) Bay of Bengal (BoB; north of 5°N, 80–92°E), (2) Andaman Sea (north of 5°N and 94–100°E), (3) Arabian Sea (AS; north of 5°N, 51–73°E), (4) Equatorial Indian Ocean (Eq.IO; 5°N–5°S) and (5) Indonesian Throughflow and Indian Subtropical Gyre (ITF–ISG; south of 5°S) region. Stations GI-06/11 and GI-06/12 (Fig. 1) were considered to be in the transitional region from the southern BoB to the Eq.IO. Fig. 1 shows the stations occupied in different sub-basins (defined above) during the GI-01 and GI-06 cruises in the Indian Ocean.

3.1. Surface and thermocline waters

The large annual river water influx from the Himalayan rivers (the Ganga and the Brahmaputra), Indian peninsular rivers (the Mahanadi, the Godavari and the Krishna) and Indo–Myanmar rivers (the Irrawaddy and the Salween) to the north-eastern Indian Ocean (i.e., the BoB and the Andaman Sea) is manifested as low salinity, Bay of Bengal Water (BBW) in the surface water layer of the region. The thickness of the low salinity (<34) surface layer gets shallower in the southern BoB (<50 m) and the Andaman Sea compared to the northern and central BoB (50–100 m;

Fig. 3a and 4a). Dominating the contributions from all the rivers, the Ganga-Brahmaputra (G-B) river system annually discharges freshwater and suspended sediments on the order of 10^3 km^3 and 10^3 Mt (1 Mt = 10^9 kg), respectively, to the BoB (Galy and France-Lanord, 2001; Sengupta et al., 2006, Singh et al. 2008). A comparable freshwater flux and about half of the suspended sediment flux from the G-B river system is discharged by the Irrawaddy and Salween (I-S) river system to the Andaman Sea (Damodararao et al., 2016; Robinson et al., 2007). During the late fall intermonsoon to the late winter monsoon period (November to February), the low salinity BBW is transported to the surface layers of the Arabian Sea by the Northeast Monsoon Current (NMC, Fig. 5a), centered along 5°N, and the East Indian Coastal Current (EICC), flowing southward along the east coast of India (Kumar et al., 2004; Schott et al., 2009; Wyrtki, 1973; Goswami et al., 2014). The low surface salinity (33.53–34.18) observed during the late winter period in the south-eastern Arabian Sea (GI-06/21, 22 and 24; Fig. 4c) suggests the advection of the BBW to this region.

In general, the surface waters in the BoB showed an anti-cyclonic motion during both the cruises (Fig. 5a). Over this general circulation pattern, transits of strong anti-cyclonic (warm-core) eddies at stations GI-01/3 and GI-01/5 and cyclonic (cold-core) eddies at stations GI-06/2, GI-06/10 and GI-01/7 were observed, which are marked by deepening or shoaling of the neutral density (γ^n; kg m^{-3}) isolines and salinity variations at these stations (Figs. 3a, 4a and b).

In the southern Andaman Sea, advection of low salinity, Indonesian Water from the Strait of Malacca (SoM) to the Andaman Sea may also contribute to the surface waters (Rizal et al., 2012). Further, the low salinity surface waters of the southern Andaman Sea may advect to the southern BoB as evident from the surface circulation patterns (refer Fig. 5a for a schematic representation) and low surface salinity levels (<34) at stations GI-06/8, 9, 11 and 12, and GI-01/08 in the southern BoB. However, eddy pumping of sub-surface waters to the surface layer erodes this low salinity signal at station GI-06/10 (Fig. 4b).

Mixed layer salinity (S_{ML}) in the equatorial stations was higher (33.80–35.33) compared to that in the BoB due to decreasing contribution from BBW, and increased westward (~34.63 at GI-06/13 to ~35.33 at GI-06/19, Fig. 4b), presumably, due to the admixing of the equatorial surface waters with high salinity surface waters of the southern Arabian Sea under the influence of the NMC (Fig. 5a). Sub-surface (75–100 m) salinity maxima observed in the coastal Arabian Sea and equatorial stations west of 88°E (GI-06/12 to GI-06/20, GI-01/09 and GI-01/10; Figs. 3a, 4b and c) indicate the presence of Arabian Sea High Salinity Water.

Further south in the ITF-ISG region (south of 5°S), the surface and thermocline waters (0–1000 m) at stations GI-01/11 and GI-01/12 are impacted by the low salinity, Indonesian Throughflow Water (ITW) carried by the west-flowing South Equatorial Current (SEC) across the latitude range: 8–15°S (Tomczak and Large, 1989; Fig. 5a). This is evident from the low salinity surface waters (Fig. 3a) and variations in T-S (potential temperature-salinity) curve at these stations (refer to Fig. S1(d)] resulting from mixing and interleaving between the ITW and the Indian Central Water (ICW) (Tomczak and Godfrey, 2003a; Tomczak and Large, 1989). The ICW is formed in the subtropical convergence zone (40–45°S) by subduction of subtropical surface waters (You and Tomczak, 1993) and represented by thermocline waters at station GI-01/16, showing its typical T-S curve ($\theta \sim 9$–15 °C, Fig. S1 (d)). The upper water column (<200 m) of station GI-01/16 in the subtropics (Fig. 1) comes under the influence of north-east flowing South Indian Counter Current (SICC, Fig. 5a) which is fed by retroflection of Southeast Madagascar Current (SEMC) waters (Schott et al., 2009 and references therein).

3.2. Deep and bottom waters (>2500 m)

Principle water-masses filling up the deep and bottom water column depth (>2000 m) in the Indian Ocean are: the Modified North Atlantic Deep Water (MNADW) and the Antarctic Bottom Water (AABW) (Kumar and Li, 1996; Singh et al., 2012; Goswami et al., 2014; You, 2000). The MNADW is formed by mixing and entrainment of the North Atlantic Deep Water into the Circumpolar Deep Water (CDW) of the Indian Ocean Sector of the Southern Ocean (Kumar and Li, 1996; You, 1999) and occupies the depth range of 2000–3500 m (You, 1999). The AABW fills the deepest depths (>3500 m) in the Indian Ocean Basins (Tomczak and Godfrey, 2003a; You, 1999). Fig. 5b depicts the general circulation scheme of the deep (2000–3500 m) and bottom (>3500 m) waters in the Central Indian Basin and BoB (Kumar and Li, 1996; Mantyla and Reid, 1995; Toole and Warren, 1993; You, 2000). Deep waters (2000–3500 m) are mainly derived from the South Australian Basin into the Central Indian Basin and BoB through the deep passage between the Broken Plateau and the Southeast Indian Ridge and flow northwards (Fig. 5b; You, 2000). On the other hand, bottom waters in the Central Indian Basin are primarily derived from the Western Australian Basin through the deep saddles at ~5°S and 10°S on the Ninety–East Ridge (NER, Fig. 5b; Mantyla and Reid, 1995; Tomczak and Godfrey, 2003a; Toole and Warren, 1993). In contrast to the northward movement of deep waters above, the bottom waters, after entering into the Central Indian Ocean Basin, turn and flow southwards (Mantyla and Reid, 1995; Toole and Warren, 1993; refer Fig. 5b for a schematic representation).

4. RESULTS

4.1. dAl distribution in the surface mixed layer and upper thermocline waters (0–300 m)

For better understanding and data interpretation, the BoB region was further sub-divided into the northern (N. BoB; >17°N), the central (C.BoB; 10–17°N) and the southern BoB (S.BoB; 5–10°N). The mean dAl concentrations in

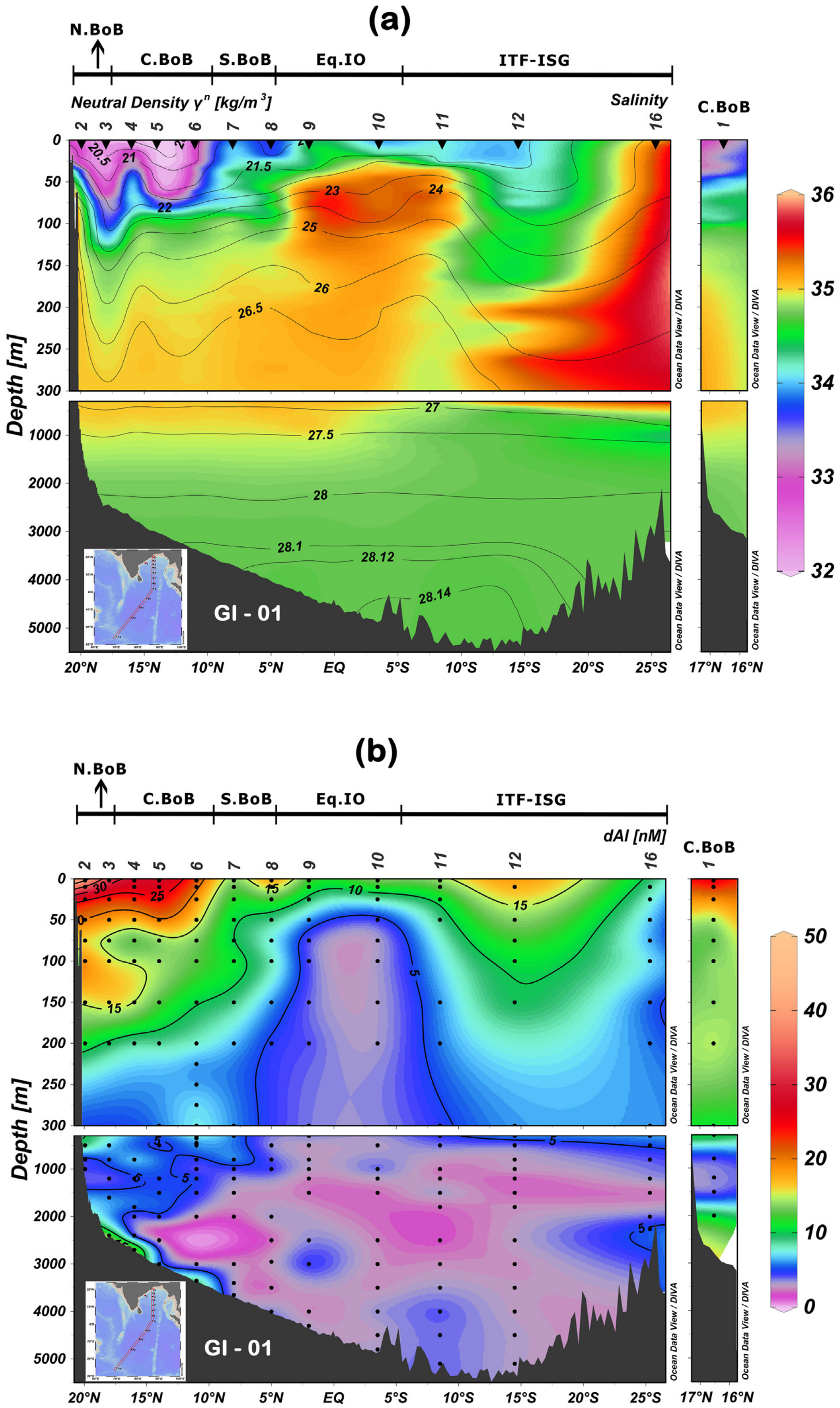

Fig. 3. (a) Salinity of and (b) dAl concentrations in the water column sampled along the GI–01 cruise transect (shown in the inset map) during the spring–intermonsoon period (March–April) of 2014. Overlain contours in the top and bottom figures represent the neutral density (γ^n, kg m^{-3}) and dAl concentration (in nM) isolines, respectively. For better visualization of the data in the more dynamic surface and upper thermocline waters ($\leq$300 m), salinity and dAl distributions are shown separately for the upper 300 m water depth and the remaining water column below ($\geq$300 m).

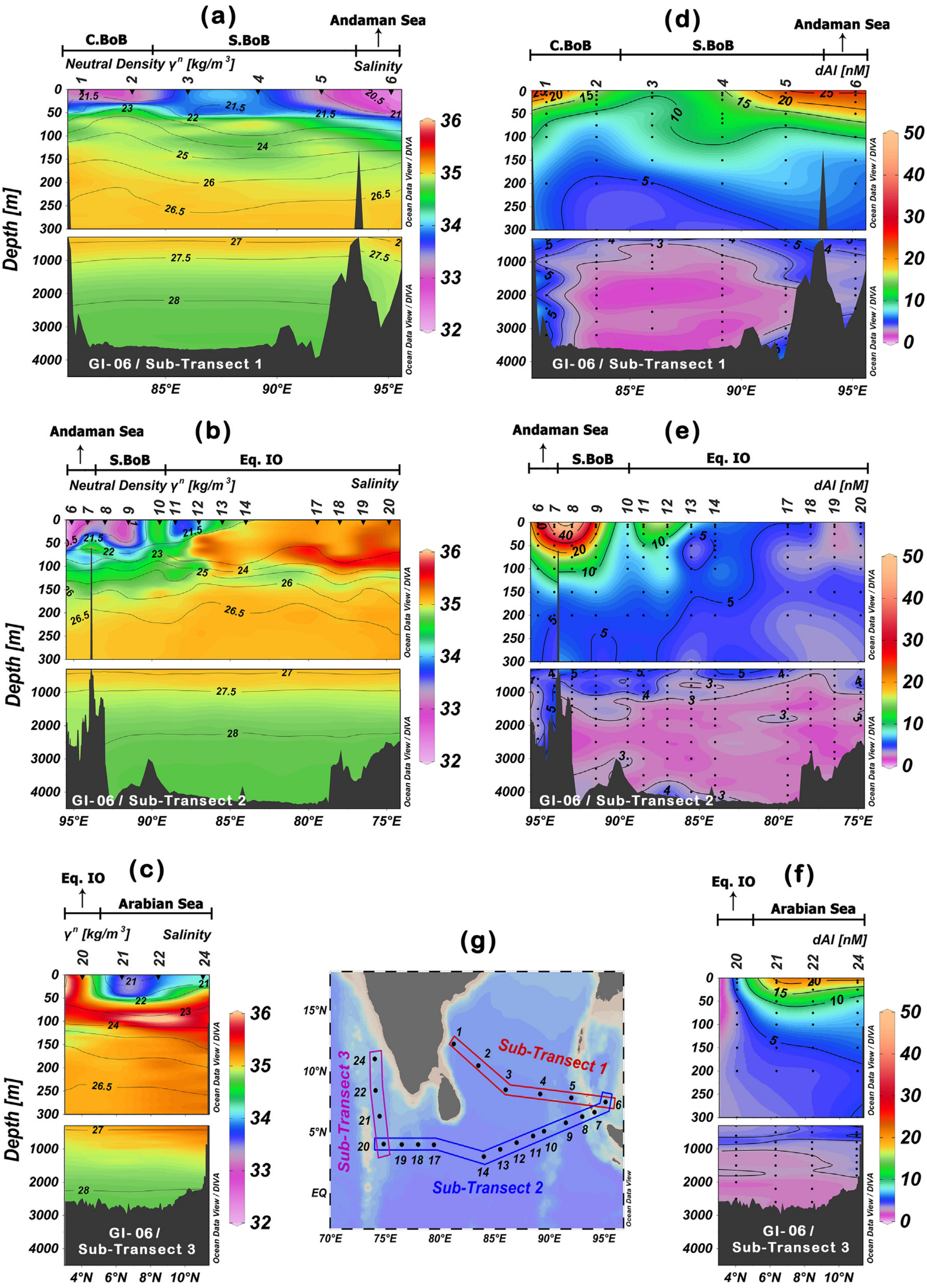

Fig. 4. Same as Fig. 3 but the salinity (a–c) and dAl observations (d–f) plotted are for the GI–06 cruise. For better visualization and interpretation, the full GI–06 cruise track was sub-divided into three separate sub-transects. Sub–transect 1 and 2 are the two zonal transects in the southern BoB and the Andaman Sea, and the equatorial Indian Ocean, respectively. Sub-transect 3 is a meridional transect, in the south-eastern Arabian Sea. Fig. (g) shows the division of the full GI–06 cruise transect into the above mentioned sub-transects.

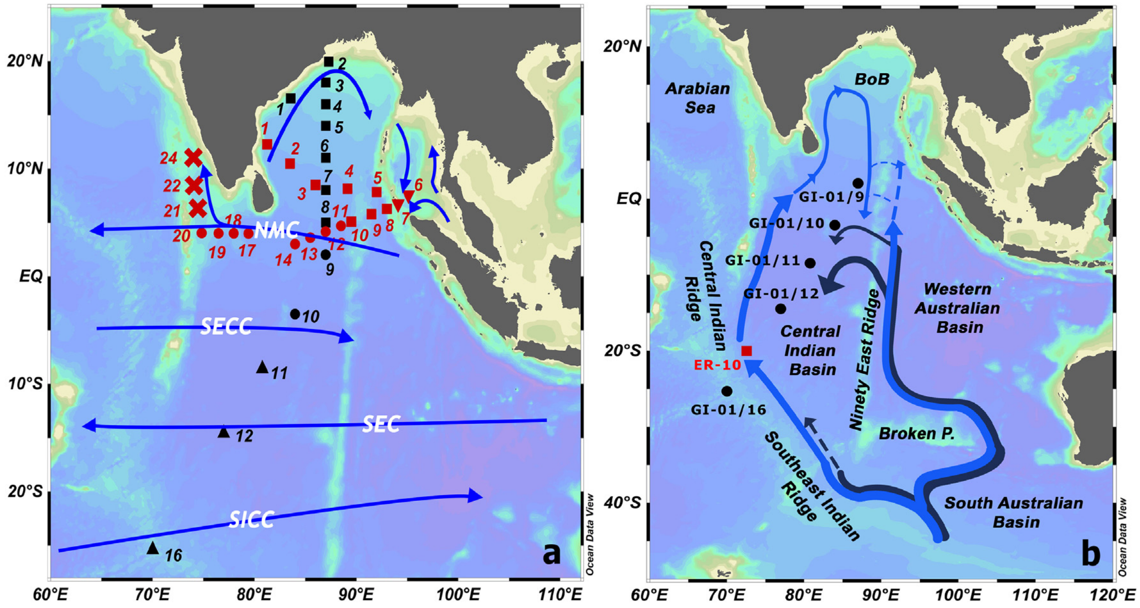

Fig. 5. (a) Schematic diagram showing the general surface water circulation during the sampling in the study regions. The diagram is deduced using the Ocean Surface Current Analysis Real-time (OSCAR) third degree (1/3 × 1/3 degree) resolution ocean surface currents data (ESR, 2009). (b) Qualitative representation of deep (light blue) and bottom water (dark blue) circulation pattern for the Central Indian Ocean Basin and the BoB. The circulation scheme is plotted after composite results from Toole and Warren (1993), Mantyla and Reid (1995), Kumar and Li (1996) and You (2000). (For interpretation of the references to colour in this figure legend, the reader is referred to the web version of this article.)

the surface mixed layer (dAl_{ML}) observed in the BoB were in the range of 9.2–48.3 nM, combining both the cruises (refer Table S1 in the supplementary dataset). The meridional section sampled in the BoB during the spring–intermonsoon period (GI–01 cruise) showed a similar latitudinal trend (Fig. 6) in the dAl_{ML} variations as reported earlier by Grand et al. (2015a), showing decreasing dAl_{ML} concentrations from the N.BoB to the S.BoB. Note the general mismatch between the dAl_{ML} observed for the C.BoB stations in this study and topmost depth sampled in the C.BoB by Grand et al. (2015a) (Fig. 6). The topmost sampling depths of Grand et al. (2015a) in the C.BoB lie below the surface mixed layer observed during their sampling period (refer Figs. 2 and 3 of Grand et al. (2015a)) and therefore probably represent the dAl levels in the strong chemocline (decreasing dAl concentrations) below the surface mixed layer. Independently, this observed mismatch in the C.BoB may also result due to the interannual variations in dAl supply from the sources and/or influence of eddies (given the 7 years of time gap between sampling periods of this study and that of Grand et al., 2015b) on the surface dAl. During the spring-intermonsoon period (GI-01 cruise), highly enriched dAl_{ML} value (~47 nM) was observed in the northernmost station, GI-01/2, situated closest to the mouths of the Ganga and Mahanadi rivers (~200 km and ~70 km from the Hooghly river (the Ganga) and the Mahanadi river mouth, respectively) and probably, most influenced by the fluvial inputs (freshwater and sediments) of the G-B river system. South of the station GI-01/2 at GI-01/1 and from stations GI-01/3 to GI-01/5 in the C.BoB, dAl_{ML} showed near-uniform values (mean

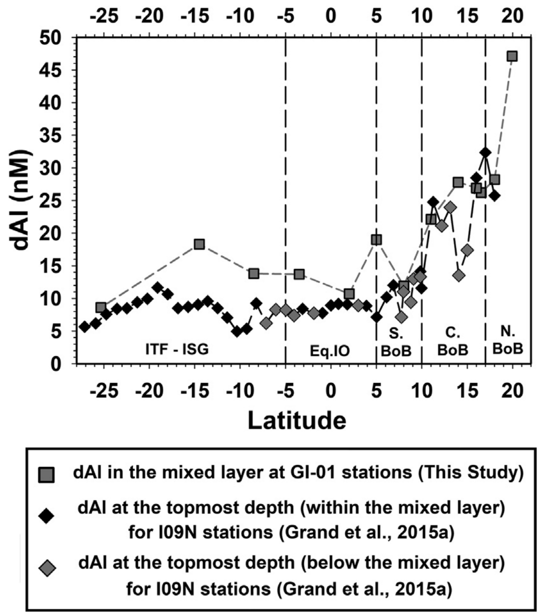

Fig. 6. Latitudinal variations of dAl_{ML} (grey squares) observed along the GI–01 cruise track and dAl concentrations measured at the topmost water depth (black and grey diamonds) sampled along the U.S. CLIVAR CO2 Repeat Hydrography I09N cruise in the Indian Ocean. The grey diamonds distinguish the stations where the topmost depth analyzed for dAl concentrations was below the observed mixed layer depth during the U.S. CLIVAR CO2 Repeat Hydrography I09N cruise (Grand et al., 2015a).

$dAl_{ML} = 27.3 \pm 0.9$ nM, Fig. 7) with significant variation in S_{ML} (31.802–33.386). Thereafter, from station GI-01/5, towards the S.BoB, dAl_{ML} decreased linearly ($R^2 = 0.90$, Fig. 7) with increasing S_{ML}. During the late winter period (GI-06 cruise), dAl enrichment together with decreasing salinity in the surface waters (≤50 m) was observed towards the southeast coast of India (GI-06/1) and the region around the Nicobar Islands (GI-06/5, 6, 7, 8 and 9; Fig. 4a, b, d and e). dAl_{ML} concentrations at GI-06/7 and 8 (~43–48 nM; Fig. 4e and Table S1) near the Nicobar Islands were one of the highest observed during this study. It is interesting to note that at stations GI-01/7 and GI-06/10 in the S.BoB (Fig. 1), where transit of cold-core eddies were observed, a sudden decrease in dAl_{ML} concentrations (Figs. 3b and 4e) accompanied with a steep increase in S_{ML}, relative to the adjacent stations (Figs. 3a and 4b), was observed.

During the spring-intermonsoon period (GI-01 cruise), sub-surface maxima were observed in the dAl profiles of the BoB around 100–150 m (Fig. S2). The strength of these sub-surface maxima in the dAl profiles decreased from the northern (~22.8 nM at station GI–01/2) to the southern BoB (~10.7 nM at station GI–01/8). Among the Eq.IO stations, highest dAl_{ML} levels (13.4–15.4 nM) were observed at the stations transitional to the S.BoB and the Eq.IO (GI-06/11 and 12), which gradually decreased towards the western equatorial region during the late winter period of sampling (Fig. 4e). A tight correlation ($R^2 = 0.94$, Fig. 8) is also observed between the S_{ML} and dAl_{ML} in the equatorial waters.

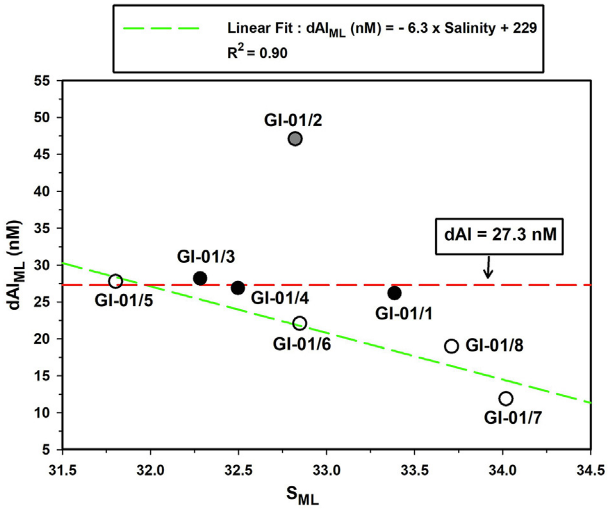

Fig. 7. dAl_{ML} plotted against S_{ML} for the stations sampled in the BoB during the GI–01 cruise. The station sampled at the northernmost point in the BoB (GI–01/2; grey circle) showed highly enriched dAl_{ML} level. The red dashed line represents the mean dAl_{ML} for stations GI–01/1, 3, 4 and 5 (see text). The green dashed line represents the apparent mixing line between the C.BoB and the S.BoB waters estimated by a least-square linear fit to the dAl_{ML} data at stations GI–01/5, 6, 7 and 8 (refer to Fig. 1 for station locations). (For interpretation of the references to colour in this figure legend, the reader is referred to the web version of this article.)

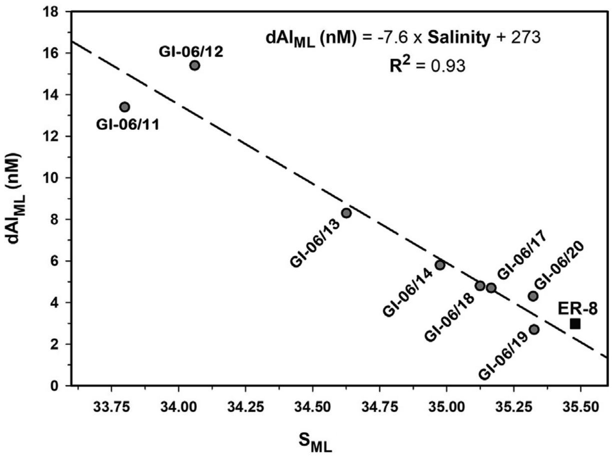

Fig. 8. dAl_{ML} variation with S_{ML} for the equatorial stations (GI–06/11 to GI–06/20) sampled during the GI–06 cruise. The plot shows a tight linear correlation between the two parameters suggesting admixing of dAl–rich, low salinity surface waters of the S.BoB and the southern Andaman Sea with relatively dAl–poor, high salinity surface waters of the southern Arabian Sea (see text). Data point for station ER–8 occupied in the southern Arabian Sea during the Japanese GEOTRACES cruise (Vu and Sohrin, 2013) is also plotted for comparison.

Highly enriched dAl_{ML} concentration (~18 nM) at GI-01/12 (~14.5°S) and relatively elevated dAl (>4 nM) throughout the upper thermocline waters (<500 m) are the most noteworthy observations in the ITF–ISG region (Fig. 3b). High resolution sampling for dAl measurement by Grand et al. (2015b) in the subtropical Indian Ocean, further east along the 95°E, also showed a similar pattern of elevated dAl concentrations (~8.5–11.7 nM) in the surface waters (<25 m) at the central and northern reaches of the subtropical gyre (12.5–23.5°S; Fig. 2c of Grand et al., 2015b). However, it should also be noted that the observed enrichment of dAl in the surface waters at ~8.5°S and ~14.5°S (GI-01/11 and 12) in this study (Fig. 6) is about 1.5–2 times higher than those observed by Grand et al. (2015b) over a similar latitudinal range (12.5–23.5°S) eastward at 95°E, which is possibly impacted by dust deposition (Grand et al., 2015a,b). Further south at the central ISG region (GI–01/16: ~25.3°S, 70°E), dAl_{ML} concentration (8.6 nM) decrease relative to that observed (~14–18 nM) in the northern reaches of the gyre.

4.2. dAl distribution in the lower thermocline and deeper waters (>300 m)

During the spring intermonsoon period (GI–01 cruise), highest dAl levels in the deeper waters (>500 m) were observed in the BoB region, reaching up to ~14–15 nM in the bottom waters of the N.BoB and the C.BoB (Fig. 3b). Increasing dAl concentrations were observed towards the seafloor (>2000 m) for all the BoB stations during the GI-01 cruise, more profoundly in the N.BoB and the C.BoB stations (Fig. 3b). Similar dAl distribution pattern was also evident near the eastern coast of India (GI-06/1, Fig. 4d) during the late winter period (GI-06 cruise), showing elevated dAl concentrations in the intermediate and deep waters (>500 m) compared to that at the open ocean stations (GI-06/2, 3 and 4).

At the center of the southern Andaman Sea (GI-06/6), dAl concentrations in the intermediate waters (500–1500 m) showed a similar distribution compared to that observed in the nearby stations in the S.BoB (GI-06/5 and 8; Fig. 4d and e). While dAl levels decreased (to ~2.5–2.7 nM) in the deeper waters below 1500 m (1800–2500 m) at the nearby S.BoB stations (GI-06/5 and 8), dAl concentrations at GI-06/6 showed remarkably uniform distribution (~3.7 nM) in the similar depth range (Figs. 4d and S3). Similar uniformities in the deep water profiles for various other physical and chemical tracers (e.g. ^{14}C, REE, ^{230}Th and major nutrients) are also reported in the Andaman Sea (Dutta et al., 2007; Nozaki and Alibo, 2003; Okubo et al., 2004). On the other hand at GI-06/7 station, sampled very close to the Nicobar Islands, dAl concentrations showed increment below 500 m towards the margin of Andaman-Nicobar Ridge (Fig. S3).

In the Arabian Sea region, the dAl concentrations in the lower thermocline and deeper waters (>1000 m) of stations GI-06/21 and 22 (2.4–3.0 nM; Figs. 4f and S4) were similar to recently reported dAl levels (2.2–2.5 nM; Fig. S4) by Vu and Sohrin (2013) at nearby station ER-7 (Fig. 1). However, close to the southeast margin of the Arabian Sea (GI–10/24), relatively, elevated dAl concentrations (3.3–3.6 nM; Figs. 4f and S4) were observed at similar deeper depths. Also, a discrete dAl maximum was observed in the thermocline waters at 600 m close to the margin of the Sea (GI-06/24; Fig. S4).

During the GI-06 cruise, dAl concentrations observed in the deeper waters (≥500 m) of the Eq.IO were low (<5 nM) relative to the N.BoB and the C.BoB but comparable to the S.BoB (Figs. 3b, 4d and 4e). In the same cruise, a continuous increase in dAl values in the bottom waters (>3500 m) towards the seafloor were observed in the eastern equatorial region (GI-06/11, 12, 13 and 14; Fig. 4e). Further south in the Eq.IO region at station GI-01/9 (~2°S), dAl maximum (~5 nM) around 3000 m was observed (Fig. 3b).

In the Indonesian Throughflow and Indian Subtropical Gyre (ITF–ISG) region, important variations in the dAl concentrations were observed in the deep and bottom waters (>2000 m; Fig. 3b). Combining the previously reported data in the region by Vu and Sohrin (2013) (ER-10: 20.00°S, 72.55°E; Fig. 1), we examined the patterns in the distribution of dAl for the deep (2000–3500 m) and bottom waters (>3500 m) in the ITF-ISG region. Average dAl concentration in the bottom waters is relatively elevated (3.9 nM) at the northernmost station of the region, GI-01/11, (~8.5°S, 80.8°E) where dAl maximum at 4000 m was also observed (Fig. 9b). At this station, a large proportion of the bottom waters presumably comes from the colder bottom waters of the Western Australian Basin, advected across the deep saddles in the Ninety–East Ridge (NER; Fig. 5b) to the Central Indian Ocean, which was also evident from the lower potential temperatures observed in the bottom waters at this station (Fig. 9a). Moving further southwest, overall, the dAl level in the bottom waters first decreased at GI-01/12 and then increased again close to the Central Indian Ridge (CIR) at ER-10 (Fig. 9b). On the other hand, average dAl concentration in the deep waters showed a continuous increase from the north (2.6 nM at GI-01/11) towards the southwest and showed highest dAl levels near the CIR (5.3 nM at GI-01/16, Fig. 9b). At GI-01/16, the dAl concentration gradually increased in the deeper waters (≥1500 m; Fig. 9b) reaching to the maximum value (5.3 nM) at the deepest sampled depth (2260 m) which coincided with the anomalously high water turbidity values around 2250 m (Fig. 9c).

5. DISCUSSION

5.1. Controls on dAl distribution in the surface mixed layer and upper thermocline waters (≤300 m)

In the surface mixed layer, deposition of atmospheric mineral dust and its subsequent partial dissolution is the key process regulating the dAl distribution. However, as

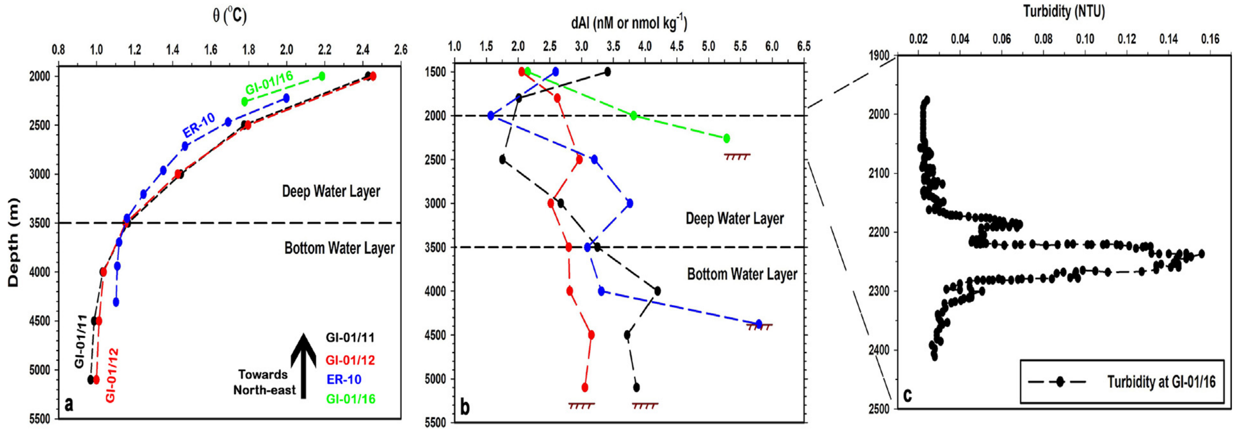

Fig. 9. Vertical profiles of (a) potential temperature (θ) and (b) dAl in the deep and bottom waters of stations sampled in the ITF–ISG region. The solid brown line below each dAl profile in (b) indicates the water depth of respective sampling station. Fig. (c) shows variations in water turbidity in the deep waters of station GI–01/16; the turbidity maximum (at ~2250 m) observed in the plot marks the presence of a hydrothermal plume. (For interpretation of the references to colour in this figure legend, the reader is referred to the web version of this article.)

noted in the introductory remarks, the huge input of fluvial derived lithogenic sediments in the north-eastern Indian Ocean (the BoB and the Andaman Sea), either in the form of suspended sediments in the surface water layer and/or resuspended after deposition over the shelf, may impact the surface dAl concentrations in these regions. Moreover, the surface and upper thermocline waters in the northern and equatorial Indian Ocean are influenced by seasonally reversing monsoonal current (Wyrtki, 1973; Schott and McCreary Jr, 2001), which may play an important role in transporting the dAl signals from one sub-basin to another. In addition to the aforementioned processes, the intrusion of Pacific waters through the Indonesian seas to the upper water column (primarily above 400 m, Schott et al., 2009) of the tropical Indian Ocean with the Indonesian Throughflow (ITF) may impact the dAl distribution.

In the following Sections 5.1.1–5.1.3, to have first-order estimates of the dAl input to the surface mixed layer, supported by the lithogenic sediments flux from atmospheric dust deposition and/or fluvial sediment discharge to the BoB, the equatorial Indian Ocean and the Arabian Sea, we used a 1-D box-model equation, which is a rearranged MADCOW model equation (Grand et al., 2015a) and given as follows:

$$\mathrm{dAl_{lith}} = \frac{\mathrm{G} \times \mathrm{MRT} \times \mathrm{f_{Al}^{sed}} \times \mathrm{Sol.}}{\mathrm{A_{wt}} \times \mathrm{MLD_c}} \times 10^6 \qquad (1)$$

where **G** is the lithogenic sediment flux (in g $\mathrm{m^{-2}\ yr^{-1}}$), **Sol.** is the fractional solubility of Al from the lithogenic sediments, $\mathbf{A_{wt}}$ is the atomic weight of Al (in g $\mathrm{mol^{-1}}$), **MRT** represents the mean residence time (in years) of dAl in the surface mixed layer, $\mathrm{f_{Al}^{sed}}$ is the fraction of Al in the sediments, $\mathbf{dAl_{lith}}$ is the estimated lithogenic sediments supported dAl concentration (in nM) in the surface mixed layer, $\mathbf{MLD_C}$ is the annual average of mixed layer depth estimated using monthly climatological mixed layer depth data (density threshold-based; Holte et al., 2017) reported closest to the sampling locations, and 10^6 is the factor to account for conversions of units.

Grand et al. (2015a) estimated the Al fractional solubility from atmospheric mineral dust deposited in the eastern Indian Ocean to be 3.6% using the observed Al solubility data from the dust deposition over the Atlantic and the Pacific surface ocean (Buck et al., 2010, 2013). The rationale behind this exercise was that the air masses carrying the mineral dust over the eastern Indian Ocean have mixed characteristics of air masses over the Atlantic (influenced by natural and anthropogenic dust) and the Pacific (from remote regions) Ocean. In the Arabian Sea, Schüßler et al. (2005) used an Al solubility of 3% with their observed surface dAl to estimate mineral dust deposition fluxes and found good agreement with the dust fluxes estimated from the direct measurements of mineral dust concentration in the ambient aerosols. Balancing the observed dAl inventory in the surface mixed layer and estimates of Al dissolution from mineral dust, Grand et al. (2015a) calculated the mean residence time of dAl in the surface mixed layer to be 1.1 years in the north-eastern Indian Ocean (north of 5° S). In the south-eastern Arabian Sea, similar estimates of the residence times, ranging from 0.5–2 years, are given by the biogeochemical modeling studies on surface dAl (Gehlen et al., 2003; Han et al., 2008).

In the following sub-sections, for consistency, we used the same Al fractional solubility and mean residence time, i.e. 3.6% and 1.1 years, respectively, to estimate the dust supported surface dAl in the BoB, the equatorial Indian Ocean and the south-eastern Arabian Sea region. Also, the fraction of Al in the atmospheric mineral dust deposited ($\mathrm{f_{Al}^{sed}}$) is assumed to be 8% (McLennan, 2001), considering the mineral dust to be originating from the upper crust.

5.1.1. The Bay of Bengal (BoB) and the Andaman Sea

Near uniform $\mathrm{dAl_{ML}}$ concentrations with significant variation in the surface water salinity in the C.BoB (GI-01/1, 3, 4 and 5; Fig. 7) and highly enriched $\mathrm{dAl_{ML}}$ at the N.BoB (47.1 nM at GI-01/2) with comparable $\mathrm{S_{ML}}$ (to that observed in the C.BoB; Fig. 7) suggests that dAl input from the huge freshwater influx of rivers play a secondary role in controlling the dAl distribution in the surface waters of the N.BoB and the C.BoB. Apart from the dissolved Al inputs from the rivers in the BoB, Al release from partial dissolution of and Al desorption from the lithogenic particulate matter supplied by the rivers, resuspension of sediments from continental margins (shelf and slope) and atmospheric mineral dust deposition, may also exert major controls on the dAl distribution in the upper water column of the BoB. Relative contributions of dissolved Al from river water and Al release from lithogenic sediments (atmospheric and fluvial derived) to the surface water layer of BoB may be determined if data on Al concentration in the sediments, sediment flux across surface water layer, fractional solubility of Al from the sediments, dissolved Al levels at the mouth of rivers discharging into the BoB and their water discharge are available. Al concentration in the sediments is considered to be 8% by weight, which is similar to the Al composition in the suspended sediments of Brahmaputra river [(7.9 ± 0.8)% (1SD), n = 13; Singh and France-Lanord, 2002) and the upper continental crust (8.04%; McLennan, 2001) but lower than that in the fine (<4 μm) silicate fraction of the Ganga bank sediments [(11.8 ± 0.6)% (1SD), n = 4; Singh et al., 2008).

First-order estimates for the Al fractional solubility from the sediments were obtained using the shallow depth lithogenic sediment flux data (Unger et al., 2003) in the BoB as representative of sediment input (both, from atmospheric dust deposition and fluvial sediment discharge) to the surface and considering the observed $\mathrm{dAl_{ML}}$ concentrations to be in steady-state with respect to the sediment derived Al input (i.e. $\mathrm{dAl_{lith}}$ in Eq. (1) equals to the observed $\mathrm{dAl_{ML}}$) and first-order removal of Al by particle scavenging processes (Eq. (1)). In the N.BoB and the C. BoB, lithogenic sediment flux data (Unger et al., 2003) from sediment trap locations NBBT-N (flux: 14.5 g $\mathrm{m^{-2}\ yr^{-1}}$; refer Fig. 1 for the location) and NBBT-S (flux: 8.7 g $\mathrm{m^{-2}}$ - $\mathrm{yr^{-1}}$; refer Fig. 1 for the location) and $\mathrm{dAl_{ML}}$ concentrations from stations GI-01/3 (28.2 nM) and GI-01/4 (26.9 nM) sampled closest to these trap locations (Fig. 1), respectively, were considered. In the S.BoB, lithogenic sediment flux data from sediment trap location SBBT (flux: 4.3 g $\mathrm{m^{-2}\ yr^{-1}}$, Unger et al., 2003; Fig. 1) and $\mathrm{dAl_{ML}}$ concentrations from stations GI-01/8 (19.0 nM) and GI-06/12 (15.4 nM) close to this trap location (Fig. 1) were used. MLD_c estimated for the stations GI-01/3, GI-01/4, GI-01/8 and GI-06/12 are 19 m, 26 m, 35 m and 35 m, respectively. Using these values of parameters in Eq. (1), the fractional release of Al from the lithogenic sedimentary input in the N.BoB, C.BoB and S.BoB is estimated as 1.1%, 2.4% and 3.8–4.7%, respectively. In the S.BoB, the estimated Al fractional solubility range of 3.8–4.7% is relatively high compared to that in the N.BoB and the C.BoB (1.1–2.4%). Additional dAl input from the advection of dAl-rich, low salinity surface waters from the southern Andaman Sea to the S.BoB with the NMC (Fig. 5a) may have lead to, relatively, overestimation of Al fractional solubility in the S.BoB (i.e. at GI-01/8 and GI-06/12) and therefore represent the upper limit in this region. This is also evident from relatively low surface salinity (<34) and high dAl concentrations (15.4–19.0 nM) observed at GI-01/8 and GI-06/12 (Figs. 3a, b and 4b, e).

dAl concentration measured at the mouth (salinity ≈29.4) of the Hooghly (the Ganga) estuary, during the summer monsoon of 2013, was of the order of ~57 nM and is taken as the average dAl concentration of the G-B river system to the BoB after passing through the estuary. Considering the water discharge of $10^3\ km^3\ yr^{-1}$ (Sengupta et al., 2006 and references therein), the estimated dissolved Al flux from the G–B river system to the BoB is $\sim 5.7 \times 10^7$ moles yr^{-1}. To estimate the average flux of lithogenic sediments across the surface water layer of the BoB, we calculated the mean lithogenic sediment flux ($\sim 9.7 \pm 4.3$ (1SD) $g\ m^{-2}\ yr^{-1}$) over $2.2 \times 10^{12}\ m^2$ area of the BoB using the shallow depth sediment traps data of Unger et al. (2003) at different sites in the BoB (Fig. 1). Using our estimates of Al fractional solubility (1.1–4.7%) and mean lithogenic sediment flux ($9.7\ g\ m^{-2}\ yr^{-1}$), Al release in the surface waters of the BoB from the sediments is estimated to be in the range: 7.0×10^8–3.0×10^9 moles yr^{-1}. This estimated Al release in the BoB is, at least, an order of magnitude larger than that estimated for the dissolved Al flux from the G–B river system (5.7×10^7 moles yr^{-1}) and highlights the dominance of dAl input from the large sediment flux, predominantly derived from the discharge of the Himalayan and peninsular rivers, in the BoB.

Srinivas and Sarin (2013) reported the Al flux of 0.8 ± 0.5 $mg\ m^{-2}\ d^{-1}$ with dry deposition of the mineral dust over the BoB and observed an overall decrease in fluxes from the northern to the southern BoB during the spring–intermonsoon period (March–April). In the same study, the aerosol Al concentrations over different regions of the BoB during the winter period (January) were observed to be similar to that observed during the spring-intermonsoon period (March-April). The continental outflow of dust from the Indo-Gangetic Plain and south-east Asia to the BoB is only feasible during the late winter to spring intermonsoon period (January–April) as the wind patterns during remaining of the year restricts the transport of dust over the BoB from the continental sources (Srinivas and Sarin, 2013). Therefore, it had been argued that the deposition fluxes of trace metals with the dust deposition observed during these four months nearly accounts for all the annual trace metal input to the BoB from the major sources of dust, i.e. the Indo-Gangetic Plains and south-east Asia, to the region (Srinivas and Sarin, 2013). Upper ($1.3\ mg\ m^{-2}\ d^{-1}$) and lower ($0.3\ mg\ m^{-2}\ d^{-1}$) limits of the reported Al dry deposition flux over the BoB (Srinivas and Sarin, 2013) are considered to be representative of Al flux in the N.BoB and the S.BoB, respectively, during January-April. To have lower and upper limits on the annual Al deposition fluxes over the BoB, we assumed the deposition fluxes for the rest of the year to be ranging from negligible (i.e. zero) to values similar to that during the continental outflow period (January-April). This translates to Al annual fluxes from dust deposition in the ranges of 156.0–474.5 $mg\ m^{-2}\ yr^{-1}$ and 36.0–109.5 $mg\ m^{-2}\ yr^{-1}$ for the N.BoB and the S.BoB, respectively. Using these estimated ranges of Al annual fluxes and estimated MLD_c values in the N.BoB (~20 m) and the S.BoB (~30 m) in Eq. (1), the steady-state estimates of dust input supported dAl in the N.BoB and the S.BoB are found to be ~11.5–35.0 nM and ~2.0–5.5 nM, respectively. These estimates are lower than the observed dAl_{ML} concentrations in the respective regions (47.1 nM at northernmost station GI-01/2 and 11.9–19.0 nM in the S.BoB) and suggest significant dAl input from the fluvial sources in the BoB, particularly through Al release from the large lithogenic sediments discharged by the rivers. If we consider the mineral dust deposition during the continental outflow period (January-April) to be a more representative estimate of the net annual atmospheric mineral dust input to the BoB surface waters (Srinivas and Sarin, 2013), the corresponding estimates of the dust derived surface dAl in the N. BoB (~11.5 nM) and the S.BoB (~2.0 nM) accounts for only 24% and 11–17% of the total observed dAl in the surface waters of the N.BoB and the S.BoB, respectively. This would suggest that the Al release from the sediments, supplied by the fluvial discharge, is a dominant process controlling the surface dAl in the BoB. Singh et al. (2012) also highlighted the need for excess Nd released from the fluvial and/or continental margin derived lithogenic particles to account for the Nd balance in the surface waters of BoB. Al input to the surface ocean via wet deposition may also play an important role in governing the dAl_{ML} distribution (Hand et al., 2004; Jickells, 1995; Jickells et al., 2005; Vink and Measures, 2001). However, due to the unavailability of data on wet deposition fluxes of Al and insignificant contribution of wet deposition during the continental outflow period (January to April; Srinivas and Sarin, 2013) over the BoB and the Eq.IO, we neglected the impact of wet deposition in the above (and similar calculations in Section 5.1.3 for the Eq.IO) calculations.

The plausible sources and processes that may induce the increase in dAl levels in the sub-surface water depths observed during the GI-01 cruise in the BoB (Fig. S2), include, (1) remineralization of biogenic Al-carrier phases releasing adsorbed or incorporated Al from the surface waters, (2) resuspension of continental margin sediments and subsequent release of Al from partial dissolution of or Al desorption from the sediments and/or (3) release of dAl-rich pore waters, which could be induced by sediment resuspension. If we assume Al removal by the biogenic particles in the surface waters and subsequent remineralization of these particles to be the source of the dAl increase in the sub-surface waters, positive correlation between the inorganic major nutrients (H_4SiO_4, NO_3^-, PO_4^{3-}) and dAl could be expected throughout the thermocline depths (100–800 m), where remineralization of biogenic debris leads to the consumption of DO and the release of assimilated nutrients (Anand et al., 2017). Contrary to that, dAl concentrations showed an overall decrease with increasing nutrients in the thermocline waters (Fig. S5), indicating particle scavenging of dAl to be dominating in the thermocline waters. Together, the absence of correlated increase of dAl and nutrients in the thermocline waters and observation of the strongest dAl influx in the sub-surface waters close to the coast (Figs. 3b and S2) suggest dAl supply from the continental margin, which fades southward due to advective mixing and scavenging.

Elevated dAl levels in the surface waters (0–50 m) near the southeast coast of India (GI-06/1, Fig. 4d) may indicate dAl input from the dissolved and/or suspended particulate phase of peninsular rivers discharging to the Indian east coast. Resuspension of lithogenic shelf sediments, derived from and deposited by the rivers, and subsequent Al release in the surface waters may also be a source. A steep decrease in dAl_{ML} concentration from GI-06/1 (23.4 nM) to GI-06/2 (14.3 nM) with similar surface salinity levels at the two stations (~33.1, Fig. 4a) suggests that the land runoff plays an insignificant role in providing dAl to the coastal seawaters. Also, the increase in mineral dust deposition flux close to the continent (Srinivas and Sarin, 2013) may lead to an increase in surface dAl levels. In conclusion, the combined increase in sedimentary input close to the coast resulted in dAl concentration gradients from the open BoB to the southeast Indian coastal region.

Near the Nicobar Islands in the S.BoB (GI-06/5 and 8) and the Andaman Sea (GI-06/6 and 7), probable contributors of dAl to the surface waters include (1) freshwater and suspended sediments from the I-S and G-B river system, (2) resuspended sediments from the shelf of the Islands, which may also induce diffusion of Al from dAl enriched pore waters to ambient seawater, and (3) advection of Indonesian Water to the S.BoB and the southern Andaman Sea (Section 3). Surface circulation patterns (refer to Fig. 5a for a schematic representation) during the GI-06 cruise also show the freshwater influx from the I-S and G-B river system to the southern Andaman Sea and the S.BoB surface waters. Atmospheric Al deposition fluxes are low near and over the Andaman Sea (Srinivas and Sarin, 2013) and consequently could not support for the elevated dAl values in the surface waters. Comparatively, very high dAl_{ML} concentrations were observed at station GI-06/7 and 8 (~43–48 nM; Fig. 4e). Interestingly, silicic acid concentration in surface mixed layer also increased significantly at these stations (1.03–1.21 μM at GI-06/7 and 8) compared to the adjacent stations in S.BoB (0.18–0.78 μM at GI-06/4, 5 and 9) during the same period. During the winter period (December-February), the Indonesian Water makes its way to the Andaman Sea from the Strait of Malacca (SoM), which is also evident in the surface circulation pattern (refer Fig. 5a for a schematic representation) and discussed by Rizal et al. (2012). Indonesian Water outflow from the SoM to the southern Andaman Sea during the winter has a significant contribution from the southeast South China Sea surface waters (Rizal et al., 2012). There is no available dAl data in the surface waters flowing through the SoM to the Andaman Sea. However, extremely elevated ^{228}Ra activities (625–725 dpm m^{-3}; Nozaki and Yamamoto, 2001), in the SoM demonstrate a significant interaction between the surface waters and the local sediments. Limited available dAl data in the surface waters at the center of the South China Sea (~33.7 nM; PA-11, Obata et al., 2004), the Sulu Sea (16.7 nM; PA-1, Obata et al., 2004) and the surface ITW entering to the Indian Ocean from the south of Java and the Timor Sea (~11–12 nM, PA-2 and PA-7, Obata et al., 2004) seems inadequate to account for highly enriched dAl levels (~43–48 nM at GI–10/7 and 8) near the Nicobar Islands. This could also be inferred from the dAl_{ML} concentration observed at the centre of the southern Andaman Sea (24.2 nM at GI-06/6), which is much lower than dAl value at GI-06/7 and 8, even though station GI-06/6 also receives waters outflowing from the SoM to the Andaman Sea before it turns south towards the S.BoB and the Eq.IO (Fig. 5a for a schematic representation and Rizal et al. (2012)). Consequently, in addition to dAl contribution from the fluvial sources and the outflow of Indonesian Water, localized and correlated increase in dAl and silicic acid at GI-06/7 and 8 suggest the dAl and dissolved Si input from the dissolution of and/or Al desorption from resuspended terrigenous sediments from the insular shelf of the Nicobar Islands. The increase in the upper water column turbidity around the Nicobar Islands (Fig. 10) provides further evidence for the resuspension of the shelf sediments. Recent studies (Fripiat et al., 2011; Jeandel et al., 2011; Tréguer and De La Rocha, 2013) have also shown and suggested the release of Si from the terrigenous margin sediments as an important source of dissolved Si to the ambient seawater.

dAl concentration observed in the surface waters (17.2 nM; PA-10, Fig. 1, Obata et al., 2004) further north (~10°N) at the center of the Andaman Sea, during the same period, was apparently lower than at GI-06/6 southward (24.2 nM; ~7.5°N) and therefore, suggest some additional contribution from the Indonesian Sea surface waters outflowing from SoM to the Andaman Sea, apart from the fluvial inputs of the I-S and G-B river systems from the north.

5.1.2. The Arabian Sea (AS)

Advection of low salinity BBW waters to the surface water layer of the south-eastern Arabian Sea (see Section 3) may carry the dAl-rich signature of the BoB surface waters to this region. It is apparent with, relatively, higher dAl levels and lower salinity observed in the upper 25 m at station GI-06/21 (22.0–23.2 nM) compared to the other stations, GI-06/22 and GI-06/24 (10.0–20.5 nM), in this region (also refer to Table S1). Additionally, high atmospheric mineral dust deposition fluxes at the south-eastern Arabian Sea (Kumar et al., 2012; Measures and Vink,

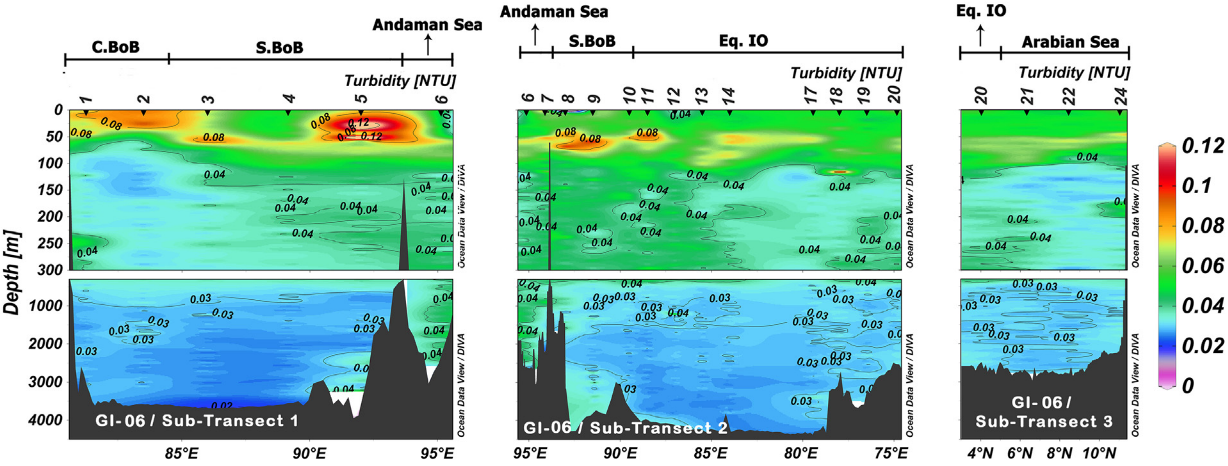

Fig. 10. Variation of seawater turbidity in the upper water column (0–300 m) and waters below 300 m along the sub-transects sampled during the GI-06 cruise. Refer to Fig. 4g to identify the sub-transects along the full transect of the GI-06 cruise.

1999) may also contribute to the elevated dAl_{ML} values compared to that observed in the north-western, central and southern Arabian Sea during the same season in the earlier studies (Measures and Vink, 1999; Vu and Sohrin, 2013). Deposition of mineral dust, particularly, in the southern Arabian Sea is more dominant during the winter (December–February) and the spring–intermonsoon (April–May) period compared to the rest of the year (Kumar et al., 2008; Tindale and Pease, 1999). During the winters (December, 2007), Kumar et al. (2012) observed highest Al concentrations ($2.27 \pm 0.98\ \mu g\ m^{-3}$) in aerosols collected from the atmospheric boundary layer near the eastern boundary of the Arabian Sea compared to any other season (Kumar et al., 2008; Schüßler et al., 2005 and references therein), which they attributed to: (1) transport of a large amount of mineral aerosols ($13.3–50.7\ \mu g\ m^{-3}$) through continental outflow, under the influence of north-easterlies winds, transacting a large area over the Indian subcontinent, and (2) closeness with the continent. During the spring-intermonsoon period (April–May), the mean Al concentration in aerosol from atmospheric boundary layer in the southern Arabian Sea (8–12°N) is observed to be $1.13\ \mu g\ m^{-3}$ (Kumar et al., 2008). Considering the above (mean) Al concentration in aerosol during the winter (December-February: $2.27\ \mu g\ m^{-3}$) and the spring-intermonsoon (April-May: $1.13\ \mu g\ m^{-3}$), annual mean Al concentration over the southern Arabian Sea is assumed to be in the range: $1.13–2.27\ \mu g\ m^{-3}$. This translates to Al dry deposition flux of $0.32–0.64\ g\ m^{-2}\ yr^{-1}$ using dry deposition velocity of $0.9\ cm\ s^{-1}$ (Kumar et al., 2008). Using this range of Al flux and MLD_c estimate (~25 m) near stations (GI-06/21, 22 and 24) in the south-eastern Arabian Sea in Eq. (1), a steady-state dAl concentration of ~ 19–38 nM is estimated in the mixed layer. This is comparable to the observed dAl_{ML} (18.6–22.7 nM) and shows that the dust derived Al is a prominent source for the surface dAl near the south-eastern Arabian Sea. The dominant impact of dust dissolution on the surface water chemistry of dissolved Nd near the eastern coast of AS was also highlighted by Goswami et al., (2014).

5.1.3. The Equatorial Indian Ocean

Significantly correlated variation (Fig. 8) between S_{ML} and dAl_{ML} in the equatorial waters suggests that the dAl_{ML} distribution in the Eq.IO is primarily controlled by the advective mixing of the dAl-rich, low salinity surface waters of the S.BoB and the Andaman Sea with relatively dAl-poor, high salinity waters of the southern Arabian Sea, under the influence of the NMC. This argument is consistent with the observed dAl_{ML} (Vu and Sohrin, 2013) in the southern Arabian Sea during the winters (December 2009), which apparently bound the lower end of the linear dAl_{ML} variations with S_{ML} in the Eq.IO region (Fig. 8).

The observed atmospheric dry deposition Al flux in the Eq.IO region during the winter and spring intermonsoon period was $\sim 0.3\ mg\ m^{-2}\ d^{-1}$(Srinivas and Sarin, 2013). In the Eq.IO region, atmospheric models (composite model: Jickells et al., 2005; Mahowald et al., 2005 and DEAD model: Zender et al., 2003) estimate total mineral dust deposition flux on the order of $20\ mg\ m^{-2}\ d^{-1}$ which is about $1.5\ mg\ m^{-2}\ d^{-1}$ of Al flux with the assumption of 8% Al in the mineral dust. This is relatively large compared to the observed Al flux ($\sim 0.3\ mg\ m^{-2}\ d^{-1}$) during the winter and spring intermonsoon period (January–April, Srinivas and Sarin, 2013). However, assuming a constant 8% Al in the deposited mineral dust throughout the surface dAl residence timescale of ~1 year (Grand et al., 2015a) in the region would result in overestimation of Al flux given that continental outflow is only prominent during the winter and the spring intermonsoon period (Srinivas and Sarin, 2013) and for the rest of the year winds sourced from marine environment would be richer in sea salts. Assuming Al flux of $0.3\ mg\ m^{-2}\ d^{-1}$ (Srinivas and Sarin, 2013) and MLD_c in the range: 30–35 m (Holte et al., 2017), contribution of dAl to the surface mixed of the Eq.IO region from the atmospheric dust deposition will lie in the range: 4.6–5.3 nM. These dust supported (and steady-state) dAl estimates are lower than those observed in the eastern equatorial region (8.3–15.4 nM at GI-06/11, 12 and 13; Fig. 4e) and again suggest additional dAl input from advection of dAl-rich, low salinity surface waters of the S.BoB and the southern Andaman Sea. However, mixed layer dAl observed towards the western equatorial region and the southern Arabian Sea (2.7–4.3 nM at GI-06/19, GI-06/20 and ER-8) are relatively lower than the dust derived dAl estimates (4.6–5.3 nM). This mismatch may result from overestimation of Al dust fluxes in the residence time scale of dAl (∼1 year), particularly in the southern Arabian Sea where the seasonal variations in Al concentrations of dust are large, showing order of magnitude lesser Al concentrations during the southwest monsoon season compared to that in northwest monsoon and spring intermonsoon period due to changes in dust source regions with changing wind patterns (Schüßler et al., 2005; Tindale and Pease, 1999).

5.1.4. The Indonesian Throughflow and Indian Subtropical Gyre Region

As discussed earlier, the distinct increase of dAl in the upper water column of stations GI–01/11 and 12, situated in the northern reaches of the Indian Subtropical Gyre (ISG), are consistent with the pattern observed in the earlier study (Grand et al., 2015b) in the similar latitudinal range further east at 95°E. In the previous study, this dAl increment in the surface waters at the northern end of the ISG was primarily attributed to the deposition and subsequent dissolution of mineral dust, which is emitted from the Australian continent and mostly deposited east of 90°E (Grand et al., 2015a; Mahowald et al., 2005). Here, we argue that under the prevailing westward SEC flow (Fig. 5a), the dAl enriched surface waters may be advected from the zone of high dust deposition at east to our sampling sites at GI-01/11 and 12 westward and therefore imparting the high dAl_{ML} signal in this region. However, the significantly higher (1.5–2 times) dAl enrichment observed in the surface waters of the northern subtropical gyre in this study (GI-01/11 and 12) compared to that in the previous results (Grand et al., 2015b) may thus suggest inter-annual variations in the dust load, emanating from the Australian dust source regions and which finally reaches to the northern ISG, if atmospheric mineral dust deposition and its partial dissolution is considered the primary source of Al to the surface waters. Atmospheric dust emission events from the Australian sources are very episodic in nature compared to the Northern Hemisphere source regions, which emit more regularly (Mackie et al., 2008 and references therein). Mackie et al. (2008) computed the Dust Storm Index (DSI), using the dust storm frequency and visibility data, as a measure of annual dust activity and reported its variation for 46 years (1960–2005) in Australia. They found that high dust events correlate with the periods of intense drought years in the continent. After the record rainfall in most of the Australian basins with the onset of the La-Nina conditions in the Pacific Ocean during the period of 2010–12, arid conditions again started building up in Australia from 2013 (Australian Annual Climate Summary 2010, 2011, 2012 and 2013; Available at: http://www.bom.gov.au/climate/current). Such a situation may lead to an increase in dust influx from Australia to the ISG before the sampling period in the subtropics (April 2014), but this still remains a speculation.

In the northern reaches of the ISG (8–15°S), advection of Indonesian Throughflow Water (ITW) may also play a major role in governing the surface dAl concentrations and more importantly in the depths below the surface mixed layer, where the Al release from the settling mineral dust particles is deemed negligible (Grand et al., 2015b; Maring and Duce, 1987; Measures et al., 2010). Elevated ^{228}Ra activities (>100 dpm m^{-3}; Nozaki and Yamamoto, 2001) observed in the surface waters at ∼10°S, 103°E (PA–7, Fig. 1) and ∼13°S, 117°E (PA–2, Fig. 1), from where the ITW enters to the tropical Indian Ocean, suggest strong interactions of the surface waters with the sediments of continental shelf surrounding the Indonesian Seas. Such a process may also result in Al release from the shelf sediment to the surface waters, therefore enriching the dAl values in these waters. dAl concentration in the ITW entering the eastern Indian Ocean should then be a function of the extent of its interaction with sediments and discharge, which may vary seasonally and inter-annually (Tomczak and Godfrey, 2003b; Liu et al., 2015; Potemra and Schneider, 2007). In their observations at the eastern Indian Ocean (∼95°E), Grand et al. (2015b) also highlighted the significant contribution of dAl from the advection of ITW to the upper thermocline water depths (200–400 m) of the northern ISG region. Fig. 11 shows the comparison of dAl profiles, observed in the upper 500 m, between GI-01/12 (this study), receiving prominent input from the ITW, and I09N-113 (∼14.6°S) sampled at similar latitude at 95°E transect of Grand et al. (2015b). Similar pattern and magnitude of dAl distribution in the upper thermocline (Fig. 11; $\gamma^n > 23$ kg m^{-3}, i.e., >100–500 m) observed in this study supports the earlier inference of dAl input to the tropical Indian Ocean with the inflow of ITF waters and spreads further westward along the advective pathway. However, due to advective mixing and scavenging along the SEC carrying the ITW, relatively lower dAl concentration should be expected towards the west (at GI-01/12) compared to that at I09N-113, if the ITW are considered the source of dAl in the thermocline depths. Moreover, both GI-01/12 and I09N-113 (Grand et al., 2015b) showed dAl levels in the thermocline waters much larger than that observed at station PA-2 (Fig. 11), sampled by Obata et al. (2004) in the year of 1997 (17 years before this study and 7 years before the study by Grand et al. (2015b)), further east near the Timor Sea (Fig. 1) from where the ITF waters are sourced to the tropical Indian Ocean. These observations may suggest interannual variation in dAl input with the ITW advection. Earlier studies (Liu et al., 2015; Potemra and Schneider, 2007) have confirmed that large interannual variations occur in the Indonesian Throughflow (ITF) discharge to the tropical Indian Ocean. Liu et al. (2015), using expendable bathythermograph data, showed that the mean annual ITF transport monotonously increased during 30 years of their study period, from 1984-2013, at the rate of 1 Sverdrup per 10 years. These results, therefore, underscore the need of time-series studies in the future to understand the impact of ITF discharge on dAl and other trace elements distribution.

At the center of the subtropical gyre (GI-01/16), relative decrease (to 8.6 nM) in surface dAl compared to the northern gyre region (∼14–18 nM) correlates with the decline in mineral dust deposition flux (Grand et al., 2015a; Mahowald et al., 2005).

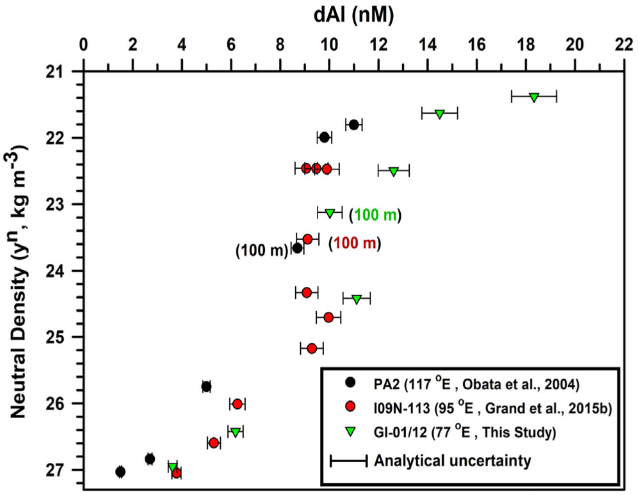

Fig. 11. Comparison between dAl distribution observed in the upper 500 m water column at GI–01/12, I09N–113 (Grand et al., 2015b) and PA-2 (Obata et al., 2004) sampled along the South Equatorial Current carrying the Indonesian Throughflow Water. Due to large distances between the stations, the dAl data is plotted against the neutral density. dAl observed at 100 m for each station is also highlighted to indicate the relative difference in neutral density at this depth for different stations. Analytical uncertainties indicated for the GI-01/12 and PA-2 data were that observed (5%, 1SD) after repeat analysis of in-house reference seawater, InStd-D, in this study and at 2.0 nM by Obata et al. (2004), respectively. Precision for dAl analysis for I09N cruise samples was not indicated by Grand et al. (2015b) and therefore, considered as 5% here for comparison.

5.2. Controls on dAl distribution in the lower thermocline and deeper waters (>300 m)

In the open ocean, most of the dissolvable Al from the mineral dust deposited on the ocean surface is released in the surface mixed layer with no significant dissolution below the mixed layer (Maring and Duce, 1987; Measures et al., 2010). Also, residence time estimates (Orians and Bruland, 1986) for dAl in the open ocean surface waters are short (4 weeks–4 years) vis-a-vis deep water residence time, which is an order of magnitude higher (50–200 years). Given the above conditions, the dAl distribution in the intermediate and deep water depths of open ocean waters is largely controlled by the water advection and reversible scavenging of Al adsorbed on the particulate phases as they sink through the water column below the surface layer. Though, this assertion may break in the regions close to the ocean boundaries (continental margins and seafloor) due to external dAl contributions from partial dissolution of and/or Al desorption from the fluvial derived and resuspended boundary sediments, and diffusion of pore waters rich in dAl (Grand et al., 2015b; Caschetto and Wollast, 1979; Van Beueskom et al., 1997). In the next sections, we will describe the dAl distribution observed in the intermediate, deep and bottom waters of different regions sampled in the Indian Ocean and discuss the probable sources and processes leading to the observed distribution.

5.2.1. The Bay of Bengal (BoB) and the Andaman Sea

The sediment trap data of Unger et al. (2003) in the BoB showed higher mean lithogenic particle flux (6.0–19.5 g m^{-2} yr^{-1}) for the deep sediment traps (~2000–3000 m) compared to the lithogenic sediment flux (4.3–14.5 g m^{-2} yr^{-1}) across the shallow traps (700–1500 m). This indicates that the resuspension of sediments from the continental slope supplies additional lithogenic matter to the deeper waters of the BoB together with the fluvial and shelf derived particulate lithogenic matter. During the GI-01 cruise, the general increase in dAl levels close to the continental slope and seafloor (Fig. 3b) suggest that the resuspension of the slope and benthic sediments along with probable influx of dAl enriched pore waters, upon sediment resuspension, act as sources of dAl in the deep and bottom waters of the BoB. Also, note that dAl maxima near seafloor showed a decrease in magnitude from the N.BoB to the S.BoB (Fig. 3b). This may result from a decrease in the fraction of lithogenic sediments settling through the BoB water column (Unger et al., 2003), providing the necessary reactive mineral phases in the form of aluminosilicates and clay minerals to the margin sediments, from which Al could be released to the water column upon their resuspension. Singh et al. (2012) estimated the particulate matter derived excess dissolved Nd (Nd$_{xs}$) needed, in addition to the dissolved Nd contribution resulting from the mixing of water masses, to balance the total mass of dissolved Nd observed in the BoB. Their results showed the hotspots of Nd$_{xs}$ in the deep and bottom waters of BoB apparently, focused near the continental slope and rise. This result also suggests resuspension of sediments from the continental margin and their subsequent partial dissolution as a process of trace metal supply to the deep and bottom waters. During the late winter period (GI-06 cruise), the increase in dAl levels observed in the intermediate and deep waters (>500 m) towards the eastern coast of India (GI-06/1, Fig. 4d) suggests that sediment resuspension is a ubiquitous process along the continental margins of BoB, providing additional dAl input to the deeper waters of the region.

One of the striking observations in the deeper waters of the southern Andaman Sea (at GI-06/6) is the near-uniform dAl (~3.7 nM) below 1000 m (1500–2400 m, Figs. 4d and S3) in contrast to the nearby S.BoB stations (GI-06/5 and 8, Fig. 4d and e), which show about 1 nM lower dAl levels in the similar depth range (~2.5–2.7 nM at 1800–2500 m; Fig. 4d and e). Also, the uniform dAl composition in the deeper waters at GI-06/6 was similar to that observed in the lower thermocline depth (~1200 m) at the nearby S. BoB stations (GI-06/5 and 8, Fig. 4d and e). The deeper waters of Andaman Sea (>1000 m) are predominantly derived from the lower thermocline waters of the BoB, entering through the Ten degree channel and the Great Passage, as the shallow sills of the Andaman–Nicobar Ridge isolates the deep basin of Andaman Sea from that of the BoB below ~1800 m (Dutta et al., 2007 and references therein). Apparently, rapid renewal of the deep waters (within 6 years, Okubo et al., 2004) in the Andaman Sea compared to the scavenging residence time of dAl, ensures similar dAl composition in the deep and lower thermocline waters (~1200 m) of the Andaman Sea and the BoB, respectively. Moreover, rapid vertical mixing of the Andaman deep waters (timescale: ≤5 years, Dutta et al., 2007) leads to near-uniform dAl concentrations.

Dutta et al. (2007) suggested that internal solitary waves induced by the tidal currents over rough topography of the Andaman Sea could cause rapid vertical mixing in the deep waters. This process may also induce sediment resuspension from the sea margins, which is supported by higher water turbidity observed within the deeper (>1000 m) waters of the sea compared to the surrounding waters in the BoB (Fig. 10). The relative increase in dAl concentrations observed below 500 m close to the Andaman-Nicobar Ridge (GI-06/7, Figs. 4e and S3) may, therefore, suggest additional dAl input from the resuspended sediments due to water turbulence over the ridge within the sea.

5.2.2. The Arabian Sea (AS)

In the deeper waters (>1000 m) of the Arabian Sea, the observed increase in dAl towards the continental margin (at station GI-06/24, refer Figs. 4f and S4) suggests for an additional external source of dAl. The increase in the lithogenic sediment flux from the central Arabian Sea to the eastern Arabian Sea is evident from the deep (~3000 m) sediment trap data (Ramaswamy and Nair, 1994). This increment in lithogenic flux results from the supply of fluvial sediments from the Indus, Narmada and Tapi rivers discharging to the eastern Arabian Sea (Ramaswamy and Nair, 1994). Further, the observed discrete maximum in the thermocline waters of station GI-06/24 at 600 m depth (Figs. 4f and S4) suggest for Al input either due to the resuspension of margin sediments or diffusion of dAl enriched pore waters. In either of the cases, lithogenic sediments settling over the continental margin must play an important role in the supply of reactive Al mineral phases. It is important to note that the enrichment in the dAl levels observed in the deep waters near the coast of the Arabian Sea were much lower compared to that observed near the coastal region of the BoB presumably due to much smaller fluvial (and associated sediment) discharge in the eastern Arabian Sea compared to the coastal BoB (Ramaswamy and Nair, 1994; Unger et al, 2003).

5.2.3. The Equatorial Indian Ocean

The dAl maximum observed at station GI-01/9 around 3000 m correlates with the increase in dissolved Fe (dFe) concentrations in similar deep waters depths at the same station (refer to Fig. 11(I) of Chinni et al., 2019). Chinni et al. (2019) proposed this increase in the dFe to be resulting from the advection of dFe-rich deeper waters (>2500 m) close to the Java Trench, which constitutes the subduction zone between the Indian and the Indonesian plate. The interaction of re-circulated seawater (through the faults) with poly-metallic modules is suggested to be the source of dFe-rich deeper waters near the trench. In the absence of dAl data near the trench, it is unclear if such a process may also lead to the enrichment of dAl concentrations in the deeper water. Alternatively, here, we argue that the deep and bottom waters flowing as the western boundary currents along the eastern boundary of the NER (Tomczak and Godfrey, 2003a; You, 1999) may produce sufficient turbulence over the NER to resuspend the margin sediments, which may subsequently act as the source of dFe and dAl to the deep and bottom waters. This could be inferred from the elevated dAl concentrations and the turbidity values observed in the deep and bottom waters of the S.BoB close to the eastern margin of the NER at station GI-06/9 (Figs. 4e and 10). These dAl rich deep waters (2000–3500 m) are subsequently advected from the east of the NER to the Central Indian Ocean Basin at GI–01/9 (Fig. 5b) and result in the observed dAl maximum. Such an enrichment in dAl was not observed in the bottom waters (below 3500 m, Fig. 3b) at GI–01/9 due to the topographical barrier for the advection of bottom waters (>3500 m) to the region near station GI–01/9 from the east of the NER (Fig. 5b).

The increase in dAl towards the seafloor in the bottom waters (>3500 m) observed at the eastern Eq.IO stations (GI-06/11, 12, 13 and 14, Fig. 4e) during the GI-06 cruise imply dAl flux from the bottom sediments in these regions.

5.2.3.1. Residence time of the dissolved Al in the deep waters of Equatorial Indian Ocean.

We estimated the residence time of dAl against removal by particle scavenging in the deep waters (2000–3500 m) of the Eq.IO using the one-dimensional (1-D) scavenging-advection-diffusion model (Craig, 1974). This model has two inherent assumptions: (1) horizontal concentration gradients in the distribution of the modeled dissolved constituent in the region of application are negligible and (2) vertical mixing is the dominant process with absence of any significant horizontal advection of a distinct water mass in the model layer. As recognized by previous studies (Mantyla and Reid, 1995; You, 1999; You, 2000), the Indian deep waters represent the modified Circumpolar Deep Water (CDW) and occupy the depth range 2000–3500 m. Due to significant vertical upwelling and dianeutral mixing, the northern Indian deep waters (north of 30°S) show remarkable linearity in the potential temperature-salinity plot (Fig. S1) and, therefore, could be treated as a 'z-diffusive layer' where the 1-D advection-diffusion model is applicable (Craig, 1969). The water column below 3500 m is majorly filled by the AABW as a distinct water mass (Tomczak and Godfrey, 2003a; You, 1999) and hence dAl below 3500 is not considered for the fitting using the 1-D scavenging-advection-diffusion model. Also, we restricted the model application to the Eq.IO stations sampled during the GI-06 cruise as important horizontal dAl concentration gradients were observed for the deep waters of the northern Indian Ocean (the BoB, the Andaman Sea and the Arabian Sea; Sections 5.2.1 and 5.2.2), the southern end of the Eq.IO region (station GI–01/9; refer Section 5.2.3) and the ITW–ISG region (refer Section 5.2.4). Fig. 12 shows the best model fits (black solid lines) to the deep water dAl profiles of the Eq.IO stations sampled during the GI-06 cruise, considering the conservative mixing due to vertical advection-diffusion of dAl and setting the boundary dAl concentrations to be free variables (refer to Eq. (3) and its description in the Appendix A). At stations GI-06/11, 14 and 17, significant and discrete positive dAl deviations (>5%) from the conservative mixing line (denoted by arrows in Fig. 12) within the deep water layer boundaries suggest the additional, non–uniform dAl input in between the model boundaries. This additional input may be produced due to horizontal advection or net *in situ* Al release from the particulate matter within the deep waters. It is particularly evident for the GI-06/11 where the transport of dAl-rich deep waters from region near the NER (GI-06/10 and 9) could be seen (Fig. 4e). In any of the two cases, the deep water dAl profiles at these stations could not be convincingly simulated with a 1-D scavenging-advection-diffusion model used in this study. Therefore, we applied the model to the deep water dAl profiles of stations GI-06/12, 13 and 19 (blue lines) to constrain the deep water residence time of dAl in the region. Other stations (GI-06/18 and GI-06/20) are not examined due to lack of enough data points in the deep waters ($\leq$3) compared to the number of free variables (3, i.e., $\mathbf{C_m}$, $\mathbf{C_o}$ and ψ/ω; refer to Eq. (2) of Appendix A) in the model.

The best fits for the 1-D scavenging-advection-diffusion model (refer to Eq. (2) of Appendix A) to the deep water dAl at GI-06/12, 13 and 19 (blue lines, Fig. 12) gives the ratio of the dAl scavenging rate to the vertical advection velocity (i.e, ψ/ω; refer to Table 2 for estimated values). From these ψ/ω estimates, the scavenging residence time ($\tau = 1/\psi$) could be estimated if data on ω is available.

Srinivasan et al. (2000) estimated the mean upwelling velocity, ω, north of 30°S across the lower deep water layer boundary (~3500 m) to be 10 m yr^{-1} upward using the adjusted ^{14}C concentration profiles ('corrected for the

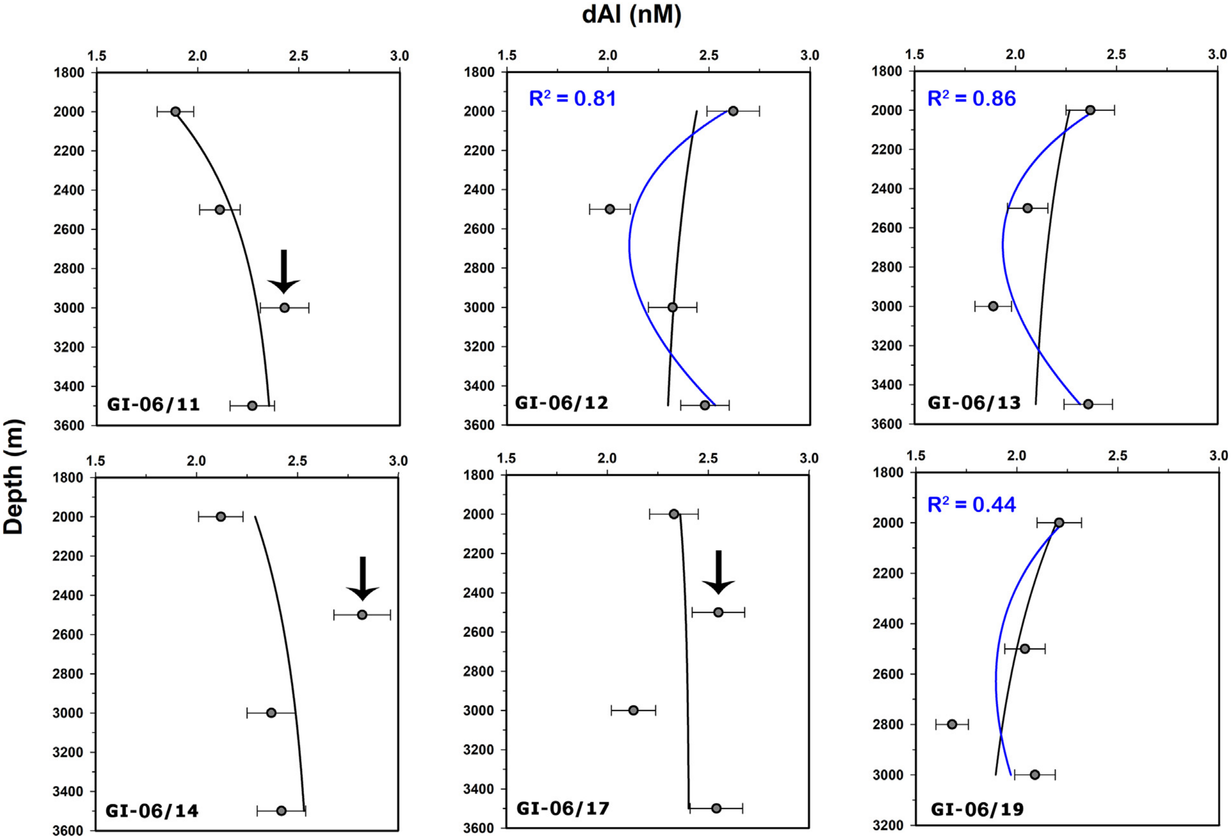

Fig. 12. Deep water (2000–3500 m) dAl distribution at the selected Eq.IO stations (see text) overlain by best model fits (in least square sense) to the distribution using 1-D advection-diffusion, i.e. vertical conservative mixing, model (black solid lines; also refer to Eq. (3) and its description in the Appendix A) and 1-D scavenging-advection-diffusion model (blue solid lines; also refer Eq. (2) and its description in the Appendix A). Horizontal bars represent the precision of analysis (~5%, see text) achieved at similar dAl concentrations. Arrows in the graph point to the dAl values within the deep water layers showing significant dAl excess with respect to the conservative mixing line (black solid lines). (For interpretation of the references to colour in this figure legend, the reader is referred to the web version of this article.)

Table 2
Results estimated for ψ/ω and τ by fitting the 1–D scavenging-advection-diffusion model to the deep water dAl profiles at the Eq. IO stations GI–06/12, 13 and 19. z* values are estimated by fitting the 1-D advection-diffusion model to the deep water salinity distribution in the respective stations.

Station ID	z* (km)	ψ/ω (km^{-1})	ω[1] (km/yr)	τ (yr)
GI-10/12	1.04	0.78	0.010	128
			0.014	92
GI-10/13	0.95	0.71	0.010	141
			0.014	101
GI-10/19	0.78	0.51	0.010	196
			0.014	140

[1] Data sources: Robbins and Toole (1997), Srinivasan et al. (2000) and Warren (1981).

effects of addition of particulate radiocarbon to the deep waters'; Srinivasan et al., 2000). This is relatively smaller than the upwelling velocity of ~12.5 m yr^{-1} given by Warren (1981) across ~2000 m at ~ 18°S and the basin-mean upwelling velocity of ~14 m yr^{-1} across ~2000 m north of 32°S determined by Robbins and Toole (1997) by considering, together, the hydrographic data and advective flux of the dissolved silica. Assuming $\boldsymbol{\omega}$ to be varying in the range of 10–14 m yr^{-1}, the variations in the scavenging residence time of the dAl in the deep waters of the Eq.IO are reported here (Table 2). The estimated residence time of dAl against scavenging in the deep waters lies in the range: 92–196 yrs (Table 2). However, the model fit to the deep water profile at GI-06/19 was comparatively poor ($R^2 = 0.44$, Fig. 12) and may suggest horizontal dAl input, probably, from relatively dAl enriched deep and bottom waters near the margin of Chagos-Laccadive Ridge as also visible in the slight increase in dAl ~ 1800 m at GI-06/20 and 21 (Fig. 4f). Accordingly, neglecting the residence time estimates from GI-06/19, the inferred range of 92–141 yrs, using dAl profiles of stations GI-06/12 and 13, is considered to be more representative. This range of residence time is similar to that observed in the deep Pacific Ocean (50–200 yrs, Orians and Bruland, 1985, 1986). It is, however, relatively larger than the basin-averaged deep water dAl replacement time (50 ± 10 yrs) calculated in the North Atlantic (Hayes et al., 2018b). Replacement time is a measure of the time needed to replace the trace element inventory, for a given volume of seawater, by the source(s) considered for the element. The replacement time is equal to the removal residence time only if the distribution of the element, in the region of interest, is in a steady-state. Considering the deep water dAl distribution in the North Atlantic to be in a steady-state, the smaller estimate of deep water dAl replacement time presumably results due to more intense scavenging of dAl by the particulate matter, particularly by diatoms associated with the North Atlantic spring bloom (Malviya et al., 2016). Deep water scavenging of dAl near the ocean margins is also indicated by significant depletion (compared to that in the African dust and Bulk Continental Crust) of Ti:Al ratio in the fine particulate matter and, in general, continuous increase in the particulate Al levels in the deeper waters (>500 m) of the North Atlantic (Hayes et al., 2018a and supporting information therein; Ohnemus and Lam, 2015), more significant near the continental margins.

5.2.4. Indonesian Throughflow and Indian Subtropical Gyre

Our sampling station GI–01/16, lies very close to the Kairei vent field discovered (Gamo et al., 2001) over the Central Indian Ridge (CIR) and is just north of the Rodrigues Triple Junction (RTJ). At this station, we observed anomalously high deep water turbidity values in the narrow depth range of ~ 2150–2300 m with turbidity maximum around 2250 m depth (Fig. 9c). Coinciding with this high turbidity signal, was the deep water dAl maximum (at 2250 m; Fig. 9b and c). At the same station and identical depth (2250 m), Chinni et al. (2019) also observed highly enriched dissolved Fe concentration (20.86 nM), about 28 times higher than the background deep water dissolved Fe level (~0.75 nM) and suggested it to be of hydrothermal origin. Various earlier studies have also reported the active hydrothermal venting in vicinity of the RTJ and over the CIR, either through indirect clues from hydrothermal plume signals of prominent suspended sediment and chemical anomalies (Gamo et al., 1996; Jean-Baptiste et al., 1992; Vu and Sohrin, 2013) or direct observation of hydrothermal venting sites over the CIR (Gallant and Von Damm, 2006; Gamo et al., 2001). Therefore, dAl maximum coinciding with the turbidity and dissolved Fe maxima, may suggest that the dAl input is sourced from the dAl-enriched hydrothermal fluids emanating from the active vents over the CIR. However, the gradual increase in dAl concentrations to the dAl maximum close to the seafloor at GI–01/16 (Fig. 9b) may also, in principle, result from the dAl flux due to the sediment resuspension and/or diffusion of dAl-rich pore water from the sea bottom as the primary source(s). Further north at ER-10, Vu and Sohrin (2013) also reported the dAl enrichment in the deep water hydrothermal plume encountered during their study (around 3000 m, Fig. 9b) and, based on the relationship between ^{3}He, dAl and other trace metal data, suggested that the observed enrichment at ER-10 is probably due to resuspended sediments. To better constrain the source(s) of dAl, higher resolution sampling, both vertical and lateral, of deep waters in this region is needed for the measurement of dAl and other chemical constituents of hydrothermal origin.

The trend in the dAl distribution for bottom water depths in the Central Indian Ocean Basin (Fig. 9b) indicates advection of dAl-rich bottom waters at GI-01/11 across the NER from the Western Australian Basin. This is also supported by the dAl maximum in the bottom waters of station GI–01/11, which is observed much above the seafloor (~1200 m above the seafloor at 4000 m; Fig. 9b) and therefore, discards the possibility that bottom sediments were the primary source of dAl increase in the bottom waters. Again, as suggested for the southern equatorial region (station GI-01/9; see Section 5.2.3), interaction of the bottom waters, flowing as the western boundary current along the eastern NER, with the sediments over the ridge may enrich the dAl concentrations in the bottom waters. More studies on dAl distribution in the deep and bottom waters along the eastern margin of NER are needed to confirm this hypothesis. Further, the dAl levels in the bottom waters decrease as they turn and move southward at GI–01/12 (Fig. 9b), presumably, due to mixing and scavenging loss. The mean dAl concentration in the bottom waters again increased close to the CIR at ER–10 (Fig. 9b), however, here, the dAl profile showed sudden increase close to the seafloor, suggestive of external dAl input from the bottom sediments.

6. CONCLUSION

A comprehensive study on the cycling of dAl in the water columns of the northern, equatorial and subtropical gyre region of the Indian Ocean has been carried out and forms the first extensive evaluation of sources, sinks and internal cycling of dAl in the deep and bottom waters of the BoB and the equatorial Indian Ocean. The dAl distribution throughout the water column of the BoB is predominantly influenced by the lithogenic sedimentary input, from fluvial and continental margin sources, enriched in reactive clay minerals. Using the estimated range of the Al fractional solubility from the lithogenic sediments in the BoB surface waters, the dAl flux to the surface waters of BoB from the dissolution of / Al desorption from the lithogenic sediments is calculated to be at least an order of magnitude higher than that supplied by the G-B river system waters. This suggests that the Al release from the sediments is a dominant process controlling the surface dAl distribution in the BoB. In the southern Andaman Sea, partial dissolution of resuspended local shelf sediments from the Nicobar Islands and advection of Indonesian Water from the SoM results in elevated dAl levels in the surface mixed layer and the upper thermocline waters. Rapid ventilation of and vertical mixing in the deep waters of the Andaman Sea and, apparently, the lower scavenging removal rate of dAl result in near-uniform distribution of dAl in the deeper waters at the center of the southern Andaman Sea.

Overall, dAl concentrations in the surface and upper thermocline waters of the equatorial Indian Ocean region were controlled by the advective mixing of the low salinity, dAl-rich waters of the S.BoB and the Andaman Sea with the high salinity, dAl-poor waters of the southern Arabian Sea under the influence of NMC. Using the 1-D scavenging-advection–diffusion model, the scavenging residence time of dAl in the deep waters of the Eq.IO region is estimated to lie in the range: 92–141 years.

During the winter monsoon, continental outflow, predominantly from the Indian subcontinent, leads to the high atmospheric deposition of mineral aerosols close to the south-eastern boundary of the Arabian Sea; this, in turn, translates to the elevated dAl levels in the surface mixed layer. In the deeper waters of Arabian Sea, the relative increase in the dAl levels close to the continental margin hints at the net Al release from the boundary sediments.

At the northern reaches of the subtropical gyre region, significant enrichment of dAl throughout the upper water column (<500 m) agrees with the dAl distribution pattern observed in the similar depth range further east at ∼95°E (Grand et al., 2015b) and is primarily attributed to the atmospheric dust flux from the Australian continent, which is the major dust source to the ISG region, and the advection of the ITW. However, higher (compared to the previous study) dAl levels in the surface mixed layer were observed in this study and, presumably, reflects the inter-annual variations in the dust deposition flux to the ISG region. The increase in dAl concentrations in the deep waters (2000–3500 m) over the eastern flank of the CIR seems to result from bottom sediment resuspension close to the ridge. This enrichment in the deep water dAl levels dies out due to water–mass mixing and scavenging along the advective pathway of deep waters towards the north in the subtropical gyre region. The advection of the dAl enriched AABW (below 3500 m) from the Western Australian Basin to the northern Central Indian Basin across the deep saddles of the NER is observed.

ACKNOWLEDGMENTS

We are thankful to the captains, the crew and all the participants of GI-01 and GI-06 cruises for their invaluable support during the clean seawater sampling and onboard analysis of chemical parameters. We sincerely thank Prof. M.M. Sarin (Physical Research Laboratory) for his valuable discussions and suggestions in the course of preparation of this manuscript. Authors are grateful to Prof. Maeve Lohan (University of Southampton) and Dr. Angela Milne (University of Plymouth) for their support provided during the establishment of the dissolved aluminium flow injection system (Al-FIS). We also thank Prof. Greg Cutter (Old Dominion University) and Prof. Christopher Measures (University of Hawaii) for their help in establishing the clean sampling system in India. We are sincerely thankful to Bruland Research Lab for providing the batches of SAFe and GEOTRACES seawater reference samples. We are grateful to Mr. Manan S Shah for the automation of Al-FIS and Mr. Mahesh Gaddam for his help in onboard measurement of major nutrient during the GI-06 cruise. We would like to sincerely thank Dr. Maxime Grand and the other two anonymous reviewers for providing their constructive comments and suggestions which helped us improve the manuscript. This work has been done under the GEOTRACES-India programme with the generous financial support from the Ministry of Earth Sciences (MoES), Government of India, and Physical Research Laboratory, Ahmedabad, India.

APPENDIX A

The dAl distribution in the deep waters is modeled using steady-state, 1-D scavenging-advection-diffusion model for a stable and non-conservative (SNC) tracer, considering no *in situ* production (Craig, 1974). The model equation is given as

$$\mathbf{K}\cdot\frac{\partial^2\mathbf{C_z}}{\partial\mathbf{z}^2}-\boldsymbol{\omega}\cdot\frac{\partial\mathbf{C_z}}{\partial\mathbf{z}}-\psi\cdot\mathbf{C_z}=0 \tag{1}$$

WHICH HAS A GENERAL SOLUTION

$$\mathbf{C_z}=\left\{\mathbf{C_m}\times\left[\exp\frac{-(\mathbf{z_m}-\mathbf{z})}{2\mathbf{z}^*}\right]\times\sinh\left(\frac{\mathbf{Az}}{2\mathbf{z}^*}\right)+\mathbf{C_o}\times\left[\exp\frac{\mathbf{z}}{2\mathbf{z}^*}\right]\times\sinh\left[\frac{\mathbf{A}(\mathbf{z_m}-\mathbf{z})}{2\mathbf{z}^*}\right]\right\}\times\left\{\sinh\left[\frac{\mathbf{Az_m}}{2\mathbf{z}^*}\right]\right\}^{-1} \tag{2}$$

where $\mathbf{z^*} = \mathbf{K/\omega}$ is the mixing parameter and $\mathbf{A = [1 + 4z^*(\psi/\omega)]^{1/2}}$.

In the above equations, **K** denotes the vertical diffusivity; **ω** represents the vertical advection velocity; **ψ** is the scavenging rate; and $\mathbf{C_z}$ is the dAl concentration at the vertical depth '**z**', taken positive towards the ocean surface. $\mathbf{C_m}$ and $\mathbf{C_o}$ are the dAl concentrations at the model's upper ($\mathbf{z = z_m}$) and lower ($\mathbf{z = z_o}$) boundaries. The lower model boundary $\mathbf{z = z_o}$ is also considered as the point of reference, i.e., $\mathbf{z_o = 0}$. The value of the mixing parameter, **z***, is estimated by fitting the general solution of the steady-state, 1-D advection-diffusion model for a stable and conservative (SC) tracer (Craig, 1974) to the salinity distribution in the deep waters. The general solution of the steady-state, 1-D advection-diffusion model for a SC tracer is given as

$$C_z = C_o + (C_m - C_o) \times \left[\exp\frac{z}{z^*} - 1\right] \times \left[\exp\frac{z_m}{z^*} - 1\right]^{(-1)} \qquad (3)$$

Next, we find the best fit for the dAl distribution in the deep waters to Eq. (2) with $\mathbf{C_m}$, $\mathbf{C_o}$ and $\mathbf{\psi/\omega}$ as free variables.

APPENDIX B. SUPPLEMENTARY MATERIAL

Supplementary data to this article can be found online at https://doi.org/10.1016/j.gca.2019.09.028.

REFERENCES

Anand S. S., Rengarajan R., Sarma V. V. S. S., Sudheer A. K., Bhushan R. and Singh S. K. (2017) Spatial variability of upper ocean POC export in the Bay of Bengal and the Indian Ocean determined using particle-reactive 234Th. *J. Geophys. Res. Oceans* **122**(5), 3753–3770. https://doi.org/10.1002/2016JC012639.

Brown M. T. and Bruland K. W. (2008) An improved flow-injection analysis method for the determination of dissolved aluminum in seawater. *Limnol. Oceanogr. Methods* **6**, 87–95. https://doi.org/10.4319/lom. 2008.6.87.

Buck C. S., Landing W. M., Resing J. A. and Measures C. I. (2010) The solubility and deposition of aerosol Fe and other trace elements in the North Atlantic Ocean: observations from the A16N CLIVAR/CO2 repeat hydrography section. *Mar. Chem.* **120**(1–4), 57–70. https://doi.org/10.1016/j.marchem.2008.08.003.

Buck C. S., Landing W. M. and Resing J. (2013) Pacific Ocean aerosols: Deposition and solubility of iron, aluminum, and other trace elements. *Mar. Chem.* **157**, 117–130. https://doi.org/10.1016/j.marchem.2013.09.005.

Caschetto S. and Wollast R. (1979) Dissolved aluminium in interstitial waters of recent marine sediments. *Geochim. Cosmochim. Acta* **43**(3), 425–428. https://doi.org/10.1016/0016-7037(79)90207-2.

Chinni V., Singh S. K., Bhushan R., Rengarajan R. and Sarma V. (2019) Spatial variability in dissolved iron concentrations in the marginal and open waters of the Indian Ocean. *Mar. Chem.*. https://doi.org/10.1016/j.marchem.2018.11.007.

Chou L. and Wollast R. (1997) Biogeochemical behavior and mass balance of dissolved aluminum in the western Mediterranean Sea. *Deep Sea Res. Part II Top. Stud. Oceanogr.* **44**, 741–768. https://doi.org/10.1016/s0967-0645(96)00092-6.

Craig H. (1974) A scavenging model for trace elements in the deep sea. *Earth Planet. Sci. Lett.* **23**(1), 149–159. https://doi.org/10.1016/0012-821X(74)90042-9.

Craig H. (1969) Abyssal carbon and radiocarbon in the Pacific. *J. Geophys. Res.* **74**(23), 5491–5506. https://doi.org/10.1029/JC074i023p05491.

Damodararao K., Singh S. K., Rai V. K., Ramaswamy V. and Rao P. S. (2016) Lithology, monsoon and sea-surface current control on provenance, dispersal and deposition of sediments over the andaman continental shelf. *Front. Mar. Sci.* **3**. https://doi.org/10.3389/fmars.2016.00118.

Dixit S. and Van Cappellen P. (2002) Surface chemistry and reactivity of biogenic silica. *Geochim. Cosmochim. Acta* **66**(14), 2559–2568. https://doi.org/10.1016/S0016-7037(02)00854-2.

Dutta K., Bhushan R. and Somayajulu B. L. K. (2007) Rapid vertical mixing rates in deep waters of the Andaman Basin. *Sci. Total Environ.* **384**(1-3), 401–408. https://doi.org/10.1016/j.scitotenv.2007.04.041.

Dymond J., Collier R., McManus J., Honjo S. and Manganini S. (1997) Can the aluminum and titanium contents of ocean sediments be used to determine the paleoproductivity of the oceans? *Paleoceanography* **12**(4), 586–593. https://doi.org/10.1029/97PA01135.

ESR, 2009. OSCAR third degree resolution ocean surface currents. Ver. 1. PO.DAAC, CA, USA. Dataset accessed [2018-04-20] at https://doi.org/10.5067/OSCAR-03D01.

Fripiat F., Cavagna A.-J., Savoye N., Dehairs F., André L. and Cardinal D. (2011) Isotopic constraints on the Si-biogeochemical cycle of the Antarctic Zone in the Kerguelen area (KEOPS). *Mar. Chem.* **123**(1-4), 11–22. https://doi.org/10.1016/j.marchem.2010.08.005.

Gaillardet J., Viers J. and Dupré B. (2014) Trace elements in river waters. In *Treatise on Geochemistry*. Elsevier, pp. 195–235. https://doi.org/10.1016/B978-0-08-095975-7.00507-6.

Gallant R. M. and Von Damm K. L. (2006) Geochemical controls on hydrothermal fluids from the Kairei and Edmond Vent Fields, 23°-25°S, Central Indian Ridge. *Geochem. Geophys. Geosyst.* **7**. https://doi.org/10.1029/2005gc001067.

Galy A. and France-Lanord C. (2001) Higher erosion rates in the Himalaya: Geochemical constraints on riverine fluxes. *Geology* **29**, 23. https://doi.org/10.1130/0091-7613(2001)029%3C0023:HERITH%3E2.0.CO;2.

Gamo T., Chiba H., Yamanaka T., Okudaira T., Hashimoto J., Tsuchida S., Ishibashi J.-ichiro., Kataoka S., Tsunogai U., Okamura K., Sano Y. and Shinjo R. (2001) Chemical characteristics of newly discovered black smoker fluids and associated hydrothermal plumes at the Rodriguez Triple Junction, Central Indian Ridge. *Earth Planet. Sci. Lett.* **193**(3–4), 371–379. https://doi.org/10.1016/S0012-821X(01)00511-8.

Gamo T., Nakayama E., Shitashima K., Isshiki K., Obata H., Okamura K., Kanayama S., Oomori T., Koizumi T., Matsumoto S. and Hasumoto H. (1996) Hydrothermal plumes at the Rodriguez triple junction, Indian ridge. *Earth Planet. Sci. Lett.* **142**(1-2), 261–270. https://doi.org/10.1016/0012-821X(96)00087-8.

Gehlen M., Beck L., Calas G., Flank A.-M., Van Bennekom A. J. and Van Beusekom J. E. E. (2002) Unraveling the atomic structure of biogenic silica: evidence of the structural association of Al and Si in diatom frustules. *Geochim. Cosmochim. Acta* **66**(9), 1601–1609. https://doi.org/10.1016/S0016-7037(01)00877-8.

Gehlen M., Heinze C., Maier-Reimer E. and Measures C. I. (2003) Coupled Al-Si geochemistry in an ocean general circulation model: A tool for the validation of oceanic dust deposition fields? *Global Biogeochem. Cycles* **17**(1). https://doi.org/10.1029/2001GB001549.

Goswami V., Singh S. K. and Bhushan R. (2014) Impact of water mass mixing and dust deposition on Nd concentration and ε Nd of the Arabian Sea water column. *Geochim. Cosmochim. Acta* **145**, 30–49. https://doi.org/10.1016/j.gca.2014.09.006.

Grand M. M., Measures C. I., Hatta M., Hiscock W. T., Buck C. S. and Landing W. M. (2015a) Dust deposition in the eastern Indian Ocean: the ocean perspective from Antarctica to the Bay of Bengal. *Global Biogeochem. Cycles* **29**(3), 357–374. https://doi.org/10.1002/gbc.v29.310.1002/2014GB004898.

Grand M. M., Measures C. I., Hatta M., Hiscock W. T., Landing W. M., Morton P. L., Buck C. S., Barrett P. M. and Resing J. A. (2015b) Dissolved Fe and Al in the upper 1000 m of the eastern Indian Ocean: a high-resolution transect along 95°E from the Antarctic margin to the Bay of Bengal. *Global Biogeochem. Cycles* **29**(3), 375–396. https://doi.org/10.1002/gbc.v29.310.1002/2014GB004920.

Grand M. M., Measures C. I., Hatta M., Morton P. L., Barrett P., Milne A., Resing J. A. and Landing W. M. (2015c) The impact of circulation and dust deposition in controlling the distributions of dissolved Fe and Al in the south Indian subtropical gyre. *Mar. Chem.* **176**, 110–125. https://doi.org/10.1016/j.marchem.2015.08.002.

Han Q., Moore J. K., Zender C., Measures C. and Hydes D. (2008) Constraining oceanic dust deposition using surface ocean dissolved Al. *Global Biogeochem. Cycles* **22**(2). https://doi.org/10.1029/2007GB002975.

Hand J. L., Mahowald N. M., Chen Y., Siefert R. L., Luo C., Subramaniam A. and Fun I. (2004) Estimates of atmospheric-processed soluble iron from observations and a global mineral aerosol model: Biogeochemical implications. *J. Geophys. Res.* **109**.

Hansen H. P. and Koroleff F. (1999) Determination of nutrients. In *Methods of Seawater Analysis* (eds. K. Grasshoff, K. Kremling and M. Ehrhardt). Wiley-VCH Verlag GmbH, Weinheim, Germany, pp. 159–228. https://doi.org/10.1002/9783527613984.ch10.

Holte J., Talley L. D., Gilson J. and Roemmich D. (2017) An Argo mixed layer climatology and database. *Geophys. Res. Lett.* **44**, 5618–5626. https://doi.org/10.1002/2017gl073426.

Hydes D. J. (1979) Aluminum in seawater: control by inorganic processes. *Science* **205**, 1260–1262. https://doi.org/10.1126/science.205.4412.1260.

Hayes C. T., Black E. E., Anderson R. F., Baskaran M., Buesseler K. O., Charette M. A., Cheng H., Cochran J. K., Edwards R. L. and Fitzgerald P. (2018a) Flux of particulate elements in the north atlantic ocean constrained by multiple radionuclides. *Global Biogeochem. Cycles* **32**, 1738–1758. https://doi.org/10.1016/j.marchem.2010.08.00510.1029/2018GB005994.

Hayes C. T., Anderson R. F., Cheng H., Conway T. M., Edwards R. L., Fleisher M. Q., Ho P., Huang K.-F., John S. G., Landing W. M., Little S. H., Lu Y., Morton P. L., Moran S. B., Robinson L. F., Shelley R. U., Shiller A. M. and Zheng X.-Y. (2018b) Replacement times of a spectrum of elements in the North Atlantic based on thorium supply. *Global Biogeochem. Cycles* **32**(9), 1294–1311. https://doi.org/10.1029/2017GB005839.

Jean-Baptiste P., Mantisi F., Pauwells H., Grimaud D. and Patriat P. (1992) Hydrothermal3He and manganese plumes at 19°29′S on the Central Indian Ridge. *Geophys. Res. Lett.* **19**, 1787–1790. https://doi.org/10.1029/92gl00577.

Jeandel C., Peucker-Ehrenbrink B., Jones M. T., Pearce C. R., Oelkers E. H., Godderis Y., Lacan F., Aumont O. and Arsouze T. (2011) Ocean margins: The missing term in oceanic element budgets? *Eos Trans. AGU* **92**(26), 217–218. https://doi.org/10.1029/2011EO260001.

Jickells T. (1995) Atmospheric inputs of metals and nutrients to the oceans: their magnitude and effects. *Mar. Chem.* **48**(3-4), 199–214. https://doi.org/10.1016/0304-4203(95)92784-P.

Jickells T. D., An Z. S., Andersen K. K., Baker A. R., Bergametti G., Brooks N., Can J. J., Boyd P. W., Duce R. A., Hunter K. A. and Kawahata H. (2005) Global iron connections between desert dust, ocean biogeochemistry, and climate. *Science* **308**, 67–71. https://doi.org/10.1126/science.1105959.

Koning E., Gehlen M., Flank A.-M., Calas G. and Epping E. (2007) Rapid post-mortem incorporation of aluminum in diatom frustules: evidence from chemical and structural analyses. *Mar. Chem.* **106**(1-2), 208–222. https://doi.org/10.1016/j.marchem.2006.06.009.

Kumar A., Sarin M. and Sudheer A. (2008) Mineral and anthropogenic aerosols in Arabian Sea–atmospheric boundary layer: sources and spatial variability. *Atmos. Environ.* **42**, 5169–5181. https://doi.org/10.1016/j.atmosenv.2008.03.004.

Kumar A., Sudheer A., Goswami V. and Bhushan R. (2012) Influence of continental outflow on aerosol chemical characteristics over the Arabian Sea during winter. *Atmos. Environ.* **50**, 182–191. https://doi.org/10.1016/j.atmosenv.2011.12.040.

Kumar S. P., Narvekar J., Kumar A., Shaji C., Anand P., Sabu P., Rijomon G., Jose J., Jayaraj K. A., Radhika A. and Nai K. K. C. (2004) Intrusion of the Bay of Bengal water into the Arabian Sea during winter monsoon and associated chemical and biological response. *Geophys. Res. Lett.* **31**, 4–7. https://doi.org/10.1029/2004gl020247.

Kumar M. D. and Li Y.-H. (1996) Spreading of water masses and regeneration of silica and 226Ra in the Indian Ocean. *Deep Sea Res. Part II* **43**(1), 83–110. https://doi.org/10.1016/0967-0645(95)00084-4.

Liu Q.-Y., Feng M., Wang D. and Wijffels S. (2015) Interannual variability of the Indonesian Throughflow transport: a revisit based on 30 year expendable bathythermograph data. *J. Geophys. Res. Oceans* **120**, 8270–8282. https://doi.org/10.1002/2015jc011351.

Locarnini R. A., Mishonov A. V., Antonov J. I., Boyer T. P., Garcia H. E., Baranova O. K., Zweng M. M., Paver C. R., Reagan J. R., Johnson D. R., Hamilton M. and Seidov D. (2013) *World Ocean Atlas 2013, Volume 1: Temperature*. NOAA Atlas NESDIS, 40 pp.

Lunel T., Rudnicki M., Elderfield H. and Hydes D. (1990) Aluminium as a depth-sensitive tracer of entrainment in submarine hydrothermal plumes. *Nature* **344**, 137–139. https://doi.org/10.1038/344137a0.

Mackie D. S., Boyd P. W., McTainsh G. H., Tindale N. W., Westberry T. K. and Hunter K. A. (2008) Biogeochemistry of iron in Australian dust: From eolian uplift to marine uptake. *Geochem. Geophys. Geosyst.* **9**. https://doi.org/10.1029/2007gc001813.

Mackin J. E. and Aller R. C. (1984) Processes affecting the behavior of dissolved aluminum in estuarine waters. *Mar. Chem.* **14**(3), 213–232. https://doi.org/10.1016/0304-4203(84)90043-4.

Mackin J. E. and Aller R. C. (1986) The effects of clay mineral reactions on dissolved Al distributions in sediments and waters of the Amazon continental shelf. *Cont. Shelf Res.* **6**(1-2), 245–262. https://doi.org/10.1016/0278-4343(86)90063-4.

Mahowald N. M., Baker A. R., Bergametti G., Brooks N., Duce R. A., Jickells T. D., Kubilay N., Prospero J. M. and Tegen I. (2005) Atmospheric global dust cycle and iron inputs to the ocean. *Global Biogeochem. Cycles* **19**(4). https://doi.org/10.1029/2004GB002402.

Malviya S., Scalco E., Audic S., Vincent F., Veluchamy A., Poulain J., Wincker P., Iudicone D., de Vargas C., Bittner L., Zingone

A. and Bowler C. (2016) Insights into global diatom distribution and diversity in the world's ocean. *Proc. Natl. Acad. Sci. USA* **113**(11), E1516–E1525. https://doi.org/10.1073/pnas.1509523113.

Mantyla A. W. and Reid J. L. (1995) On the origins of deep and bottom waters of the Indian Ocean. *J. Geophys. Res.* **100**(C2), 2417. https://doi.org/10.1029/94JC02564.

Maring H. B. and Duce R. A. (1987) The impact of atmospheric aerosols on trace metal chemistry in open ocean surface seawater, 1. Aluminum. *Earth Planet. Sci. Lett.* **84**(4), 381–392. https://doi.org/10.1016/0012-821X(87)90003-3.

McLennan S. M. (2001) Relationships between the trace element composition of sedimentary rocks and upper continental crust. *Geochem. Geophys. Geosyst.* **2**(4). https://doi.org/10.1029/2000GC000109.

Measures C. I. and Vink S. (1999) Seasonal variations in the distribution of Fe and Al in the surface waters of the Arabian Sea. *Deep Sea Res. Part II* **46**(8–9), 1597–1622. https://doi.org/10.1016/S0967-0645(99)00037-5.

Measures C. I. and Edmond J. M. (1988) Aluminium as a tracer of the deep outflow from the Mediterranean. *J. Geophys. Res.* **93**(C1), 591. https://doi.org/10.1029/JC093iC01p00591.

Measures C. I. and Edmond J. M. (1990) Aluminium in the South Atlantic: steady state distribution of a short residence time element. *J. Geophys. Res.* **95**(C4), 5331. https://doi.org/10.1029/JC095iC04p05331.

Measures C. I. and Vink S. (2000) On the use of dissolved aluminum in surface waters to estimate dust deposition to the ocean. *Global Biogeochem. Cycles* **14**(1), 317–327. https://doi.org/10.1029/1999GB001188.

Measures C. I., Brown M. T. and Vink S. (2005) Dust deposition to the surface waters of the western and central North Pacific inferred from surface water dissolved aluminum concentrations. *Geochem. Geophys. Geosyst.* **6**(9). https://doi.org/10.1029/2005GC000922.

Measures C., Hatta M., Fitzsimmons J. and Morton P. (2015) Dissolved Al in the zonal N Atlantic section of the US GEOTRACES 2010/2011 cruises and the importance of hydrothermal inputs. *Deep Sea Res. Part II* **116**, 176–186. https://doi.org/10.1016/j.dsr2.2014.07.006.

Measures C. I., Sato T., Vink S., Howell S. and Li Y. H. (2010) The fractional solubility of aluminium from mineral aerosols collected in Hawaii and implications for atmospheric deposition of biogeochemically important trace elements. *Mar. Chem.* **120**(1-4), 144–153. https://doi.org/10.1016/j.marchem.2009.01.014.

Middag R., de Baar H. J. W., Laan P. and Bakker K. (2009) Dissolved aluminium and the silicon cycle in the Arctic Ocean. *Mar. Chem.* **115**(3-4), 176–195. https://doi.org/10.1016/j.marchem.2009.08.002.

Middag R., de Baar H. J. W., Laan P. and Huhn O. (2012) The effects of continental margins and water mass circulation on the distribution of dissolved aluminum and manganese in Drake Passage. *J. Geophys. Res.* **117**(C1). https://doi.org/10.1029/2011JC007434.

Middag R., van Hulten M., Van Aken H., Rijkenberg M., Gerringa L., Laan P. and de Baar H. (2015) Dissolved aluminium in the ocean conveyor of the West Atlantic Ocean: effects of the biological cycle, scavenging, sediment resuspension and hydrography. *Mar. Chem.* **177**, 69–86. https://doi.org/10.1016/j.marchem. 2015.02.015.

Moran S. B. and Moore R. M. (1988) Evidence from mesocosm studies for biological removal of dissolved aluminium from sea water. *Nature* **335**(6192), 706–708. https://doi.org/10.1038/335706a0.

Moran S. B. and Moore R. M. (1991) The potential source of dissolved aluminum from resuspended sediments to the North Atlantic Deep Water. *Geochim. Cosmochim. Acta* **55**(10), 2745–2751. https://doi.org/10.1016/0016-7037(91)90441-7.

Nozaki Y. and Alibo D. S. (2003) Importance of vertical geochemical processes in controlling the oceanic profiles of dissolved rare earth elements in the northeastern Indian Ocean. *Earth Planet. Sci. Lett.* **205**(3-4), 155–172. https://doi.org/10.1016/S0012-821X(02)01027-0.

Nozaki Y. and Yamamoto Y. (2001) Radium 228 based nitrate fluxes in the eastern Indian Ocean and the South China Sea and a silicon-induced "alkalinity pump" hypothesis. *Global Biogeochem. Cycles* **15**(3), 555–567. https://doi.org/10.1029/2000GB001309.

Obata H., Nozaki Y., Alibo D. S. and Yamamoto Y. (2004) Dissolved Al, In, and Ce in the eastern Indian Ocean and the Southeast Asian Seas in comparison with the radionuclides 210Pb and 210Po. *Geochim. Cosmochim. Acta* **68**(5), 1035–1048. https://doi.org/10.1016/j.gca.2003.07.021.

Ohnemus D. C. and Lam P. J. (2015) Cycling of lithogenic marine particles in the US GEOTRACES North Atlantic transect. *Deep Sea Res. Part II* **116**, 283–302. https://doi.org/10.1016/j.dsr2.2014.11.019.

Okubo A., Obata H., Nozaki Y., Yamamoto Y. and Minami H. (2004) 230Th in the Andaman Sea: Rapid deep-sea renewal. *Geophys. Res. Lett.* **31**, 1–5. https://doi.org/10.1029/2004gl020226.

Orians K. J. and Bruland K. W. (1985) Dissolved aluminium in the central North Pacific. *Nature* **316**(6027), 427–429. https://doi.org/10.1038/316427a0.

Orians K. J. and Bruland K. W. (1986) The biogeochemistry of aluminum in the Pacific Ocean. *Earth Planet. Sci. Lett.* **78**(4), 397–410. https://doi.org/10.1016/0012-821X(86)90006-3.

Potemra J. T. and Schneider N. (2007) Interannual variations of the Indonesian throughflow. *J. Geophys. Res.*, 112.

Ramaswamy V. and Nair R. R. (1994) Fluxes of material in the Arabian Sea and Bay of Bengal—Sediment trap studies. *Proc. Indian Acad. Sci. (Earth Planet Sci.)* **103**, 189–210. https://doi.org/10.1007/BF02839536.

Resing J. A. and Measures C. I. (1994) Fluorometric determination of Al in seawater by flow injection analysis with in-line preconcentration. *Anal. Chem.* **66**(22), 4105–4111. https://doi.org/10.1021/ac00094a039.

Resing J. A., Sedwick P. N., German C. R., Jenkins W. J., Moffett J. W., Sohst B. M. and Tagliabue A. (2015) Basin-scale transport of hydrothermal dissolved metals across the South Pacific Ocean. *Nature* **523**(7559), 200–203. https://doi.org/10.1038/nature14577.

Rizal S., Damm P., Wahid M. A., Sundermann J., Ilhamsyah Y. and Iskandar T. (2012) General circulation in the Malacca Strait and Andaman Sea: a numerical model study. *Am. J. Environ. Sci.* **8**, 479–488. https://doi.org/10.3844/ajessp.2012.479.488.

Robbins P. E. and Toole J. M. (1997) The dissolved silica budget as a constraint on the meridional overturning circulation of the Indian Ocean. *Deep Sea Res. Part I* **44**(5), 879–906. https://doi.org/10.1016/S0967-0637(96)00126-4.

Robinson R. A., Bird M. I., Oo N. W., Hoey T. B., Aye M. M., Higgitt D. L., Swe A., Tun T. and Win S. L. (2007) The irrawaddy river sediment flux to the Indian Ocean: the original nineteenth-century data revisited. *J. Geol.* **115**, 629–640. https://doi.org/10.1086/521607.

Schlitzer, R., 2016. Ocean Data View. https://odv.awi.de.

Schott F. A. and McCreary, Jr., J. P. (2001) The monsoon circulation of the Indian Ocean. *Prog. Oceanogr.* **51**(1), 1–123. https://doi.org/10.1016/S0079-6611(01)00083-0.

Schott F. A., Xie S.-P. and McCreary, Jr., J. P. (2009) Indian Ocean circulation and climate variability. *Rev. Geophys.* **47**(1). https://doi.org/10.1029/2007RG000245.

Schüßler U., Balzer W. and Deeken A. (2005) Dissolved Al distribution, particulate Al fluxes and coupling to atmospheric Al and dust deposition in the Arabian Sea. *Deep Sea Res. Part II* **52**(14-15), 1862–1878. https://doi.org/10.1016/j.dsr2.2005.06.005.

Selavka C. M., Jiao K. S. and Krull I. S. (1987) Construction and comparison of open tubular reactors for post-column reaction detection in liquid chromatography. *Anal. Chem.* **59**(17), 2221–2224. https://doi.org/10.1021/ac00144a048.

Sengupta D., Bharath Raj G. N. and Shenoi S. S. C. (2006) Surface freshwater from Bay of Bengal runoff and Indonesian Throughflow in the tropical Indian Ocean Geophys. *Res. Lett.* **33**. https://doi.org/10.1029/2006gl027573.

Shenoi S. S. C., Shetye S. R., Gouveia A. D. and Michael G. S. (1993). *Salinity Extrema in the Arabian Sea* **76**, 37–49.

Shetye S. R., Gouveia A. D. and Shenoi S. S. C. (1994) Circulation and water masses of the Arabian Sea. *Proc. Indian Acad. Sci. (Earth Planet Sci.)* **103**, 107–123. https://doi.org/10.1007/BF02839532.

Singh S. K. and France-Lanord C. (2002) Tracing the distribution of erosion in the Brahmaputra watershed from isotopic compositions of stream sediments. *Earth Planet. Sci. Lett.* **202** (3-4), 645–662. https://doi.org/10.1016/S0012-821X(02)00822-1.

Singh S. K., Rai S. K. and Krishnaswami S. (2008) Sr and Nd isotopes in river sediments from the Ganga Basin: sediment provenance and spatial variability in physical erosion. *J. Geophys. Res.* **113**. https://doi.org/10.1029/2007jf000909.

Singh S. P., Singh S. K., Goswami V., Bhushan R. and Rai V. K. (2012) Spatial distribution of dissolved neodymium and εNd in the Bay of Bengal: Role of particulate matter and mixing of water masses. *Geochim. Cosmochim. Acta* **94**, 38–56. https://doi.org/10.1016/j.gca.2012.07.017.

Srinivas B. and Sarin M. M. (2013) Atmospheric dry-deposition of mineral dust and anthropogenic trace metals to the Bay of Bengal. *J. Mar. Syst.* **126**, 56–68. https://doi.org/10.1016/j.jmarsys.2012.11.004.

Srinivasan A., Rooth C. G. H., Top Z. and Olson D. B. (2000) Abyssal upwelling in the Indian Ocean: radiocarbon diagnostics. *J. Mar. Res.* **58**, 755–778. https://doi.org/10.1357/002224000321358891.

Tindale N. and Pease P. (1999) Aerosols over the Arabian Sea: Atmospheric transport pathways and concentrations of dust and sea salt. *Deep Sea Res. Part II* **46**, 1577–1595. https://doi.org/10.1016/s0967-0645(99)00036-3.

Tomczak M. and Godfrey J. S. (2003a) Chapter 12-Hydrology of the Indian Ocean. In *Regional Oceanography: An Introduction*, second ed, pp. 199–213 https://www.mt-oceanography.info/regoc/pdfversion.html.

Tomczak M. and Godfrey J. S. (2003b) Chapter 13-Adjacent seas of the Indian Ocean and the Australasian Mediterranean Sea (the Indonesian throughflow). In *Regional Oceanography: An Introduction*, second ed, pp. 215–228 https://www.mt-oceanography.info/regoc/pdfversion.html.

Tomczak M. and Large D. G. B. (1989) Optimum multiparameter analysis of mixing in the thermocline of the eastern Indian Ocean. *J. Geophys. Res.* **94**(C11), 16141. https://doi.org/10.1029/JC094iC11p16141.

Toole J. M. and Warren B. A. (1993) A hydrographic section across the subtropical South Indian Ocean. *Deep Sea Res. Part I* **40**(10), 1973–2019. https://doi.org/10.1016/0967-0637(93)90042-2.

Tréguer P. J. and De La Rocha C. L. (2013) The world ocean silica cycle. *Annu. Rev. Mar. Sci.* **5**(1), 477–501. https://doi.org/10.1146/annurev-marine-121211-172346.

Unger D., Ittekkot V., Schäfer P., Tiemann Jör and Reschke S. (2003) Seasonality and interannual variability of particle fluxes to the deep Bay of Bengal: influence of riverine input and oceanographic processes. *Deep Sea Res. Part II* **50**(5), 897–923. https://doi.org/10.1016/S0967-0645(02)00612-4.

Van Beueskom J. E. E., Van Bennekom A. J., Tréguer P. and Morvan J. (1997) Aluminium and silicic acid in water and sediments of the Enderby and Crozet Basins. *Deep Sea Res. Part II* **44**(5), 987–1003. https://doi.org/10.1016/S0967-0645(96)00105-1.

van Hulten M. M. P., Sterl A., Middag R., de Baar H. J. W., Gehlen M., Dutay J.-C. and Tagliabue A. (2014) On the effects of circulation, sediment resuspension and biological incorporation by diatoms in an ocean model of aluminium*. *Biogeosciences* **11**(14), 3757–3779. https://doi.org/10.5194/bg-11-3757-2014.

van Hulten M. M. P., Sterl A., Tagliabue A., Dutay J.-C., Gehlen M., de Baar H. J. W. and Middag R. (2013) Aluminium in an ocean general circulation model compared with the West Atlantic Geotraces cruises. *J. Mar. Syst.* **126**, 3–23. https://doi.org/10.1016/j.jmarsys.2012.05.005.

Vink S. and Measures C. I. (2001) The role of dust deposition in determining surface water distributions of Al and Fe in the South West Atlantic. *Deep Sea Res. Part II* **48**(13), 2787–2809. https://doi.org/10.1016/S0967-0645(01)00018-2.

Vu H. D. and Sohrin Y. (2013) Diverse stoichiometry of dissolved trace metals in the Indian Ocean. *Sci Rep* **3**(1). https://doi.org/10.1038/srep01745.

Warren B. A. (1981) Transindian hydrographic section at Lat. 18° S: Property distributions and circulation in the South Indian Ocean. *Deep Sea Res. Part A. Oceanogr. Res. Pap.* **28**, 759–788. https://doi.org/10.1016/S0198-0149(81)80001-5.

Wyrtki K. (rtki) Physical oceanography of the Indian Ocean. In *The Biology of the Indian Ocean* (ed. B. Zeitschel). Springer-Verlag, Berlin, pp. 18–36 https://link.springer.com/chapter/10.1007%2F978-3-642-65468-8_3.

You Y. (1997) Seasonal variations of thermocline circulation and ventilation in the Indian Ocean. *J. Geophys. Res. Ocean.* **102**, 10391–10422. https://doi.org/10.1029/96jc03600.

You Y. (1999) Dianeutral mixing, transformation and transport of the deep water of the Indian Ocean. *Deep Sea Res. Part I Oceanogr. Res. Pap.* **46**, 109–148. https://doi.org/10.1016/s0967-0637(98)00058-2.

You Y. (2000) Implications of the deep circulation and ventilation of the Indian Ocean on the renewal mechanism of North Atlantic Deep Water. *J. Geophys. Res.* **105**, 23895–23926. https://doi.org/10.1029/2000jc900105.

You Y. and Tomczak M. (1993) Thermocline circulation and ventilation in the Indian Ocean derived from water mass analysis. *Deep Sea Res. Part I Oceanogr. Res. Pap.* **40**, 13–56. https://doi.org/10.1016/0967-0637(93)90052-5.

Zender C. S., Bian H. and Newman D. (2003) Mineral Dust Entrainment and Deposition (DEAD) model: description and 1990s dust climatology. *J. Geophys. Res.*, 108.

Zweng M. M., Reagan J. R., Antonov J. I., Locarnini R. A., Mishonov A. V., Boyer T. P., Garcia H. E., Baranova O. K., Johnson D. R., Seidov D. and Biddle M. M. (2013). In *World Ocean Atlas 2013, Volume 2: Salinity*, 74 (eds. S. Levitus and A. Mishonov). NOAA Atlas NESDIS, 39 pp.

Associate Editor: Tina van de Flierdt